Universitat Politècnica de València
Departamento de Máquinas y Motores Térmicos

Implementation and Development of an Eulerian Spray Model for CFD simulations of diesel Sprays

Doctoral Thesis
Presented by:
Adrián Pandal Blanco
Directed by:
Dr. José María García Oliver

Valencia, June 2016

Doctoral Thesis

Implementation and Development of an Eulerian Spray Model for CFD simulations of diesel Sprays

Presented by: Adrián Pandal Blanco
Directed by: Dr. José María García Oliver

Examining Board:

President:	Prof. Raúl Payri Marín (Universitat Politècnica de València)
Secretary:	Dr. Bertrand Naud (CIEMAT, Madrid)
Examiner:	Dr. Gianluca D'Errico (Politecnico di Milano)

Valencia, June 2016

Abstract.

The main objective of this work is the modeling of diesel sprays under engine conditions, including the atomization, transport and evaporation processes pivotal in the diesel spray formation and its development. For this purpose, an Eulerian single fluid model, embedded in a RANS environment, is implemented in the CFD platform OpenFOAM.

The modeling approach implemented here is based on the Σ-Y model. The model is founded on the assumption of flow scales separation. In actual injection systems, it can be assumed that the flow exiting the nozzle is operating at large Reynolds and Weber numbers and thus, it is possible to assume a separation of features such as mass transport (large scales) from the atomization process occurring at smaller scales. The liquid/gas mixture is treated as a pseudo-fluid with variable density and which flows with a single velocity field. Moreover, the mean geometry of the liquid structures can be characterized by modeling the mean surface area of the liquid-gas interphase per unit of volume. Additionally, an evaporation model has been developed around the particular characteristics of the current engine technologies. This means that vaporization process is limited by fuel-air mixing rate and fuel droplets evaporate as long as there is enough air for them to heat up and vaporize. Consequently, the evaporation model is based on the Locally Homogeneous Flow (LHF) approach. Under the assumption of an adiabatic mixing, in the liquid/vapor region, the spray is supposed to have a trend towards adiabatic saturation conditions and to determine this equilibrium between phases Raoult's ideal law is considered. Finally, the spray model is coupled with an advanced combustion model based on approximated diffusion flames (ADF), which reduces the computational effort especially for complex fuels and is a natural step for modeling diesel sprays.

First, the model is applied to a basic external flow case under non-vaporizing conditions, extremely convenient due to both the experimental database available and the symmetric layout which allows important simplification of the modeling effort. Good agreement between computational results and experimental data is observed, which encourages its application to a more complex configuration. Secondly, the model is applied to the "Spray A" from the Engine Combustion Network (ECN), under non-vaporizing conditions, in order to reproduce the internal structure of diesel sprays as well as to produce accurate predictions of SMD droplets sizes. Finally, vaporizing "Spray A" studies are conducted together with the baseline reacting condition of this database. The calculated spray penetration, liquid length, spray velocities, ignition delay and lift-off length are compared with experimental data and analysed in detail.

Resumen.

El objetivo principal de este trabajo es el modelado de chorros diésel en condiciones de motor, incluyendo los fenómenos de atomización, transporte y evaporación fundamentales en la formación y desarrollo del chorro. Para este fin, se implementa un modelo de spray euleriano de tipo monofluido en un entorno RANS en la plataforma CFD OpenFOAM.

El enfoque de modelado aplicado aquí sigue la idea de un modelo del tipo Σ-Y. El modelo se fundamenta en la hipótesis de separación de escalas del flujo. En los sistemas de inyección actuales, es posible asumir que el flujo que sale de la tobera opera a altos números de Reynolds y Webber y por tanto, es posible considerar la independencia de fenómenos como el transporte de masa (grandes escalas del flujo) de los procesos de atomización que ocurren a escalas menores. La mezcla líquido/gas se trata como un pseudo-fluido con densidad variable y que fluye según un único campo de velocidad. Además, la geometría promedio de las estructuras de líquido se puede caracterizar mediante el modelado de la superficie de la interfase líquido/gas por unidad de volumen. Completando el modelo de chorro, se ha desarrollado un modelo de evaporación alrededor de las características particulares de las tecnologías actuales de los motores. Esto supone que el proceso de evaporación está controlado por mezcla aire-combustible y las gotas de combustible se evaporan siempre que exista suficiente aire para calentarlas y evaporarlas. Debido a esto, el modelo de evaporación implementado está basado en el enfoque de Flujos Localmente Homogéneos (LHF). Considerando una mezcla adiabática, en la región líquido/vapor, se supone que el chorro tiende a las condiciones adiabáticas de saturación y para determinar este equilibrio entre fases, se utiliza la ley ideal de Raoult. Finalmente, el modelo de chorro se acopla con un modelo avanzado de combustión basado en llamas de difusión aproximadas (ADF), que reduce el coste computacional especialmente para combustibles complejos y supone el paso lógico en el desarrollo del modelo para simular chorros diesel.

En primer lugar, el modelo se aplica al cálculo de un caso básico de flujo externo no evaporativo, muy adecuado tanto por la extensa base de datos experimentales disponible como por la simetría geométrica que presenta, permitiendo una importante simplificación de la simulación. Los resultados obtenidos presentan un buen acuerdo con los experimentos, lo cual estimula su aplicación en configuraciones más complejas. En segundo lugar, el modelo se aplica al cálculo del "Spray A" del Engine Combustion Network (ECN), no evaporativo, para reproducir la estructura interna del chorro diesel así como predecir tamaños de gota (SMD) de forma precisa. Finalmente, se realizan estudios evaporativos del "Spray A" junto con la condición nominal reactiva de esta base de datos. La penetración de vapor, la longitud líquida, velocidad, el tiempo de retraso y la longitud de despegue de llama calculados se comparan con los datos experimentales y se analizan en detalle.

Resum.

L'objectiu principal d'aquest treball és el modelatge de dolls dièsel en condicions de motor, incloent els fenòmens d'atomització, transport i evaporació fonamentals en la formació i desenvolupament del doll. Amb aquesta finalitat, s'implementa un model de doll eulerià de tipus monofluid en un entorn RANS a la plataforma CFD OpenFOAM.

L'enfocament de modelatge aplicat ací segueix la idea d'un model del tipus Σ-Y. El model es fonamenta en la hipòtesi de separació d'escales del flux. En els sistemes d'injecció actuals, és possible assumir que el flux que surt de la tovera opera a alts nombres de Reynolds i Webber, i per tant és possible considerar la independència de fenòmens com el transport de massa (grans escales del flux) dels processos d'atomització que ocorren a escales menors. La mescla líquid / gas es tracta com un pseudo-fluid amb densitat variable i que flueix segons un únic camp de velocitat. A més, la geometria mitjana de les estructures de líquid es pot caracteritzar mitjançant el modelatge de la superfície de la interfase líquid / gas per unitat de volum. Completant el model, s'ha desenvolupat un model d'evaporació al voltant de les característiques particulars de les tecnologies actuals dels motors. Això suposa que el procés d'evaporació està controlat per la mescla aire-combustible i les gotes de combustible s'evaporen sempre que hi hagi suficient aire per escalfar i evaporar. A causa d'això, el model d'evaporació implementat està basat en el plantejament de fluxos Localment Homogenis (LHF). Considerant una mescla adiabàtica, a la regió líquid / vapor, se suposa que el doll tendeix a les condicions adiabàtiques de saturació i per determinar aquest equilibri entre fases, s'utilitza la llei ideal de Raoult. Finalment, el model de doll s'acobla amb un model avançat de combustió basat en flamelets de difusió aproximades (ADF), que redueix el cost computacional especialment per a combustibles complexos i suposa el pas lògic en el desenvolupament del model per simular dolls dièsel.

En primer lloc, el model s'aplica al càlcul d'un cas bàsic de flux extern no evaporatiu, molt adequat tant per l'extensa base de dades experimentals disponible com per la simetria geomètrica que presenta, permetent una important simplificació de la simulació. Els resultats obtinguts presenten un bon acord amb els experiments, la qual cosa estimula la seva aplicació en configuracions més complexes. En segon lloc, el model s'aplica al càlcul del "Spray A" no evaporatiu de la xarxa Engine Combustion Network (ECN), per reproduir l'estructura interna del doll dièsel així com predir mides de gota (SMD) de forma precisa. Finalment, es realitzen estudis evaporatius del "Spray A" juntament amb la condició nominal reactiva d'aquesta base de dades. La penetració de vapor, la longitud líquida, velocitat, el temps de retard i la longitud d'enlairament de flama calculats es comparen amb les dades experimentals i s'analitzen en detall.

to my parents
my sister
and Gemma

Table of Contents

Index of Figures

Index of Tables

Nomenclature

Latin

c_p	Specific heat capacities at constant pressure
C_a	Area coefficient
C_d	Discharge coefficient
C_M	Momentum coefficient
C_v	Velocity coefficient
h	Enthalpy
L	Orifice length
l_t	Turbulent length scale
$\dot{m}$	Mass flow
$\dot{M}$	Momentum flux
Oh	Ohnesorge number
p	Pressure
Pr	Prandtl number
Re	Reynolds number
S	Spray penetration
S_c	Schmidt number
t	Time
T	Temperature
Ta	Taylor number
u	Velocity
V	Volume
We	Weber number
Y	Mass fraction

Greek

α_T	Turbulent thermal difussivity
Δ	Increment
μ	Turbulent dynamic viscosity
θ	Spray angle
ρ	Density
σ	Surface tension

Superscripts

o	Standard conditions

Subscripts

amb	Relative to ambient
eff	Effective
eq	Equivalent
$evap$	Relative to evaporative conditions
f	Relative to fuel
l	Relative to fuel liquid phase
g	Relative to gas
i	Inlet conditions of the injection orifice
inj	Relative to fuel injection
o	Outlet conditions of the injection orifice
th	Theoretical conditions

Initials and acronyms

CCD	Central composite design
CDM	Continuum droplets model
CFD	Computational fluid dynamics
CFL	Courant-Friedrichs-Lewy
CI	Compression-ignition engine
DBI	Diffused back-illumination
DDM	Discrete droplets model
DI	Direct injection
DIC	Diagonal incomplete cholesky
DNS	Direct numerical simulation
DOE	Design of experiments
ECN	Engine Combustion Network

ELSA	Eulerian lagrangian spray atomization
EVM	Eddy viscosity model
FDIC	Faster diagonal incomplete cholesky
GAMG	Geometric-algebraic multi-grid method
HBT	Hankinson-Brobst-Thomson
HP	High pressure
ICE	Internal combustion engine
ID	Ignition delay
IDI	Indirect injection
LES	Large eddy simulation
LHF	Locally homogeneous flow
LHS	Left-hand side
LL	Maximum liquid length
LOL	Lift-off length
MAC	Marker-and-cell
MP	Medium pressure
MW	Molecular weight
NVD	Normalised varaible diagram
PCG	Preconditioned conjugate gradient
PBiCG	Preconditioned bi-conjugate gradient
PDF	Probability density function
PDPA	Phase doppler particle analyser
PIV	Particle image velocimetry
PMD	Projected mass density
RANS	Reynolds average Navier-Stokes
RHS	Right-hand side
ROI	Rate of injection
RSM	Reynolds stress model / Response surface method
SMD	Sauter mean diameter
SOI	Start of injection
TH	Top-hat profile
TIM	Transverse integrated mass
TVD	Total variation diminishing
UFPV	Unsteady flamelet/progress varaible

USAXS	Ultra-small angle x-ray scattering
VCO	Valve closed orifice
VOF	Volume-of-fluid

Chapter 1

Introduction

Contents

1.1 Introduction

This introductory chapter serves to provide an overview of the whole document. In order to accomplish this, the diesel spray will be situated in the realm of reciprocating internal combustion engines. Moreover, the motivation behind this work of research will be explained as well as the planned objectives to be fulfilled. Finally, the methodology and contents of this document will be explained in detail.

1.2 Motivation of the study

The internal combustion engine (ICE) is one the greatest inventions since the industrial revolution. Since its appearance, the developer spirit of engineers together with growing knowledge of thermodynamics and combustion contributed to the rapid improvement of internal combustion engines which made them more reliable and efficient to use. It drives all manner of utility devices (pumps, mowers, generators, etc.), as well as all type of means of transport (tractors, propeller aircraft, ships, passenger cars and other road vehicles). Indeed, the transportation sector has been dominated by this type of engine for a century due to the high thermal efficiency and high power output to volume ratio as major features of it.

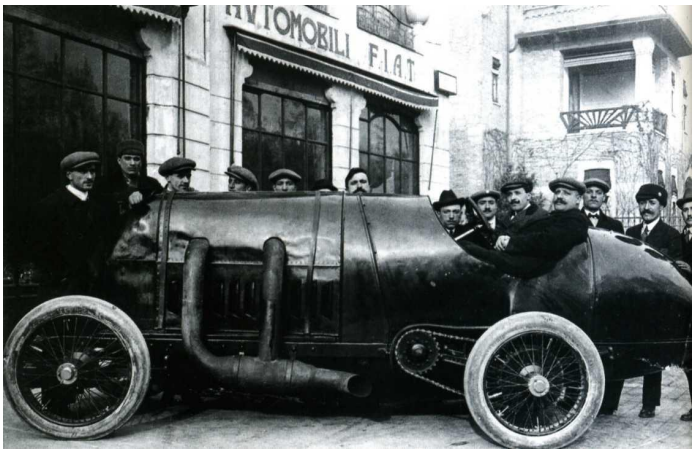

Figure 1.1. *The largest reciprocating engine ever purpose-built in a car. The FIAT S76 - also known as "The Beast of Turin", at over 28 litres, four cylinder, 300 hp.*

Its increasing use was linked to the economic growth and the industrialisation of the modern world and produced a steep rise of consumption of fossil fuels that continues until now. At first, people were not concerned about that and even more largest engines were produced to reach more power (see Figure 1.1). However, the situation has changed specially in the last decades. Nowadays, there is an ongoing demand for clean and efficient combustion devices and is in this context where the diesel engine has a paramount importance.

The compression-ignition (CI) engine is the most efficient, mass-produced internal combustion engine ever built for transportation purposes and is widely used all over the world for more than a century. However, environmental regulations and fuel economy requirements have become more restrictive in the last years all over the world and specially in the European Union [1, 2]. Furthermore, the prices of the fossil fuels, mostly used by means of transport, have been continuously increasing and are expected to do so in the near future. Thus, it is necessary to achieve both a maximum fuel-efficiency as well as a reduction of pollutant emissions in CI engines to maintain its viability as the primary power source in vehicles. In order to accomplish this goal, the understanding of fuel injection process and subsequent fuel-air mixing formation and evaporation is essential because they play a major role in combustion and pollutant formation. Otherwise, the mixture preparation may not be adequate and it could also results in zones with local equivalence ratios that are too poor or too rich, which could reduce the performance of the engine and increase the emission of air pollutants. Therefore, an accurate prediction of these processes is required.

At present, diesel engines are so sophisticated systems that any kind of improvement requires a really great effort. Fortunately, the advent of computers has created this new branch of scientific and engineering research, namely numerical simulation, which in combination with experimental tools has made possible advancements in this complicated field of science. Computer simulations became therefore an integral part in the design process of combustion systems and they can drastically speed up the design process at reduced costs. Simulations furthermore can provide additional information about the underlying problem, difficult or even impossible to obtain with experiments, which allows to study the different complex phenomena (heat transfer, gas dynamics, multi-phase flows, and turbulence-chemistry interactions) and hence increase the understanding of the pivotal processes in combustion. Nevertheless, as pointed out previously, it is impossible to have accurate combustion and pollutant predictions without the correct simulation of the spray formation process. In this sense, diesel spray modeling is still a

challenging task due to the complex interrelated phenomena involved [3, 4]; some of them, such as primary atomization [5] or nozzle cavitation [6], are not fully understood.

Thus, the further development of advanced spray models that enable a high-fidelity representation of such complex processes is crucial in the research, improvement and design of future diesel engines.

1.3 Objectives of the study

The main goal of this thesis is the numerical simulation of diesel sprays under engine conditions. Although one application of reacting sprays is considered, this work is mainly focused on inert spray conditions. This implies account for the atomization, transport and evaporation processes pivotal in the diesel spray formation and development. The reliable prediction of characteristic parameters like spray penetration and liquid length, together with fuel distribution is thus an important measure for spray models applied in this area.

In order to reach this objective, the implementation and validation of an advanced spray model in a CFD platform are the main tasks in this work. The necessity of an advanced model able to properly reproduce the physics of diesel sprays is a consequence of the well-known issues that typical Lagrangian particle models suffer for simulating this particular problem, further discussed in Section 3.1.1, as well as the lack of capabilities to directly include nozzle effects in the simulations. Thus, working on an Eulerian model seems to be more suitable to overcome the commented obstacles in order to fulfil the main target of this thesis. Moreover, a RANS approach has been chosen as working environment, mainly due to the reduced computational cost in comparison with more advanced techniques. Nevertheless, it is possible to extend the atomization model to LES approach without major modifications.

1.4 Methodology

The global methodology of this work is briefly outlined in the following. The first step consists on a bibliographic review of the spray formation process itself and the state of the art of spray modeling. Then, considering the pros and cons of each available approach and their future potential, it was decided to implement an Eulerian spray model based on the Σ-Y model [7]. Hence, in a such complex task, at the beginning an initial evaluation of

the implemented model on a basic configuration case should be the best procedure. As a result, the model is applied to a basic external flow case under non-vaporizing conditions, generated by a single-hole conical nozzle with the orifice oriented along the injector axis, extremely convenient due to both the experimental database available and the symmetric layout which allows important simplification of the modeling effort. Different studies have been preformed to define a proper modeling set-up (mesh, turbulence, etc.) in a first term and then, a wide range of operating conditions has been studied. The quality of the predictions achieved in this work encourages its application to a more complex configuration.

The spray model is then extended to coupled internal/external flow simulations and to external vaporazing flow, under inert and reacting conditions. In order to validate all these investigations, the database of the Engine Combustion Network (ECN) is selected due to it has available experimental measurements for all the conditions studied. The spray test cases simulated are different configurations of the so-called "Spray A", which uses n-dodecane as a surrogate for diesel fuel. Firstly, simulations are focused on the dense zone of the spray within the first few millimeters of the injector, the aim of which is to correctly reproduce the internal structure and the primary break-up process present in a diesel spray. Because of that, nozzle effects are included by coupling internal and external flow simulations that leads to a better representation of reality. After that, the investigation is moved to evaporative sprays. Under inert conditions the evaporation model implemented is validated against experimental measurements including a complete parametric variation set of studies (ambient temperature and density as well as injection pressure) in order to reflect operating conditions similar to those of modern diesel engines. Finally, the coupling of the spray model with an advanced combustion model based on approximated diffusion flames [8] is evaluated on diesel-like reactive sprays of the same ECN database, i.e. the reacting baseline operation condition of the "Spray A". This final test is a preliminary study to show the capabilities of the complete CFD model able to simulate the spray formation from the injection process, inside the nozzle, till the final combustion of the spray.

1.5 Outline of this work

The structure of the document is presented in the following:

- **Chapter 1**. The first and current chapter provides an overview of the whole document, it introduces the general frame of the work here developed and justifies it.

- **Chapter 2**. This chapter consists of a comprehensive bibliographic review that starts with some basic concepts about the fuel injection process, followed by some physics of the spray formation and its characterization and ends with an overview of trends in spray modeling.

- **Chapter 3**. The third chapter gives a complete description of the implemented Eulerian spray model, ranging from the initial implementation to the improvements developed within this PhD Thesis. First, fuel modeling approach is discussed in detail, including the benefits of the Eulerian treatment for DI diesel sprays. After that, in a first step, model fundamental transport equations are introduced together with its implementation on the CFD platform. The chapter is closed with the description of the developed sub–models, which complete the usefulness and accuracy of the model, including the coupling with an advanced turbulent combustion model based on the flamelet concept.

- **Chapter 4**. A first evaluation of the Eulerian spray model to simulate diesel sprays is presented in this chapter. A basic non-vaporizing configuration is simulated to test the spray model capabilities and to establish a proper modeling set-up. Moreover, parametric studies for different ambient and injection conditions are conducted in order to confirm the validity of the model in a wide range of operating conditions. The chapter ends with some preliminary conclusions.

- **Chapter 5**. In this chapter, the simulation of coupled internal/external flow is investigated as well as the effectiveness of decoupled simulations on a n-Dodecane spray non-vaporizing condition of the ECN. Model predictions, with a especial focus on the near nozzle spray structure are investigated and compared with experimental data. Conclusions of the obtained findings close this chapter.

- **Chapter 6**. A final application of the model is presented in this chapter. The n-Dodecane spray vaporizing condition of the ECN is simulated to validate the implemented evaporation model. After that, all the parametric variations (ambient temperature, ambient density and injection pressure) are investigated by comparison with experimental data. Finally, the coupled spray/combustion model is applied to the reference case of this n-Dodecane ECN spray under reacting conditions. The chapter is closed with the conclusions of the obtained results.

- **Chapter 7**. The document is closed in this last chapter with a summary of the main results and some general conclusions about the present work. Moreover, the proposal of potential future works of research will be presented.

Bibliography

[1] "Regulation (EC) No 715/2007 of the European Parliament and of the Council of 20 June 2007 on type approval of motor vehicles with respect to emissions from light passenger and commercial vehicles (Euro 5 and Euro 6) and on access to vehicle repair and maintenance information and amending Regulations (EC) No 692/2008, (EC) No 595/2009, (EC) No 566/2011 and (EC) No 459/2012". *Official Journal of the European Union*, 2007.

[2] "Regulation (EC) No 595/2009 of the European Parliament and of the Council of 18 June 2009 on type-approval of motor vehicles and engines with respect to emissions from heavy duty vehicles (Euro VI) and on access to vehicle repair and maintenance information and amending Regulation (EC) No 715/2007 and Directive 2007/46/EC and repealing Directives 80/1269/EC, 2005/55/EC and 2005/78/EC". *Official Journal of the European Union*, 2009.

[3] Faeth G.M. "Mixing, transport and combustion in sprays". *Progress in Energy and Combustion Science*, Vol. 13 n^o 4, pp. 293 – 345, 1987.

[4] Faeth G.M, Hsiang L.-P and Wu P.-K. "Structure and breakup properties of sprays". *International Journal of Multiphase Flow*, Vol. 21, Supplement, pp. 99 – 127, 1995. Annual Reviews in Multiphase Flow 1995.

[5] Gorokhovski Mikhael and Herrmann Marcus. "Modeling Primary Atomization". *Annual Review of Fluid Mechanics*, Vol. 40, pp. 343–366, 2008.

[6] Schmidt D. P. and Corradini M. L. "The internal flow of diesel fuel injector nozzles: a review". *Journal of Engine Research*, Vol. 2 n^o 1, pp. 1–22, 2001.

[7] Vallet A. and Borghi R. "Modélisation Eulerienne de l'atomisation d'un jet liquide". *C.R. Acad. Sci, Paris*, Vol. 327, pp. 1015–1020, 1999.

[8] Winklinger J.F. *Implementation of a Combustion Model based on the Flamelet Concept and its Application to turbulent reactive Sprays*. Doctoral Thesis, Departamento de Máquinas y Motores Térmicos, Universidad Politécnica de Valencia, España, 2014.

Chapter 2

Bibliographic review

Contents

2.1 Introduction

The understanding of physical processes behind the diesel spray formation is essential because they play a major role in combustion and pollutant formation of CI engines, used in several industrial applications. This processes are mainly fuel injection and the subsequent fuel-air mixing. Their studying is a challenging task due to the turbulent and transient character of the spray and the small spatial and temporal scales in which it evolves. As a result, nowadays, CFD simulations gives support to experimental investigations in order to help in the understanding of diesel spray and the design and developing of combustion systems.

In this chapter general aspects of the fuel injection process are introduced as well as a physical description of diesel spray and its modeling.

2.2 Injection process – Basic concepts

The injection system is in charge of the fuel supply to the internal combustion engine and the preparation of the fuel-air mixing for the combustion process. Thus, both combustion process efficiency and pollutant emissions formation are to a large degree dependent on the injection system performance. According to how the fuel is delivered into the combustion chamber, injection systems can be classified in two categories: indirect injection (IDI) and direct injection systems (DI). Nevertheless, over the last years DI systems have been the most used system because of the lower fuel consumption and the higher efficiency achieved with them. Nowadays the most used is the *Common-Rail* system.

In Figure 2.1 a schematic representation of a *Common-Rail* injection system is displayed. Between the high pressure pump and the injectors there is an intermediate element. Using this rail or *Common-Rail*, it is possible to give a constant and controlled injection pressure. The injectors are electronically actuated, which allows a great control over the start and duration of the injection process. Thus, the process can be divided in several stages in order to reduce the noise problem, improve the combustion and limit the pollutant emissions. In addition, these systems can work at very high injection pressures (more than 200 MPa) that enhances fuel atomization, the evaporation process and the mixing with the gas present inside the combustion chamber.

In the present work, the study is focused on the external spray flow (outside the nozzle) and it is only considered the internal flow simulation (without

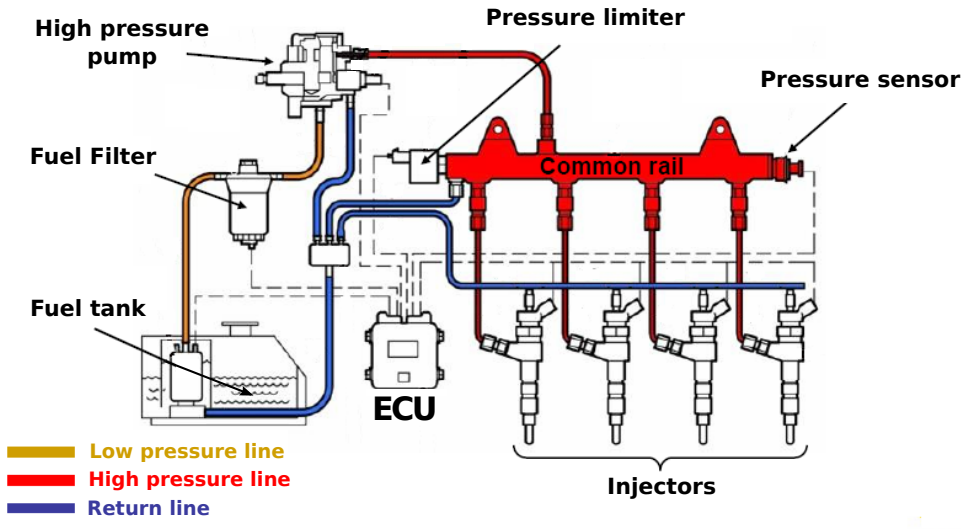

Figure 2.1. *Common-rail system general scheme.*

cavitation phenomena) in order to quantify how it affects the external flow development of the spray. For this reason, it is necessary to know some characteristics of the injector nozzles and the parameters used to describe the flow at the nozzle exit.

2.2.1 Injector nozzle geometry

Studying the diesel spray formation, injector nozzle characteristics are key parameters and play a major role in the spray behaviour inside the combustion chamber.

Figure 2.2, shows a representation of the typical geometry of a injector nozzle. The two types of nozzle most widely used are shown: VCO (valve closed orifice) and microsac. In the VCO nozzles, needle position strongly influences the fuel flow characteristics during opening/closing transients of the injector, while in the other type, the volume of the sac minimizes this effect. However, microsac nozzles present a problem of residual fuel injection that, after needle closing, remains into the sac. This fuel injection, under not well defined conditions, can result in a low efficiency combustion process, increasing unburned hydrocarbons and soot formation.

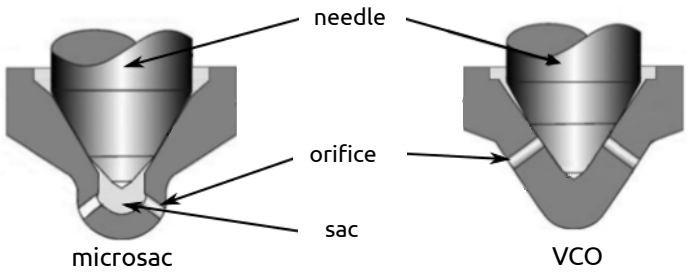

Figure 2.2. *Injection nozzle types, microsac (left), VCO (right).*

Nozzle orifices are responsible of the flow acceleration when fuel is forced to move through the injector channels by the injection pressure (pressure difference). As a result, geometric parameters have a great influence on the spray characteristics. In Figure 2.3, an schematic representation of a injector nozzle orifice is shown, where its main geometric parameters are depicted: inlet diameter (D_i), outlet diameter (D_0), orifice length (L) and entrance radius (r_e). From these dimensions, some parameters can be defined which characterize the shape of the orifice. Among them, the orifice convergence is usually defined in the literature in terms of the *k-factor* [1] which is calculated by Equation 2.1:

$$k - factor = \frac{D_i - D_0}{10\ [\mu m]} \tag{2.1}$$

However, the inlet/outlet diameters ratio (D_i/D_0), also gives an adequate characterization of the conical or cylindrical shape of the nozzle orifice.

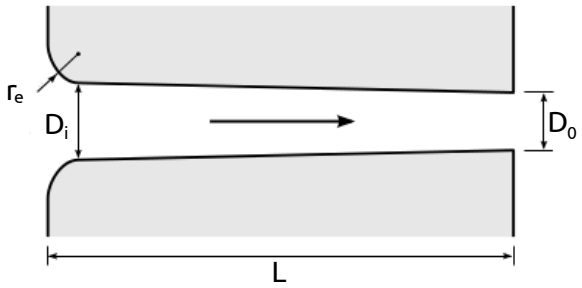

Figure 2.3. *Geometric parameters of the nozzle orifice.*

2.2.2 Hydraulic characterization of the nozzle

The complexity of the study of fuel flow through the injector nozzle orifice lies in the small geometric dimensions of the orifices and the high velocities that are reached inside them. This is the reason why the analysis of the internal flow through the injector channels is commonly made with parameters measured at the orifice exit. One of them is the discharge coefficient (C_d), calculated as the ratio between the real mass flow and the theoretical one from Bernoulli's equation. The theoretical mass flow rate can be evaluated by the Equation 2.2, being u_{th} (Equation 2.3) the theoretical velocity obtained from Bernoulli's equation between a point upstream and the orifice exit, A_0 the geometric area and ρ_f the density of the injected liquid fuel.

$$\dot{m}_{f,th} = \rho_f \; u_{th} \; A_0 \tag{2.2}$$

$$u_{th} = \sqrt{\frac{2\Delta p}{\rho_f}} \tag{2.3}$$

Thus, the discharge coefficient can be calculated by the following expression:

$$C_d = \frac{\dot{m}_f}{\dot{m}_{f,th}} = \frac{\dot{m}_f}{A_0\sqrt{2\rho_f\Delta p}} \tag{2.4}$$

This coefficient measures the efficiency of an orifice in delivering a given mass flow, and this includes the wall friction pressure losses but also losses due to non-uniform velocity profile at the orifice exit. Having this into account, it is possible to define a uniform velocity profile that ensures the real mass flow rate (Figure 2.4). The value of this velocity profile is the effective velocity, u_{eff}, and the section where it flows through is the effective area, A_{eff}.

$$\dot{m}_f = \rho_f \; u_{eff} \; A_{eff} \tag{2.5}$$

Therefore, losses included in the discharge coefficient can be divided into two parts: area reduction due to the non-uniform velocity profile, which is accounted for in the area coefficient (C_a), and the pressure losses, included in the velocity coefficient (C_v).

$$C_d = C_a \; C_v = \frac{A_{eff}}{A_0} \; \frac{u_{eff}}{u_{th}} \tag{2.6}$$

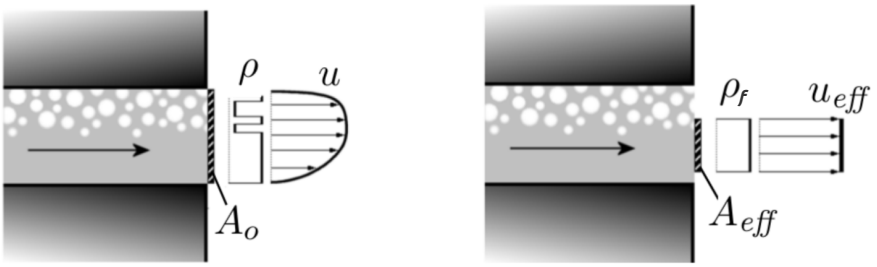

Figure 2.4. *Schematic view of the injection nozzle outlet hole. Effective area and velocity.*

It is reasonably easy to measure the value of the discharge coefficient, however its decomposition into the area and velocity contributions is really challenging. In order to solve this problem, some methodologies have been developped to measure the momentum flux of the spray at the orifice exit [2–4].

In the same way as with the mass flow rate, it is possible to determine a theoretical momentum flux (Equation 2.7) and thus, define a momentum coefficient C_M (Equation 2.8):

$$\dot{M}_{th} = \rho_f \; u_{th}^2 \; A_0 \tag{2.7}$$

$$C_M = \frac{\dot{M}}{\dot{M}_{th}} = \frac{\dot{M}}{2 \; A_0 \; \Delta p} \tag{2.8}$$

In addition, effective area and velocity are defined to ensure that the momentum flux is also the real one [2]:

$$\dot{M} = \rho_f \; u_{eff}^2 \; A_{eff} \tag{2.9}$$

As a result, by measuring the mass flow rate and momentum flux together, the effective values that characterize the flow through the nozzle orifice can be obtained without knowing the internal geometry parameters of it.

$$u_{eff} = \frac{\dot{M}}{\dot{m}_f} \tag{2.10}$$

$$A_{eff} = \frac{\dot{m}_f^2}{\rho_f \; \dot{M}} \tag{2.11}$$

2.3 Diesel spray development

Diesel spray formation occurs when the liquid fuel is mixed with the surrounding gas of the discharge chamber. This mixing is a consequence of several physical processes, which have been studied for years due to the spray formation playing a major role in the subsequent stages of the combustion process. However, some of these processes and some aspects of the internal structure of the spray, are still not fully understood.

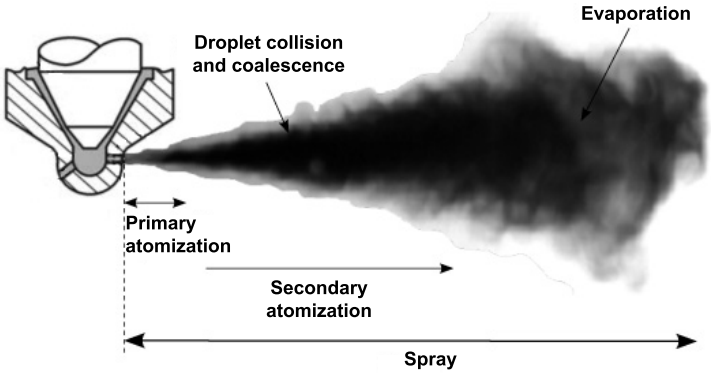

Figure 2.5. *Diesel spray structure.*

In general, physical phenomena which drive the fuel spray formation are: atomization and coalescence, momentum transfer between the droplets and surrounding air, turbulent interaction and evaporation. In Figure 2.5, a schematic view of a free spray is shown, i.e., neglecting the phenomena involved when the spray reaches the wall of the combustion chamber (impingement). Considering the spray at the injector orifice outlet, the first millimeters make up the so-called "liquid core", where the liquid vein remains unbroken. Then, internal instabilities caused by inertial effects together with the turbulent flow, induced by the injector nozzle, produce the segregation of the liquid core into relatively large liquid structures called ligaments. This first stage is known as *primary atomization*. Afterwards, these ligaments break into smaller formations (droplets) as a result of the interaction between the surface tension and the aerodynamic forces, produced by the relative velocity to the surrounding gas. This second segregation is called *secondary atomization*. At the end of the process, an heterogeneous distribution of fuel droplet sizes is achieved. These droplets mix with the surrounding gas at the chamber

(air entrainment) and, if the environmental conditions are adequate, fuel is evaporated.

2.3.1 Atomization

Atomization of the liquid fuel is the phenomenon that takes place after the injection process has been initiated. It consists in the conversion of the liquid core of the fuel into very fine droplets which increase the area in contact between the fuel and air, and therefore help the subsequent processes of air entrainment and evaporation. The break-up of liquid jet is a consequence of interaction occurring at microscopic scale, involving aerodynamic interactions and surface tension forces, ones promoting the liquid disintegration and others keeping it compact, respectively. As a result, it is caused by a sum of several independent effects, which depending on the injection conditions and the nozzle geometry, present different level of influence [5–10]. According to the role of the turbulent flow and the aerodynamic forces on the spray break-up, two different phases of the atomization process can be distinguished:

- **Primary atomization**. This process takes place in the first millimeters of the spray and is responsible of the disintegration of the intact liquid core. This break-up occurs due to the action of internal forces such as, inertial instabilities, effects of the turbulent flow, the reorganization of the velocity profile at the nozzle orifice outlet [5] and the cavitation phenomenon.
- **Secondary atomization**. Ligaments or relatively large droplets, formed during the primary atomization, are still moving at high speed in the discharge gaseous atmosphere and, thus, aerodynamic forces affect them and cause a new disintegration which results in smaller droplets.

Primary atomization regimes

Physical processes occurring during the atomization have been studying, both experimentally and theoretically, for many years. Starting with the Rayleigh [11, 12] theory for non-viscous fluids injected with low velocity, conditions at which atomization occurs due to surface tension forces. Then, the experimental studies conducted by Haenlein [13] that motivate the theoretical parallel research by Weber [14], in which Rayleigh theory were extended to viscous fluids and accounts for the effect of aerodynamic interactions. Following with Ohnesorge [15] studies, where the transition between the

different documented atomization regimes was investigated. Finally, the studies by Reitz [16, 17], where the break-up regimes can be classified as follows for a cylindrical jet (see Figure 2.6):

- **Rayleigh regime**. This regime is observed at the lowest jet velocities. In this case, the perturbations at the surface of the jet caused by the effect of surface tension deform the liquid vein until is separated in droplets, whose sizes are uniform and larger than the outlet orifice diameter.
- **First wind-induced regime**. As a consequence of increasing velocity, the effect of the forces generated by the relative velocity between the jet and the surrounding ambient become more important. In this way, the friction forces effect plays the same role of the surface tension and ease droplet formation. In this regime, as in the first one, the droplets are generated far downstream of the discharge orifice and their size is similar to the outlet orifice diameter.
- **Second wind-induced regime**. Increasing again the jet velocity, the atomization process is more efficient. The initial perturbations are amplified by the aerodynamic forces and the break-up occurs closer to the orifice. The average size of the formed droplets is much smaller than the outlet orifice diameter (comparable to the wavelength of the initial perturbations).
- **Atomization regime**. The jet disintegration occurs in the immediate proximity of the orifice (closer as highest injection velocity). In this case, there are two possibilities depending on the presence of the intact liquid core[1]. Thus, two atomization regimes are commonly defined: incomplete and complete, in which the intact core can be observed or not. The size of the formed droplets is again much smaller than the outlet orifice diameter.

Probably, even more important than identifying the different atomization regimes, is quantifying their transitional limits, both quantitative and qualitative. For this purpose, some pivotal physical parameters affecting the atomization process are the following:

[1]Distance from the outlet orifice till the point where the break-up of the jet takes place due to the atomization process.

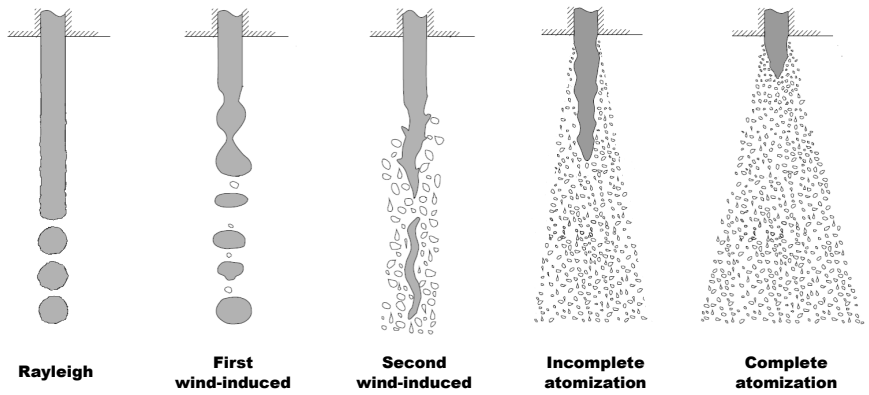

Figure 2.6. *Schematic representation of spray structure under the different atomization regimes.*

- Fuel density, ρ_f.
- Gas density, ρ_g.
- Relative velocity between fuel and gas or effective velocity, u_{eff}.
- Effective diameter, D_{eff}.
- Fuel viscosity, μ_f.
- Fuel surface tension, σ.

In this quantification study, Ohnesorge [15] showed that the disintegration process can be described by the Weber number (Equation 2.12) of the fuel and the Reynolds number (Equation 2.13).

$$We_f = \frac{u_{eff}^2 \; D_{eff} \rho_f}{\sigma} \tag{2.12}$$

$$Re = \frac{u_{eff} \; D_{eff} \rho_f}{\mu_f} \tag{2.13}$$

And operating with both numbers in order to eliminate the spray velocity u_{eff}, Ohnesorge derived the dimensionless Ohnesorge number:

$$Oh = \frac{\sqrt{We_f}}{Re} = \frac{\mu_f}{\sqrt{\sigma \rho_f \; D_{eff}}} \tag{2.14}$$

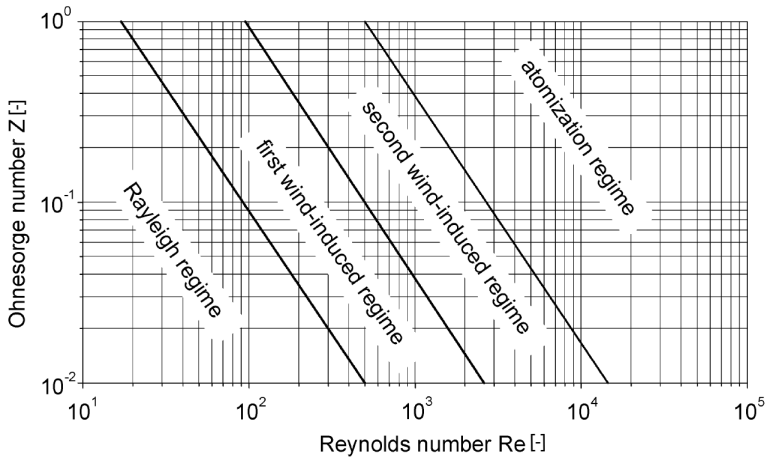

Figure 2.7. *Ohnesorge diagram: atomization regimes. Figure adapted from Baumgarten [18].*

In Figure 2.7, the *Ohnesorge diagram* is shown. In this representation, the borders between the four atomization regimes are identified as in [19]. However, only the fuel properties are considered on this diagram, which results insufficient because of not taking into account the ambient gas phase effects (pressure-density), as evaluated by Torda [20]. As a result, Reitz [16] propose to include the density ratio ρ_g/ρ_f and in this way, extend the two-dimensional Ohnesorge diagram to a new three-dimensional one, Figure 2.8.

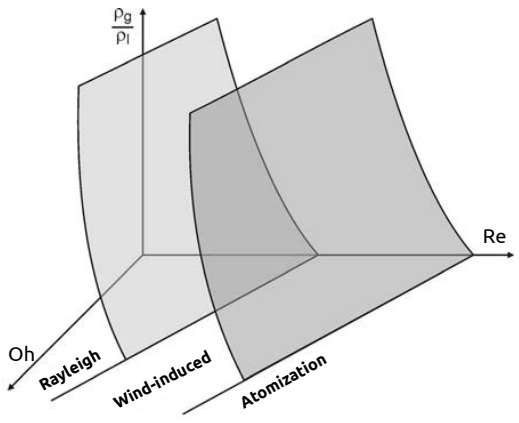

Figure 2.8. *Schematic diagram of atomization regimes including the effect of density ratio. Figure adapted from Baumgarten [18].*

Finally, using a fixed injector nozzle geometry and a liquid with constant properties, the only variable is the jet exit velocity. For this reason, disintegration mechanisms can be characterized by the relationship between velocity at the orifice outlet and intact core length (McCarthy and Molloy [21], Lefebvre [8], Lin and Reitz [22], Dumouchel [23]), see Figure 2.9. In this profile five different regimes are shown: dripping[2] (region A), Rayleigh regime (region B), first wind-induced regime (region C), second wind-induced regime (region D) and atomization regime (region E). The four last regimes can be related with the turbulence level at the orifice exit [8]: laminar flow (region B), transitional flow (region C), turbulent flow (regions D and E).

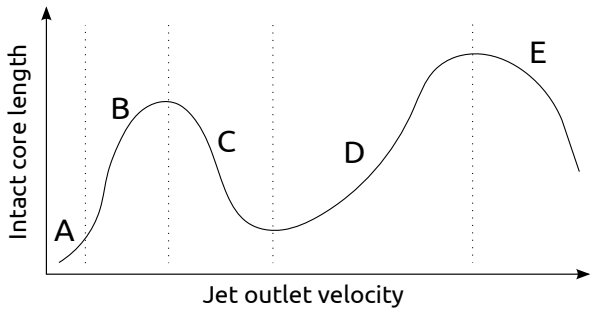

Figure 2.9. *Surface of intact core length of a cylindrical liquid spray as function of velocity at the orifice outlet.*

The quantification of the atomization regimes borders has been studied for decades. Table 2.1 shows some of the existing criteria to define them, where We_g is the ambient gas Weber number (Equation 2.12 with the gas density). In the expression proposed by Reitz [16], to characterize the transition to the atomization regime, the constant A is calculated from the spray angle, which has to be experimentally measured and Ta is the dimensionless Taylor number (Equation 2.15). Thus, internal flow parameters, which are key to determine the atomization at high Weber numbers [17], are somehow considered.

$$Ta = \frac{\rho_f}{\rho_g}\left(\frac{Re}{We_g}\right)^2 \tag{2.15}$$

Nonetheless, under the actual operating conditions of present diesel engines, as Arrègle [27] establishes, the spray characteristics fall into the two last regimes: the second wind-induced and the atomization regimes. At the

[2]Dripping regime has no interest in diesel spray studies, which are characterized by a high injection velocity of the fuel.

Table 2.1. *Definition of the transition criteria between atomization regimes.*

Regime	Expression	Reference
B - C	$We_g = 0.4$	[24]
	$We_g = 1.2 + 3.41Oh^{0.9}$	[25]
C - D	$We_g = 13$	[24]
D - E	$We_g = 40.3$	[19]
	$\frac{\rho_g}{\rho_f} = \frac{\sqrt{A}-1.15}{744} f(Ta)^{-2}$	[16]
	$f(Ta) = \frac{\sqrt{3}}{6}(1 - e^{-10Ta})$	[26]

latter regime, if it exists, intact core length is about a few orifice diameters becoming independent of the fuel exit velocity and the size of the droplets.

In summary, primary atomization is a pivotal process because of being responsible of the ligaments formation near the spray surface, and the aforementioned ligaments lead to the atomization process itself [28]. In addition, it defines the initial conditions of the dispersed multiphase flow region and controls the extension of the intact liquid core. However, the knowledge about this zone is limited due to is a dense spray region that can not be measured using conventional optical techniques. Recently, many studies of this region of the spray have been conducted with special diagnostics such as x-ray radiography [29–33] or ballistic imaging [34].

Secondary atomization regimes

In the case of secondary atomization, aerodynamic forces produce some deformation in the droplet surface that can lead to the break-up of them into smaller ones. This occurs when the opposite forces, associated to the surface tension, that tend to maintain the original spherical shape of the droplet are exceeded. The surface tension depends on the curvature and thus, smaller droplets present higher cohesive forces. In the study of the secondary atomization, in order to quantify the magnitude of these forces the Weber number of the droplet[3] is used, which is defined using the gas density, the relative velocity between the droplets and the surrounding gas and the droplet diameter, Equation 2.16. It is also common to use the Ohnesorge number together with the previous one [35].

[3]The Weber number of the droplet represents the ratio between aerodynamic forces and surface tension.

$$We_d = \frac{u_{rel}^2 D_d \rho_g}{\sigma} \tag{2.16}$$

Over the years, several experimental studies have shown that depending on the Weber number exist different mechanisms of droplets break-up [36–39]. According to Wierzba [40], five different regimes depicted in Figure 2.10 of secondary atomization can be distinguished. In terms of transitional Weber numbers among regimes, the values present in the literature can differ, especially in the case of break-up mechanisms under high Weber numbers, see Table 2.2.

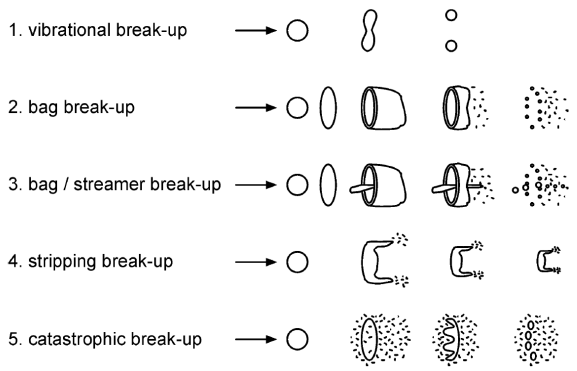

Figure 2.10. *Secondary atomization regimes according to Wierzba [40].*

Table 2.2. *Definition of the transition Weber numbers between secondary atomization regimes.*

Regime	**Wierzba [40]**	**Arcoumanis et al. [41]**
Vibrational	$We_d \approx 12$	$We_d \approx 12$
Bag	$We_d < 20$	$We_d < 18$
Bag and streamer	$We_d < 50$	$We_d < 45$
Stripping	$We_d < 100$	$We_d < 1000$
Catastrophic	$We_d > 100$	$We_d > 1000$

Under engine conditions, although all the atomization mechanisms take place, the majority of the processes of disintegration occur in the near nozzle

region where the Weber number is really large and thus, the dominant mechanism is the catastrophic break-up.

Droplet collision and coalescence

At the same time and location that the second atomization takes place, the coalescence phenomenon as well as bouncing of droplets (droplet-droplet interactions) also occurs. The coalescence is defined as the process by which two or more droplets merge during contact to form a single droplet. The contact or collision probability depends on the relative velocity between the droplets, their relative direction and the local fuel concentration. Therefore, collision is more frequent in the dense region of the spray, i.e. in the near nozzle region and the axis of the spray.

Droplet collision processes are really complex and depends on different characteristics of the droplets and the ambient conditions. There are four important dimensionless parameters governing the collision phenomenon [18]: the Reynolds and Weber numbers of collision, the droplet diameter ratio between the droplets that collide $D_{d,2}/D_{d,1}$($D_{d,1}$ the diameter of the larger drop and $D_{d,2}$ of the smaller) and the impact parameter B, which value varies from 0 to 1 depending on the type of collision.

$$Re_{coll} = \frac{u_{rel} D_{d,1} \rho_f}{\mu_f} \tag{2.17}$$

$$We_{coll} = \frac{u_{rel}^2 D_{d,2} \rho_f}{\sigma} \tag{2.18}$$

Collision result can be classified in five different regimes: bouncing, coalescence, reflexive separation, stretching separation and shattering collision. In Figure 2.11 a schematic representation of the different coalescence regimes is shown. But a criterion has to be specified to determine which of the different regimes occurs [42, 43]. Qian y Law [42] defined the transition between these five collision regimes in terms of the collision Weber number and the impact parameter, see Figura 2.12. They also proved that an increase of gas density promotes bouncing, while a gas atmosphere with a high content of evaporated fuel promotes coalescence. Finally, they highlight that the numbers and size of the new droplets resulting from a collision event strongly depend on the diameter ratio of the parent droplets.

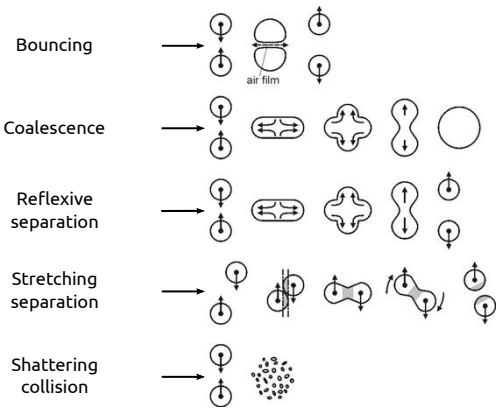

Figure 2.11. *Mechanisms of droplet collision, coalescence regimes. Figure adapted from Baumgarten [18].*

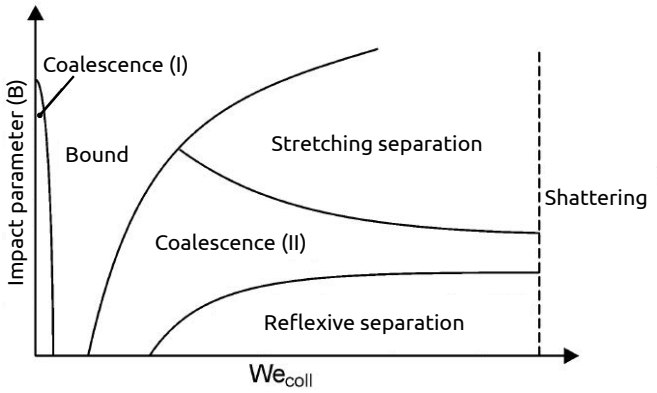

Figure 2.12. *Schematic map of droplet collision regimes borders. Figure adapted from Baumgarten [18].*

2.3.2 Evaporation

At the end of the whole atomization process, the injected fuel has been transformed into a distribution of small droplets that exchange energy with the surrounding gas present at the combustion chamber. When the temperature of the gas is high enough, heat is transferred to the droplet surface due to conduction and convection [8], increasing droplet temperature and, as a result, vapor pressure. This phenomenon leads to the liquid fuel evaporation and the local mixture approaches the adiabatic saturation conditions [44].

Examining the evaporation process in detail, three phenomena area found to determine the evolution of a fuel drop under engine conditions [45]:

- Deceleration of the droplets due to aerodynamic drag
- Heat transfer to droplets from the air
- Mass transfer of vaporized fuel away from the droplets

As the droplets travel through the air, their velocity decreases due to aerodynamic drag having more time to exchange heat with the air. Additionally, since the surface area of the droplet is largest, the heat transferred from the air is high, leading to a rapidly increasing evaporation rate, as the evaporation is a surface phenomenon. The heat transfer also rises the temperature, which causes the vapor pressure to increase and so does the evaporation rate [45]. Droplet sizes become increasingly smaller but its surface area is decreasing quadratically. This causes the heat transfer to change dramatically and the evaporation rate to reach a maximum peak. The temperature of the droplet starts reaching an asymptotic state, as its temperature is much closer to that of the air than that of the injected fuel, and also becuase the surface area of the drop keeps getting smaller until it eventually disappears. Figure 2.13 shows the evolution of the aforementioned phenomenon of a single droplet under engine conditions. An important remark to be made is the difference between the heat transferred from the air and the heat transferred to the liquid droplet. The latter is smaller, as part of the air energy is spent on the change of phase of the fuel at the surface and the heating up of the vaporized fuel.

The study of the evaporation process from the microscopic point of view is complex and multidisciplinary, it involves heat and mass transport as well as fluid dynamics problems [46]. That is why many researchers prefer a macroscopic study of diesel spray evaporation under engine conditions, i.e. in terms of *maximum liquid length*[4]. While at first instants of the injection the liquid phase reaches the tip of the spray, from a particular distance (liquid length), fuel on liquid phase disappears and is only present on vapour phase mixed with the air [47–50].

From experimental observations, liquid length depends on different parameters that affects the spray development, such as nozzle diameter, temperature and gas density at the chamber and thermodynamic properties of the injected fuel. However, injection pressure seems to have not a great

[4]Since now only 'liquid length'.

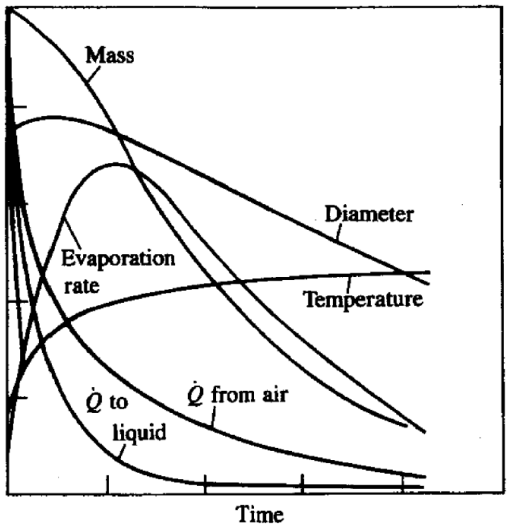

Figure 2.13. *Schematic time evolution of mass, diameter, temperature, evaporation rate, heat-transfer rates during evaporation process of individual droplet in diesel environment as shown in [45].*

influence [50–52]. Siebers [52] concluded that the evaporation process of DI diesel sprays, under engine conditions, is mainly *mixing-controlled*. The energy that allows the fuel evaporation is transferred from the entrained air as a consequence of the turbulent mixing and therefore the liquid evaporates till reaching a characteristic mixture fraction. In addition, the processes of mass, momentum and energy diffusion between phases seem to be not as pivotal as turbulent mixing and that reinforces the hypothesis of local thermodynamic equilibrium at the spray under vaporization conditions. Thus, many researchers study the diesel vaporizing spray assuming a behaviour similar to a gas jet [53–55].

2.4 Spray characterization

Once the atomization process and spray formation has been described, it is essential to know the parameters used for studying sprays. The diesel spray characterization is usually made from two points of view: macroscopic, which investigates the global shape of the spray (mainly spray penetration, angle

and liquid length) and microscopic, focused on local parameters (velocity and concentration distributions and droplet size).

Before analysing in depth the different parameters that characterize the spray, one can defined two zones from a macroscopic point of view (see Figure 2.14). The first one is the steady zone, i.e. a zone that not evolves with time, that extends till the $60 - 70\%$ of the length of the spray and at which the spray has a conical aspect. The second one, placed at the tip of the spray and semi-elliptic due to the aerodynamic interaction with the ambient gas, is the transient zone.

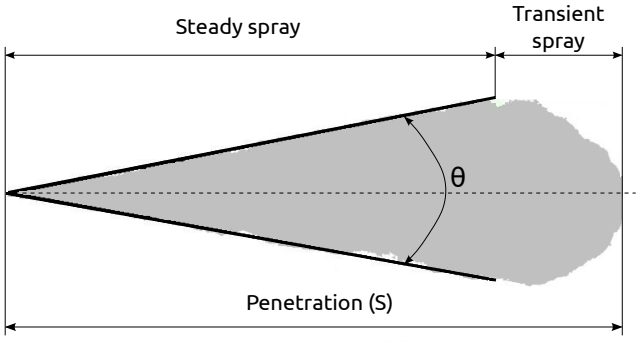

Figure 2.14. *Spray macroscopic description: penetration and angle.*

Spray penetration

Spray penetration (S) is the furthest axial distance reached by the tip of the spray (see Figure 2.14). Studying of the spray tip penetration is really important, it is a fundamental parameter not only because it measures the fuel-air mixing but also because it determines the possible wall impingement, a key factor for the combustion process and pollutant emissions formation.

The spray penetration depends mainly on the spray momentum, the ambient density, the spray spreading angle and, obviously, the time of injection. From the wide number of studies that can be found in the literature, many correlations have been proposed, based on the analysis of the diesel spray as a gas jet, to link the spray penetration to the characteristic injection conditions, that can be easily measured, such as injection pressure, orifice diameter, ambient density, etc. Hay and Jones [56], after a huge review of the literature available at the time, highlighted that spray penetration correlations are in the form of Equation 2.19.

$$S(t) \propto \rho_g^{-1/4}\ \Delta p^{1/4}\ D_0^{1/2}\ t^{1/2} \tag{2.19}$$

Correlations available at the literature differ on the proportionality constant value. Some examples appear at Table 2.3.

Table 2.3. *Values of the proportional constant in the correlations for the spray penetration, following Equation 2.19.*

Author	**Expression**
Wakuri et al. [57]	$\frac{(2\ C_d^3)^{1/4}}{(tan\theta/2)^{1/2}}$
Dent [58]	$3.33\ C_d^{1/2}\left(\frac{295}{T}\right)$
Hiroyasu y Arai [59]	2.95

A similar expression written in terms of spray momentum flux is developed by Desantes et al. [60]. However, this theoretical penetration law (Equation 2.20) is perhaps more predictable due to the spray penetration, as previously introduced, depends mainly on the spray momentum flux, which characterizes the flow at the orifice exit in a better way than the pressure difference.

$$S(t) \ = \ \left(\frac{2\alpha}{\pi}\right)^{1/4}\ \left(\frac{2}{K_u}\right)^{1/2}\ tan(\theta/2)^{-1/2}\ \dot{M_0}^{1/4}\ \rho_g^{-1/4}\ t^{1/2} \tag{2.20}$$

where α and K_u are two universal constants with values of 4.605 and 2.076 respectively.

Using all this expressions fairly good predictions are achieved to describe the spray penetration at positions relatively far from the orifice exit. However, the first millimeters of the penetration present a linear proportionality with the time, reason why some correlations are divided into two parts. Hiroyasu and Arai [59] related the lineal behaviour with the break-up length:

$$S(t < t_b) \ = \ 0.39\sqrt{\frac{2\Delta p}{\rho_g}}\ t \tag{2.21}$$

where the time t_b is

$$t_b = 28.65 \frac{\rho_f \ D_0}{(\rho_g \ \Delta p)^{1/2}} \tag{2.22}$$

While other authors relate this behaviour with the moment at which the spray penetration is controlled by air entrainment (Naber and Siebers [61]), or with the time needed by the needle to reach its maximum lift (Desantes et al. [62]), giving slightly different correlations to the one proposed by Hiroyasu and Arai [59].

Spray Angle

As penetration, the spray angle (θ) is one of the most widely studied parameters in the literature. It is usually defined as the angle included by two lines fitting the two sides of the spray contour, see Figure 2.14. This is also a fundamental parameter driving the entrainment of air in the spray and thus, having great influence on the fuel evaporation and combustion processes. After a transient short time after start of injection, this angle stabilizes at a certain value.

Again, different correlations to predict the behaviour of the spreading angle can be found in the literature. One of the first, was presented by Ranz [24], giving the Equation 2.23, where F_t represents an analytical expression that, for typical Diesel injection conditions, reaches its limit value F_t of 0.288. However, this expression contains a constant, C, that needs to be tuned for the specific nozzle geometry.

$$tan\left(\frac{\theta}{2}\right) = \frac{4\pi}{C}\sqrt{\frac{\rho_f}{\rho_g}} F_t \left(\frac{\rho_g}{\rho_f}\frac{\sigma^2}{\mu_f^2 u_0^2}\right) \tag{2.23}$$

Reitz and Bracco [63] carried out an extensive experimental study including several variations in the internal geometry, which led them to obtain Equation 2.24 as the solution for the constant C. However, this definition gives good predictions only for geometries similar to the ones employed by Ranz [24] but loses its effectiveness when the geometry is radically changed.

$$C = 3 + \frac{L/D_0}{3.6} \tag{2.24}$$

Hiroyasu and Arai [59], based on their experiments, assessed the following correlation for determining the spray spreading angle, where D_s is the diameter of the injector nozzle sac.

$$\theta = 83.5\left(\frac{L}{D_0}\right)^{-0.22}\left(\frac{D_0}{D_s}\right)^{0.15}\left(\frac{\rho_g}{\rho_f}\right)^{0.26} \tag{2.25}$$

Other empirical studies proposed similar results [61, 62, 64]. In all these works there is an agreement on the main parameter that affect the spray spreading angle, the density ratio (present in all the correlations), which shows the aerodynamic phenomena influence on the spreading of the spray. However, parameters like injection pressure or fuel viscosity have been neglected in the studies of the spray angle.

Liquid length

Under vaporizing conditions, as previously mention in Section 2.3.2, liquid length (LL) or liquid phase penetration is the maximum axial distance reached by the liquid fuel before its complete evaporation. It is a parameter experimentally measured during the whole time of injection, thus at first instants its value is equal to the spray penetration (liquid is present at the tip of the spray), till it stabilizes to a particular value which keeps almost constant for the remaining time of fuel injection, see Figure 2.15. It characterizes the mixing process and its dependency with several parameters, such as the type of fuel, nozzle geometry, discharge and injection pressures, has been studied by many researchers [50, 62, 65].

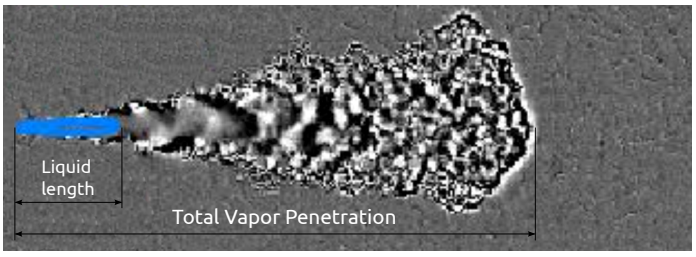

Figure 2.15. *Vapor penetration and liquid length of a diesel inert spray. Figure adapted from Pickett et al. [66].*

In other works, different empirical correlations are proposed to describe its behaviour [67, 68], however, the relationship obtained by dimensional analysis by Pastor et al. [69] seems to be a more general reference, Equation 2.26. In this expression, the constant K_p depends on ambient conditions and $Y_{f,evap}$ is the fuel vapor mass fraction under saturation conditions.

$$LL = K_p \frac{\sqrt{C_a} D_0 \sqrt{\frac{\rho_f}{\rho_a}}}{Y_{f,evap}\ tan\left(\frac{\theta}{2}\right)} \tag{2.26}$$

Droplet size

The measurement of the droplet size is important for the understanding of the complex atomization process. This size is the result of the interaction between the atomization phenomena (primary and secondary) and coalescence. For this reason, droplet size distributions are hugely variable, in space and time, during the injection process and can be only described using a statistical approach that leads to complex results and analysis.

In order to overcome this constraint, a characteristic mean diameter is normally employed to describe the atomization. This quantity can be defined in different ways. Mugele and Evans [70] classified these definitions proposing the notation represented in Table 2.4 which even nowadays is used.

Table 2.4. *Definitions of mean droplet diameters.*

Notation	Factor	Expression
D_{10}	Diameter	$\frac{\sum_i N_i D_{d,i}}{\sum_i N_i}$
D_{20}	Surface	$\left(\frac{\sum_i N_i D_{d,i}^2}{\sum_i N_i}\right)^{\frac{1}{2}}$
D_{30}	Volume	$\left(\frac{\sum_i N_i D_{d,i}^3}{\sum_i N_i}\right)^{\frac{1}{3}}$
D_{32}	Vol./Surf.	$\frac{\sum_i N_i D_{d,i}^3}{\sum_i N_i D_{d,i}^2}$

In the study of diesel sprays, the characteristic diameters most employed in the literature are the average diameter (D_{10}) and the Sauter Mean Diameter (SMD or D_{32}). SMD is an important indicator in order to analyse drag droplet forces, due to it is proportional to the rate between inertia and aerodynamic forces, as well as to fuel evaporation rate.

Finally, several experimental results show that droplet size depends on ambient gas density [27], injection pressure [71], orifice diameter and phenomena that take place in the internal nozzle flow [72–74].

Velocity and concentration distributions

The efficiency in the fuel-air mixing process is a pivotal factor on the diesel spray study and the velocity and concentration distributions characterization allows its proper evaluation. For this reason many researchers analyse these parameters. The majority of these studies are based on the similarity between diesel spray and gas jet, theory proposed by Adler and Lyn [75], and accepted to describe the behaviour of the steady spray at a relatively far distance from the orifice, when the spray is fully atomized [61, 76, 77]. From this similarity, diesel spray present self-similar velocities and concentration profiles at every section [78–80]. In the case of the velocity distribution:

$$\frac{u(x,r)}{u_{axis}(x)} = f(r/R) \tag{2.27}$$

where x and r are the axial and radial positions of the spray where velocity is evaluated, R is the total radius at the corresponding axial position and f is a generic function which accounts for the radial velocity profile. Different expressions have been proposed to model this radial velocity profile, but one option widely used in the literature [60, 77, 81, 82] is the gaussian profile originally proposed by Hinze [83], though in this case the expression proposed by Correas [77] is shown:

$$\frac{u(x,r)}{u_{axis}(x)} = exp\left(-4.6\left(\frac{r}{R}\right)^2 \right) \tag{2.28}$$

These gaussian profiles can be extended to the characterization of concentration by means of the Schmidt number, Equation 2.29, defined as the relationship between the momentum and the mass diffusivities.

$$S_c = \frac{\mu}{\rho k_m} \tag{2.29}$$

$$\frac{c(x,r)}{c_{axis}(x)} = \left(\frac{u(x,r)}{u_{axis}(x)}\right)^{S_c} \tag{2.30}$$

Nevertheless, establishing the axial evolution of velocity and concentration is more challenging because they deeply depend on complex phenomena like atomization and droplet coalescence. But Spalding [84] achieved an analytical solution for a laminar and turbulent gas jet, assuming that $S_c = 1$:

$$c_{axis}(x) = \frac{u_{axis}(x)}{u_0} \propto \frac{1}{x} \tag{2.31}$$

This Spalding's result has been used by several authors and extended to the diesel spray [76, 85, 86]. Thus, concentration and velocity centerline profiles are characterized by two different zones. The first one, related to the intact length, where the velocity and concentration variables remain constant and at certain axial distance, the second one, where both are proportional to 1/x.

2.5 Model approaches for simulation

Nowadays the use of computational models, in order to predict the fuel spray behaviour or even a whole engine performance, is of vital importance due to the fact that different solutions or configurations can be evaluated without using an expensive physical facility. A primary classification of these models, attending to their complexity, divides them into two groups: thermodynamic and fluid-dynamic models.

Thermodynamic models are the simplest ones and are based on the first law of thermodynamics and mass conservation. They can be *zero-dimensional*, which are unable to predict any geometric aspect of the fluid flow, or *phenomenological or 1-dimensional*, like for example the ones which consider the shape of the spray. Using this last approach, the spray can be considered as a gaseous jet, semi-stationary and 1-dimensional (local effects at droplet scale are neglected) [69] or can be discretized in so-called packages that model the local subprocesses, such as fuel atomization and evaporation [87].

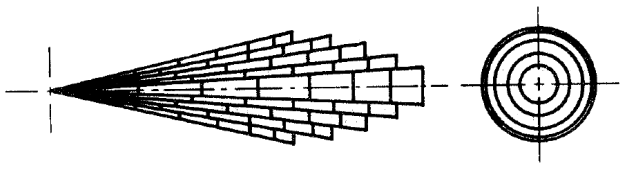

Figure 2.16. *Schematic diagram of the discretized spray in packages [87].*

Thermodynamic models are useful to have a fast initial estimation, but fluid-dynamic models are more complete and accurate. Their basic fundamentals are the resolution of a set of equations that govern the flow (continuity, momentum, energy, etc.). Due to the complex problem to solve, it is necessary to make use of the computational fluid dynamics

(CFD) environment with all their numerical algorithms for discretization and resolution.

Numerical treatment of turbulent flow is a characteristic or parameter of each CFD model and thus, it represents a first method of classification.

Direct numerical simulation (DNS). The first option describes the turbulent flow without using any model, i.e. turbulent flow equations are directly solved. The concept behind this approach is its main advantage however, a numerical mesh fine enough to resolve all turbulent length scales is mandatory together with small time steps. As a result, the huge computational cost of this methodology (increases with Reynolds number Re^3 [88]) for current computing power is the greatest drawback. Due to this fact, its application remains outside the industrial level and it is only adopted in simple, academic cases in which gives support to fundamental research.

Large eddy simulation (LES). The second type of numerical approach of turbulence is a compromise between the direct resolution and the modeling. Large scales of the turbulent flow are directly resolved whereas the smallest scales of the turbulent flow are modeled. An important consequence of that is the great reduction of the computational cost. The cell size of the calculation mesh is usually the determining factor of what scales may be resolved (spatial filtering) and the effect of the modeled scales on the resolved ones is taken into account by the subgrid-scale model. Many structural details of the turbulent flow can be retained with this approach. This is the main reason for the increasing use of this methodology, even at industrial level recently. However, a significant issue is that several LES simulations have to be done of the same problem in order to obtain statistically significant mean values to compare with experimental data.

Reynolds average Navier-Stokes (RANS). RANS computations are the last methodology, in which the whole range of turbulent scales are modeled. Equations for the mean values of the flow are solved, which are obtained by Reynolds (or Favre) averaging of the instantaneous balance equations. Computational cost is relatively low even for large and complex problems, hence being still the most widely used approach for CFD simulations. The disadvantage of RANS is that new unknowns arise during the averaging process that make it necessary to solve additional equations to overcome this closure problem. For this purpose a variety of turbulence models have been developed with the attempt to best describe the effect of turbulent motion. On the one hand, the **Reynolds stress models** (RSM) in which additional equations are solved, one for each component of the Reynolds stress tensor [89] and represents the most elaborate type of RANS turbulence models. On the

other hand, the the **Eddy viscosity models** (EVM) based on the Boussinesq hypothesis which introduces the concept of an eddy viscosity. The Reynolds stresses are here treated in an analogous manner to the stresses caused by molecular viscosity and linked to the mean rate of deformation:

$$-\overline{\rho}\widetilde{u_i'' u_j''} = \mu_t \left(\frac{\partial \widetilde{u}_i}{\partial x_j} + \frac{\partial \widetilde{u}_j}{\partial x_i} - \frac{2}{3}\frac{\partial \widetilde{u}_k}{\partial x_k}\delta_{ij} \right) - \frac{2}{3}\overline{\rho}\, k\delta_{ij} \tag{2.32}$$

where μ_t is the eddy viscosity (or turbulent viscosity) and $k = \frac{1}{2}\left(\widetilde{u_k'' u_k''}\right)$ is the turbulent kinetic energy. The eddy viscosity can be interpreted as the increase in viscosity due to turbulent fluctuations and is usually much larger than the molecular viscosity. The last term in Equation 2.32 is necessary in order to ensure correct results for the normal Reynolds stresses [90]. In any case, no universal turbulence model exists and each one has its pros and cons and a limited range of applicability.

Different type of results can be achieved by each methodology, as can be schematically seen at Figure 2.17, where the temporal evolution of a property (e.g. velocity, pressure) at a point in a turbulent flow is shown. DNS reproduces all turbulent fluctuations while LES omits fast and small fluctuations. Finally RANS represents the (here temporal) mean value of the flow variable ϕ(t).

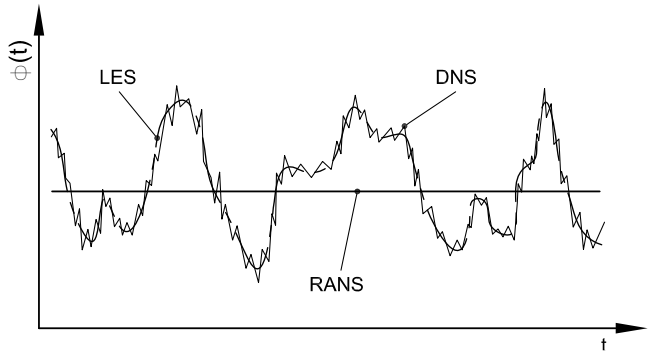

Figure 2.17. *Temporal evolution of a variable in turbulent flow calculated with different numerical approaches [91].*

In this work, RANS methodology and particularly an Eddy viscosity model, is used due to its relatively low computational cost, its good predictions and its applicability to industrial problems.

Additionally to the different turbulent methodology used, multiphase CFD models can be classified into three groups depending on the interphase treatment: interphase tracking methods, interphase capturing methods and diffuse interphase methods. Moreover, these models can belong to three different types: Eulerian-Lagrangian models, Eulerian multi-fluid models and homogeneous flow models.

2.5.1 Approaches for the definition of the interphase

Flows with free surfaces are an especially difficult class of flows with moving boundaries. The position of the boundary is known only at initial time but then, its location at later times has to be determined as part of the solution [92]. Many methods have been used to find the shape of the free surface. They can be classified into three major groups:

- **Interphase tracking methods**. They treat the free surface as a sharp interphase whose motion is followed. In this type of method, the flow field is discretized by a conservative finite difference approximation, and the interphase is explicitly represented by a separate, unstructured grid that moves through the stationary grid. Since the interphase deforms continuously, it is necessary to restructure its grid as the calculation proceed [93, 94]. This method stands out for its high accuracy [95], but the generation of the interphase grid, its spatial distribution and its dependency on time, together with the high computational cost remain as the main drawbacks.

- **Interphase capturing methods**. In this case, the computation is performed on a fixed grid and the shape of the free surface is determined by computing the fraction of each near-interphase cell that is partially filled. This can be achieved by introducing massless particles at the free surface at the initial time and following their motion, what is called Marker-and-Cell (MAC) scheme. Another option is to solve a transport equation for the fraction of the cell occupied by the liquid phase, known as Volume-of-Fluid (VOF) [96] method, or to define the surface as the one on which a level-set function is equal to zero (level-set formulation) [97].

- **Diffuse interphase methods**. In these methods the surface of the interphase is not captured nor tracked, but is modeled using algebraic expressions to construct additional transport equations. The greatest exponent of this type of models applied to fuel spray simulations is the mean interphase surface area density equation, originally proposed

by Vallet and Borghi [98] (explained in detail in next chapter). In addition to this fully Eulerian model, some implementations often makes a transition to Lagrangian models in the downstream, sparse regions, which is referred to the ELSA (Eulerian Lagrangian Spray Atomization model) approach [99].

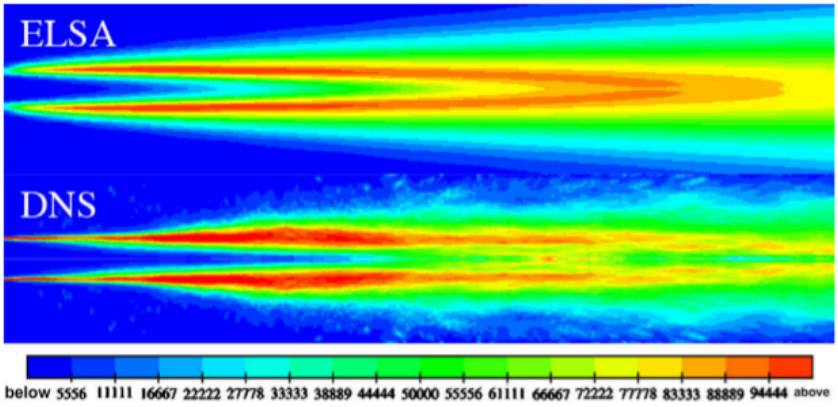

Figure 2.18. *Comparison of interphase surface area density contours from ELSA model and DNS simulations [100].*

2.5.1.1 Volume-of-Fluid method

In the VOF method, in addition to the conservation equations for mass and momentum, an equation for the filled fraction of each cell, X, is solved so that X = 1 in filled cells and X = 0 in empty cells. From the continuity equation, one can show that the evolution of X is governed by Equation 2.33.

$$\frac{\partial X}{\partial t} + div(XU) = 0 \tag{2.33}$$

The critical issue in this type of method is the characterization of convective term in Equation 2.33. Low-order schemes introduce artificial mixing of the two fluids, so higher-order schemes are preferred, fortunately there are numerical schemes that overcome this issue. However, the main drawback of this methodology is that any topological change associated to break-up or coalescence of droplets or bubbles is hardly obtained except if the grid resolution is extremely fine.

Alternatively, both fluids can be treated as a single fluid whose properties vary in space according to the volume fraction of each phase [92]. In this case the interphase is not treated as a boundary so no boundary conditions need to be prescribed on it. The interphase is simply the location where the fluid properties change abruptly.

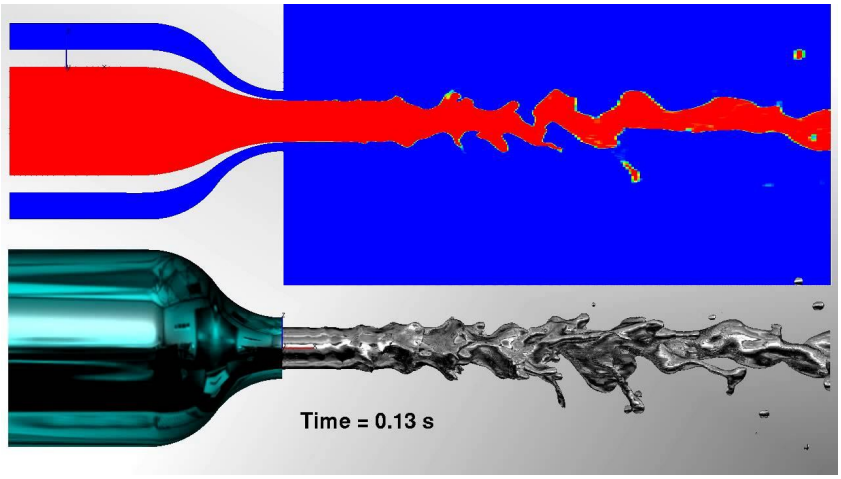

Figure 2.19. *VOF-LES simulation. Air-blast assisted injection (AVL FIRE).*

2.5.1.2 Level-set method

Another class of interphase-capturing methods is based on the level-set formulation. The surface is defined as the one on which a level-set function $\varphi = 0$. This function is allowed to evolve as a solution of a transport equation (Equation 2.34), and if it becomes too complicated, it can be re-initialized. As in VOF methods, fluid properties are determined by the local value of φ but here, only the sign is important.

$$\frac{\partial \varphi}{\partial t} + div(\varphi U) = 0 \tag{2.34}$$

The advantage of this approach relative to the VOF scheme is that φ varies smoothly across the interphase while the volume fraction is discontinuous there. However, as noted above, the computed φ need to be re-initialized. Sussman et al. [101] proposed to do this by solving Equation 2.35 until steady state is reached.

$$\frac{\partial \varphi}{\partial t} = sign(\varphi_0)(1 - |grad(\varphi)|) \tag{2.35}$$

Since φ does not explicitly occur in any of the conservation equations, the original level-set method did not exactly conserve mass. However, there are methods that allow to enforce mass conservation. The more frequently this equation is solved, the fewer iterations are needed to reach steady state, but frequent solution increases the computational cost so there is a trade-off.

Regarding the description of the interphase discontinuities, two approaches can be used, namely the continuous force formulation, which assumes that the interphase is 2 or 3 grid cells thick, and the ghost fluid method (GFM) which was derived by Fedkiw et al. [102] to capture jump conditions on the interphase. The GFM approach not only avoids the introduction of a fictitious interphase thickness, but it is also suitable to provide a more accurate discretization of discontinuous terms, reducing parasitic current and improving the resolution on the pressure jump condition [103].

2.5.2 Eulerian-Lagrangian models

The Eulerian-Lagrangian model is the classical methodology in computational studies of fuel sprays, due to its high efficiency to predict global parameters of the spray (penetration and angle) and because all processes taking place in a combustion chamber (evaporation, combustion, emissions, etc.) can be easily added to the simulation. It was originally developed for dispersed sprays, with a maximum limit for the volume fraction around 0.1, in order to assure a correct coupling and solution of all the equations. However, its reasonable efficiency has spread its use to dense jets, such as diesel spray.

In this model two numerical approaches are combined, gaseous phase is resolved using an Eulerian description on one side and a Lagrangian description is used for the liquid on the other. This last methodology is based on the discretization of the liquid in computational particles (*parcels*) that are injected in the flow and tracked since the start of injection. Every *parcel* represents a group of fuel droplets with the same characteristics (same radius, velocity, temperature, etc.) which do not interact among them and are used to statistically describe the spray. In this statistical treatment of the *parcels*, originally proposed by Dukowicz [104] and known as Discrete Droplets Model (DDM), governing equations are solved by a *Monte-Carlo* method. This approach reduces the computational cost, especially in comparison with the

Continuum Droplets Model (CDM) where each single droplet is represented and calculated.

The interaction between both phases in the model is made through source terms, weighted by the void fraction, added to the governing equations. These source terms are calculated making use of different sub-models which represent the processes that happen in the spray since the start of the injection till the evaporation occurs (atomization, collision and coalescence of droplets, turbulent dispersion, evaporation, etc.) and, as a result, they play a major role in the efficiency of this type of model. Other key parameters in this type of simulations are the computational mesh, with great dependency on both size and structure, and the computational time step due to the fact that an inadequate spatial resolution of the large velocity and concentration gradients produces excessive numerical diffusion [105]. Thus, the grid resolution must not be too coarse, but at the same time it cannot be too fine due to the limitation to the void fraction. This is the main reason why modeling diesel sprays with this CFD approach leads to an insufficient resolution in the near nozzle spray region.

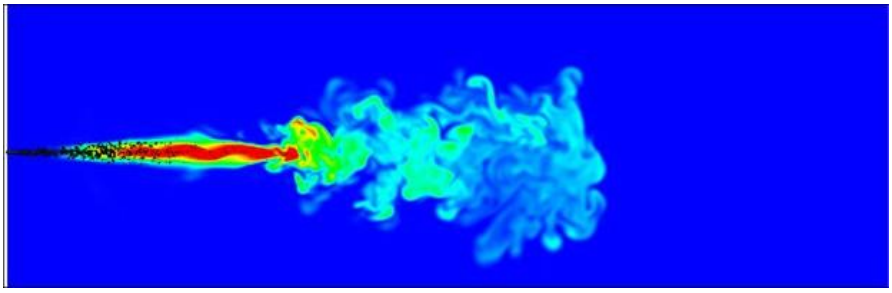

Figure 2.20. *Eulerian-Lagrangian LES spray simulation.*

2.5.3 Eulerian multi-fluid models

In the Eulerian multi-fluid model, gas and liquid phases are treated as inter-penetrating continua in an Eulerian framework with separate velocity and temperature fields. The gas phase is considered as the primary phase, whereas the liquid phase is considered as dispersed or secondary phase. Both phases are characterized by volume fractions, and by definition, the volume fractions of all phases must sum to unity.

The governing equations of the multi-fluid model can be derived by conditionally ensemble averaging of the local instant conservation equations of single-phase flow. However, since the averaged fields of one phase are not independent of the other phase, interaction terms are needed for the mass, momentum and energy transfers to the phase from the interfaces.

The methods used to compute these flows are similar to those used for single-phase flows, except for the addition of the interaction terms and boundary conditions and, of course, twice as many equations need to be solved. The transfer processes of each phase are expressed by their own balance equations, the model can predict more detailed changes and phase interactions than the mixture or homogeneous model. Due to their characteristics, they offer a great efficiency and detail in the analysis of transient phenomena, wave propagations and flow regime changes taking into account dynamic and non-equilibrium interaction between phases. On the contrary, when both phases are highly coupled these models present unnecessary complications and an elevated computational cost for practical applications.

2.5.4 Homogeneous flow or Single-fluid models

The other option are the single-fluid models. A computational particle is not a real physical particle, i.e. Lagrangian parcels. Alike, a computational phase in multiphase CFD is not the same as a phase in the physical sense, computational phase represents a mass moving at a single velocity.

Homogeneous flow approach is the simplest multiphase CFD model. The basic concept of this model is to consider the mixture as a whole, therefore the field equations should be written for the balance of mixture mass, momentum and energy in terms of the mixture properties. These three macroscopic mixture conservation equations are then supplemented by a diffusion equation that takes account for the concentration changes. A local equilibrium between the continuous, carrier, and dispersed phases is assumed (all phases share the same pressure), i.e. at every point the particles move with the terminal slip velocity relative to the gaseous phase. This allows to calculate velocity components of the liquid through algebraic equations.

The main advantages compared to previous models are: it is a fast approach because there are significantly less equations to be solved, it provides with an adequate description of particle size and other distributions, as well as the effect of turbulence on dispersed phase mixing. The main drawbacks are: long computing times due to small time steps as well as limitations to study flows where phase dynamics are not fully coupled.

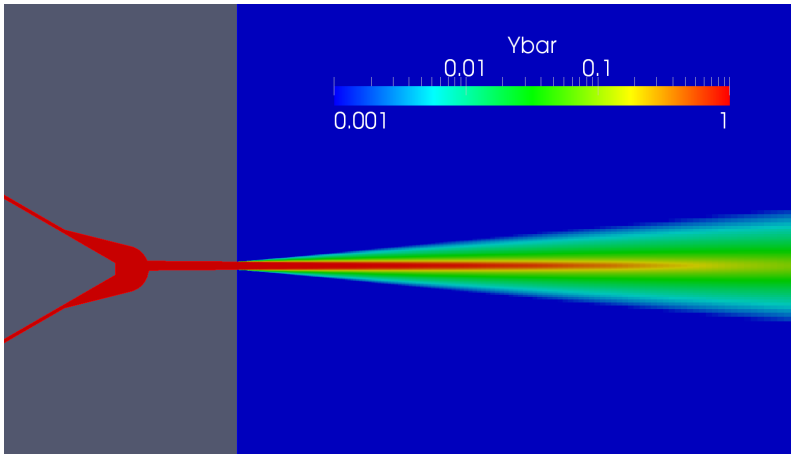

Figure 2.21. *Single Fluid RANS internal/external spray simulation. Liquid volume fraction.*

Bibliography

[1] Macian V., Bermudez V., Payri R. and Gimeno J. "New technique for determination of internal geometry of a diesel nozzle with the use of silicone methodology". *Experimental Techniques*, Vol. 27 n^o 2, pp. 39–43, 2003.

[2] Payri R., García-Oliver J.M., Salvador F.J. and Gimeno J. "Using spray momentum flux measurements to understand the influence of diesel nozzle geometry on spray characteristics". *Fuel*, Vol. 84 n^o 5, pp. 551 – 561, 2005.

[3] Gimeno J. *Desarrollo y aplicación de la medida del flujo de cantidad de movimiento de un chorro Diesel.* Doctoral Thesis, Departamento de Máquinas y Motores Térmicos, Universidad Politécnica de Valencia, España, 2008.

[4] Sangiah D.K. and Ganippa L.C. "Application of spray impingement technique for characterisation of high pressure sprays from multi-hole diesel nozzles". *International Journal of Thermal Sciences*, Vol. 49 n^o 2, pp. 409 – 417, 2010.

[5] Brennen C. "An oscillating-boundary-layer theory for ciliary propulsion". *Journal of Fluid Mechanics*, Vol. 65, pp. 799–824, 10 1974.

[6] Reitz R. D. and Diwakar R. "Effect of Drop Breakup on Fuel Sprays". *SAE Technical Paper*, n^o 860469, 1986.

[7] Reitz R. D. and Diwakar R. "Structure of High-Pressure Fuel Sprays". *SAE Technical Paper*, n^o 870598, 1987.

[8] Lefebvre A.H. *Atomization and sprays.* Hemisphere Publishing Corporation, New York, 1989.

[9] Soteriou C., Andrews R. and Smith M. "Direct Injection Diesel Sprays and the Effect of Cavitation and Hydraulic Flip on Atomization". *SAE Technical Paper*, n^o 950080, 1995.

[10] Morena J. *Estudio de la influencia de las características del flujo interno en toberas sobre el proceso de inyección Diésel en campo próximo.* Doctoral Thesis, Departamento de Máquinas y Motores Térmicos, Universidad Politécnica de Valencia, España, 2011.

[11] Rayleigh L. "On The Instability Of Jets". *Proceedings of the London Mathematical Society*, Vol. s1-10 n^o 1, pp. 4–13, 1878.

[12] Rayleigh L. "On the Capillary Phenomena of Jets". *Proceedings of the Royal Society of London*, Vol. 29 n^o 196-199, pp. 71–97, 1879.

[13] Haenlein A. "Über den Zerfall eines Flüssigkeitsstrahles". *Forschung auf dem Gebiet des Ingenieurwesens A*, Vol. 2 n^o 4, pp. 139–149, 1931.

[14] Weber C. "Disintegration of Liquid Jets". *Z. Angew., Math. Mech.*, Vol. 11 n^o 2, pp. 136–154, 1931.

[15] Ohnesorge Wolfgang V. "Die Bildung von Tropfen an Düsen und die Auflösung flüssiger Strahlen". *ZAMM - Journal of Applied Mathematics and Mechanics / Zeitschrift für Angewandte Mathematik und Mechanik*, Vol. 16 n^o 6, pp. 355–358, 1936.

[16] Reitz R. D. *Atomization and other breakup regimes of a liquid jet.* Doctoral Thesis, 08544, Princeton, New Jersey, United States of America: Princeton University, 1978.

[17] Reitz R. D. and Bracco F. V. "Mechanism of atomization of a liquid jet". *Physics of Fluids*, Vol. 25 n^o 10, pp. 1730–1742, 1982.

[18] Baumgarten C. *Mixture formation in internal combustion engines.* Springer, 2006.

[19] Miesse C.C. "Correlation of Experimental Data on the Disintegration of Liquid Jets". *Industrial & Engineering Chemistry*, Vol. 47 n^o 9, pp. 1690–1701, 1955.

[20] Torda T. P. "Evaporation of drops and breakup of sprays". *Astronautica Acta*, Vol. 18, pp. 383–393, 1973.

[21] McCarthy M.J. and Molloy N.A. "Review of stability of liquid jets and the influence of nozzle design". *The Chemical Engineering Journal*, Vol. 7 n^o 1, pp. 1 – 20, 1974. An International Journal of Research and Development.

[22] Lin S. P. and Reitz R. D. "Drop and spray formation from a liquid jet". *Annual Review of Fluid Mechanics*, Vol. 30 n^o 1, pp. 85–105, 1998.

[23] Dumouchel C. "On the experimental investigation on primary atomization of liquid streams". *Experiments in Fluids*, Vol. 45 n^o 3, pp. 371–422, 2008.

[24] Ranz W.E. "Some experiments on orifice sprays". *The Canadian Journal of Chemical Engineering*, Vol. 36 n^o 4, pp. 175–181, 1958.

[25] Sterling A. M. and Sleicher C. A. "The instability of capillary jets". *Journal of Fluid Mechanics*, Vol. 68, pp. 477–495, 4 1975.

[26] Dan T., Yamamoto, T. amd Senda J. and Fujimoto H. "Effect of nozzle configurations for characteristics of non-reacting diesel fuel sprays". *SAE technical paper*, n^o 970355, 1997.

[27] Arrègle J. *Análisis de la estructura y dinámica interna de chorros Diesel*. Doctoral Thesis, Departamento de Máquinas y Motores Térmicos, Universidad Politécnica de Valencia, España, 1998.

[28] Faeth G.M. "Spray combustion phenomena". *Symposium (International) on Combustion*, Vol. 26 n^o 1, pp. 1593 – 1612, 1996.

[29] Yue Y., Powell C. F., Poola R., Wang J. and Schaller J. K. "Quantitative measurements of Diesel fuel spray characteristics in the near-nozzle region using X-Ray absorption". *Atomization and Sprays*, Vol. 11 n^o 4, pp. 471–490, 2001.

[30] Kastengren A. and Powell C.F. "Spray density measurements using X-ray radiography". *Proceedings of the Institution of Mechanical Engineers, Part D: Journal of Automobile Engineering*, Vol. 221 n^o 6, pp. 653–662, 2007.

[31] Kastengren Alan L., Powell Christopher F., Wang Yujie, Im Kyoung-Su and Wang Jin. "X-ray radiography measurements of diesel spray structure at engine-like ambient density". *Atomization and Sprays*, Vol. 19 n^o 11, pp. 1031–1044, 2009.

[32] Kastengren A.L., Tilocco F.Z., Duke D., Powell C.F., Moon S. and Zhang X. "Time-Resolved X-Ray Radiography of Diesel Injectors from the Engine Combustion Network". In *12th Triennial International Conference on Liquid Atomization and Spray Systems*, pp. 2–6, 2012.

[33] Pickett L., Manin J., Kastengren A. and Powell C. "Comparison of Near-Field Structure and Growth of a Diesel Spray Using Light-Based Optical Microscopy and X-Ray Radiography". *SAE Int. J. Engines*, Vol. 7 n^o 2, 2014.

[34] Linne M., Paciaroni M., Hall T. and Parker T. "Ballistic imaging of the near field in a diesel spray". *Experiments in Fluids*, Vol. 40 n^o 6, pp. 836–846, 2006.

[35] Guildenbecher D.R., López-Rivera C. and Sojka P.E. "Secondary atomization". *Experiments in Fluids*, Vol. 46 n^o 3, pp. 371–402, 2009.

[36] Krzeczkowski S.A. "Measurement of liquid droplet disintegration mechanisms". *International Journal of Multiphase Flow*, Vol. 6 n^o 3, pp. 227 – 239, 1980.

[37] Pilch M. and Erdman C.A. "Use of breakup time data and velocity history data to predict the maximum size of stable fragments for acceleration-induced breakup of a liquid drop". *International Journal of Multiphase Flow*, Vol. 13 n^o 6, pp. 741 – 757, 1987.

[38] Liu A. B., Mather D. and Reitz R. D. "Modeling the Effects of Drop Drag and Breakup on Fuel Sprays". *SAE Technical Paper*, n^o 930072, 1993.

[39] Reitz R. D., Liu Z. and Hwang S. S. "Breakup mechanisms and drag coefficients of High-Speed vaporizing liquid drops". *Atomization and Sprays*, Vol. 6 n^o 3, pp. 353–376, 1996.

[40] Wierzba A. "Deformation and breakup of liquid drops in a gas stream at nearly critical Weber numbers". *Experiments in Fluids*, Vol. 9, pp. 59–64, Abril 1990.

[41] Arcoumanis C., Gavaises M. and French B. "Effect of Fuel Injection Processes on the Structure of Diesel Sprays". *SAE Technical Paper*, n^o 970799, 1997.

[42] Qian J. and Law C. K. "Regimes of coalescence and separation in droplet collision". *Journal of Fluid Mechanics*, Vol. null, pp. 59–80, 1 1997.

[43] Post S.L. and Abraham J. "Modeling the outcome of drop – drop collisions in Diesel sprays". *International Journal of Multiphase Flow*, Vol. 28 n^o 6, pp. 997 – 1019, 2002.

[44] Arcoumanis C. and Kamimoto T. *Flow and Combustion in Reciprocating Engines.* Springer-Verlag, 2009.

[45] Heywood J. *Internal Combustion Engine Fundamentals.* McGraw-Hill Education, 1988.

[46] Sirignano W.A. *Fluid Dynamics and Transport of Droplets and Sprays.* Cambridge University Press, 1999.

[47] Browne K., Partridge I. and Greeves G. "Fuel Property Effects on Fuel/Air Mixing in an Experimental Diesel Engine". *SAE Technical Paper*, n^o 860223, 1986.

[48] Yeh C., Kamimoto T., Kobori S. and Kosaka H. "2-D Imaging of Fuel Vapor Concentration in a Diesel Spray via Exciplex-Based Fluorescence Technique". *SAE Technical Paper*, n^o 932652, 1993.

[49] Espey C. and Dec J. "The Effect of TDC Temperature and Density on the Liquid-Phase Fuel Penetration in a D. I. Diesel Engine". *SAE Technical Paper*, n^o 952456, 1995.

[50] Siebers D. "Liquid-Phase Fuel Penetration in Diesel Sprays". *SAE Technical Paper*, n^o 980809, 1998.

[51] Kamimoto T., Yokota H. and Kobayashi H. "Effect of High Pressure Injection on Soot Formation Processes in a Rapid Compression Machine to Simulate Diesel Flames". *SAE Technical Paper*, n^o 871610, 1987.

[52] Siebers D. "Scaling Liquid-Phase Fuel Penetration in Diesel Sprays Based on Mixing-Limited Vaporization". *SAE Technical Paper*, n^o 1999-01-0528, 1999.

[53] Arcoumanis C., Whitelaw J. and Wong K. "Gaseous Simulation of Diesel-Type Sprays in a Motored Engine". *SAE Technical Paper*, n^o 890793, 1989.

[54] Hiroyasu H. "Experimental and Theoretical studies on the structure of fuel sprays in Diesel engines". In *The Fifth International Conference on Liquid Atomization and Spray Systems, ICLASS-91, paper B*, 1991.

[55] García-Oliver J.M. *Aportaciones al Estudio del Proceso de Combustión Turbulenta de Chorros en Motores Diesel de Inyección Directa*. Doctoral Thesis, Departamento de Máquinas y Motores Térmicos, Universidad Politécnica de Valencia, España, 2003.

[56] Hay N. and Jones P. "Comparison of the Various Correlations for Spray Penetration". *SAE Technical Paper*, n^o 720776, 1972.

[57] Wakuri Y., Fujii M., Amitani T. and Tsuneya R. "Studies on the Penetration of Fuel Spray in a Diesel Engine". *Bulletin of the Japan Society of Mechanical Engineers*, Vol. 3 n^o 9, 1960.

[58] Dent J. "A Basis for the Comparison of Various Experimental Methods for Studying Spray Penetration". *SAE Technical Paper*, n^o 710571, 1971.

[59] Hiroyasu H. and Arai M. "Structures of Fuel Sprays in Diesel Engines". *SAE Technical Paper*, n^o 900475, 1990.

[60] Desantes J.M., Payri R., Salvador F.J. and Gil A. "Development and validation of a theoretical model for diesel spray penetration". *Fuel*, Vol. 85 n^o 7-8, pp. 910 – 917, 2006.

[61] Naber J. and Siebers D. "Effects of Gas Density and Vaporization on Penetration and Dispersion of Diesel Sprays". *SAE Technical Paper*, n^o 960034, 1996.

[62] Desantes J.M., Payri R., Salvador F.J. and Soare V. "Study of the Influence of Geometrical and Injection Parameters on Diesel Sprays Characteristics in Isothermal Conditions". *SAE Technical Paper*, n^o 2005-01-0913, 2005.

[63] Reitz R. and Bracco F. "On the Dependence of Spray Angle and Other Spray Parameters on Nozzle Design and Operating Conditions". *SAE Technical Paper*, n^o 790494, 1979.

[64] Delacourt E., Desmet B. and Besson B. "Characterisation of very high pressure diesel sprays using digital imaging techniques". *Fuel*, Vol. 84, pp. 859 – 867, 2005.

[65] Bardi M., Payri R., Malbec L.M., Bruneaux G., Pickett L.M., Manin J., Bazyn T. and Genzale C. "ENGINE COMBUSTION NETWORK: Comparison of spray development, vaporization, and combustion in different combustion vessels". *Atomization and Sprays*, Vol. 22 n^o 10, pp. 807–842, 2012.

[66] Pickett L.M., Kook S. and Williams T.C. "Visualization of Diesel Spray Penetration, Cool-Flame, Ignition, High-Temperature Combustion, and Soot Formation Using High-Speed Imaging". *SAE Int. J. Engines*, Vol. 2 n^o 1, pp. 439–459, 2009.

[67] Payri R., Salvador F.J., Gimeno J. and Zapata L.D. "Diesel nozzle geometry influence on spray liquid-phase fuel penetration in evaporative conditions". *Fuel*, Vol. 87 n^o 7, pp. 1165 – 1176, 2008.

[68] Payri R., García-Oliver J. M., Bardi M. and Manin J. "Fuel temperature influence on diesel sprays in inert and reacting conditions". *Applied Thermal Engineering*, Vol. 35 n^o 0, pp. 185–195, Marzo 2012.

[69] Pastor J. V., López J. J., García-Oliver J. M. and Pastor J. M. "A 1D model for the description of mixing-controlled inert diesel sprays". *Fuel*, Vol. 87 n^o 13–14, pp. 2871–2885, Octubre 2008.

[70] Mugele R. A. and Evans H. D. "Droplet Size Distribution in Sprays". *Industrial & Engineering Chemistry*, Vol. 43 n^o 6, pp. 1317–1324, 1951.

[71] Hiroyasu H. and Kadota T. "Fuel droplet size distribution in Diesel combustion chamber". *SAE Technical Paper*, n^o 740715, 1974.

[72] Soare V. *Phase doppler measurement in diesel dense sprays: optimisation of measurements and study of the orifice geometry influence over the spray at microscopic level*. Doctoral Thesis, Departamento de Máquinas y Motores Térmicos, Universidad Politécnica de Valencia, España, 2007.

[73] Park S. H., Suh H. K. and Lee C. S. "Effect of Cavitating Flow on the Flow and Fuel Atomization Characteristics of Biodiesel and Diesel Fuels". *Energy & Fuels*, Vol. 22 n^o 1, pp. 605–613, 2008.

[74] Suh H. K. and Lee C. S. "Effect of cavitation in nozzle orifice on the diesel fuel atomization characteristics". *International Journal of Heat and Fluid Flow*, Vol. 29 n^o 4, pp. 1001 – 1009, 2008.

[75] Adler D. and Lyn W-T. "The Evaporation and Mixing of a Liquid Fuel Spray in a Diesel Air Swirl". *Proceedings of the Institution of Mechanical Engineers, Conference Proceedings*, Vol. 184 n^o 10, pp. 171–180, 1969.

[76] Prasad C. M. and Subir K. "An Investigation of the Influence of Back Pressure on the Diffusion of Mass and Momentum of Fuel in Diesel Spray". *ASME J. Eng. Power*, pp. 1–11, 1976.

[77] Correas D. *Estudio teórico–experimental del chorro libre Diesel isotermo*. Doctoral Thesis, Departamento de Máquinas y Motores Térmicos, Universidad Politécnica de Valencia, España, 1998.

[78] Abramovich G.N. *The theory of turbulent jets*. MIT Press. ISBN 0-262-01008-9, 1963.

[79] Beér J.M. and Chigier N.A. *Combustion Aerodynamics*. Robert E. Krieger Publishing Company, Inc. ISBN 0-89874-545-4, 1983.

[80] Tindal M.J., Williams T.J. and Harcombe A.T. "Fuel spray modelling in swirling flows". *ASME ICE*, Vol. 6, pp. 51–60, 1989.

[81] Malmström Tor G., Kirkpatrick Allan T., Christensen Brian and Knappmiller Kevin D. "Centreline velocity decay measurements in low-velocity axisymmetric jets". *Journal of Fluid Mechanics*, Vol. 346, pp. 363–377, 9 1997.

[82] Desantes J.M., Salvador F.J., López J.J. and De la Morena J. "Study of mass and momentum transfer in diesel sprays based on X-ray mass distribution measurements and on a theoretical derivation". *Experiments in Fluids*, Vol. 50 n^o 2, pp. 233–246, 2011.

[83] Hinze J. O. *Turbulence*. New York, N.Y. : McGraw-Hill, 2nd edition edition, 1975.

[84] Spalding D. B. *Combustion and Mass Transfer*. Pergamon Press, ISBN 0-08-022105-8, 1979.

[85] Rife J. and Heywood J. "Photographic and Performance Studies of Diesel Combustion With a Rapid Compression Machine". *SAE Technical Paper*, n^o 740948, 1974.

[86] Chiu W., Shahed S. and Lyn W. "A Transient Spray Mixing Model for Diesel Combustion". *SAE Technical Paper*, n^o 760128, 1976.

[87] Hiroyasu H., Kadota T. and Arai M. "Development and Use of a Spray Combustion Modeling to Predict Diesel Engine Efficiency and Pollutant Emissions : Part 1 Combustion Modeling". *Bulletin of JSME*, Vol. 26 n^o 214, pp. 569–575, 1983.

[88] Pope S. B. *Turbulent Flows*. Cambridge University Press, 2000.

[89] Launder B. E., Reece G. J. and Rodi W. "Progress in the development of a Reynolds-stress turbulence closure". *Journal of Fluid Mechanics*, Vol. 68, pp. 537–566, 4 1975.

[90] Versteeg H. K. and Malalasekera W. *An Introduction to Computational Fluid Dynamics*. Pearson, 2007.

[91] Winklinger J.F. *Implementation of a Combustion Model based on the Flamelet Concept and its Application to turbulent reactive Sprays*. Doctoral Thesis, Departamento de Máquinas y Motores Térmicos, Universidad Politécnica de Valencia, España, 2014.

[92] Ferziger J.H. and Peric M. *Computational Methods for Fluid Dynamics*. Springer, Berlin, 2002. pp. 176–178.

[93] Unverdi Salih Ozen and Tryggvason Grétar. "A front-tracking method for viscous, incompressible, multi-fluid flows". *Journal of Computational Physics*, Vol. 100 n^o 1, pp. 25 – 37, 1992.

[94] Hayashi Kosuke and Tomiyama Akio. "Interface Tracking Simulation of Mass Transfer from a Dissolving Bubble". *The Journal of Computational Multiphase Flows*, Vol. 3 n^o 4, pp. 247–262, 2011.

[95] Hayashi Kosuke, Hosoda Shogo, Tryggvason Gretar and Tomiyama Akio. "Effects of shape oscillation on mass transfer from a Taylor bubble". *International Journal of Multiphase Flow*, Vol. 58, pp. 236 – 245, 2014.

[96] Hirt C.W and Nichols B.D. "Volume of fluid (VOF) method for the dynamics of free boundaries". *Journal of Computational Physics*, Vol. 39 n^o 1, pp. 201 – 225, 1981.

[97] Osher Stanley and Sethian James A. "Fronts propagating with curvature-dependent speed: Algorithms based on Hamilton-Jacobi formulations". *Journal of Computational Physics*, Vol. 79 n^o 1, pp. 12 – 49, 1988.

[98] Vallet A. and Borghi R. "Modélisation Eulerienne de l'atomisation d'un jet liquide". *C.R. Acad. Sci, Paris*, Vol. 327, pp. 1015–1020, 1999.

[99] Blokkeel G., Barbeau B. and Borghi R. "A 3D Eulerian Model to Improve the Primary Breakup of Atomizing Jet". *SAE Technical Paper 2003-01-005*, 2003.

[100] Lebas R., Menard T., Beau P.A., Berlemont A. and Demoulin F.X. "Numerical simulation of primary break-up and atomization: DNS and modelling study". *International Journal of Multiphase Flow*, Vol. 35 n^o 3, pp. 247 – 260, 2009.

[101] Sussman Mark, Smereka Peter and Osher Stanley. "A Level Set Approach for Computing Solutions to Incompressible Two-Phase Flow". *Journal of Computational Physics*, Vol. 114 n^o 1, pp. 146 – 159, 1994.

[102] Fedkiw Ronald P, Aslam Tariq, Merriman Barry and Osher Stanley. "A Non-oscillatory Eulerian Approach to Interfaces in Multimaterial Flows (the Ghost Fluid Method)". *Journal of Computational Physics*, Vol. 152 n^o 2, pp. 457 – 492, 1999.

[103] Tanguy Sébastien and Berlemont Alain. "Application of a level set method for simulation of droplet collisions". *International Journal of Multiphase Flow*, Vol. 31 n^o 9, pp. 1015 – 1035, 2005.

[104] Dukowicz John K. "A particle-fluid numerical model for liquid sprays". *Journal of Computational Physics*, Vol. 35 n^o 2, pp. 229 – 253, 1980.

[105] Barroso G., Schneider B. and Boulouchos K. "An Extensive Parametric Study on Diesel Spray Simulation and Verification with Experimental Data". *SAE Technical Paper*, 10 2003.

Chapter 3

Spray model description and implementation

Contents

3.1 Introduction

The fuel spray model developed and implemented in this work is detailed in the following sections. According to the classification presented in Section 2.5, the chosen modeling strategy can be classified as a fully Eulerian single-fluid model, which uses a diffuse interphase method to represent the surface between the two phases. This type of approach is called Σ-Y atomization model and was initially proposed by Vallet and Borghi [1].

First, the general characteristics of the fuel spray modeling issue are presented, including some recent important results in order to make the requirements for the model and the best choice of computational approach clear. Then, a short overview of the fundamentals and key concepts used in the present spray model is given.

After this introductory part, the fundamental transport equations of the model, are introduced with special attention to its implementation on the OpenFOAM CFD open source c++ library [2]. This initial implementation is based on the work of Trask [3]. Furthermore, some sub–models have been developed in order to complete the basic spray model or improving accuracy and representing better the physical behaviour of fuel sprays, such as turbulence model, evaporation, an advanced liquid equation of state together with a thermodynamic model and even the coupling with a combustion model, which are presented throughout this chapter.

3.1.1 Fuel spray modeling approach

Despite great practical interest in how sprays emanate from fuel injectors, because injector design is a critical factor in internal combustion engine design, the near-nozzle region has remained a challenge for spray modelers. This optically dense space within the first few millimeters of the injector is only penetrable with special diagnostics such as x-ray radiography [4–6]. This leaves modelers with very speculative ideas of how the dense spray evolves. In contrast, the sparse spray region is much easier to investigate, since optical diagnostics work well and produce reliable results.

For this reason, modeling of primary atomization is particularly challenging. Though numerous primary atomization models have received wide-spread attention, these models are not necessarily predictive. This region of the spray spans the whole range of liquid volume fractions, from zero to unity. Furthermore, the dense spray core is so heavily loaded with fuel that the ubiquitous Lagrangian particle tracking approach fails in this region, because

nearly all existing drag, collision, breakup, and vaporization models are based on assumptions of near-spherical droplets in a sparse spray. The classical Lagrangian approach shows here a clear drawback that can rarely be overcome.

On the contrary, recent Eulerian models [1, 7–12] have shown promise in capturing the fast gas-liquid interactions in the near field. These are approaches that emphasize the turbulent mixing of the gas and liquid, which is consistent with the observations of Siebers [13–15], based on numerous experiments, that "the processes of atomization and the consequent interphase transport of mass and energy at droplet surfaces are not limiting steps with respect to fuel vaporization in DI diesel sprays." Additionally, more recent work by Oefelein et al. [16–18] indicates that the in-cylinder conditions for diesel fuel injection are supercritical or near-supercritical. Even if the spray is not quite above the critical point, the elevated temperatures and pressures indicate a very small surface tension and an extremely high Weber number. Under these conditions, the gas/liquid interface disappears and spray modeling becomes entirely an exercise in modeling turbulent mixing. So fully Eulerian treatments of the spray, with the emphasis on turbulent mixing, seems to present a more appropriate physics description.

These Eulerian models often transition the liquid phase of the spray to the Lagrangian reference frame in the downstream sparse region. These are referred to as ELSA approach [8, 19], as presented in Chapter 2. The focus of the present spray model, however, is strictly Eulerian since the Lagrangian phase may not be necessary for high-ambient pressure diesel simulations [20–22]. In addition to this, the transition to the Lagrangian environment is not simple and could lead to some problems, such as conservation of mass [23], difficulties to optimise for parallel computing [24] and the selection of a proper criterion to conduct the transition together with the initialization of the droplets sizes (single value - SMD) and their velocities [25].

3.1.2 Model fundamentals

The fundamentals and key concepts adopted in the present modeling approach are briefly outlined here. As originally proposed, the model is founded on four assumptions [12]:

- **Flow scales separation**. Surface tension and viscosity act only at small length scales (associated with high curvature of the liquid-gas interphase and large velocity gradients), because of that and considering Equations 2.12 and 2.13, the large scales features of the flow must

be independent of surface tension and viscosity at infinite Reynolds and Weber numbers. This implies that the large scale features of the flow will be dependent only upon density variations. As a result, assuming that the flow exiting the injector is operating at large Reynolds and Weber numbers, it is possible to assume a separation of the large scale flow features such as mass transport from the atomization process occurring at smaller scales.

- **Mean velocity field**. Although the small scale velocity fluctuations of the flow are unpredictable, the mean velocity field can be predicted using standard closures such as those used in Reynolds-averaged turbulence models. The liquid/gas mixture is treated as a pseudo-fluid with variable density and which flows with a single velocity field.

- **Liquid mass dispersion**. The dispersion of the liquid phase into the gaseous phase is modeled via a turbulent diffusion liquid flux, which captures the effect of the relative velocity between the two phases.

- **Liquid spray geometry**. The mean geometry of the liquid structures can be characterized by modeling the mean surface area of the liquid-gas interphase per unit of volume.

3.2 Fundamental model equations and initial implementation

In this section the implementation of the spray model equations into the OpenFOAM environment is briefly described. The OpenFOAM CFD platform is written in C++, an object-oriented programming language. This platform provides different applications such as solvers or postprocessing tools and a wide range of different models (e.g. turbulence models, thermophysical models, etc.) implemented as classes. Model equations implemented are summarized below and presented in a usual index notation as well as in the corresponding OpenFOAM syntax. A direct comparison between the two presented notations can be made, since the terms of each equation are written in the same order for both notations.

3.2.1 Governing equations

Transport equation for the mass conservation law

The conservation of mass for a compressible fluid is represented by the continuity equation

$$\frac{\partial \bar{\rho}}{\partial t} + \frac{\partial \bar{\rho}\tilde{u}_i}{\partial x_i} = 0 \tag{3.1}$$

with the density ρ of the fluid and the velocity u_i of the component i.

The above continuity equation is implemented in OpenFOAM as:

```
fvScalarMatrix rhoEqn
(
    fvm::ddt(rho)
  + fvm::div(phi, rho)
);

rhoEqn.solve();
```

The equation `rhoEqn` is defined as type `fvScalarMatrix` since the density is a scalar. Mathematical operations such as time derivative or divergence operator (in the order they are used in the equation above) are pre-implemented functions in OpenFOAM, which facilitates the readability of equations written in OpenFOAM syntax. Finally, the term `phi` corresponds to the velocity flux at the cell faces.

Transport equation for the mean liquid mass fraction

To track the dispersion of the liquid phase an indicator function is used taking a value of unity in the liquid phase and zero in the gas phase. The mean liquid volume fraction is denoted by $\overline{Y}$ or in OpenFOAM syntax by Ybar, and the mean mass averaged fraction is defined as $\tilde{Y} = \frac{\overline{\rho_{liq} Y}}{\bar{\rho}}$. Favre averaging [26, 27] the transport equation for the liquid mass fraction yields,

$$\frac{\partial \bar{\rho}\tilde{Y}}{\partial t} + \frac{\partial \bar{\rho}\tilde{u}_i\tilde{Y}}{\partial x_i} = -\frac{\partial \bar{\rho}\widetilde{u'_i Y'}}{\partial x_i} - S_{evap} \tag{3.2}$$

The liquid mass fraction is a conserved property, however a source term appears in its transport equation, second term on the right-hand side (RHS) of Equation. 3.2, to account for the evaporation process. This source term is explained latter on this chapter, Section 3.3.2.

Ignoring the source term, the RHS of Equation 3.2 corresponds to the turbulent diffusion liquid flux term, which captures the effect of the relative velocity between the two phases [12] and is a fundamental parameter of this type of model. In this term u' denotes the density weighted turbulent fluctuations in velocity and Y' denotes turbulent fluctuations in liquid mass fraction. The term can be modeled based on several hypotheses, a gradient law closure was initially proposed by Vallet et al. [12] then, an specific model was introduced by Demoulin et al. [9], in order to account for Rayleigh-Taylor instabilities in turbulent liquid flux, improving accuracy in air blast atomization simulations. And even a transport equation to solve the turbulent diffusion liquid flux term can be introduced [7]. However, in a recent work by the same group [10], it is stated that the gradient law successfully worked for diesel sprays, based on comparisons to DNS results. For this reason, in the current work a standard turbulent diffusion formulation is used,

$$\bar{\rho}\widetilde{u_i'Y'} = -\frac{\mu_t}{Sc}\frac{\partial \tilde{Y}}{\partial x_i} \tag{3.3}$$

where μ_t is the turbulent viscosity and Sc is the Schmidt number. While the approach used here assumes that the resolved momentum of the liquid/gas mixture can be characterized by a single bulk velocity, the slip velocity can be expressed explicitly as derived by Demoulin et al. [9] and seen in Equation 3.4.

$$u_i|_l - u_i|_g = \frac{1}{\tilde{Y}\left(1-\tilde{Y}\right)} \cdot \widetilde{u'_i Y'} \tag{3.4}$$

Finally, Equation 3.2 becomes 3.5:

$$\frac{\partial \bar{\rho}\tilde{Y}}{\partial t} + \frac{\partial \bar{\rho}\tilde{u}_i\tilde{Y}}{\partial x_i} - \frac{\partial}{\partial x_i}\left(\frac{\mu_t}{Sc}\frac{\partial \tilde{Y}}{\partial x_i}\right) = -S_{evap} \tag{3.5}$$

This equation reads in OpenFOAM syntax as:

```
fvScalarMatrix YEqn
(
    fvm::ddt(rho, Y)
  + fvm::div(rhoPhi, Y)
  - fvm::laplacian(turbulence->mut()/Sc, Y)
  ==
  - Sevap
);

YEqn.solve();
```

In a finite volume implementation, the fluxes `rhoPhi` are the normal component of mass flux at the cell faces. The equation YEqn is of type fvScalarMatrix since the liquid mass fraction is a scalar too. Another pre-implemented operator in OpenFOAM, like the Laplace operator ('laplacian') appears in the equation. Finally the actual solution process of the equation is called by YEqn.solve();.

Transport equation of momentum

Velocity is solved from the momentum equation:

$$\frac{\partial \bar{\rho}\tilde{u}_j}{\partial t} + \frac{\partial \bar{\rho}\tilde{u}_i\tilde{u}_j}{\partial x_i} + \frac{\partial}{\partial x_i}\left(\bar{\rho}\widetilde{u_i'u_j'} - \mu\frac{\partial \tilde{u}_j}{\partial x_i}\right) = -\frac{\partial \tilde{p}}{\partial x_j} \tag{3.6}$$

In this equation, the third term on the left-hand side (LHS) is the corresponding to the Reynolds stresses ($\bar{\rho}\widetilde{u_i'u_j'}$) collected with the viscous normal and shear stress terms ($\mu\frac{\partial \tilde{u}_j}{\partial x_i}$).

In OpenFOAM syntax, the equation reads as:

```
fvVectorMatrix UEqn
(
    fvm::ddt(rho, U)
  + fvm::div(rhoPhi, U)
  + turbulence->divDevRhoReff(U)
  ==
  - fvc::grad(p)
);

UEqn.solve();
```

The equation `UEqn` is defined as type `fvVectorMatrix` since the velocity is a vector. Another useful utility of OpenFOAM is the term corresponding to the Reynolds stresses ('turbulence->divDevRhoReff(U)'), in every turbulence model is this function pre-implemented allowing and easy and valid implementation for every turbulence model.

Transport equation of energy

The law of conservation of energy states that the total energy of an isolated system remains constant, i.e. it is conserved over time and energy is neither created nor destroyed but is transformed from one form to another. Moreover, in most multiphase problems with large heat additions, the mechanical energy effects can be neglected, and the only important effect to be taken into account is the diffusion of the transport of thermal energy because of the large difference on the phase enthalpies. As a result, a separation of the mechanical and thermal energy can be carried out [28, 29] and only enthalpy is considered. Here we consider h, the static mixture enthalpy implemented through the following conservation equation, where α_{eff} is the effective thermal diffusivity composed of a laminar and a turbulent contribution with the turbulent thermal diffusivity $\alpha_t = \mu_t/P_r$. A constant value is usually used for the turbulent Prandtl number (P_r). And $\tau_{ij}\frac{\partial \tilde{u}_j}{\partial x_i}$ term is the viscous dissipation:

$$\frac{\partial \bar{\rho}\tilde{h}}{\partial t} + \frac{\partial \bar{\rho}\tilde{u}_i\tilde{h}}{\partial x_i} - \frac{\partial}{\partial x_i}\left(\alpha_{eff}\frac{\partial \tilde{h}}{\partial x_i}\right) = \frac{\partial \tilde{p}}{\partial t} + \tilde{u}_i\frac{\partial \tilde{p}}{\partial x_i} + \tau_{ij}\frac{\partial \tilde{u}_j}{\partial x_i} \tag{3.7}$$

In OpenFOAM:

```
fvVectorMatrix hEqn
(
    fvm::ddt(rho, h)
  + fvm::div(rhoPhi, h)
  - fvm::laplacian(turbulence->alphaEff(), h)
  ==
  + fvc::DDt(phi, p)
  + turbulence->muEff()*
  ((fvc::grad(U) + fvc::grad(U)().T()) && fvc::grad(U))
);

hEqn.solve();
```

In this implementation, the effective turbulent thermal diffusivity is directly calculated as 'turbulence->alphaEff()', another pre-implemented function in every turbulence model. Then, the two first terms on the RHS of the Equation 3.7 correspond to the total derivative of the pressure that can be evaluated with the operator ('DDt') and the final term on the OpenFOAM implementation corresponds to the viscous dissipation.

Finally, in order to determine the evolution of temperature from this transported enthalpy, initially constant specific heat capacities at constant pressure ($c_{p,k}$) are considered and temperature can be expressed as:

$$\tilde{h} = \tilde{Y} \cdot h_{f,l}(T) + (1 - \tilde{Y}) \cdot h_g(T) = \tilde{Y} \cdot c_{p,l} T + (1 - \tilde{Y}) \cdot c_{p,g} T \tag{3.8}$$

$$T = \frac{\tilde{h}}{\tilde{Y} \cdot c_{p,l} + (1 - \tilde{Y}) \cdot c_{p,g}} \tag{3.9}$$

Then, it is developed an iterative process, which is explained in the section 3.3.3.2 of this chapter, in order to calculate the evolution of temperature while considering temperature dependent specific heat capacities at constant pressure ($c_{p,k}(T)$), with the aim of improving accuracy and representing better the physical behaviour of fuel sprays.

Transport equation for the mean interphase surface area density

The small scale atomization is modeled by solving a transport equation for the evolution of the interphase surface area density Σ. This surface density can be understood as the amount of spatial surface per unit volume at a given time and spatial position. It is not easy to establish even an unclosed form of the balance equation of this quantity. Ishii [28] and Delhaye et al. [30] made some attempts on two phase flow applications, and by means of the spatial averaging operator, the averaged surface density equation is introduced by Ishii [28] in a similar form to the development of flame surface area density [31, 32] used in combustion applications. Then, Ishii's original equation was adopted by Vallet and Borghi [1], in which nearly all the models in the literature are based, and gives the following evolution equation for this quantity, assuming a gradient law closure for the turbulent diffusion flux term, where D_Σ is a

suitable diffusion coefficient usually taken as the turbulent kinematic viscosity (ν_t) over a Schmidt number (Sc_Σ).

$$\frac{\partial\tilde{\Sigma}}{\partial t}+\frac{\partial\tilde{u}_j\tilde{\Sigma}}{\partial x_j}-\frac{\partial}{\partial x_j}\left(D_\Sigma\frac{\partial\tilde{\Sigma}}{\partial x_j}\right)-a\tilde{\Sigma}+b\tilde{\Sigma}^2-S_{\Sigma_{evap}}-S_{\Sigma_{init}}=0 \qquad (3.10)$$

where the inverse time-scale a and coefficient b can be understood as the surface generation due to the growth of fluid instabilities (i.e. Kelvin-Helmholtz) and the destruction of surface due to droplet coalescence (in the case of dispersed flow), respectively. However, the most common form for the combination of these two source terms is the restoration to an equilibrium value ($\bar{\Sigma}_{eq}$) [12, 20]:

$$\frac{\partial\tilde{\Sigma}}{\partial t}+\frac{\partial\tilde{u}_j\tilde{\Sigma}}{\partial x_j}-\frac{\partial}{\partial x_j}\left(D_\Sigma\frac{\partial\tilde{\Sigma}}{\partial x_j}\right)-C_\Sigma\tilde{\Sigma}\left(1-\frac{\tilde{\Sigma}}{\bar{\Sigma}_{eq}}\right)-S_{\Sigma_{evap}}-S_{\Sigma_{init}}=0 \qquad (3.11)$$

The term $S_{\Sigma_{evap}}$, corresponds to the contribution of evaporation in a source term form, which is explained later on this chapter, Section 3.3.2. Finally, the last term on LHS, corresponds to an initialization term which is later discussed.

In the OpenFOAM syntax this equation results:

```
fvScalarMatrix SigmaEqn
(
    fvm::ddt(Sigma)
  + fvm::div(phi, Sigma)
  - fvm::laplacian(nut/ScSigma, Sigma)
  - fvm::Sp(Csigma, Sigma)
  + fvm::Sp(Csigma*Sigma/SigmaEq, Sigma)
  - fvm::Sp(SsigmaEvap, Sigma)
  - Sinit
);

SigmaEqn.solve();
```

The $\bar{\Sigma}_{eq}$, already mentioned, is the equilibrium or critical surface density to which the local surface density is driven and it is set by a suitable equilibrium droplet radius (r_{eq}):

$$\bar{\Sigma}_{eq} = \frac{3\bar{\rho}\tilde{Y}}{\rho_l r_{eq}} \tag{3.12}$$

As proposed by Vallet et al. [12] assuming that droplet collision is the principal mechanism in the droplet breakup the equilibrium radius can be derived. Thus, considering the collision between two identical droplets with the initial velocity difference Δv, the minimum radius of droplets r produced after collision is such that the kinetic energy of colliding droplets equals the minimum increase of the surface tension energy at the breakup [20], which gives

$$\frac{4}{3}\pi\rho_l r^3(\Delta v)^2 = 4\pi\sigma r^2(2^{1/3} - 1) \tag{3.13}$$

where r is also an equilibrium characteristic length scale for the liquid droplets under the Kolmogorov assumption of equilibrium between convective forces and viscous forces, i.e., r = r_{eq}. In order to estimate the mean velocity difference (Δv) between two colliding droplets, it is assumed to be the corresponding to the classical Kolgomorov spectrum [12], that is, $\Delta v \simeq (\tilde{\varepsilon} l)^{1/3}$, where $\tilde{\varepsilon}$ is the turbulent dissipation rate of the turbulent kinetic energy ($\tilde{k}$) and l is the averaged spacing between droplets given by $l = n^{-1/3}$, with n the drop number density, i.e., drop number per unit of volume (m^{-3}):

$$n = \frac{\rho_l^2 \bar{\Sigma}^3}{36\pi\bar{\rho}^2\tilde{Y}^2} \tag{3.14}$$

Combining with Equation 3.12 that has to be imposed on Equation 3.14, the equilibrium droplet size r_{eq} is derived:

$$r_{eq} = \alpha_2 \frac{\sigma^{3/5}}{\tilde{\varepsilon}^{2/5}} \frac{(\bar{\rho}\tilde{Y})^{2/15}}{\rho_l^{11/15}} \tag{3.15}$$

Then, the coefficient C_Σ is modeled as the inverse of the turbulent time scale:

$$C_\Sigma = \alpha_1 \frac{\tilde{\varepsilon}}{\tilde{k}} \tag{3.16}$$

note the presence of two modeling constants (α_1, α_2), which by default are equal to 1 [12], although other values have been evaluated [12, 20, 33, 34].

Finally, as can be seen all the source terms that are involved in this equation are proportional to the interface surface density Σ (including the evaporation one Equation 3.58). As a result, there will be no production if there is no interface. Therefore, a proper initialization should be made by means of the term $S_{\Sigma_{init}}$. For that purpose, a minimum value of Σ is considered in any computational cell which is not filled with pure liquid or gas. In a similar way as in Wang et al. [35], this minimum value is estimated as $V^{-1/3}$ where V is the volume of the CFD cell. The source term only takes a positive value if the interface field is lower than this Σ_{min}:

$$S_{\Sigma_{init}} = \frac{\Sigma_{min} - \Sigma}{\Delta t} pos(\Sigma_{min} - \Sigma) \tag{3.17}$$

where pos is a boolean pre-implemented operator in OpenFOAM:

$$pos(x) = \begin{cases} 1 & \text{if } x > 0 \\ 0 & \text{if } x \leqslant 0 \end{cases}$$

Together with the mass averaged liquid fraction, the interphase surface area density can be used to derive results for droplet sizing, such as the local SMD (D_{32}) of the spray and the drop number density (previously defined).

$$D_{32} = \frac{6\bar{\rho}\tilde{Y}}{\rho_l \tilde{\Sigma}} \tag{3.18}$$

3.2.2 Density equation

Under the assumption that the two phases form an immiscible mixture, the mean liquid mass fraction is related to the density by

$$\frac{1}{\bar{\rho}} = \frac{\tilde{Y}}{\rho_l} + \frac{1 - \tilde{Y}}{\rho_g} \tag{3.19}$$

An equation of state is then assigned to each phase. The gas phase obeys an ideal gas law,

$$\rho_g = \frac{p}{R_g T} \tag{3.20}$$

where R_g is the specific gas constant of the mixture of gases present in the combustion chamber, which is given by the universal gas constant (R_u =

8.314472 J/mol K) divided by the molecular weight (MW) of the mixture. Note that in that way the presence of other gas components, i.e. fuel vapor as a consequence of evaporation or gaseous species produced after a combustion process, are taken into account. As a result, this equation will be kept in the same way for vaporizing and reacting cases developed within the thesis.

On the other hand, for the liquid phase two options are implemented. The first one corresponds to the assumption that the liquid has a linear compressibility, denoted by ψ_l

$$\rho_l = \rho_{l,o} + \psi_l(p - p_o) \tag{3.21}$$

where $\rho_{l,o}$ and p_o denote reference density and pressures, respectively, about which the equation of state is linearized. These equation of state is used for applications in which the fuel is not a surrogate (pure component). However, for simulations of pure substances, an advanced liquid equation of state based on the HBT (Hankinson-Brobst-Thomson) correlation [36] has been implemented, as explained in Section 3.3.3.1.

3.2.3 Pressure equation – Pressure-velocity coupling

In order to obtain an equation for solving the pressure, the momentum equation must be forced to satisfy the continuity equation. The single-phase, incompressible algorithm outlined by Jasak [37] has been extended to account for compressible, multi-phase, variable temperature flow as in Trask et al. [38]. This is achieved by recasting the momentum equation in the semi-discretized form:

$$a_p U_p = H(U) - \nabla p \tag{3.22}$$

where the momentum matrix has been split into a diagonal part a_p and an off-diagonal part H(U). Rearranging Equation 3.22, interpolating to faces and taking the divergence of it gives:

$$\nabla U_p = \nabla\left(\frac{H(U)}{a_p}\right) - \nabla\left(\frac{1}{a_p}\nabla p\right) \tag{3.23}$$

For the case of multiphase, compressible flow the velocity divergence is nonzero and can be split between the effects of compressibility, thermal expansion and turbulent mixing by applying the chain rule to the continuity equation.

$$\nabla U_p = -\frac{1}{\rho}\frac{D\rho}{Dt} = -\frac{1}{\rho}\frac{\partial\rho}{\partial P}\frac{DP}{Dt} - \frac{1}{\rho}\frac{\partial\rho}{\partial T}\frac{DT}{Dt} - \frac{1}{\rho}\frac{\partial\rho}{\partial Y}\frac{DY}{Dt} + \frac{\rho-\rho_{EOS}}{\delta_t k_r \rho} \tag{3.24}$$

In order to obtain a fully closed transport equation for pressure, each one of these terms must be treated in a numerically stable manner.

Compressibility effects. The divergence caused by compressibility at high Mach numbers is caused by the term

$$-\frac{1}{\rho}\frac{\partial\rho}{\partial P}\frac{DP}{Dt} \tag{3.25}$$

The derivative $\frac{\partial\rho}{\partial P}$ is the effective isothermal compressibility of the liquid/air mixture and is defined as ψ. This compressibility is obtained by taking the derivative of Equation 3.19 with respect to pressure:

$$-\frac{1}{\rho^2}\frac{\partial\rho}{\partial P} = -\frac{\tilde{Y}}{{\rho_l}^2}\frac{\partial\rho_l}{\partial P} - \frac{1-\tilde{Y}}{{\rho_g}^2}\psi_g \tag{3.26}$$

Simplifying with the relation $\tilde{Y} = \frac{\rho_l}{\rho}\bar{Y}$ and $\psi_g = \frac{1}{R_g T}$

$$-\frac{1}{\rho^2}\frac{\partial\rho}{\partial P} = -\frac{\bar{Y}}{\rho_l\rho}\frac{\partial\rho_l}{\partial P} - \frac{1-\tilde{Y}}{\rho_g}\frac{1}{P} \tag{3.27}$$

And taking into account that $\rho(1-\tilde{Y}) = \rho_g(1-\bar{Y})$, the effective isothermal compressibility results:

$$\frac{\partial\rho}{\partial P} = \frac{\bar{Y}\rho}{\rho_l}\frac{\partial\rho_l}{\partial P} + \frac{(1-\bar{Y})\rho}{P} = \rho\left(\frac{\bar{Y}}{\rho_l}\frac{\partial\rho_l}{\partial P} + \frac{1-\bar{Y}}{P}\right) \tag{3.28}$$

Total derivative of pressure is

$$\frac{DP}{Dt} = \frac{\partial P}{\partial t} + u\nabla P \tag{3.29}$$

And thus, finally the compressibility term can be obtained as:

$$-\frac{1}{\rho}\frac{\partial\rho}{\partial P}\frac{DP}{Dt} = -\left(\frac{\bar{Y}}{\rho_l}\frac{\partial\rho_l}{\partial P} + \frac{1-\bar{Y}}{P}\right)\left(\frac{\partial P}{\partial t} + u\nabla P\right) \tag{3.30}$$

Note that derivation of the term is conducted for a generic liquid equation of state and thus, liquid partial derivative with respect to pressure is explicitly depicted, while considering the barotropic equation the constant liquid compressibility would be the desired quantity. Additionally, this term will be kept in the same way for vaporizing and reacting cases developed within the thesis, due to R_g (which changes among cases) is simplified on the derivation.

Thermal expansion effects. To determine the effect of temperature change upon the density (term in Equation 3.19), a similar approach is used.

$$-\frac{1}{\rho}\frac{\partial \rho}{\partial T}\frac{DT}{Dt} \tag{3.31}$$

The derivative of Equation 3.19 with respect to temperature is taken and using Equation 3.20:

$$-\frac{1}{\rho^2}\frac{\partial \rho}{\partial T} = -\frac{\tilde{Y}}{{\rho_l}^2}\frac{\partial \rho_l}{\partial T} - \frac{1-\tilde{Y}}{{\rho_g}^2}\frac{\partial \rho_g}{\partial T} = -\frac{\tilde{Y}}{{\rho_l}^2}\frac{\partial \rho_l}{\partial T} - \frac{1-\tilde{Y}}{{\rho_g}^2}\frac{-P}{R_g T^2} \tag{3.32}$$

Again operating and simplifying with the relationship $\rho(1-\tilde{Y}) = \rho_g(1-\bar{Y})$

$$-\frac{1}{\rho^2}\frac{\partial \rho}{\partial T} = -\frac{\tilde{Y}}{{\rho_l}^2}\frac{\partial \rho_l}{\partial T} + \frac{1-\bar{Y}}{\rho T} \tag{3.33}$$

And taking into account that $\tilde{Y} = \frac{\rho_l}{\rho}\bar{Y}$, the desired term results:

$$\frac{\partial \rho}{\partial T} = \frac{\bar{Y}\rho}{\rho_l}\frac{\partial \rho_l}{\partial T} - \frac{(1-\bar{Y})\rho}{T} = \rho\left(\frac{\bar{Y}}{\rho_l}\frac{\partial \rho_l}{\partial T} - \frac{1-\bar{Y}}{T}\right) \tag{3.34}$$

Total derivative of temperature is

$$\frac{DT}{Dt} = \frac{\partial T}{\partial t} + u\nabla T \tag{3.35}$$

And thus, finally the thermal expansion term can be obtained as:

$$-\frac{1}{\rho}\frac{\partial \rho}{\partial T}\frac{DT}{Dt} = -\left(\frac{\bar{Y}}{\rho_l}\frac{\partial \rho_l}{\partial T} - \frac{1-\bar{Y}}{T}\right)\left(\frac{\partial T}{\partial t} + u\nabla T\right) \tag{3.36}$$

Note here again, the generic partial derivative of liquid density with respect to temperature, which would disappear in case of the barotropic

liquid equation of state. In a similar way as for the term corresponding to the compressibility effects, this one will be kept the same construction for vaporizing and reacting cases.

Multiphase turbulent mixing effects. Along a streamline in the flow, the turbulent mixing of high density liquid with low density gas can cause a significant divergence in the velocity field, which is accounted for in the term

$$-\frac{1}{\rho}\frac{\partial\rho}{\partial\tilde{Y}}\frac{D\tilde{Y}}{Dt} \tag{3.37}$$

The partial derivative is given by

$$\frac{\partial\rho}{\partial\tilde{Y}} = -\rho^2\left(\frac{1}{\rho_l} - \frac{1}{\rho_g}\right) \tag{3.38}$$

And the total derivative of liquid mass fraction is

$$\frac{D\tilde{Y}}{Dt} = \frac{\partial\tilde{Y}}{\partial t} + u\nabla\tilde{Y}, \tag{3.39}$$

which is related to the transport equation of $\tilde{Y}$ (Equation 3.5). Taking only the LHS of the equation and applying the chain rule:

$$\begin{aligned}\frac{\partial\rho\tilde{Y}}{\partial t} + \nabla(\rho u\tilde{Y}) =& \rho\frac{\partial\tilde{Y}}{\partial t} + \tilde{Y}\frac{\partial\rho}{\partial t} + \tilde{Y}\nabla\rho u + \rho u\nabla\tilde{Y} \\ =& \rho\left(\frac{\partial\tilde{Y}}{\partial t} + u\nabla\tilde{Y}\right) + \tilde{Y}\left(\frac{\partial\rho}{\partial t} + \nabla\rho u\right)\end{aligned} \tag{3.40}$$

In this expression, the first term on the RHS (multiplied by ρ) is just the total derivative of Y and the second one, in brackets, corresponds to the continuity equation. So this last term is zero. As a result,

$$\frac{\partial\rho\tilde{Y}}{\partial t} + \nabla(\rho u\tilde{Y}) = \rho\frac{D\tilde{Y}}{Dt}, \tag{3.41}$$

and the total derivative of Y, from Equation 3.5, is:

$$\frac{D\tilde{Y}}{Dt} = \frac{1}{\rho}\left(\frac{\partial}{\partial x_i}\left(\frac{\mu_t}{Sc}\frac{\partial\tilde{Y}}{\partial x_i}\right) - S_{evap}\right) \tag{3.42}$$

And thus, finally the turbulent mixing term can be obtained as:

$$-\frac{1}{\rho}\frac{\partial\rho}{\partial\tilde{Y}}\frac{D\tilde{Y}}{Dt} = \left(\frac{1}{\rho_l}-\frac{1}{\rho_g}\right)\left(\frac{\partial}{\partial x_i}\left(\frac{\mu_t}{Sc}\frac{\partial\tilde{Y}}{\partial x_i}\right)-S_{evap}\right) \tag{3.43}$$

The last term on the RHS of the Equation 3.24 was introduced in [22] due to the fact that the implementation of Trask et al. [38] did not guarantee that the consistency between density and mass fraction is always maintained. The solution to this issue was to create a small penalty function in the pressure projection step. This penalty function relaxes the density calculated from the continuity equation towards the value stipulated by Equation 3.19 (ρ_{EOS}). The constant multiplier, K_r, in this term represents the approximate number of time steps for relaxation to the correct density and δ_t is the already mentioned time step.

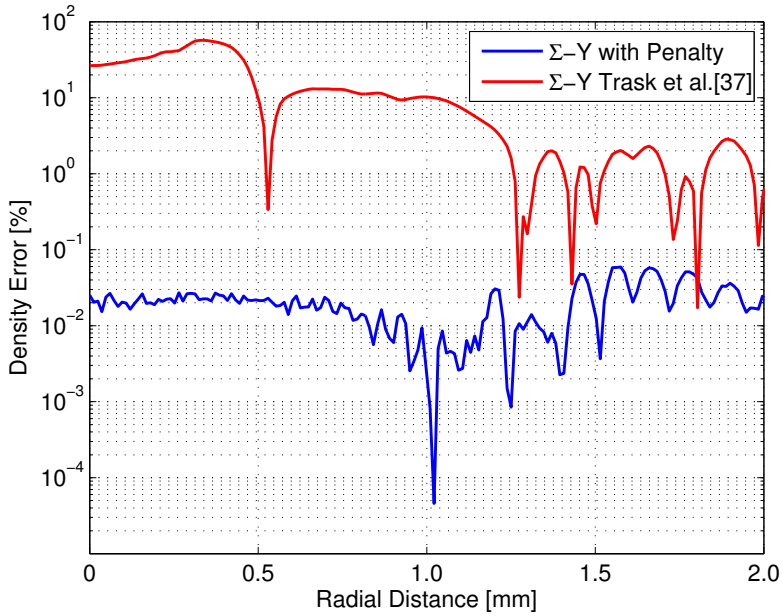

Figure 3.1. *Assessment of consistency between the equation of state and conservation of mass.*

In order to better understand the effects of this penalty function, Figure 3.1 shows the percentage discrepancy (note the logarithmic y-axis scale) between the density of the equation of state (Equation 3.19) and conservation of mass (Equation 3.1) along a transverse section of the spray, which is the actual density in the simulation. Two curves are shown, each corresponding to the two different numerical methods already commented for simulating compressible Eulerian mixing. The original scheme employed by Trask et al. [38] made no attempt to maintain consistency between these two densities. The second curve represents the method used in this work with the addition of the ad-hoc penalty function in the pressure equation to maintain consistency, with a remarkable improvement in performance.

Substituting each of these terms back into Equations 3.24 and 3.23, the final transport equation for the pressure is:

$$\begin{aligned}\nabla\left(\frac{1}{a_p}\nabla p\right) - \nabla\left(\frac{H(U)}{a_p}\right) =& \left(\frac{\bar{Y}}{\rho_l}\frac{\partial \rho_l}{\partial P} + \frac{1-\bar{Y}}{P}\right)\left(\frac{\partial P}{\partial t} + u\nabla P\right) \\ &+ \left(\frac{\bar{Y}}{\rho_l}\frac{\partial \rho_l}{\partial T} - \frac{1-\bar{Y}}{T}\right)\left(\frac{\partial T}{\partial t} + u\nabla T\right) \\ &+ \left(\frac{1}{\rho_l} - \frac{1}{\rho_g}\right)\left(-\frac{\partial}{\partial x_i}\left(\frac{\mu_t}{Sc}\frac{\partial \tilde{Y}}{\partial x_i}\right) + S_{evap}\right) \\ &+ \frac{\rho_{EOS} - \rho}{\delta_t k_r \rho}\end{aligned} \tag{3.44}$$

As can be seen, this pressure projection is inspired by the pressure/velocity coupling of the PISO method [39] and the LHS of Equation 3.44 includes the standard terms in a pressure projection step. Note that the coupling among equations is treated using a segregated implicit approach, in which equations are formulated for each dependent variable and solved sequentially, with the possibility of iteration over the system of equations until convergence is achieved.

In OpenFOAM syntax, the equation reads as:

```
fvScalarMatrix pEqn
(
    fvm::laplacian(rUAf, p)
  - fvc::div(phi)
  ==
    (Ybar/rholiq*devRholiqP+(1-Ybar)/p)*
  (fvm::ddt(p)+fvm::div(phi, p)-fvm::Sp(fvc::div(phi), p))

  + (Ybar/rholiq*devRholiqT-(1-Ybar)/T)*
  (fvm::ddt(T)+fvm::div(phi, T)-fvm::Sp(fvc::div(phi), T))

  + Prho*(-fvm::laplacian(turbulence->mut()/Sc, Y)+Sevap)

  + (rhoEOS-rho)/runTime.deltaT()/rhoRelaxationFactor/rho
);

pEqn.solve();
```

The term `rUAf` represents the diagonal coefficient from the momentum equation (as typical treated in OpenFOAM), `devRholiqP` and `devRholiqT` correspond to the numerical evaluations of the partial derivatives of liquid density and `Ybar` is the liquid volume fraction. `runTime.deltaT()` is the value of the time step and `rhoRelaxationFactor` the constant k_r.

3.3 Model development

In this section, as previously mentioned, the implementation of a turbulence model which better represents the physical behaviour of dense fuel sprays is presented as well as the procedures that account for the physical process of evaporation (mandatory in order to simulate sprays under diesel engine conditions). Together with them, an advanced liquid equation of state in combination with a thermodynamic model and the coupling methodology of the present spray model with a combustion one are given in the following.

3.3.1 Turbulence Model

As previously mentioned in Chapter 2, Section 2.5, in this work a RANS approach is followed to account for the effect of turbulence. In OpenFOAM there are some turbulence models available based on the eddy viscosity

assumption (standard k-ε, RNG k-ε, Realizable k-ε). A comparative study has been conducted to select the most adequate one for diesel spray simulations, as depicted in Section 4.2.3 of Chapter 4. However, an especially developed turbulence model for this type of simulations (high density ratio k-ε [9]) is not present in the main distribution. Thus, this model has been implemented and because of that, it is explained in the following lines.

High density ratio k-ε

This turbulence model was developed by Demoulin et al. [9]. It consists on a new derivative of the k-ε model [40], with the aim to deal with limitations existing in the available models at that time for application of spray atomization: first, the density ratio can be of the order of 1000 and second, at small scales there is no dissipation of the density gradient by molecular diffusion.

The model is based on the eddy viscosity assumption described above and additionally consists of two transport equations for the turbulent kinetic energy k and its rate of dissipation ε and the following specification of the eddy viscosity [41]:

$$\mu_t = \bar{\rho}\, C_\mu \frac{k^2}{\varepsilon}. \tag{3.45}$$

The transport equation for the turbulent kinetic energy is given by

$$\frac{\partial \bar{\rho} k}{\partial t} + \frac{\partial \bar{\rho} \widetilde{u}_j k}{\partial x_j} = \frac{\partial}{\partial x_j}\left[\left(\mu + \frac{\mu_t}{\sigma_k}\right)\frac{\partial k}{\partial x_j}\right] + P_k - \overline{u_i''}\frac{\partial \bar{p}}{\partial x_i} - \bar{\rho}\varepsilon \tag{3.46}$$

and its rate of dissipation by

$$\begin{aligned}\frac{\partial \bar{\rho} \varepsilon}{\partial t} + \frac{\partial \bar{\rho} \widetilde{u}_j \varepsilon}{\partial x_j} = \frac{\partial}{\partial x_j}\left[\left(\mu + \frac{\mu_t}{\sigma_\varepsilon}\right)\frac{\partial \varepsilon}{\partial x_j}\right] + C_{\varepsilon 1}\frac{\varepsilon}{k}\left(P_k - \overline{u_i''}\frac{\partial \bar{p}}{\partial x_i}\right) \\ - C_{\varepsilon 2}\bar{\rho}\frac{\varepsilon^2}{k} - C_{\varepsilon 3}\bar{\rho}\varepsilon\frac{\partial \widetilde{u}_j}{\partial x_j}\end{aligned} \tag{3.47}$$

This derivation includes an additional term ($\overline{u_i''}\frac{\partial \bar{p}}{\partial x_i}$) which accounts for the production caused by large density fluctuations between the heavy and the light fluids under the effect of the same pressure gradient. The averaged

velocity fluctuation in Equation 3.46 and Equation 3.47 is exactly given [12] by:

$$\overline{u_i''} = \bar{\rho}\widetilde{u_i' Y'} \left(\frac{1}{\rho_l} - \frac{1}{\rho_g} \right) \tag{3.48}$$

and using Equation 3.3 and Equation 3.45 gives the final expression of the averaged velocity fluctuation:

$$\overline{u_i''} = -\bar{\rho} \frac{C_\mu}{Sc} \frac{k^2}{\varepsilon} \left(\frac{1}{\rho_l} - \frac{1}{\rho_g} \right) \frac{\partial \tilde{Y}}{\partial x_i} \tag{3.49}$$

The production term P_k in the above equations is defined as

$$P_k = -\bar{\rho}\widetilde{u_i'' u_j''} \frac{\partial \widetilde{u_i}}{\partial x_i}, \tag{3.50}$$

where the Boussinesq hypothesis given by Equation 2.32 is adopted to determine the Reynolds stresses $\bar{\rho}\widetilde{u_i'' u_j''}$. The coefficients of the high density k-ε model are summarized in Table 3.1. The Schmidt numbers σ_k and σ_ε link the diffusivity of k and ε to the eddy viscosity μ_t.

Table 3.1. *Coefficients of the high density k-ε turbulence model.*

C_μ	$C_{\varepsilon 1}$	$C_{\varepsilon 2}$	$C_{\varepsilon 3}$	σ_k	σ_ε	Sc
0.09	1.44	1.92	-0.33	1.0	1.3	0.9

3.3.2 Evaporation Model

The evaporation model has been developed around the particular characteristics of the current engine technologies. The high boost and injection pressure, and small nozzle hole diameter result in a complete atomization regime inside the spray very near the nozzle exit. The process of atomization produces so tiny droplets, under realistic engine conditions, that the transport of mass and energy at its surfaces is no longer a limitation in the subsequent physical processes of evaporation and mixing in DI diesel sprays. Several experimental results by different authors have shown that the maximum liquid length is controlled by in-cylinder air density and temperature, nozzle orifice diameter and fuel type [13–15, 42]. These results confirm the hypothesis

that the vaporization process is limited by fuel-air mixing rate. Fuel droplets reach a dynamic equilibrium with the surrounding air very close to the nozzle, which leads to a very fast local transfer rates of momentum, mass and energy. Therefore, fuel droplets evaporate as long as there is enough air for them to heat up and vaporize. Consequently, vaporizing diesel sprays fit adequately in the Locally Homogeneous Flow (LHF) approach [43], i.e. local equilibrium exists both in thermal and dynamic conditions.

In order to account for the spray evaporation in the CFD model, both an additional transport equation for vapor fuel mass fraction and also a procedure for calculating the source term, S_{evap}, of Equation 3.5 have to be added. The transport equation can be written in a similar way to the conservation of liquid fuel as:

$$\frac{\partial \bar{\rho}\tilde{Y}_v}{\partial t} + \frac{\partial \bar{\rho}\tilde{u}_i\tilde{Y}_v}{\partial x_i} - \frac{\partial}{\partial x_i}\left(\frac{\mu_t}{Sc}\frac{\partial \tilde{Y}_v}{\partial x_i}\right) = S_{evap} \tag{3.51}$$

Again the standard turbulent gradient law is used for closure in this transport equation and note that the source evaporation term has the opposite effect with respect to the liquid mass fraction equation (Equation 3.2). This sink/source terms for fuel liquid/vapor transport equations are calculated in terms of a rate needed to achieve the local adiabatic saturation conditions. This can be written as

$$S_{evap} = \frac{Y_{v,sat} - \tilde{Y}_v}{\tau_{evap}} \tag{3.52}$$

where $\tilde{Y}_v$ is the local vapor fuel mass fraction, $Y_{v,sat}$ is the value of vapor fuel mass fraction under adiabatic saturation conditions and τ_{evap} is a relaxation time set equal to the computational time step.

In order to calculate the evaporation source term, under the assumption of an adiabatic mixing, the liquid/vapor region in the spray is supposed to have a trend towards adiabatic saturation conditions and to determine the liquid-vapor equilibrium, Raoult's ideal law is considered. The two major hypothesis of Raoult's law are:

- The vapor phase behaves as an ideal gas.
- The liquid phase behaves as an ideal solution (note that in this case a single component liquid is considered).

Using this law it is possible to relate the composition of the vapor and liquid phases, specifically the vapor mole fraction at saturation conditions ($X_{v,sat}$) through the local vapor pressure (p_v) and the total system pressure (p). Mathematically, Raoult's law for a single component in an ideal solution is stated as:

$$p_v = X_{v,sat} \cdot p \tag{3.53}$$

The actual sequence of calculation starts from local temperature, which is used to obtain the vapor pressure and then, $X_{v,sat}$ is evaluated in order to finally obtain $Y_{v,sat}$. The aforementioned local vapor pressure is determined using the Lee and Kesler correlation [44]:

$$\ln \frac{p_v}{p_c} = f_1(T_r) + \omega f_2(T_r) \tag{3.54}$$

where p_c is the critical pressure of the fuel and f_i are evaluated as:

$$f_1(T_r) = 5.92714 - \frac{6.09648}{T_r} - 1.28862 \cdot \ln(T_r) + 0.169347 \cdot T_r^6 \tag{3.55}$$

$$f_2(T_r) = 15.2518 - \frac{15.6875}{T_r} - 13.4721 \cdot \ln(T_r) + 0.43577 \cdot T_r^6 \tag{3.56}$$

Then, the equilibrium saturated local fuel vapor mass fraction is then related to the vapor pressure by:

$$Y_{v,sat} = X_{v,sat} \frac{MW_f}{MW_{mix}} = \frac{MW_f}{MW_f + (\frac{p}{p_v} - 1) \cdot MW_{air}} \tag{3.57}$$

where MW_f corresponds to the molecular weight of fuel phase, MW_{air} molecular weight of ambient air phase and MW_{mix} is the molecular weight of the whole mixture.

Additionally, fuel evaporation also produces a change in the interphase surface and as a result, a source term appear in the Equation 3.11. This $S_{\Sigma_{evap}}$ term is modeled as in Lebas et al. [11].

$$S_{\Sigma_{evap}} = \frac{2}{3} \frac{\Sigma}{\tilde{Y}} S_{evap} \tag{3.58}$$

Finally, the addition of this fuel vapor phase leads to a new contribution in Equation 3.24, when the chain rule is applied to the continuity equation.

$$-\frac{1}{\rho}\frac{\partial\rho}{\partial Y_v}\frac{DY_v}{Dt} \tag{3.59}$$

Similarly to the steps followed in the derivation of the corresponding term for the liquid phase, from Equation 3.38 to 3.43, this term in the case of the fuel vapor phase is given by:

$$-\frac{1}{\rho}\frac{\partial\rho}{\partial Y_v}\frac{DY_v}{Dt} = \left(\frac{1}{\rho_v}-\frac{1}{\rho_g}\right)\left(\frac{\partial}{\partial x_i}\left(\frac{\mu_t}{Sc}\frac{\partial\tilde{Y}_v}{\partial x_i}\right)+S_{evap}\right) \tag{3.60}$$

where ρ_v is the fuel density of the vapor phase that obeys an ideal gas law.

3.3.3 Fluid properties definition

In this section the implementation of an advanced liquid equation of state together with a developed thermodynamic model are presented.

3.3.3.1 Liquid equation of state – HBT Correlation

The development of the liquid equation of state is obtained through a liquid volume correlation that accounts for the influence of both pressure and temperature. This correlation was proposed by Hankinson and Thomson [45] for saturated densities of liquids and is referred as the HBT correlation [36]:

$$V_s = V^* V_R^0(1-\omega_{SRK}V_R^\delta) \tag{3.61}$$

where V^* is a pure component characteristic volume, whose value is close to the critical volume and ω_{SRK}, is that value of the acentric factor that causes the Soave equation of state to give the best fit to pure component vapor pressures. Values of both constants are tabulated for several compounds in [45]. The values of V_R^0 and V_R^δ are calculated from

$$V_R^0 = 1 + a(1-T_r)^{1/3} + b(1-T_r)^{2/3} + c(1-T_r) + d(1-T_r)^{4/3} \tag{3.62}$$

$$V_R^\delta = \frac{e + fT_r + gT_r^2 + hT_r^3}{T_r - 1.00001} \tag{3.63}$$

these equations may be used in the range $0.25 < T_r < 0.95$ for Equation 3.62 and Equation 3.63 may be used when $0.25 < T_r < 1$, being T_r the reduced temperature (T/T_c) and T_c the critical temperature. Constants a through h are given by

a	-1.52816	b	1.43907
c	-0.81446	d	0.190454
e	-0.296123	f	0.386914
g	-0.0427258	h	-0.0480645

More recently, the HBT method have been extended by Thomson et al. [46] to allow prediction of compressed liquid volumes by generalizing the constants in the Tait equation of state [47]. Thus, the molar volume of the liquid is:

$$V = V_s\left(1 - c' \ln \frac{\beta + p}{\beta + p_v}\right) \tag{3.64}$$

V_s, the saturated liquid volume at the vapor pressure P_{vp} (which evaluation is explained at Section 3.3.2), should be obtained from Equation 3.61. β and c are obtained from

$$\beta = P_c\left(-1 + a'(1-T_r)^{1/3} + b'(1-T_r)^{2/3} + d'(1-T_r) + e'(1-T_r)^{4/3}\right) \tag{3.65}$$

$$e' = exp(f' + g'\omega_{SRK} + h'\omega_{SRK}^2) \tag{3.66}$$

$$c' = j' + k'\omega_{SRK} \tag{3.67}$$

Values of P_c, critical pressure are also tabulated for several compounds and the constants a' through $'$ are:

a'	-9.070217	b'	62.45326
d'	-135.1102	f'	4.79594
g'	0.250047	h'	1.14188
j'	0.0861488	k'	0.0344483

Once the molar volume is obtained, the density of the liquid fuel is calculated as:

$$\rho_l = \frac{MW_f}{V} \tag{3.68}$$

3.3.3.2 Thermodynamic Model

To close the above system of equations, the temperature is obtained from a bulk mixture enthalpy equation, under the assumption of local thermodynamic equilibrium, expressed in the following terms:

$$h\left(T\right) = \tilde{Y} \cdot h_{f,l}\left(T\right) + \tilde{Y}_v \cdot h_{f,v}\left(T\right) + \left(1 - \tilde{Y} - \tilde{Y}_v\right) \cdot h_a\left(T\right) \tag{3.69}$$

Here $h_{f,l}$, $h_{f,v}$ and h_a denote the enthalpy of the fuel on liquid and vapor phases and the enthalpy of the ambient gas respectively. These enthalpies are calculated using the respective specific heat capacities at constant pressure ($c_{p,i}$), evaluated as a function of temperature T from a set of coefficients taken from JANAF tables of thermodynamics to feed the 7-coefficient NASA polynomials. Additionally, on this thermodynamic tables a function to relate temperature with the enthalpy is also available:

$$C_p^0 = R \cdot \left(a_1 + a_2 T + a_3 T^2 + a_4 T^3 + a_5 T^4\right) \tag{3.70}$$

$$h^0 = RT \cdot \left(a_1 + \frac{a_2}{2} T + \frac{a_3}{3} T^2 + \frac{a_4}{4} T^3 + \frac{a_5}{5} T^4 + \frac{a_6}{T}\right) \tag{3.71}$$

This expressions can be directly applied to the ambient gas h_a and $c_{p,a}$, but not for the fuel. In this case, upon the principle of corresponding states, the Rowlinson-Bondi equation (initially proposed by Bondi [48] and later modified by Rowlinson [49]) that makes use of the departure heat capacity function is applied:

$$\begin{aligned} C_{p,l}(T) = C_p^0 + R \cdot \Big(&1.45 + 0.45(1 - T_r)^{-1} + 0.25\omega\big[17.11 \\ &+25.2(1 - T_r)^{1/3} T_r^{-1} + 1.742(1 - T_r)^{-1}\big]\Big) \end{aligned} \tag{3.72}$$

Using this liquid specific heat capacity, the liquid enthalpy is given by:

$$h_{f,l}(T) = h^0 + \int_{298}^{T} R \cdot \Big(1.45 + 0.45(1-T_r)^{-1} + 0.25\omega_{SRK}\big[17.11 + 25.2(1-T_r)^{1/3}T_r^{-1} + 1.742(1-T_r)^{-1}\big]\Big)\, dT \tag{3.73}$$

Vapor fuel phase is evaluated by means of the enthalpy of vaporization ΔHv, sometimes referred to as the latent heat of vaporization, which is obtained from the Pitzer et al. [50] corresponding states correlation:

$$\Delta Hv(T) = RT_c + \left(7.08(1-T_r)^{0.354} + 10.95\omega_{SRK}(1-T_r)^{0.456}\right) \tag{3.74}$$

Then, vapor fuel phase enthalpy is evaluated with two different expressions depending on the presence of liquid fuel:

- if liquid is present:

$$h_{f,v}(T) = h_{f,l}(T) + \Delta Hv(T) \tag{3.75}$$

- if only vapor is present:

$$h_{f,v}(T) = h_{f,l}(T_{evap}) + \Delta Hv(T_{evap}) + \int_{T_{evap}}^{T} C_p^0\, dT \tag{3.76}$$

Finally, the algorithm to calculate the temperature from the mixture enthalpy uses the iteration method, which first guesses a temperature (T_0) and then, updates it (obtaining the new value of T) until the difference between both temperatures is less than the given convergence tolerance or when the number of iteration exceeds a maximum number. The process used to update the temperature corresponds to the Newton-Raphson method.

$$T = T_0 + \frac{h\,(T) - h\,(T_0)}{dh\,(T_0)} \tag{3.77}$$

where $h\,(T)$ is the enthalpy value from the transport Equation 3.7 and, $h\,(T_0)$ and $dh\,(T_0)$ the enthalpy and its first derivative from Equation 3.69 evaluated at the guessed temperature T_0.

3.3.4 Coupling with a combustion model

In this section the coupling of the spray model, developed in this Ph.D. work, with a combustion model is explained. This coupling represents a natural step in the simulation process of diesel sprays, a simplified representation of the combustion process of a fuel spray is shown in Fig.3.2.

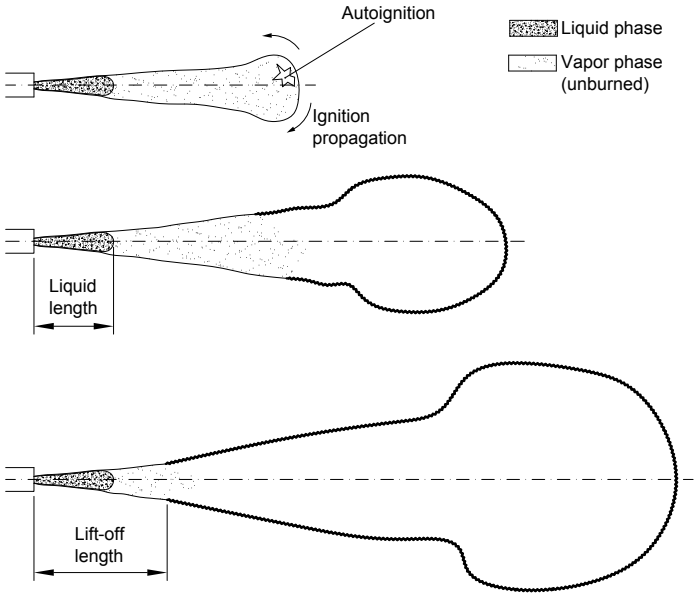

Figure 3.2. *Simplified representation of ignition and combustion process of reactive spray.*

The combustion modeling strategy can be classified as an Unsteady Flamelet/Progress Variable (UFPV) approach, especifically the model used in this work was implemented by Winklinger [51]. This combustion model is based on the following concepts:

- **Flamelet concept.** The combustion model is based on the flamelet concepts which suggests that a turbulent flame can be represented by a set of laminar flamelets.

- **Presumed PDF modeling.** In order to consider the effect of turbulence on the combustion process, presumed PDFs are adopted to describe the statistical distribution of the independent variables of the process.

- **Flamelet manifold.** A flamelet manifold is generated which allows to store all properties involved in the combustion process as a function of reduced number of independent variables in a look-up table.

In [51] there are two different ways of tabulation, but here only the one considering the tabulation of species mass fractions is used, as this method was developed for application to engine simulations, and as a result it is more suitable for modeling reacting diesel sprays. Further details of the combustion model can be found in [51], but here the description is focused on the additional model equations needed to complete the inert spray code and the particularity of the application case. A transport equation for the mean mixture fraction, the mixture fraction variance and the mean scalar dissipation rate are needed. While the first one is already implemented through Equation 3.51 for the vapor fuel mass fraction, the other two appear in the following lines:

Transport equation for the mixture fraction variance

The equation for the mixture fraction variance $\tilde{Z}''^2$ is given by:

$$\frac{\partial \bar{\rho}\tilde{Z}''^2}{\partial t} + \frac{\partial \bar{\rho}\tilde{u}_i\tilde{Z}''^2}{\partial x_i} - \frac{\partial}{\partial x_i}\left(\frac{\mu_t}{Sc}\frac{\partial \tilde{Z}''^2}{\partial x_i}\right) = 2\,\frac{\mu_t}{Sc}\left(\frac{\partial \tilde{Y}_v}{\partial x_i}\right)^2 - \bar{\rho}\tilde{\chi} \tag{3.78}$$

Model for the mean scalar dissipation rate

The mean scalar dissipation rate is modeled in a standard way as:

$$\tilde{\chi} = C_\chi\,\frac{\varepsilon}{k}\,\tilde{Z}''^2, \tag{3.79}$$

where the turbulent dissipation ε and the turbulent kinetic energy k are directly obtained from the employed turbulence model. The constant C_χ represents a parameter of the combustion model.

In this method not all the species involved in the combustion process are transported and only a limited number N_M of carefully chosen species, which represent the total mixture are considered in the CFD solver. Compared to the application by Winklinger [51] to the "Spray H", here the simulated spray is the "Spray A" cases, from the Engine Combustion Network (ECN) database (see Chapter 6)), where n-dodecane is used as a surrogate for diesel, the method is detailed for that fuel in the

following. In this case, eleven species are transported in the CFD code of which CO, CO_2, $C_{12}H_{26}$, H, H_2O OH, C_2H_2, and CH_2O are tabulated and C_7H_{14}, H_2, O_2 represent the reconstructed species responsible for mass conservation, which are obtained from the atomic balance equations:

$$Y_{O_2} = -\frac{MW_{O_2}}{2}\left(\frac{Y_{CO}}{MW_{CO}} + 2\frac{Y_{CO_2}}{MW_{CO_2}} + \frac{Y_{H_2O}}{MW_{H_2O}} + \frac{Y_{CH_2O}}{MW_{CH_2O}} + \frac{Y_{OH}}{MW_{OH}}\right) + Y^0_{O_2}, \tag{3.80}$$

$$Y_{C_7H_{14}} = -\frac{MW_{C_7H_{14}}}{7}\left(-12\frac{Y^0_{C_{12}H_{24}} - Y_{C_{12}H_{24}}}{MW_{C_{12}H_{24}}} + \frac{Y_{CH_2O}}{MW_{CH_2O}} + 2\frac{Y_{C_2H_2}}{MW_{C_2H_2}} + \frac{Y_{CO}}{MW_{CO}} + \frac{Y_{CO_2}}{MW_{CO_2}}\right), \tag{3.81}$$

$$Y_{H_2} = -\frac{MW_{H_2}}{2}\left(-24\frac{Y^0_{C_{12}H_{24}} - Y_{C_{12}H_{24}}}{MW_{C_{12}H_{24}}} + 14\frac{Y_{C_7H_{14}}}{MW_{C_7H_{14}}} + 2\frac{Y_{H_2O}}{MW_{H_2O}} + \frac{Y_H}{MW_H} + 2\frac{Y_{CH_2O}}{MW_{CH_2O}} + 2\frac{Y_{C_2H_2}}{MW_{C_2H_2}} + \frac{Y_{OH}}{MW_{OH}}\right) \tag{3.82}$$

In these equations Y_k and MW_k denote the mass fraction and the molar weight of species k and Y^0_k is the mass fraction of the tracer of species k, necessary for the correct balance. Note that the mass fractions of these three species deviate from their real concentration in the mixture, since they contain contributions from other species that are not considered in the mixture.

The remaining steps in the combustion model are identical to the ones explained in [51], deducing the progress variable from the mass fractions of the transported, tabulated species CO and CO_2 as $Y_c = Y_{CO} + Y_{CO_2}$ and obtaining the reaction rates of each species. At the end of a calculation cycle, the combustion model returns the reaction rates for all transported species to the CFD solver. The chemical mechanism, proposed by Narayanaswamy et al. [52], used in this case to describe the combustion of n-dodecane consists of 255 species and 2289 reactions.

Transport equation for the species mass fraction

The transport equations for each specie can be written in a similar way to the conservation of vapor fuel as:

$$\frac{\partial \bar{\rho}\tilde{Y}_i}{\partial t} + \frac{\partial \bar{\rho}\tilde{u}_i\tilde{Y}_i}{\partial x_i} - \frac{\partial}{\partial x_i}\left(\frac{\mu_t}{Sc}\frac{\partial \tilde{Y}_i}{\partial x_i}\right) = S_{evap} + S_{chem} \tag{3.83}$$

where $\tilde{Y}_i$ represent the mass fraction of the different species, the term S_{evap} is the evaporation source term (only different from zero for the fuel specie, $C_{12}H_{26}$) and the term S_{chem} is the reacting source term.

Finally, the effects of all these generated species, due to the combustion process, have to be taken into account on the mixture. This means that the derived pressure equation applying the chain rule to the continuity equation leads to new terms (similarly to the vapor fuel effects):

$$-\frac{1}{\rho}\frac{\partial \rho}{\partial Y_i}\frac{DY_i}{Dt}, \tag{3.84}$$

which lead to

$$-\frac{1}{\rho}\frac{\partial \rho}{\partial Y_i}\frac{DY_i}{Dt} = \left(\frac{1}{\rho_i} - \frac{1}{\rho_g}\right)\left(\frac{\partial}{\partial x_i}\left(\frac{\mu_t}{Sc}\frac{\partial \tilde{Y}_i}{\partial x_i}\right) + S_{evap} + S_{chem}\right) \tag{3.85}$$

where ρ_i is the density of the corresponding specie that obeys an ideal gas law. Note that the term for the vapor fuel is not duplicated, it is only modified by the addiction of the chemical source term.

3.4 Summary

Some concluding final remarks concerning the developed spray model are given here in order to point out main important benefits of this modeling strategy for simulating fuel sprays.

Current Eulerian spray CFD model, constructed under the PISO algorithm, overcomes the drawbacks of the classical Lagrangian approaches for modeling fuel sprays. It presents a more appropriate physics description on the dense region of the spray, where the hypothesis behind the models used in the particle tracking are not precise due to they are based on assumptions of spherical and isolated droplets. Additionally, as it is known, nozzle geometric parameters have a great influence on the spray behaviour. Thus, including nozzle effects by coupling internal and external flow simulations leads to a better representation of reality. The issues derived from the methodology

required to transfer all the spatial and temporal fields from an internal flow simulation to a primary break-up (blob) model are avoided by using an Eulerian atomization model to simulate both internal nozzle flow and external spray together in one continuous domain.

A further important aspect of the present work is its coupling with a combustion model. This connection, using a great quality multi-phase spray modeling and an advanced combustion model, should lead to a better description of the complex and multidisciplinary problems involved in the turbulent combustion processes. And from the point of view of the CFD tool, provides a complete model able to simulate a diesel spray from inside the injector nozzle until its combustion occurs.

Bibliography

[1] Vallet A. and Borghi R. "Modélisation Eulerienne de l'atomisation d'un jet liquide". *C.R. Acad. Sci, Paris*, Vol. 327, pp. 1015–1020, 1999.

[2] Weller H.G., Tabor G., Jasak H. and Fureby C. "A Tensorial Approach to Computational Continuum Mechanics Using Object-Oriented Techniques". *Computers in Physics*, Vol. 12, pp. 620–631, 1998.

[3] Trask N. "Implementation of an Eulerian atomization model to characterize primary spray formation". Master's thesis, University of Massachusetts Amherst, 2010.

[4] Kastengren Alan L., Powell Christopher F., Wang Yujie, Im Kyoung-Su and Wang Jin. "X-ray radiography measurements of diesel spray structure at engine-like ambient density". *Atomization and Sprays*, Vol. 19 n^o 11, pp. 1031–1044, 2009.

[5] Kastengren A.L., Tilocco F.Z., Duke D., Powell C.F., Moon S. and Zhang X. "Time-Resolved X-Ray Radiography of Diesel Injectors from the Engine Combustion Network". In *12th Triennial International Conference on Liquid Atomization and Spray Systems*, pp. 2–6, 2012.

[6] Pickett L., Manin J., Kastengren A. and Powell C. "Comparison of Near-Field Structure and Growth of a Diesel Spray Using Light-Based Optical Microscopy and X-Ray Radiography". *SAE Int. J. Engines*, Vol. 7 n^o 2, 2014.

[7] Beau P.A., Funk M., Lebas R. and Demoulin F.X. "Applying Quasi-Multiphase Model to Simulate Atomization Processes in Diesel Engines: Modeling of the Slip Velocity". *SAE Technical Paper 2005-01-0220*, 2005.

[8] Blokkeel G., Barbeau B. and Borghi R. "A 3D Eulerian Model to Improve the Primary Breakup of Atomizing Jet". *SAE Technical Paper 2003-01-005*, 2003.

[9] Demoulin F.X., Beau P.A., Blokkeel G., Mura A. and Borghi R. "A New Model for Turbulent Flows with Large Density Fluctuations: application to Liquid Atomization". *Atomization and Sprays*, Vol. 17, pp. 315–345, 2007.

[10] Demoulin Francois-Xavier, Reveillon Julien, Duret B., Bouali Zakaria, Desjonqueres P. and Menard Thibaut. "Toward using direct numerical simulation to improve primary break-up modeling". *Atomization and Sprays*, Vol. 23 n^o 11, pp. 957–980, 2013.

[11] Lebas R., Menard T., Beau P.A., Berlemont A. and Demoulin F.X. "Numerical simulation of primary break-up and atomization: DNS and modelling study". *International Journal of Multiphase Flow*, Vol. 35 n^o 3, pp. 247 – 260, 2009.

[12] Vallet A., Burluka A.A. and Borghi R. "Development of a Eulerian Model for the Atomization of a Liquid Jet". *Atomization and Sprays*, Vol. 11, pp. 619–642, 2001.

[13] Siebers D. "Liquid-Phase Fuel Penetration in Diesel Sprays". *SAE Technical Paper*, n^o 980809, 1998.

[14] Siebers D. "Scaling Liquid-Phase Fuel Penetration in Diesel Sprays Based on Mixing-Limited Vaporization". *SAE Technical Paper*, n^o 1999-01-0528, 1999.

[15] Arcoumanis C. and Kamimoto T. *Flow and Combustion in Reciprocating Engines*. Springer-Verlag, 2009.

[16] Dahms Rainer N., Manin Julien, Pickett Lyle M. and Oefelein Joseph C. "Understanding high-pressure gas-liquid interface phenomena in Diesel engines". *Proceedings of the Combustion Institute*, Vol. 34 n^o 1, pp. 1667 – 1675, 2013.

[17] Oefelein J., Dahms R. and Lacaze G. "Detailed Modeling and Simulation of High-Pressure Fuel Injection Processes in Diesel Engines". *SAE Int. J. Engines*, Vol. 5 n^o 3, pp. 10, 2012.

[18] Oefelein J. C., Dahms R. N., Lacaze G., Manin J. L. and Pickett L. M. "Effects of Pressure on the Fundamental Physics of Fuel Injection in Diesel Engines". *ICLASS Paper*, 2012.

[19] Lebas R., Blokkeel G., Beau P.A. and Demoulin F.X. "Coupling Vaporization Model With the Eulerian-Lagrangian Spray Atomization (ELSA) Model in Diesel Engine Conditions". *SAE Technical Paper 2005-01-0213*, 2005.

[20] Beheshti Novid, Burluka AlexeyA. and Fairweather Michael. "Assessment of $\Sigma - Y$ liq model predictions for air-assisted atomisation". *Theoretical and Computational Fluid Dynamics*, Vol. 21 n^o 5, pp. 381–397, 2007.

[21] Desantes J.M., García-Oliver J.M., Pastor J.M. and Pandal A. "A Comparison of Diesel Sprays CFD modelling approaches: DDM vs $\Sigma - Y$ Eulerian Atomization Model". *Atomization and Sprays*, Vol. 26 n^o 7, pp. 713–737, 2016.

[22] García-Oliver J.M., Pastor J.M., Pandal A., Trask N., Baldwin E. and Schmidt D.P. "Diesel Spray CFD Simulations based on the $\Sigma - Y$ Eulerian Atomization Model". *Atomization and Sprays*, Vol. 23, pp. 71–95, 2013.

[23] Lebas R. *Modélisation Eulérienne de l'Atomisation Haute Pression Influences sur la Vaporisation et la Combustion Induite.* Doctoral Thesis, Université de Rouen, 2007.

[24] Navarro-Martinez S. "Large eddy simulation of spray atomization with a probability density function method". *International Journal of Multiphase Flow*, Vol. 63, pp. 11 – 22, 2014.

[25] Lebas R., Blokkeel G., Beau P.A. and Demoulin F.X. "ELSA model for atomization: to benefit of the Eulerian and Lagrangian descriptions of the liquid phase". *ICLASS Paper*, 2006.

[26] Favre Alexandre J.A. "Équations des gaz turbulents compressibles". *Journal of Méchanique*, Vol. 4 n^o 3, pp. 361–390, 1965.

[27] Favre Alexandre J.A. "Statistical equations of turbulent gases". In *Problems of Hydrodynamics and Continuum Mechanics*, pp. 231–266. Soc. for Ind. and Appl. Mathematics, Philadelphia, 1969.

[28] Ishii M. *Thermofluid Dynamics of Two-phase Flows.* Eyrolles, Paris, France, 1975.

[29] Martí-Aldaraví P. *Development of a computational model for a simultaneous simulation of internal flow and spray break-up of the Diesel injection process.* Doctoral Thesis, Departamento de Máquinas y Motores Térmicos, Universidad Politécnica de Valencia, España, 2014.

[30] Delhaye J.M., Giot M. and Riethmuller M.L. *Thermohydraulics of two-phase systems for industrial design and nuclear engineering.* Series in thermal and fluids engineering. Hemisphere Pub. Corp., 1981.

[31] Marble F.E. and Broadwell J.E. *The Coherent Flame Model for Turbulence Chemical Reactions.* Technical report, Project Squid Headquarters. Chaffee Hall, Purdue University, West Lafayette, Indiana, 1977.

[32] Candel S.M. and Poinsot T.J. "Flame Stretch and the Balance Equation for the Flame Area". *Combustion Science and Technology*, Vol. 70 n^o 1-3, pp. 1–15, 1990.

[33] Belhadef A., Vallet A., Amielh M. and Anselmet F. "Pressure-swirl atomization: Modeling and experimental approaches". *International Journal of Multiphase Flow*, Vol. 39, pp. 13 – 20, 2012.

[34] Wang Y., Lee W., Reitz R. and Diwakar R. "Numerical Simulation of Diesel Sprays Using an Eulerian-Lagrangian Spray and Atomization (ELSA) Model Coupled with Nozzle Flow". *SAE Technical Paper*, n^o 2011-01-0386, 2011.

[35] Wang, Y. andGrover R.O., Schmidt D.P., Diwakar R. and Kuo T.-W. "Application of Interface Area Density Modeling to Define Spray Plume Boundary". *ILASS Paper*, 2015.

[36] Reid R.D., Prausnitz J.M. and Poling B.E. *The Properties of Gases and Liquids.* McGraw-Hill, 1987.

[37] Jasak H. *Error Analysis and Estimation for the Finite Volume Method with Applications to Fluid Flows.* Doctoral Thesis, Imperial College, 1996.

[38] Trask N., Schmidt D.P., Lightfoot M.D.A. and Danczyk S.A. "Compressible Modeling of the Internal Flow in a Gas-Centered Swirl-Coaxial Fuel Injector". *Journal of Propulsion and Power*, Vol. 28(4), pp. 685–693, 2012.

[39] Ferziger J.H. and Peric M. *Computational Methods for Fluid Dynamics.* Springer, Berlin, 2002. pp. 176–178.

[40] Jones W.P and Launder B.E. "The prediction of laminarization with a two-equation model of turbulence". *International Journal of Heat and Mass Transfer*, Vol. 15 n^o 2, pp. 301 – 314, 1972.

[41] Pope S. B. *Turbulent Flows.* Cambridge University Press, 2000.

[42] Bruneaux Gilles. "Liquid and vapor spray structure in high-pressure common rail diesel injection". *Atomization and Sprays*, Vol. 11 n^o 5, 2001.

[43] Faeth G.M. "Evaporation and combustion of sprays". *Progress in Energy and Combustion Science*, Vol. 9 n^o 1-2, pp. 1–76, 1983.

[44] Lee Byung Ik and Kesler Michael G. "A generalized thermodynamic correlation based on three-parameter corresponding states". *AIChE Journal*, Vol. 21 n^o 3, pp. 510–527, 1975.

[45] Hankinson R. W. and Thomson G. H. "A New Correlation for Saturated Densities of Liquids and Their Mixtures". *AIChE Journal*, Vol. 25 n^o 4, pp. 653–663, 1979.

[46] Thomson G. H., Brobst K. R. and Hankinson R. W. "An Improved Correlation Compressed Liquids and Liquid Mixtures". *AIChE Journal*, Vol. 28 n^o 4, pp. 671–676, 1982.

[47] Tait P. G. *Physics and Chemistry of the Voyage of H.M.S*, volume 2. Challenger. HMSO, London, 1888.

[48] Bondi A. "Estimation of Heat Capacity of Liquids". *Industrial & Engineering Chemistry Fundamentals*, Vol. 5 n^o 4, pp. 442–449, 1966.

[49] Rowlinson John Shipley. *Liquids and liquid mixtures.* Butterworths, London, 1969.

[50] Pitzer Kenneth S., Lippmann David Z., Jr. R. F. Curl, Huggins Charles M. and Petersen Donald E. "The Volumetric and Thermodynamic Properties of Fluids. II. Compressibility Factor, Vapor Pressure and Entropy of Vaporization1". *Journal of the American Chemical Society*, Vol. 77 n^o 13, pp. 3433–3440, 1955.

[51] Winklinger J.F. *Implementation of a Combustion Model based on the Flamelet Concept and its Application to turbulent reactive Sprays.* Doctoral Thesis, Departamento de Máquinas y Motores Térmicos, Universidad Politécnica de Valencia, España, 2014.

[52] Narayanaswamy Krithika, Pepiot Perrine and Pitsch Heinz. "A chemical mechanism for low to high temperature oxidation of n-dodecane as a component of transportation fuel surrogates". *Combustion and Flame*, Vol. 161 n^o 4, pp. 866 – 884, 2014.

Chapter 4

Model set-up and assessment. Non-vaporizing spray

Contents

4.1 Introduction

A first application of the implemented Eulerian spray model is presented in this chapter. The model is applied to a basic external flow, namely a free non-vaporizing spray, which has been simulated from the nozzle exit and downstream, with the aim of validating and evaluating its performance. Thus, model predictions have been compared to experimental data from free diesel sprays under such conditions. Some reasons why these studies were chosen for a first model test, the objectives and the methodology of this preliminary study are given in the following.

4.1.1 Motivation

The chosen experimental configuration is really attractive for an initial study of a spray model focused on simulating diesel sprays. First of all, the database selected was generated by a single-hole nozzle with the orifice oriented along the injector axis. This basic and symmetric layout is extremely convenient for a fundamental spray research and lead to an important simplification of the modeling effort. Additionally, the shape of the orifice is conical and the nozzle was submitted to hydro-erosion processes to increase the entrance radius, characteristics that help to avoid cavitation (not considered in the present work), as demonstrated by the hydraulic characterization presented in [1]. Moreover, the experiments were conducted at room temperature and using as fuel standard diesel, conditions which allow a validation and evaluation of the basic computational Eulerian spray model, i.e. without taking into account the evaporation, combustion and wall impingement phenomena. Thus, the present experimental configuration is the perfect framework because the analysis is only focused on the atomization and spray formation processes (fuel/air mixing), which are the basis of the Eulerian CFD model.

A further advantage is the comprehensive set of experimental data available for this preliminary case due to different measurements. The data includes typical spray macroscopic characteristics, namely penetration and cone angle, obtained by high-speed imaging [2], using the validated methodology for image processing developed by Pastor et al. [3]. In addition, the spatial distribution of the droplet size and velocity is available from phase doppler particle analyser (PDPA) measurements [4] optimized as described in [5]. This vast amount of data enable a complete analysis of the capability of the model to simulate diesel sprays, both in global and local terms.

4.1.2 Objectives of the study

The main objective of this preliminary study is to test the basic spray model and its implementation in the CFD code. This goal implicitly includes the validation of the assumptions made under the development of the Eulerian spray modeling approach. Moreover, it is desired to establish a well defined modeling set-up, that makes possible to reproduce accurately diesel spray behaviour. Furthermore, the predictive capabilities of the model concerning all the characteristics measured shall be investigated, including the performance to capture the experimental trends under different operating conditions, which makes it possible to prove the overall usefulness of the basic model.

4.1.3 Methodology of the study

The data for model evaluation were obtained from a database of specific test rig for diesel spray characterization, which has been generated by single-hole axisymmetric nozzle, as previously introduced, using a high-pressure common rail injection system. In those experiments, the sprays are injected into a quiescent vessel where back pressure is modified at constant room temperature, so that ambient densities from 10 to 40 kg/m^3 are obtained in a non-vaporizing environment. Additionally, injection pressures ranged between 30 and 130 MPa.

Table 4.1. *Operating conditions for non-vaporizing tests.*

Injection Pressure [MPa]	30 - 80 - 130
Ambient Density [kg/m^3]	10 - 25 - 40
Ambient Temperature [K]	298.15

The nozzle geometry characteristics were obtained by the silicone methodology technique [6]. This procedure is based on the extraction of silicone molds of the nozzle and their visualization in either an optical or a scanning electron microscope. The images obtained by the microscope are then processed by using a computer aided design software. In Table 4.2, these geometry characteristics are summarized, where D, L and r denote nozzle orifice outlet diameter, length and inlet radius, respectively. The nozzle convergence is described by the k-factor, as defined in [6].

In order to simulate these conditions of diesel sprays, a 2-D axisymmetric computational domain with 80 x 25 mm extent in the axial and radial spray

Table 4.2. *Nozzle geometric characteristics for non-vaporizing tests.*

D [μm]	L/D [-]	r/D [-]	k-factor
112	8.93	0.30	2.8

directions is considered. The mesh is structured with non-uniform grid resolution. There are 10 cells along the orifice diameter, as in [7], keeping an aspect ratio close to one in the near nozzle region, as depicted in Fig. 4.1.

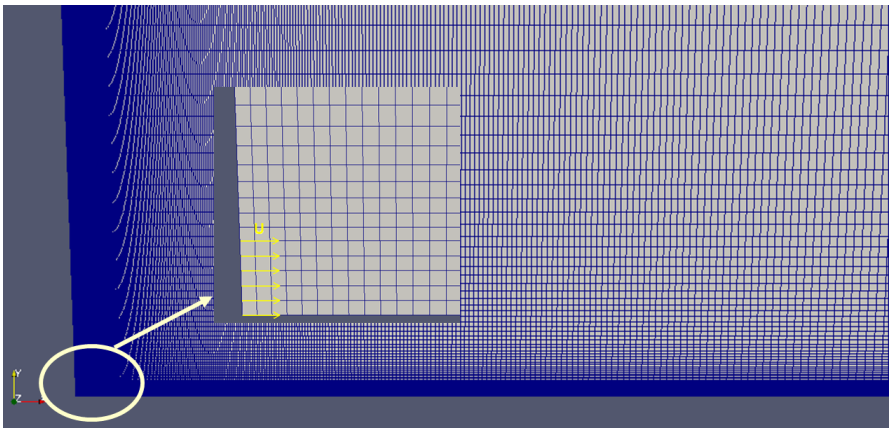

Figure 4.1. *Computational grid. The inset shows the mesh near the nozzle exit.*

The inlet velocity boundary condition is obtained from mass flow rate and momentum flux measurements, applying a constant radial profile of axial velocity and density at nozzle outlet, as described in Section 2.2.2 of Chapter 2. Regarding the turbulence model, turbulent intensity was set to 5% [7–11] and the turbulent integral length scale to 10% of nozzle diameter, as stated in [12]. Symmetry conditions are imposed on the grid longitudinal axis and no-slip boundary conditions are selected for all the walls of the domain together with a non-reflective boundary condition for the outlet.

Gas (Nitrogen) properties such as constant R = 296.9 J/(kg K) and viscosity $\nu_g = 1.79\ 10^{-5}\ m^2/s$ are introduced to the model together with the liquid surface tension $\sigma = 0.025$ N/m for standard diesel fuel [13]. Prandtl and Schmidt numbers are considered equals and set to $S_c = P_r = 0.9$, in order to give the same diffusivity to both, the transport of mass and enthalpy.

Then it is necessary to specify each linear solver that is used for each discretized equation. OpenFOAM solvers (summarized in Table 4.3) distinguish between symmetric matrices and asymmetric matrices, i.e. PCG is used for symmetric matrices, and PBiCG for asymmetric ones.

Table 4.3. *Linear solvers available in OpenFOAM.*

Solver	**Keyword**
Preconditioned (bi-)conjugate gradient	PCG/PBiCG
Solver using a smoother	smoothSolver
Generalized geometric-algebraic multi-grid	GAMG
Diagonal solvers for explicit systems	diagonal

Most of these solver are described in detail by Ferziger and Peric [14] except for GAMG. The generalized method of geometric-algebraic multi-grid uses the principle of: generating a quick solution on a mesh with a small number of cells; mapping this solution onto a finer mesh and using it as an initial guess to obtain an accurate solution on the fine mesh. GAMG is faster than standard methods when the increase in speed by solving first on coarser meshes outweighs the additional costs of mesh refinement and mapping of field data. In practice, GAMG starts with the mesh specified by the user and coarsens/refines the mesh in stages. Then, there are multiple options for preconditioning of matrices listed in Table 4.4.

Table 4.4. *Preconditioner options available in OpenFOAM.*

Preconditioner	**Keyword**
Diagonal incomplete-Cholesky (symmetric)	DIC
Faster diagonal incomplete-Cholesky (DIC with caching)	FDIC
Diagonal incomplete-LU (asymmetric)	DILU
Diagonal	diagonal
No preconditioning	none

In the present work, linear solvers for partial differential equations are PBiCG with DILU as preconditioner for all variables but for the pressure, where GAMG is used with DIC as preconditioner. The absolute tolerance, which represent the level at which the residual is small enough that the solution

can be deemed sufficiently accurate, varies from 10^{-8}, for pressure equation to 10^{-15}, for continuity equation.

The temporal resolution is limited by setting a maximum Courant number of CFL = 1.0 (in some cases it is possible to have numerical stability even with a value of CFL = 2.0). First order Euler scheme is applied for time derivative terms and linear schemes for the resolution of the gradient and laplacian terms of the equations.

This general configuration is kept constant while several simulations are conducted in order to define a definitive modeling reference set-up in the next section. In Section 4.2.1, a mesh size convergence study is performed in order to achieve grid independent results. Also numerical divergence schemes (the ones with more influence on the spray behaviour as can be seen in [15]) of equation solver and turbulence models are evaluated in Sections 4.2.2 and 4.2.3. These initial simulations are run for the 80 MPa injection pressure and 40 kg/m^3 ambient density conditions, taking it as the baseline condition. Once the mesh, turbulence and numerical settings are chosen attending to large scale flow features, i.e. spray dispersion together with velocity field, the capabilities of the mean interphase surface area density (Σ) to predict droplet size are investigated. After that, in the second part of the chapter, once a reference set-up is defined, further calculations are run to explore the performance of the model under different operating conditions.

The analysis of the simulation results is based on the following parameters: spray tip penetration as well as centerline axial velocity are considered in a first step, together with the evaluation of axial velocity radial profiles. Additionally, computed mass flow values are considered in order to explain spray penetration behaviour when necessary, which is calculated in a section transverse to the axial direction as:

$$\dot{m}(x) = \int_0^R \rho \; U(x,r) \; 2\pi r \, dr \tag{4.1}$$

where R is the spray radial limit. Then, the final macroscopic characteristic taken into account is the spray angle and in terms of microscopic ones, droplet sizes predictions are considered.

Finally, the chapter is closed with some preliminary conclusions about the implemented model and the obtained results.

4.2 Model set-up

In order to define a modeling reference set-up, as mentioned before, three pivotal parameters for CFD simulations are investigated (mesh size, turbulence model and divergence numerical schemes) as well as the intrinsic to this model interface surface area density (Σ). Modeling predictions are compared with experimental measurements of spray penetration, axial velocity and droplet size. Note here that the computational spray penetration is calculated as defined by the Engine Combustion Network (ECN), the furthest distance along the injector axis having a liquid volume fraction higher than 0.1% [16].

4.2.1 Mesh study

In a first step, mesh sensitivity has to be studied to ensure that the solution is not dependent on grid structure and resolution. This study has been divided in two parts: variation of the number of elements in the axial direction (first) and in the radial direction (second), so both directions are analysed independently to finally achieve an optimum number of elements.

In each of the two studies, four different meshes are evaluated. In the case of the axial variation, all meshes keep the same number of cells in the radial direction, which is set to 85 while in the radial variation study, it is the number of elements in the axial direction which are kept constant to 435, see Table 4.5 where together with the number of elements in each direction the size of the largest cell in the domain is indicated.

In Figure 4.2, liquid spray penetration predicted by the Σ-Y model using the four different meshes are compared, showing the axial variation study on the left and the radial one on the right. In this case, only spray penetration is investigated due to no noticeable differences have been seen in terms of axial velocity. Penetration results show that the coarse meshes are not good enough for this simulation and penetration is overpredicted with respect to the other grid resolutions. On the other hand, when the two most refined meshes are compared, for both studies (axial and radial), almost the same predictions are shown which demonstrate that grid convergent results are reached.

In addition to spray tip penetration, an analysis of the air entrainment process is made in terms of the total to initial mass flux ratio ($\dot{m}/\dot{m}_0$) to better understand the model predictions in Figure 4.3. This air entrainment is computed as a function of axial distance, considering that the spray radial limit is located at the radial position where the velocity is equal to 1% of the on-axis velocity. Entrainment plots show that the coarse meshes result in

Table 4.5. *Mesh resolutions tested in the mesh sensitivity study.*

Mesh	Axial Elements	Radial Elements	Maximum size [mm]
Mesh 150 Axial	150	85	2.947 x 1.401
Mesh 300 Axial	300	85	1.241 x 1.401
Mesh 435 Axial	435	85	0.793 x 1.401
Mesh 565 Axial	565	85	0.566 x 1.401
Mesh 20 Radial	435	20	0.793 x 7.176
Mesh 50 Radial	435	50	0.793 x 2.127
Mesh 85 Radial	435	85	0.793 x 1.401
Mesh 110 Radial	435	110	0.793 x 1.020

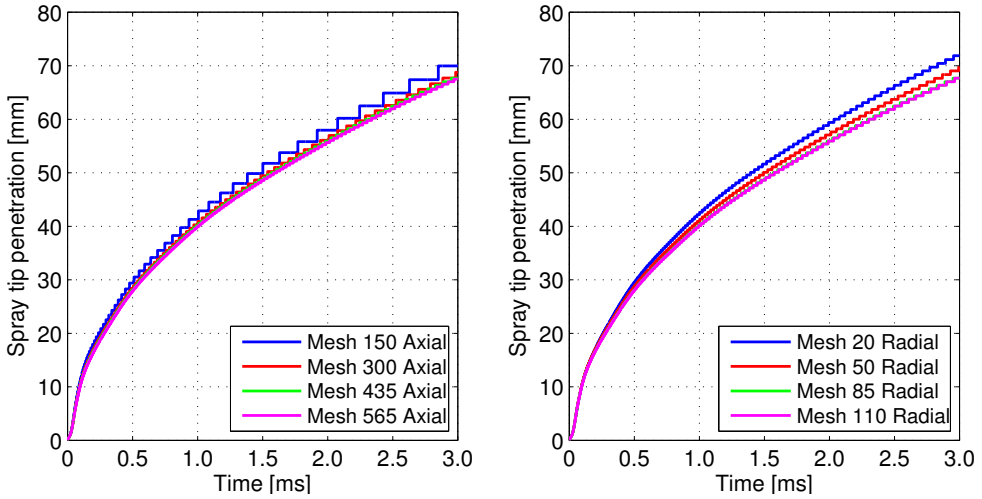

Figure 4.2. *Computed spray tip penetration for the baseline condition (P_{inj} = 80 MPa and $\rho_{amb} = 40kg/m^3$), mesh calibration study. Different number of elements in the axial direction [left] and different number of elements in the radial direction [right].*

a significantly lower entrainment in the region near to the tip of the spray, specially for the radial coarse mesh (20 cells), which explains the higher penetration reached for these cases compared to the other three, respectively due to a worse solution of this region because of too large elements.

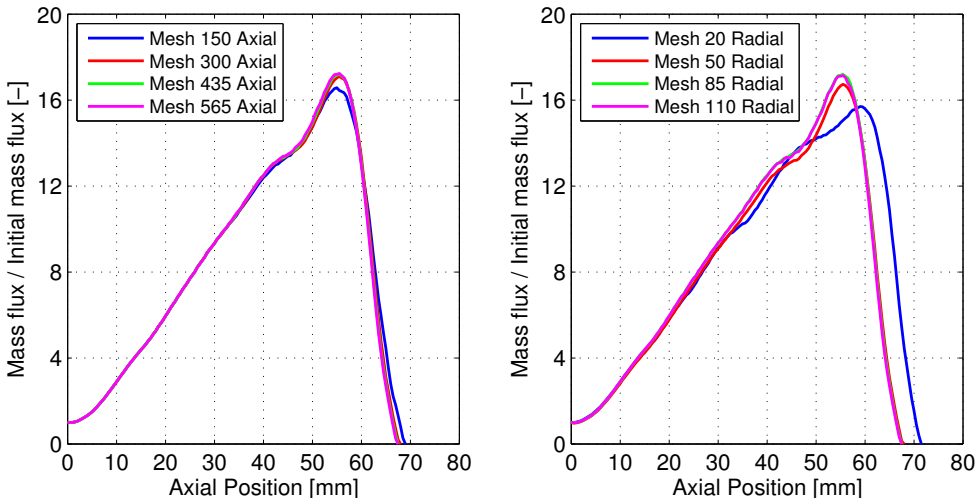

Figure 4.3. *Computed air entrainment normalized at 2.8 ms after SOI for the baseline condition (P_{inj} = 80 MPa and ρ_{amb} = 40kg/m^3), mesh calibration study. Different number of elements in the axial direction [left] and different number of elements in the radial direction [right].*

Regarding the selection of the optimum mesh, it is evident that the computational cost is higher for a more refined resolution, and because of that, between the two resolutions that show grid convergent results the coarsest one is selected. Thus, the final grid comprised of 435 x 85 cells is used in the following calculations, which corresponds with a cell expansion ratio of 1.01 and 1.06 in the axial and radial directions, respectively.

4.2.2 Numerical schemes

Numerical schemes have a major influence over convergence and accuracy of the simulation and especially the ones applied to resolve the divergence terms of the equations. The Gauss scheme is the only choice of discretization and requires a selection of the interpolation scheme for the dependent field. In OpenFOAM, there are three categories of schemes used primarily in conjunction with Gaussian divergence terms, referred as: general convection, normalised variable diagram (NVD) and total variation diminishing (TVD). In this study, one member of each family is tested: Gauss upwind (first order, bounded), Gauss Gamma (second order, bounded) and Gauss LimitedLinear (second order, bounded), respectively.

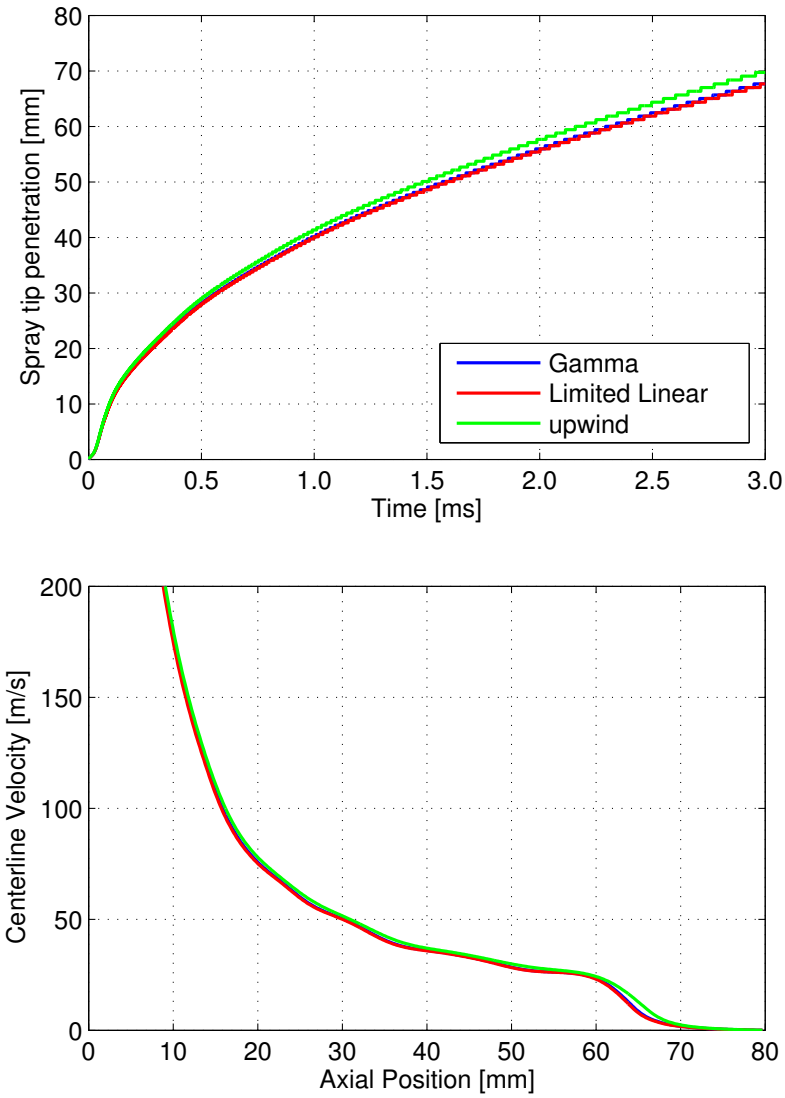

Figure 4.4. *Computed and measured spray tip penetration [top] and centerline axial velocity at 2.8 ms after SOI [bottom] for different numerical schemes: Baseline condition ($P_{inj} = 80$ MPa and $\rho_{amb} = 40 kg/m^3$).*

Results shown in Figure 4.4 indicate that good convergent results of spray penetration is obtained when using any of the second order schemes, while in the case of the upwind scheme, penetration is slightly overpredicted. In terms of centerline velocity, no great differences can be depicted. Thus, in

first term the decision among them is clear in favour of one second order, bounded scheme. But between this two the choice is more complex.

However, the Gamma NVD scheme was proposed by Jasak et al. [17] to overcome the problem of the existing NVD and TVD schemes to be applicable to unstructured meshes, where the 'standard' bounded differencing schemes is not appropriate. As a result, in order to make use of this advantage, the Gamma NVD scheme is used for discretization of divergence terms.

4.2.3 Turbulence model

One of the main assumptions of the Σ-Y model is the calculation of spray dispersion from a variable density turbulent mixing flow. Thus, it is expected that turbulence modeling will have a strong effect on spray predictions as seen in [18]. As described in Section 3.3.1, a modified form of the k-ε model accounting for density variations is employed. Due to the well known round jet spreading overprediction of k-ε type models [19], two different values for $C_{1\epsilon}$ constant are evaluated: the standard (1.44) and a corrected one (1.60). Pope [19] has previously suggested that the latter value should be used for round jets, as the one simulated in the present study. Additionally, the RNG k-ε and the Realizable k-ε turbulence models have been evaluated.

Table 4.6. *Turbulence models tested in the set-up study.*

Turbulence Model	**Constants**
HDR k-ε	$C_{1\epsilon} = 1.60$
HDR k-ε	$C_{1\epsilon} = 1.44$
RNG k-ε	Standar
Realizable k-ε	Standar

Results shown in Figure 4.5 indicate that good agreement of spray penetration, and also centerline velocity, is obtained when using the corrected $C_{1\epsilon}$ value for the HDR k-ε turbulence model. It is also noticeable that spray penetration is well predicted at initial stages but also far downstream of the primary atomization region. A noticeable underestimation is obtained when using the standard value as well as the Realizable turbulence model providing very similar predictions, while the worst performance is achieved by the RNG model among all options evaluated.

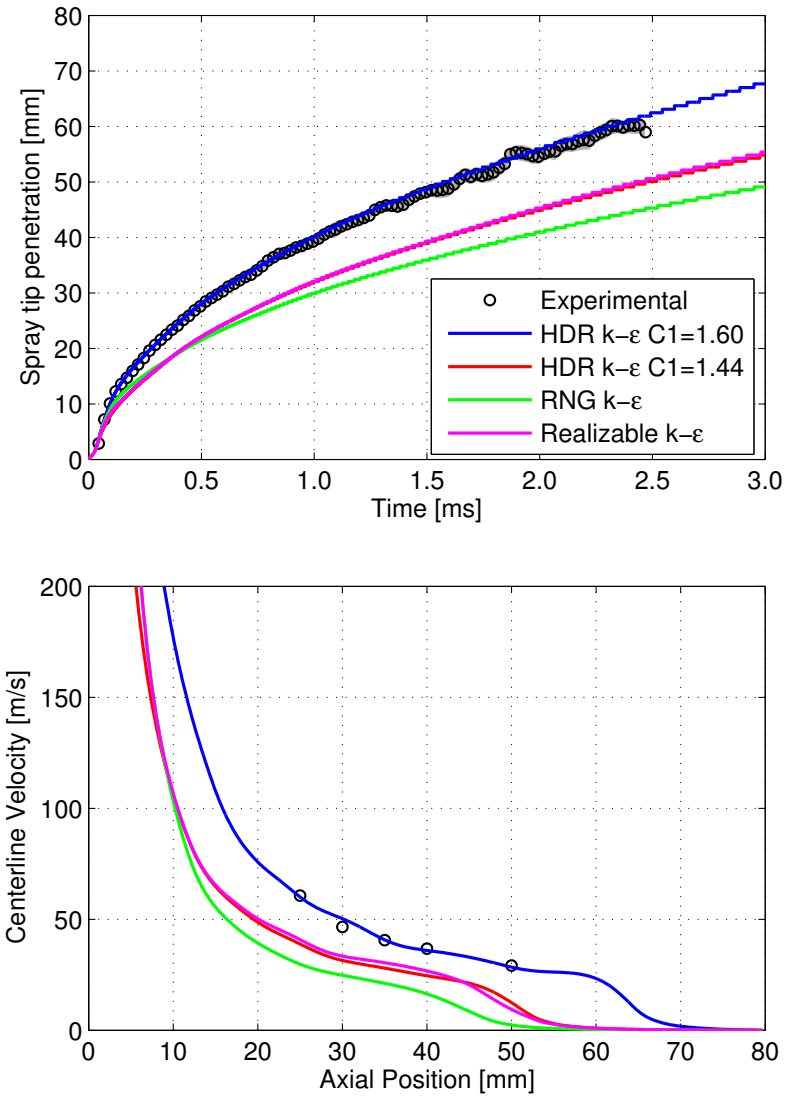

Figure 4.5. *Computed and measured spray tip penetration [top] and centerline axial velocity at 2.8 ms after SOI [bottom] for different turbulence models: Baseline condition ($P_{inj} = 80$ MPa and $\rho_{amb} = 40 kg/m^3$).*

Moreover, the measured radial profiles of axial velocity can only be captured with the corrected $C_{1\epsilon}$ value, as depicted in Figure 4.6. At the sight of these results, the wider radial profiles predicted by the RNG turbulence model explains the lower penetration as a result of higher air entrainment,

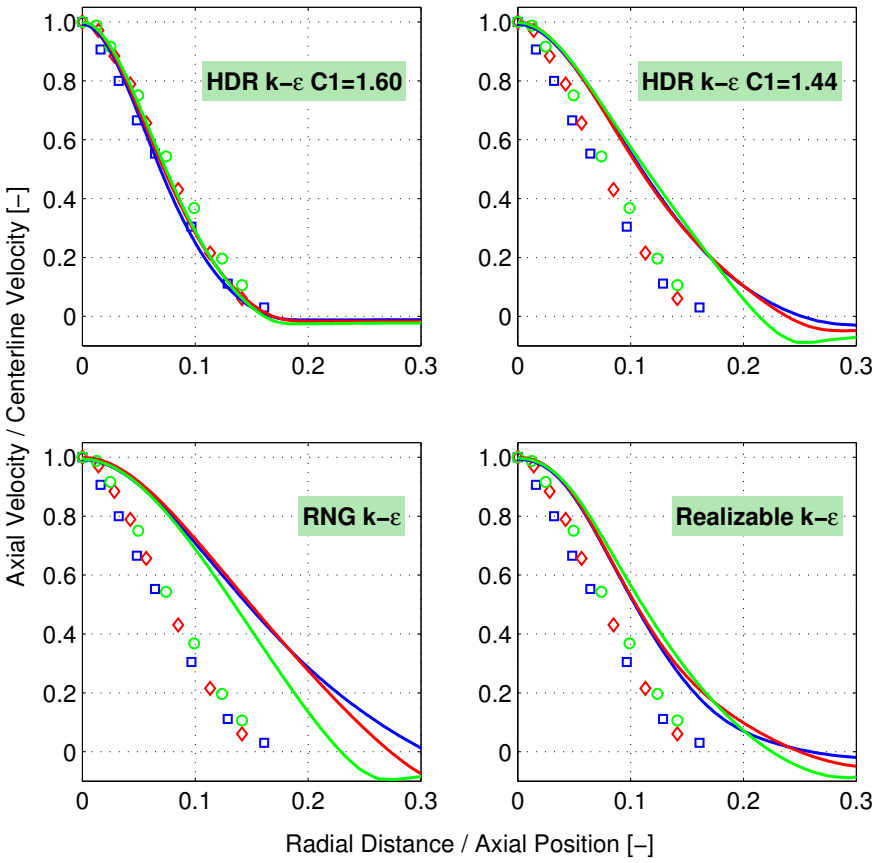

Figure 4.6. *Computed and measured velocity radial profiles normalized at 30 mm (blue elements), 35 mm (red elements) and 40 mm (green elements) at 2.8 ms after SOI for different turbulence models: Baseline condition ($P_{inj} = 80$ MPa and $\rho_{amb} = 40 kg/m^3$).*

while both Realizable and HDR k-ε with the default constants show a very similar trend as previously seen in terms of spray penetration. It is also observed from this figure, focusing on the corrected $C_{1\epsilon}$ value results, that self-similar velocities profiles are obtained for both measurements and calculations at different axial locations. These results indicate that both spray penetration and dispersion, which are related parameters, can be accurately predicted with the proposed model set-up. The agreement between the model bulk velocity and the measured liquid ones indicates very low slip between phases, at least for those conditions and measurement locations. This dynamic equilibrium

also supports the use of a gradient closure for liquid turbulent flux, which provides very low slip velocities [9, 20].

4.2.4 Surface area density model

The next step for model set-up, after validation of large-scale flow, is focused on the small-scale atomization characteristics given by the interface surface area density (Σ) and the droplet size derived from this variable. In these calculations, a modified value of α_2 model constant present in the Σ equation (Equation 3.15) is applied, setting it to 2.5 [9] in order to provide fair agreement with measured SMD results.

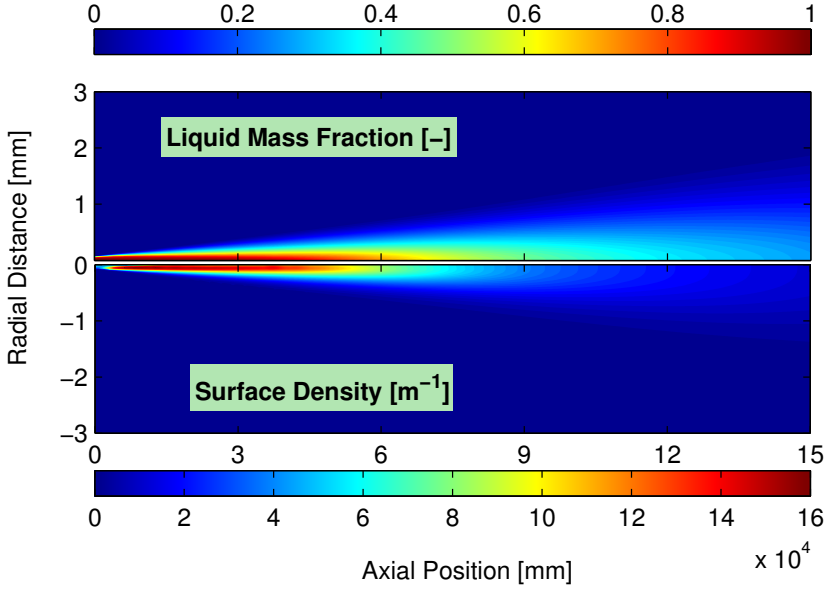

Figure 4.7. *Computed liquid mass fraction (top half contour) and interphase surface density (bottom half contour) at 2.8 ms after SOI: Baseline condition (P_{inj} = 80 MPa and $\rho_{amb} = 40 kg/m^3$).*

Droplet size results are analysed later but first, some attention is paid to the primary field Σ together with the liquid mass fraction in Figure 4.7. The axial behaviour of Σ can be seen, computing very low values below 0.5 mm for then, increasing to its maximum located within the dense region of the spray (see liquid mass fraction contour) and finally, progressively decrease. In terms of atomization, low surface density values depict no break-up or increasing sizes due to coalescence, i.e. SMD predictions should be high. Conversely, for

high surface density great atomization is computed and low SMD predictions are simulated. Thus, this results show no atomization at first axial locations due to the presence of the intact liquid core, while the break-up process begins immediately after this first region and progressively lose importance with the axial distance. This trends can be also seen in terms of SMD predictions in Figure 4.8.

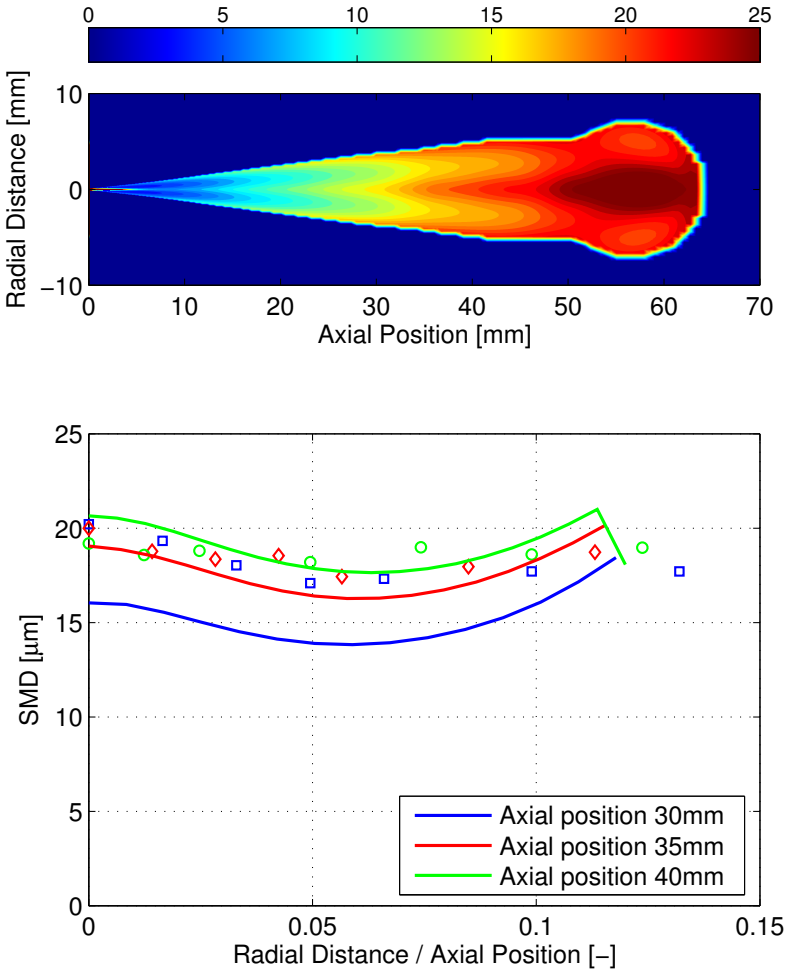

Figure 4.8. *Computed SMD contours, colorbar scale in µm [top] and computed and measured SMD radial profiles [bottom] at 30 mm (blue elements), 35 mm (red elements) and 40 mm (green elements) at 2.8 ms after SOI: Baseline condition ($P_{inj} = 80$ MPa and $\rho_{amb} = 40 kg/m^3$).*

In Figure 4.8 (top) the predicted spray SMD contour is shown for the baseline condition, where smaller drop sizes appears just downstream the liquid core and after that SMD increases progressively with axial distance. Such droplet size increase, which has been observed in non-vaporizing experiments both in the present and also in previous works [21, 22], is usually attributed to droplet coalescence. The behaviour is also obtained in calculations due to the predominance of surface density sink terms on Equation 3.11, probably caused by the increased equilibrium radius r_{eq} with lower turbulent kinetic energy k.

After that, a more detailed comparison is made in the same figure (bottom), where three radial profiles at the axial positions of 30 mm, 35 mm and 40 mm downstream of the nozzle exit are shown against the experimental measurements. Results clearly depict a greater increasing behaviour of the simulated predictions of SMD, in contrast with the smoother tendency observed in the measured SMD values. This discrepancy is especially noticed for locations nearer to the nozzle exit. However, it has to be noted the uncertainties and limitation of the PDPA technique for droplet sizing in dense sprays. It has been stated that droplet sizes always show dependence on the experimental set-up, with variation in the order of $\pm 10\%$ in optimal conditions and has been also suggested that only a small percentage of the total of droplets is detected and measured [5]. Thus, the overall performance of the model is quite remarkable.

4.3 Evaluation of the model – Parametric studies

The model set-up defined in previous section is further evaluated by simulating a series of experiments with different ambient and injection conditions. The range of validity of the model was evaluated by running cases with lower ambient density (25 and 10 kg/m^3) and increased (130 MPa) and decreased (30 MPa) injection pressures.

As shown in Figure 4.9 to Figure 4.11, the accuracy of spray penetration predictions for high and intermediate ambient densities are quite similar, though some differences in centerline velocity results can be observed for $\rho_{amb} = 25 kg/m^3$ conditions, being these predictions outperformed by the ones achieved for the highest ambient density studies. However, liquid spray penetration is under-predicted for the lower ambient density, specially for low injection pressure, and also centerline velocities are noticeable lower than PDPA measurements.

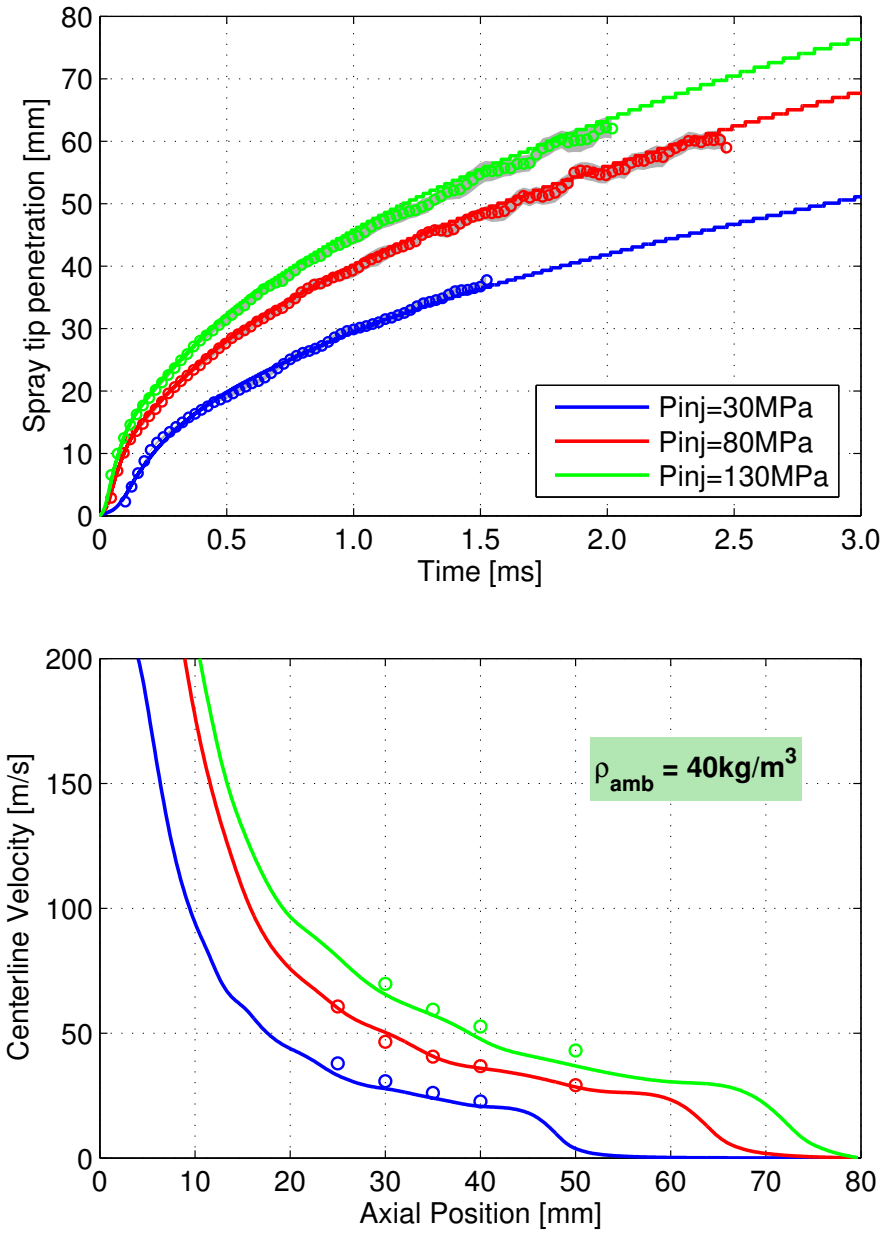

Figure 4.9. *Computed and measured spray tip penetration [top] and centerline axial velocity at 2.8 ms after SOI [bottom] for different injection pressures and* $\rho_{amb} = 40kg/m^3$.

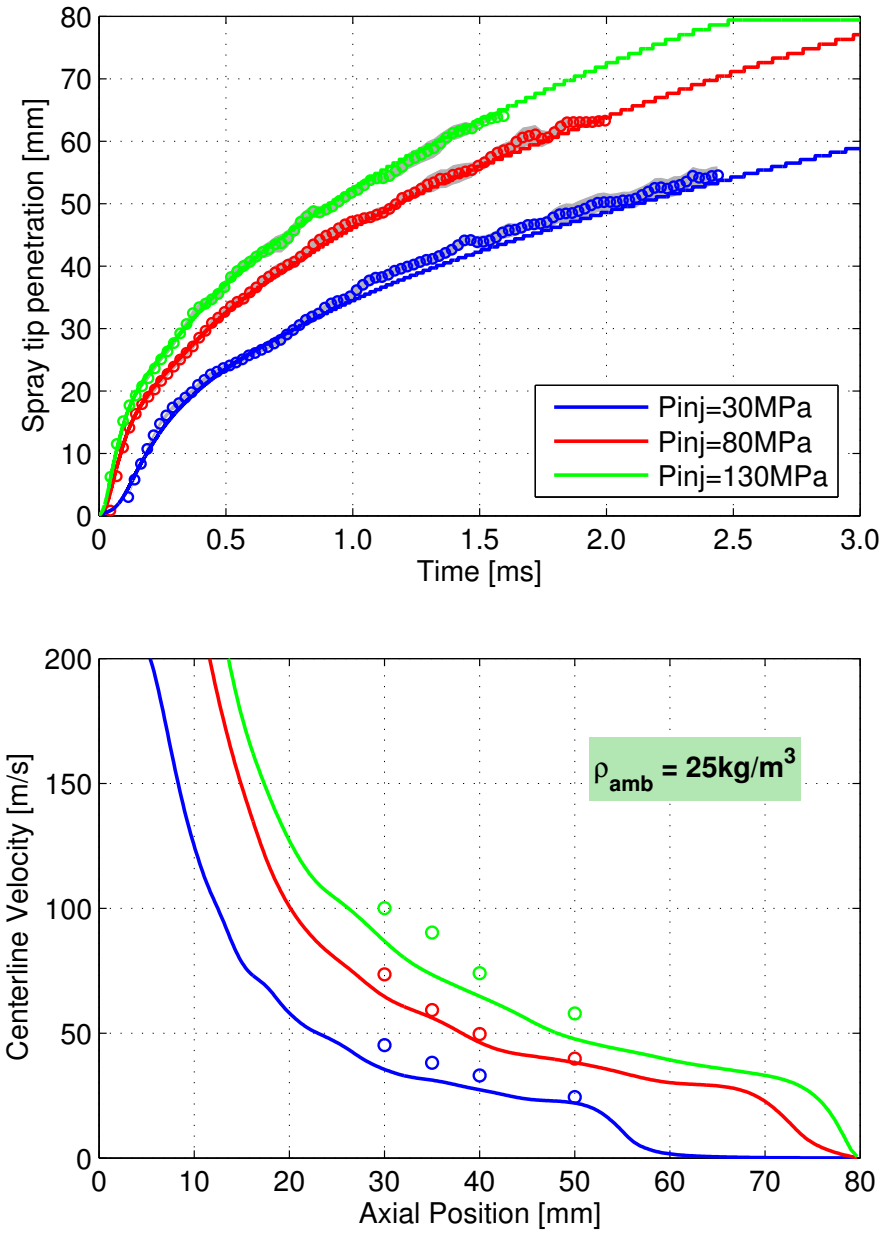

Figure 4.10. *Computed and measured spray tip penetration [top] and centerline axial velocity at 2.8 ms after SOI [bottom] for different injection pressures and* $\rho_{amb} = 25kg/m^3$.

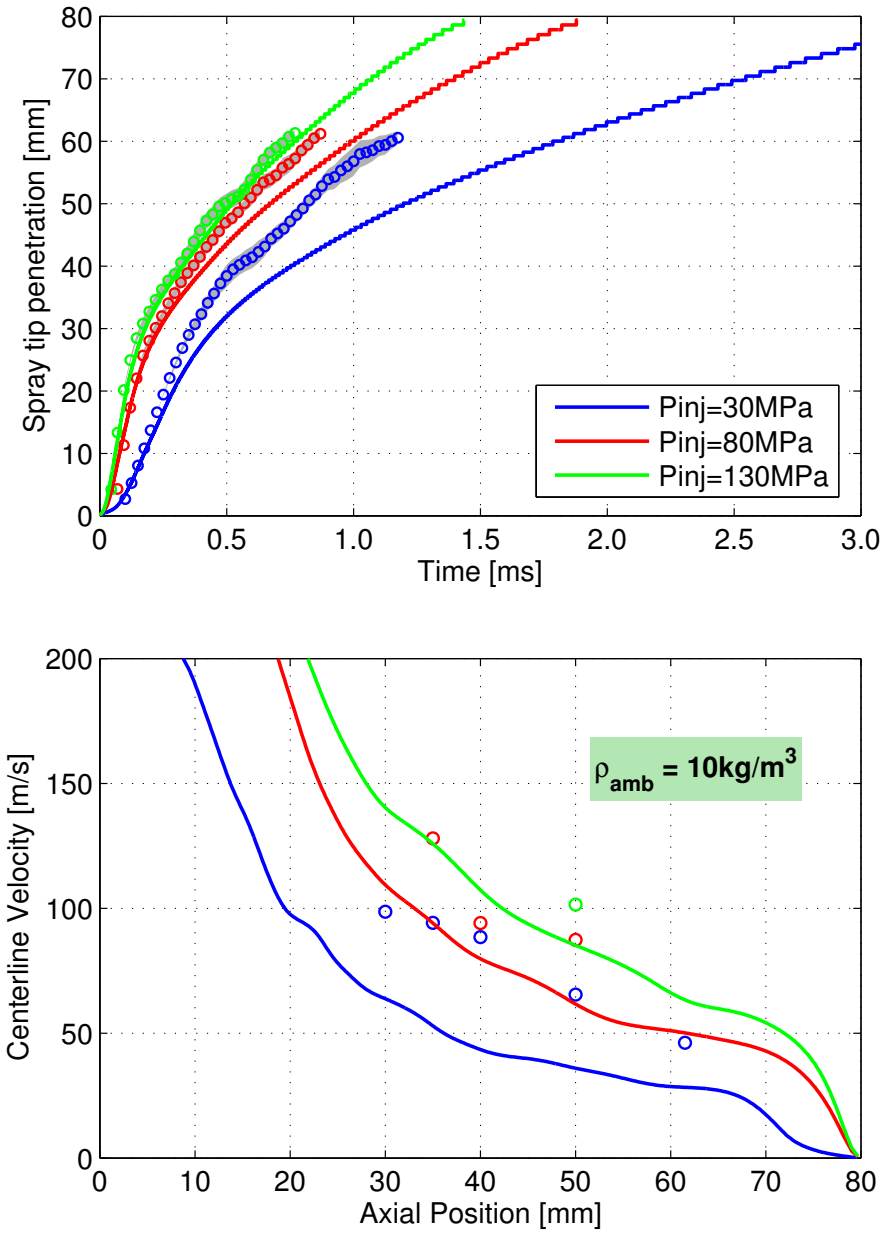

Figure 4.11. *Computed and measured spray tip penetration [top] and centerline axial velocity at 2.8 ms after SOI [bottom] for different injection pressures and* $\rho_{amb} = 10kg/m^3$.

Velocity radial profiles in Figure 4.12 are made taking as reference point the baseline condition. Then, an ambient density variation study is shown on the left and an injection pressure variation on the right, for three different axial positions 30 mm, 35 mm and 40 mm. Computed results show reduced spray dispersion as ambient density decreases, but the very narrow profiles for the ambient density case of $\rho_{amb} = 10kg/m^3$ cannot be captured by the model. All these results hint at the fact that spray dispersion is overpredicted when ambient density decreases.

Higher injection pressure does not modify the accuracy of spray characteristics predictions, and even good agreement on tip penetration is obtained for the lowest ambient density condition. Fair predictions are still found for $P_{inj} = 30$ MPa and ambient densities of 40 and 25 kg/m^3, presenting a maximum error of 6% for the ambient density of $\rho_{amb} = 25kg/m^3$. On the other hand, major discrepancies have been obtained for the lowest density and injection pressure condition, with a maximum error around 19%. In this case both Reynolds number and ambient to fuel density ratio are decreased, so this have an effect on the spray atomization regime that is no longer in the complete atomization one and compromise the validity of the model assumptions.

As explained in Section 2.3.1, limits between atomization regimes are not exact and several criteria exist. In this case, the widespread limiting Weber number criteria [23] ($We_g = 40.3$) of Table 2.1 is selected to represent the limit between the second wind-induced and the atomization regimes. On Figure 4.13, this limit is depicted together with the three test points studies conducted for the lowest density condition. For ambient densities of 40 and 25 kg/m^3, the points are included into fully atomization regime, however for lower ambient gas density, i.e. $\rho_{amb} = 10kg/m^3$, the point corresponding to $P_{inj} = 30$ MPa falls into the second wind atomization regime [15]. It should be noted that in the case of the intermediate injection pressure (80 MPa), the point is quite close to the border definition. This fact explains the failure of the model to accurately capture the experimental measurements for these two particular operating conditions. On such situation, the slip between phases is more significant and then a detailed model for the diffusion flux term closure, such as suggested by Beau et al. [20], could provide better predictions.

The study of macroscopic characteristics ends up with the spray angle comparison. This angle is calculated as the one included by the lines fitting the two sides of the spray up to 60% of the spray penetration. For that purpose the limit of the spray is defined at the 5% the on-axis mixture fraction value. In Figure 4.14, the full matrix of cases simulated are shown, lowest ambient density points with blue symbols, intermediate ambient density

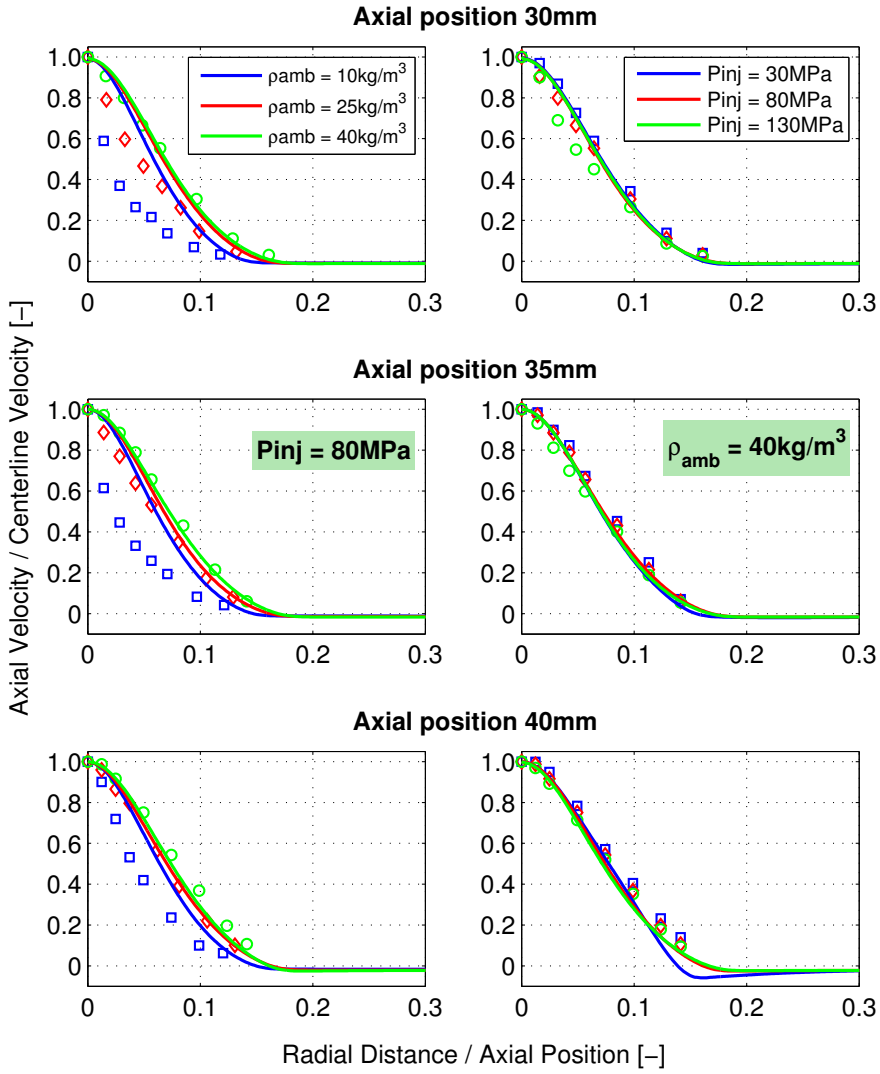

Figure 4.12. *Computed and measured velocity radial profiles normalized at 30 mm (top), 35 mm (middle), 40 mm (bottom), P_{inj} = 80 MPa [left] and $\rho_{amb} = 40kg/m^3$ [right] at 2.8 ms after SOI: Parametric studies.*

points in red and the high ambient density points with green ones. Different symbols are used to represent the different injection pressure conditions, low condition points (circles), intermediate condition (squares) and high condition (diamonds). In view of the results, the predicted spray angles, in the case of the ambient density of $\rho_{amb} = 40kg/m^3$, fall within the 5% error of measured

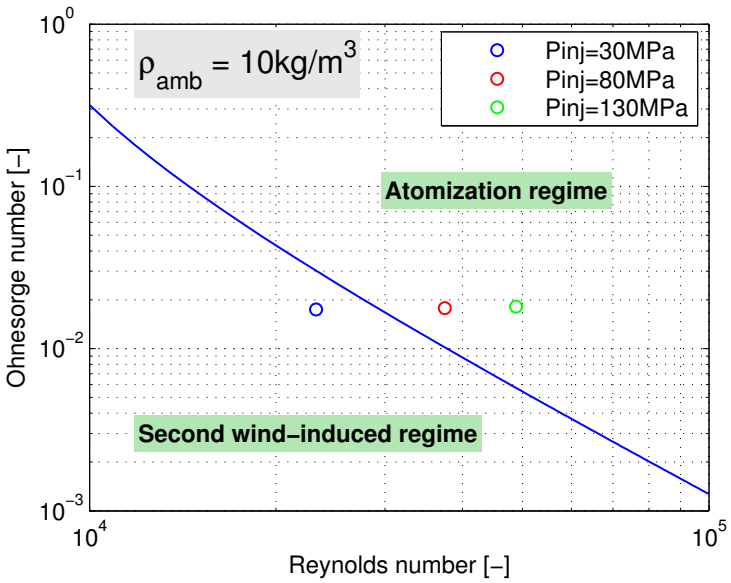

Figure 4.13. *Schematic diagram of limit between the second wind-induced and atomization regimes including the three test points studies conducted for the lowest density condition.*

values, for some conditions the model underpredicts, for other it overpredicts the experimental values. Results at ambient densitiy of $\rho_{amb} = 25kg/m^3$ depict good angle predictions for the two highest injection pressure conditions, while for P_{inj} = 30 MPa the model slightly overpredicts the experimental data. However, the largest discrepancies are found for the low density cases. Model predictions clearly overpredict the measurements. While for the intermediate and high injection conditions the error is around 25% and 22% respectively, for the lowest injection pressure the error increases till 60%, which is in accordance with the wider radial velocity profile (Figure 4.12 left) and the lower penetration (Figure 4.11) depicted in comparison with the experiments. This is another indication that, the model is not well suited at such operating conditions because of its underlying assumptions are not fully satisfied.

Finally, in a similar way to the velocity radial profiles (Figure 4.12), SMD profiles are also investigated in Figure 4.15. The predicted and measured SMD data are depicted at 35 mm downstream of the nozzle exit, taking again as reference point the baseline condition, showing the ambient density variation study on the left and the injection pressure variation on the right.

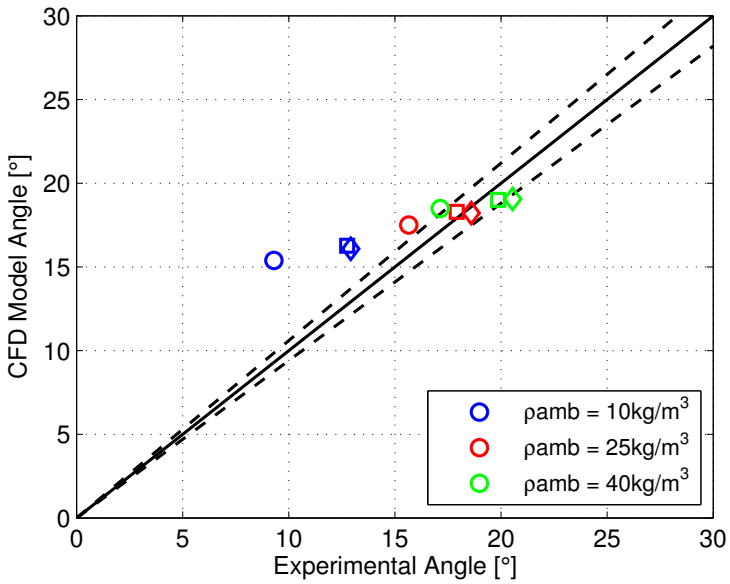

Figure 4.14. *Computed and measured spray angle including a 5% error area (dashed lines): Full matrix of cases studied. Circles (P_{inj} = 30 MPa), squares (P_{inj} = 80 MPa) and diamonds (P_{inj} = 130 MPa).*

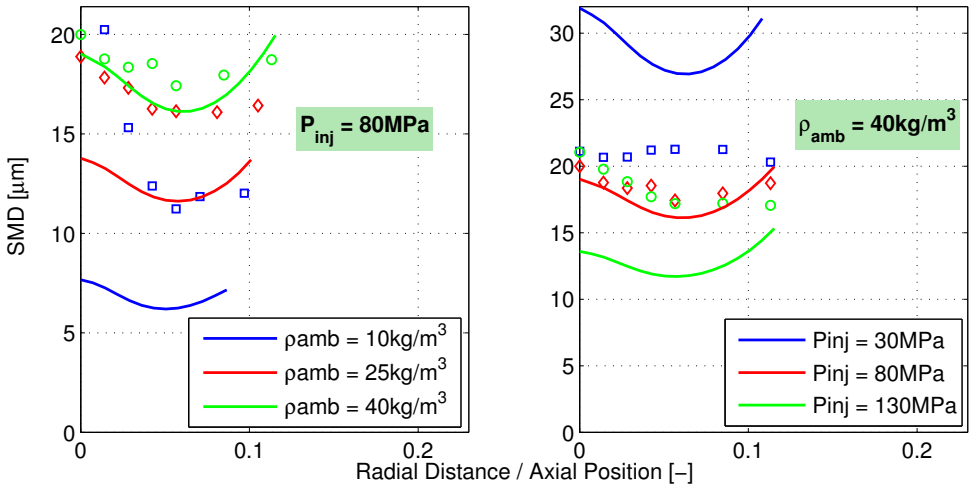

Figure 4.15. *Computed and measured SMD radial profiles at 35 mm, P_{inj} = 80 MPa [left] and $\rho_{amb} = 40kg/m^3$ [right] at 2.8 ms after SOI: Parametric studies.*

In terms of density variation, experimental SMD is shown to decrease with lower ambient density, probably due to lower coalescence after the primary atomization region [24]. This trend is well captured by the model, but the effect is overestimated. On the other hand, SMD increases for lower injection pressures and decreases for higher ones, as expected, but also here the trend is overestimated compared to experimental data, which show a much lower sensitivity.

4.4 Conclusions

The fully compressible implementation of the $\Sigma - Y$ Eulerian model has been applied to the study of direct injection diesel sprays, considering a basic external flow case.

Calculations have been validated against spray test rig experiments for non-vaporizing sprays under different operating conditions. Spray tip penetration as well as spatial distribution of axial velocity have been used for validation. However, defining a proper modeling set-up has been the first step followed in the present methodology.

A mesh convergence study is conducted, reaching a final grid resolution that produces independent results. Divergence numerical interpolation schemes have been investigated through the evaluation of one of each type available at the OpenFOAM code. At the end, the second order Gamma NVD scheme is selected. Finally, turbulence model set-up has been performed by modifying the $C_{1\epsilon}$ constant of the k-ϵ turbulence model, as previously suggested for round jets.

Predicted spray tip penetration and velocity fields are in very good agreement with the experimental data under medium and high ambient gas density conditions. However, when the ambient gas density was low, agreement was not as good, suggesting that under these conditions interfacial dynamics become more significant. Under such conditions, a detailed model for the diffusion flux term closure, such as suggested by Beau et al. [20], could provide better predictions. It is also worth mentioning that under the low density conditions model assumptions are not fulfilled due to the fact that the spray is no longer in the complete atomization regime. Additionally, spray angle predictions are evaluated. Although parametric trends were correct, the model was far less sensitive than experiments towards changes in operating conditions, being the lower density case which presents the greatest discrepancies. Finally, SMD predictions are only qualitatively

correct. Parametric studies show that the trends could be captured but model predictions are more sensitive than measurements to the variations in operating conditions. However, these initial promising results provide a quantitative idea of the capabilities of the model. In order to enhance the modeling performance, a more detailed calibration process of the Σ equation constants should be conducted (Section 5.3 of the next chapter) but a properly database, including droplet sizes in the near-nozzle region of the spray, must be selected to validate the atomization predictions, which is not possible with the data available for this initial study.

The overall usefulness of the $\Sigma - Y$ modeling approach is confirmed by the validation studies and the good quality results obtained, which encourages its application to a more complex configuration. The model is applicable to ambient gas density conditions that are normally present in diesel engines, but would be less accurate for very early injection conditions, such as those found in highly premixed combustion strategies, due to the lower ambient density. In addition, a well established modeling set-up is defined and will be used in the following studies presented in the subsequent chapters.

Bibliography

[1] Payri R, Salvador F J, Gimeno J and Garcia A. "Flow regime effects over non-cavitating diesel injection nozzles". *Proceedings of the Institution of Mechanical Engineers, Part D: Journal of Automobile Engineering*, Vol. 226, pp. 133–144, 2012.

[2] Payri R., Salvador F.J., Gimeno J. and Novella R. "Flow regime effects on non-cavitating injection nozzles over spray behavior". *International Journal of Heat and Fluid Flow*, Vol. 32 n^o 1, pp. 273 – 284, 2011.

[3] Pastor José V., Arrègle Jean, García José M. and Zapata L. Daniel. "Segmentation of diesel spray images with log-likelihood ratio test algorithm for non-Gaussian distributions". *Appl. Opt.*, Vol. 46 n^o 6, pp. 888–899, Feb 2007.

[4] Payri R., Tormos B., Salvador F.J. and Araneo L. "Spray droplet velocity characterization for convergent nozzles with three different diameters". *Fuel*, Vol. 87 n^o 15–16, pp. 3176–3182, 2008.

[5] Payri Raul, Araneo Lucio, Shakal Joseph and Soare Vlad. "Phase doppler measurements: system set-up optimization for characterization of a diesel nozzle". *Journal of Mechanical Science and Technology*, Vol. 22 n^o 8, pp. 1620–1632, 2008.

[6] Macian V., Bermudez V., Payri R. and Gimeno J. "New technique for determination of internal geometry of a diesel nozzle with the use of silicone methodology". *Experimental Techniques*, Vol. 27 n^o 2, pp. 39–43, 2003.

[7] Lebas R., Menard T., Beau P.A., Berlemont A. and Demoulin F.X. "Numerical simulation of primary break-up and atomization: DNS and modelling study". *International Journal of Multiphase Flow*, Vol. 35 n^o 3, pp. 247 – 260, 2009.

[8] Desantes J.M., García-Oliver J.M., Pastor J.M. and Pandal A. "A Comparison of Diesel Sprays CFD modelling approaches: DDM vs $\Sigma - Y$ Eulerian Atomization Model". *Atomization and Sprays*, Vol. 26 n^o 7, pp. 713–737, 2016.

[9] García-Oliver J.M., Pastor J.M., Pandal A., Trask N., Baldwin E. and Schmidt D.P. "Diesel Spray CFD Simulations based on the $\Sigma - Y$ Eulerian Atomization Model". *Atomization and Sprays*, Vol. 23, pp. 71–95, 2013.

[10] Lacaze Guilhem, Misdariis Antony, Ruiz Anthony and Oefelein Joseph C. "Analysis of high-pressure Diesel fuel injection processes using {LES} with real-fluid thermodynamics and transport". *Proceedings of the Combustion Institute*, Vol. 35 n^o 2, pp. 1603 – 1611, 2015.

[11] Ménard T., Tanguy S. and Berlemont A. "Coupling level set/VOF/ghost fluid methods: Validation and application to 3D simulation of the primary break-up of a liquid jet". *International Journal of Multiphase Flow*, Vol. 33 n^o 5, pp. 510 – 524, 2007.

[12] Sallam K. A. and Faeth G. M. "Surface Properties During Primary Breakup of Turbulent Liquid Jets in Still Air". *AIAA Journal*, Vol. 41 n^o 8, pp. 1514–1524, Agosto 2003.

[13] Bracho G.C. *Experimental and theoretical study of direct diesel injection process at low temperatures.* Doctoral Thesis, Departamento de Máquinas y Motores Térmicos, Universidad Politécnica de Valencia, España, 2011.

[14] Ferziger J.H. and Peric M. *Computational Methods for Fluid Dynamics.* Springer, Berlin, 2002. pp. 176–178.

[15] Martí-Aldaraví P. *Development of a computational model for a simultaneous simulation of internal flow and spray break-up of the Diesel injection process.* Doctoral Thesis, Departamento de Máquinas y Motores Térmicos, Universidad Politécnica de Valencia, España, 2014.

[16] Bardi M., Payri R., Malbec L.M., Bruneaux G., Pickett L.M., Manin J., Bazyn T. and Genzale C. "ENGINE COMBUSTION NETWORK: Comparison of spray development, vaporization, and combustion in different combustion vessels". *Atomization and Sprays*, Vol. 22 n^o 10, pp. 807–842, 2012.

[17] Jasak H., Weller H.G. and Gosman A.D. "High resolution NVD differencing scheme for arbitrarily unstructured meshes". *International Journal for Numerical Methods in Fluids*, Vol. 31 n^o 2, pp. 431–449, 1999.

[18] Chavez M. *Modelado CFD Euleriano-Lagrangiano del Chorro Diesel y evaluación de su combinación con modelos fenomenológicos y unidimensionales.* Doctoral Thesis, Departamento de Máquinas y Motores Térmicos, Universidad Politécnica de Valencia, España, 2013.

[19] Pope S. B. *Turbulent Flows.* Cambridge University Press, 2000.

[20] Beau P.A., Funk M., Lebas R. and Demoulin F.X. "Applying Quasi-Multiphase Model to Simulate Atomization Processes in Diesel Engines: Modeling of the Slip Velocity". *SAE Technical Paper 2005-01-0220*, 2005.

[21] Araneo L. and Tropea C. "Improving Phase Doppler Measurements in a Diesel Spray". *SAE Technical Paper*, n^o 970799, 2000.

[22] Corradini M. L., Blanchard J. P. and Baik S. "Development of micro-diesel injector nozzles via MEMS Technology and effects on spray characteristics". *Atomization and Sprays*, Vol. 13 n^o 5&6, pp. 443–474, 2003.

[23] Miesse C.C. "Correlation of Experimental Data on the Disintegration of Liquid Jets". *Industrial & Engineering Chemistry*, Vol. 47 n^o 9, pp. 1690–1701, 1955.

[24] Reitz R. D. "Modeling Atomization Processes in High-Pressure Vaporizing Sprays". *Atomization and Spray Technology*, Vol. 3, pp. 309–337, 1987.

Chapter 5

Coupled internal/external flow application

Contents

5.1 Introduction

In this second application chapter, the model is evaluated to simulate coupled/decoupled nozzle flow simulations against experimental measurements available from the database of the Engine Combustion Network [1]. In this introduction, the motivation and objectives of this study are outlined and, furthermore, the methodology followed to conduct this investigation is resumed.

5.1.1 Motivation

The present study is really attractive for both reasons, the advantages of this kind of spray model, implemented in the present work, to this particular application compared to the traditional spray modeling approaches and the experimental data available for comparison.

As already discussed in detail in Chapter 3, modeling of primary atomization is a pivotal matter in spray modeling. However, the traditionally used Discrete Droplet Model (DDM) [2] presents some well known drawbacks for dense two-phase flow simulations. It is best suited for low liquid volume fraction flows, not present in the near nozzle flow of diesel sprays and the Lagrangian particle tracking approach fails in this region, because nearly all existing drag, collision, breakup, and vaporization models are based on assumptions of near-spherical droplets in a sparse spray. On the contrary, Eulerian spray models have shown a promising performance for capturing the fast gas-liquid interactions in diesel spray simulations [3–8] by emphasizing the turbulent mixing of the gas and liquid.

In addition, nozzle geometric parameters are known to have a great influence on the spray behaviour [9, 10]. Thus, including nozzle effects by coupling internal and external flow simulations leads to a better representation of reality. Again here, the usually applied two-step methodology [11–13], which transfers all the spatial and temporal fields from an internal flow simulation to a primary break-up (blob) model to initialize droplet properties for the Lagrangian external spray simulation, presents several issues. From the mapping procedure appear some of them because of the different computational time steps required by the two simulations. Additionally, this methodology needs to use phenomenological models to capture the influence of in-nozzle flow and fuel properties on spray [12, 13]. Alternatively, these issues can be avoided by using an Eulerian atomization model to simulate internal and external flow together in one simulation [4, 14–16]. However,

3D modeling of internal and external flow together in an Eulerian framework can be computationally expensive, specially if downstream spray regions are included [15, 16]. Because of that, it seems interesting to investigate the potential suitability of eulerian decoupled simulations [4, 11, 17].

On the other hand, in terms of experimental measurements, the database of the Engine Combustion Network (ECN) [1] is used. This open forum was founded several years ago with the aim to concentrate the investigation efforts and to coordinate experimental and computational research in the complex area of engine research. This network provides a notorious and vast database of experiments of non-reactive and reactive sprays under diesel-like conditions (only non-reactive measurements are used in this chapter). The one considered in this work is the so-called "Spray A" which uses n-dodecane as a surrogate for diesel fuel. One of the most valuable measurements of this database corresponds to near-nozzle region measurements. This dense zone is a great challenge for the common optical techniques and is only penetrable with special diagnostics such as x-ray radiography [18–20], available at this database. More details about the Spray A condition and the experimental variables used for validation purposes are discussed in the methodology section.

5.1.2 Objectives of the study

The aim of this investigation is to evaluate the capabilities of the Σ-Y Eulerian model to reproduce the internal structure of a diesel spray in the near-field. In order to accomplish this goal, the implications of the coupled internal/external flow simulations are evaluated as well as the effectiveness of 2D simulations in comparison to 3D and the accuracy that can be achieved by different decoupled simulations. Moreover, it is needed to achieve a good calibration for the mean interphase surface area density (Σ), Equation 3.11, which compute the extent of the atomization process. In order to do that, an optimization of the parameters values involved in the equation is also conducted.

5.1.3 Methodology of the study

In order to evaluate and validate the model applied to coupled nozzle flow and spray simulations, the ECN Spray A database [1, 21–23] has been used. The "Spray A" condition consists of a free diesel spray injected into a quiescent environment, where well-defined boundary conditions and experimental data are available for model validation purposes. The nominal condition for Spray

A corresponds to 150 MPa injection pressure, 900 K ambient temperature and 22.8 kg/m^3 as ambient density.

In this case, the Spray A non-evaporating condition of ECN is used in order to evaluate the model in terms of the near-field structure (dense region) of diesel sprays, taking advantage of the valuable x-ray radiography measurements available at ECN database. This experiment is conducted with the ambient gas at room temperature (303 K) due to the x-ray transparent polymer windows used, which cannot be used at high temperature. Nevertheless, the same ambient density of the nominal evaporating Spray A condition is matched in order to reproduce similar conditions for the spray breakup process, assuming that density is a more critical parameter than pressure for atomization [24]. The main conditions of this experiment are presented in Table 5.1. Further details about the experimental set-up are provided in [19].

Table 5.1. *Conditions for non-evaporating Spray A baseline condition.*

Fuel	n-Dodecane
Ambient composition	100% N2
Injection pressure [MPa]	150
Ambient temperature [K]	303
Ambient density [kg/m^3]	22.8
Fuel injection temperature [K]	343

The experimental data used for validation include the projected mass density (PMD) of the fuel, which is calculated by a line-of-sight integration along the x-ray beam [19, 20], see Equation 5.1 and Figure 5.1. Another useful quantity obtained from the x-ray radiography measurements is the transverse integrated mass (TIM), which is obtained from the integral of the projected density across the transverse position at a particular axial location [18]. Moreover, liquid volume fraction can be evaluated. This measurements are made by a tomography reconstruction of radiography data for liquid volume fraction [20]. Finally, the characterization of the large scale of the flow is completed by means of a typical global spray parameter such as penetration. Additionally, measurements of droplet size made using ultra-small angle x-ray scattering (USAXS) technique [23], have been used in order to calibrate the Σ model constants to accurate predict droplet sizes. These measurements are available for different injection pressures and ambient conditions, see Table 5.2.

$$PMD(x,r) = \int \rho_l(z)dz \tag{5.1}$$

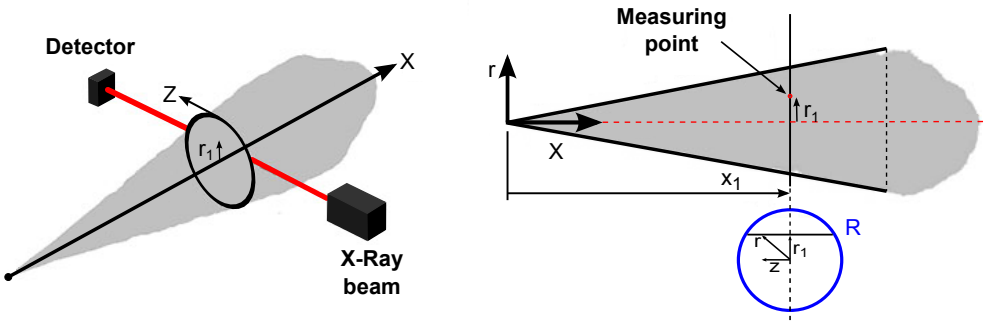

Figure 5.1. *Scheme of x-ray measurement technique and description of integration for calculating the projected mass density. Figure adapted from Desantes et al. [25].*

Table 5.2. *Spray A operating conditions available in the USAXS measurements database.*

Injector Serial#	P_{inj} [MPa]	T_{amb} [K]	P_{amb} [MPa]
210675 (Baseline)	150	303	2.0
	Ambient Conditions	Study	
210675	150	303	0.67
	Injection Pressure	Studies	
210675	100	303	2.0
210675	50	303	2.0

Detailed internal nozzle geometric characterization has been performed for the injector employed in these experiments, where the main characteristics are presented in Table 5.3. D_o, D_i, L and r denote nozzle orifice outlet diameter, nozzle orifice inlet diameter, length, and inlet radius, respectively. The nozzle convergence is described by the k-factor, as defined in [26].

The single-hole Spray A injector (Serial# 210675) presents a particularity in form of an offset of the orifice outlet with respect to the needle axis (see Table 5.3). Thus a full three-dimensional domain is needed for performing the CFD simulations, as depicted in Figure 5.2. This computational domain

Table 5.3. *Nozzle geometric characteristics for single-hole Spray A ECN injector.*

Injector Serial#	D_o[μm]	D_i[μm]	L/D_o[-]	r/D_o[-]	k-factor	exit offset [μm]
210675	89.4	116	11.5	0.23	2.7	53

includes a cylindrical spray chamber 12 *mm* in length and 14 *mm* in diameter. In Figure 5.2, the mesh structure can also be seen. It consists of 2.25 million hexahedral cells with a minimum cell size of 1.5 μm near the walls inside the nozzle and a maximum cell size of 250 μm far from the orifice exit.

In addition to the three-dimensional mesh, as previously introduced, a two-dimensional axisymmetric one is used in order to reduce the computational cost. The geometry dimensions are the same as in the 3D domain as well as the same order mesh resolution, see Figure 5.3(a). The mesh is structured with non-uniform grid resolution. There are 89000 cells with 72 elements at the orifice exit. This mesh was built following the results of a sensitivity study previously performed as indicated in [14, 27].

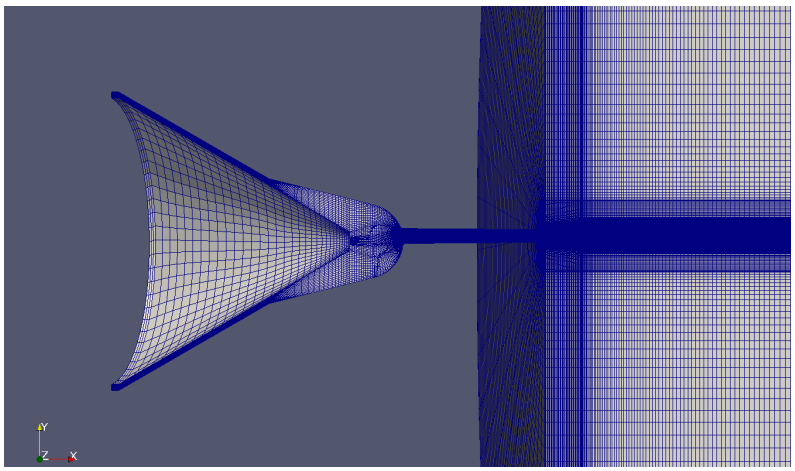

Figure 5.2. *Computational grid for 3D Spray A simulations.*

Finally, in order to simulate a fully developed spray and investigate the potential of an eulerian decoupled simulation, a 2D axisymmetric computational domain without the nozzle geometry, which consists of a spray chamber 80 *mm* in length and 25 *mm* in diameter, is considered. The mesh is structured with non-uniform grid resolution. There are 20 cells along the

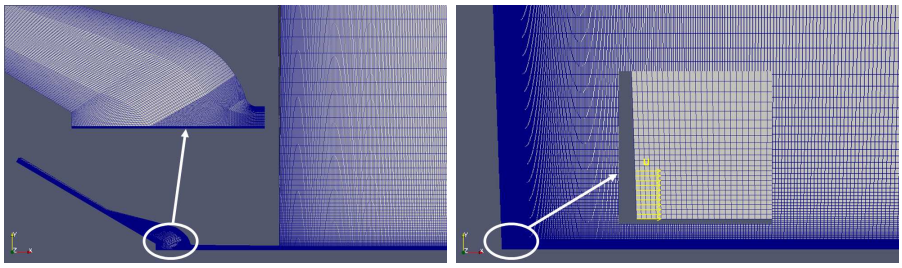

(a) Grid used for 2D coupled nozzle-spray simulations

(b) Grid used for 2D de-coupled spray simulations

Figure 5.3. *Computational grids for two-dimensional Spray A simulations.*

orifice diameter, in order to have a better definition of the near nozzle region, keeping an aspect ratio close to one, as depicted in Figure 5.3(b). The non-uniform grid resolution consists of cells with an expansion ratio of 1.01 and 1.06 in the axial and radial directions, respectively, as concluded in the previous study conducted in Chapter 4. Note that all the computational domains use the axis orientation convention from Kastengren et al. [22].

Boundary conditions selected for all the walls of the domains are no-slip. A non-reflective boundary condition is used for the outlet, symmetry conditions are imposed on the symmetry axis for 2D cases and a time varying velocity condition is used for the inlet. The inlet velocity is obtained from experimental mass flow measurements, domain inlet area and fuel density. A uniform velocity distribution at the domain inlet is assumed. This inlet condition was used instead of a constant pressure profile because a constant pressure profile would not capture the experimentally observed time oscillations in the flow. This is because these oscillations are highly influenced by the transient needle movement profile, and these simulations used a static mesh with the needle positioned at maximum lift.

In this work, all the numerical settings adopted in the previous Chapter have been kept constant (linear solvers, tolerances, Courant and Schmidt numbers and gradient, laplacian and divergence schemes). Firstly, modeling of the near-field structure of Spray A is investigated, paying attention to both accuracy and computational cost in order to achieve an optimum simulation. After that, in the second part, once the large scale of the flow is correctly captured, a statistical methodology for optimizing droplet size predictions based on the Design of Experiments (DOE) technique is applied. Finally, this chapter is closed with some conclusions about the obtained results.

5.2 Near-field internal structure

In this section, the HDR k-ε turbulence model is initially chosen using the corrected value (1.60 [28]) for $C_{1\epsilon}$. This general configuration is applied to the first study conducted, where the effectiveness of 2D coupled simulations in comparison to 3D is evaluated. Then, different turbulent models are compared, in the case of 2D coupled simulations, due to some investigations suggesting a better performance of the SST k-ω and the RNG k-ε [12, 14, 29, 30] models for inner nozzle flow simulations. In the end, the accuracy that can be achieved by different decoupled simulations is investigated.

5.2.1 3D vs 2D coupled simulations

Coupled 3D and 2D simulations are compared to the experimental x-ray data. Obviously, only the 3D geometry is capable of capturing the experimental asymmetries. However, the accuracy achieved by 2D simulations is of interest because of the benefit of reduced computational cost, see Table 5.4.

Table 5.4. *Computational cost comparison between 3D and 2D coupled simulations.*

Type of simulation	Wall Clock Time (hours)	Number of CPU
3D	936	24
2D	72	12

The projected mass density of the fuel, as explained before, is used for validation. In order to enable fair comparisons of simulated predictions against experiments, a similar calculation procedure (line-of-sight integration along the x-ray beam [19, 20]) is replicated with the CFD data. In Figure 5.4, the model projected density contours, for both simulations, are compared against the x-ray radiography measurements conducted at Argonne National Laboratory. It is seen that the model can capture the fuel distribution in the very near nozzle region (i.e., within 6 mm) with both meshes while downstream of this axial position, the radial dispersion of simulations tend to be over-predicted. In general, both grids report almost the same results and qualitatively is difficult to reach a more clear conclusion, so a more detailed comparison should be made.

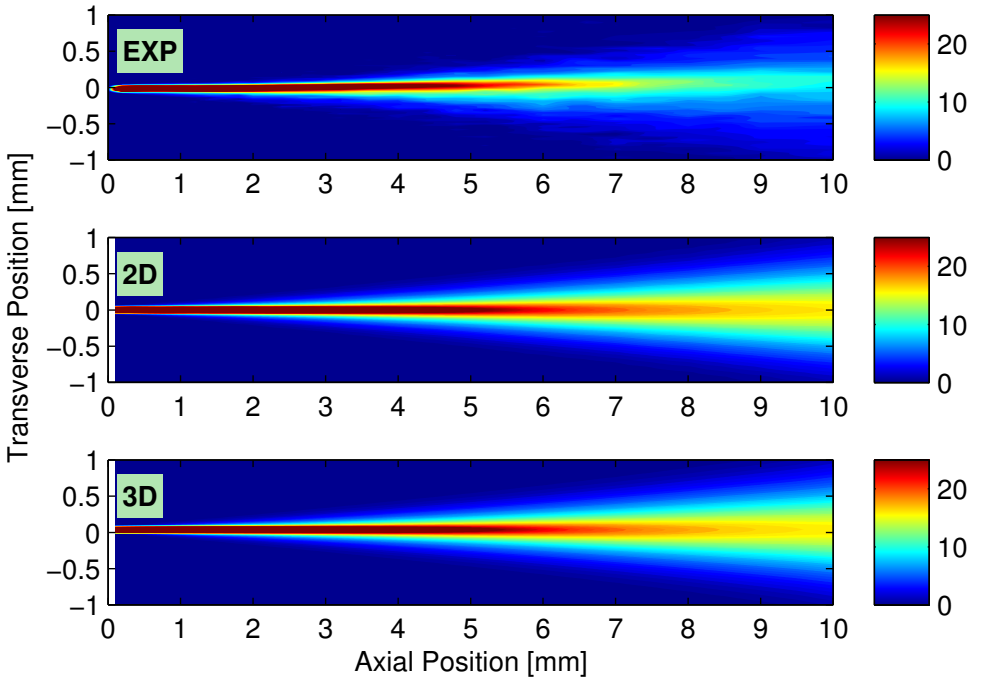

Figure 5.4. *Projected mass density distributions [$\mu g/mm^2$] at 500 μs after SOI from x-ray data and baseline CFD simulations for different computational domains.*

The projected density along the transverse direction comparing the simulations and x-ray radiography data is shown at 0.1 mm, 2 mm, and 6 mm downstream of the nozzle exit in Figure 5.5. Such plots are therefore cuts through the 2D maps shown in Figure 5.4 at 0.1 mm, 2 mm, and 6 mm, respectively. The 3D computational profiles shown in this figure were made along the transverse directions Y and Z, respectively. The profiles in both 3D directions are essentially identical; however, the profile which corresponds to the Y axis is shifted (at 0.1 mm and 2 mm) due to the off-center nozzle position. At the three axial positions, a very similar projected density profile is predicted by the model independently of the used grid. Comparing CFD predictions with experimental measurements, the largest differences can be observed at 6 mm. Here projected density is well matched in terms of radial dispersion but over-predicted in terms of peak value.

TIM, transverse integrated mass, which is obtained from the integral of the projected density across the transverse position at a particular axial location [18], is also evaluated by another integration of the CFD projected mass

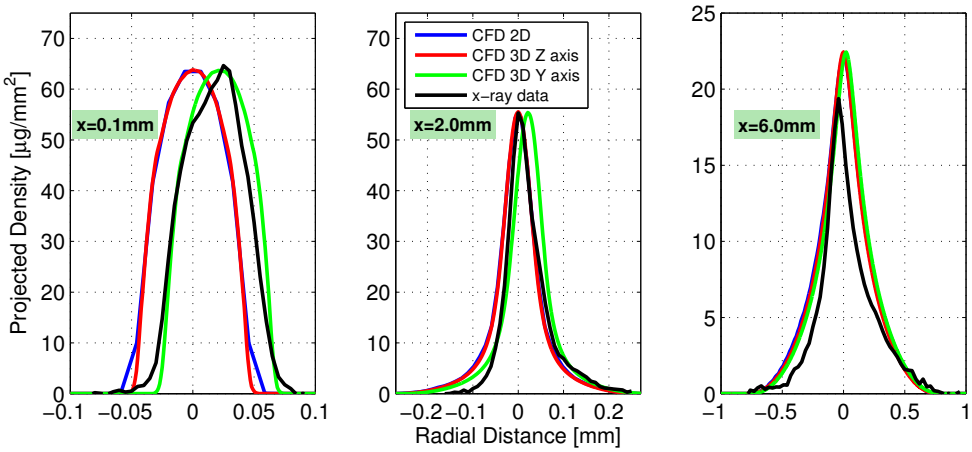

Figure 5.5. *Computed and measured profiles of projected mass density [$\mu g/mm^2$] at 500 μs after SOI at axial locations of 0.1 mm, 2 mm, and 6 mm downstream of the nozzle exit for different computational domains.*

density predictions. This is used to compare the TIM profile along the axis among the simulations and x-ray data. Figure 5.6 shows the predicted results of simulations, using the two different computational domains, compared with measurements. The TIM profiles for both 2D and 3D computations are almost identical, which shows that 2D simulations are adequate if nozzle asymmetry does not need to be captured. Compared with the experimental profile, the TIM is increasingly over-predicted with axial position, with a noticeable divergence occurring at 3 *mm* to 6 *mm*. It has to be noticed that TIM is related to spray dispersion, i.e., higher TIM indicates that spray mixing is faster [4]. This reveals that simulations predict a slightly enhanced spray mixing compared to the results derived from measurements, as also obtained by [16].

Overall, the Σ-Y model provides good agreement with experimental data and can capture the trend of the internal structure of a diesel spray fairly well in the near-field, independently of which type of computational domain is used. However, apart from the reasonable predictions of the model, a really important conclusion of this initial study is that a simulation made in a 2D axisymmetric domain is completely capable of predicting satisfactory results when asymmetry at the nozzle is not present or can be neglected.

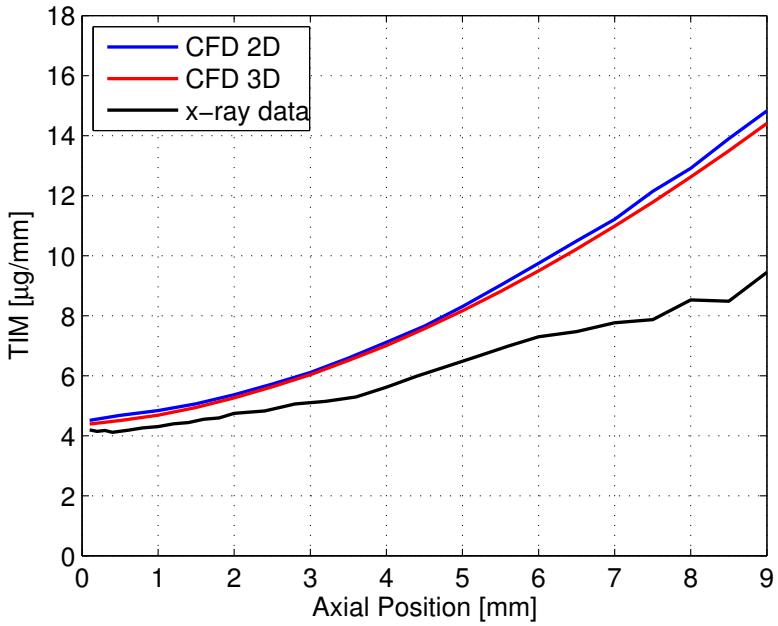

Figure 5.6. *Computed and measured transverse integrated mass along the axis at 500 µs after SOI for different computational domains.*

5.2.2 Coupled simulations – Effect of turbulence models

In addition to the HDR k-ε model which was used previously for the baseline simulation, the SST k-ω and the RNG k-ε turbulence models were evaluated due to these models are commonly used for internal nozzle flow simulations in literature [12, 14, 29, 30]. Momentum and the mass fluxes are evaluated at the nozzle exit from the different CFD calculations. Additionally, non-dimensional flow coefficients are calculated from such results according to the methodology reviewed in Chapter 2, to define the performance of the turbulence model under such conditions.

Table 5.5 shows the steady state values of momentum and mass fluxes as well as the dimensionless coefficients simulated, compared to experimental ones. At the sight of the results, no large differences could be detected among the different turbulence models tested, with maximum deviations compared to the HDR k-ε model below 1.5%. The SST k-ω model is consistently showing the largest deviations, both to the other models as well as to experimental values as well as the largest area coefficient, due to it presents stepper profiles close to the walls at the nozzle exit, see Figure 5.7. Moreover, the three models

Table 5.5. *Steady state parameters and non-dimensional flow coefficients for the turbulence models tested.*

Turbulence model	$\dot{m}$**[g/s]**	$\dot{M}$**[N]**	**Cv[-]**	**Ca[-]**	**Cd[-]**
Experimental	2.558	1.52	0.918	0.98	0.9
HDR k-ε	2.54	1.477	0.903	0.976	0.881
RNG k-ε	2.536	1.472	0.9	0.977	0.879
SST k-ω	2.546	1.465	0.893	0.99	0.884

predict values with an error lower than 5% with respect to experimental ones. Such results prove that HDR k-ε model performance for in-nozzle simulations is as good as the one provided by the other two more typically used turbulence models.

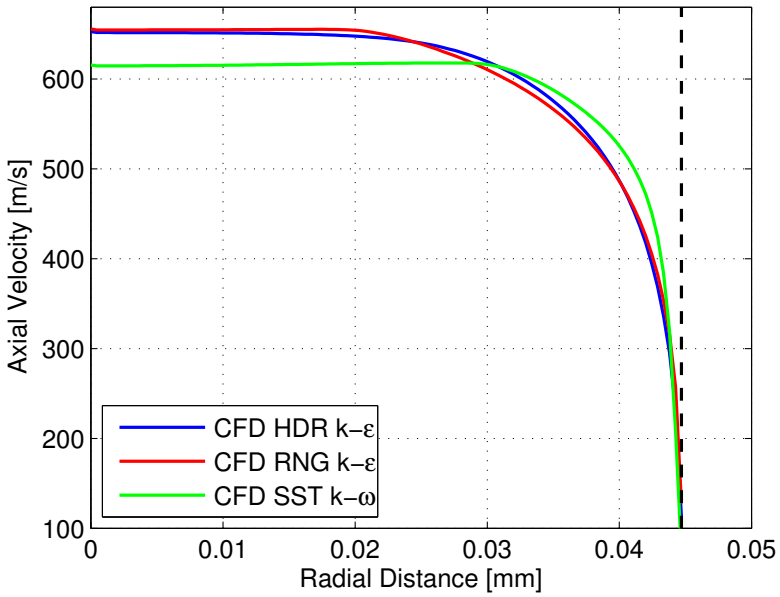

Figure 5.7. *Computed axial velocity profiles at 500 μs after SOI at the orifice exit for 2D CFD coupled simulations with different turbulence models. Black dashed line depicts the radius of the nozzle orifice.*

In order to draw a more accurate conclusion about turbulence model performance, near nozzle spray predictions should be investigated. The model

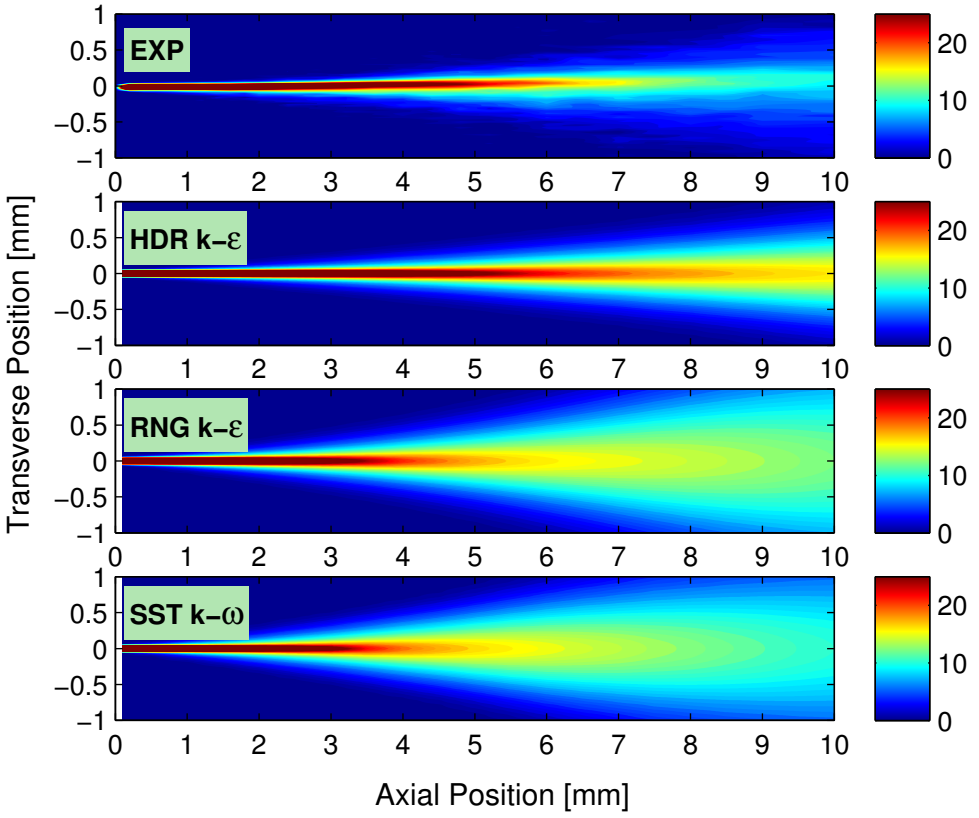

Figure 5.8. *Projected mass density distributions [$\mu g/mm^2$] at 500 μs after SOI from x-ray data and baseline 2D CFD coupled simulations for different turbulence models.*

predicted results of projected mass density with these three turbulence models are compared against x-ray radiography measurements in Figure 5.8. From these projected density contours, large differences can be observed among the three simulations. While predictions achieved with the HDR k-ε model can capture the fuel distribution in the very near-nozzle region, as seen previously in Section 5.2.1, simulations using the other two turbulence models over-predict the radial dispersion downstream 2 mm. This indicates that these two turbulence models are too diffusive for external spray modeling in this case.

In the same way as in Figure 5.5, the projected density along the transverse direction comparing the simulations and x-ray radiography data is shown at 0.1 mm, 2 mm, and 6 mm downstream of the nozzle exit in Figure 5.9.

At the first location all the models predicts almost the same profiles and no noticeable differences could be detected among them, in agreement to very similar flow coefficients previously discussed. However, predictions at 2 *mm* downstream of the nozzle exit show significant contrast. Projected mass density predictions by both the RNG k-ε and SST k-ω turbulence models are under-predicting experimental values, in terms of peak value, and over-predicting experimental values in terms of radial dispersion. At 6 *mm* downstream, the same conclusions hold, with even more important differences to the measurements.

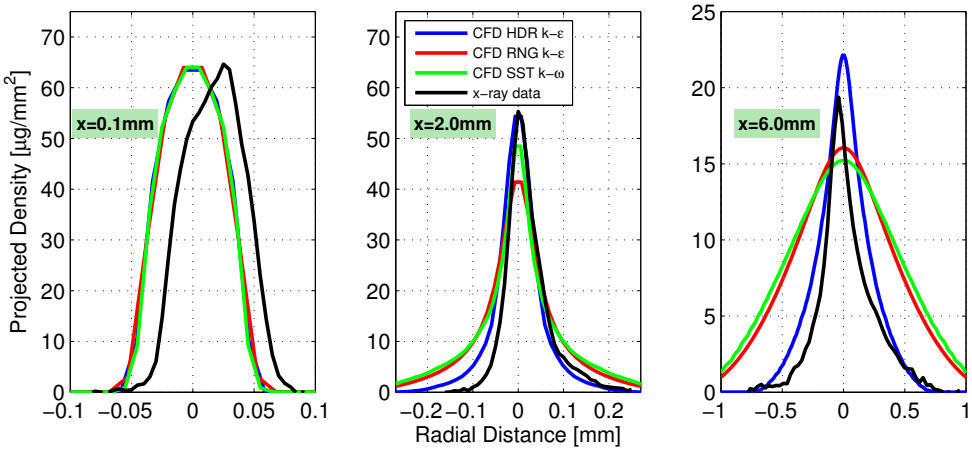

Figure 5.9. *Computed and measured profiles of projected mass density [$\mu g/mm^2$] at 500 μs after SOI at axial locations of 0.1 mm, 2 mm, and 6 mm downstream of the nozzle exit for 2D CFD coupled simulations with different turbulence models.*

Finally, the transverse integrated mass profile along the axis is evaluated. Figure 5.10 shows the predicted results of simulations, using the three different turbulence models, compared with measurements. As expected in light of the previous results, this figure shows that TIM rises faster in these simulations due to an inadequately fast spray mixing.

These simulations make it clear that the HDR k-ε turbulence model provides the best match with the experimental data for the external flow (as seen in Chapter 4) and in the near-field, where it can capture the trend of the internal structure of a diesel spray, while keeping a fair performance regarding the nozzle flow (i.e. in terms of non-dimensional coefficients) in the range of other RANS models.

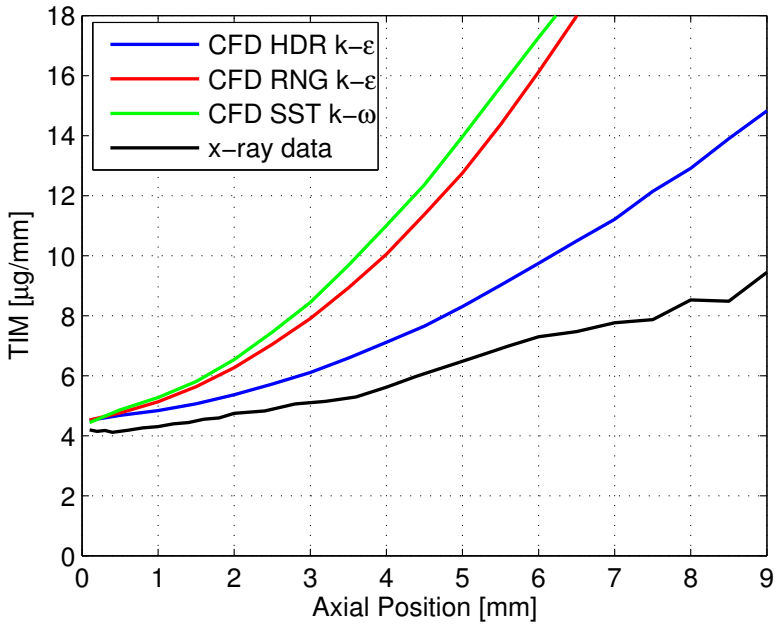

Figure 5.10. *Computed and measured transverse integrated mass along the axis at 500 µs after SOI for 2D CFD coupled simulations with different turbulence models.*

5.2.3 Decoupled simulations

To conclude the evaluation of the Σ-Y Eulerian model, two more simulations have been made using the 2D axisymmetric computational domain without the nozzle geometry. The first simulation was conducted using as an inlet boundary condition the fields obtained at the nozzle exit in the 2D coupled simulation. To do that, the mapped boundary condition of OpenFOAM is used. The other simulation was made using a top-hat (TH) constant radial profile of axial velocity obtained from mass flow rate and momentum flux measurements [9] as input, which is the usual practice when performing decoupled spray simulations. In order to clarify these configurations, in Figure 5.11 both axial velocity profiles at the nozzle orifice are shown as well as the one from the 2D coupled simulation. Moreover, regarding the turbulence model, turbulent intensity was set to 5% [3, 6, 31, 32] and the turbulent integral length scale to 10% of nozzle diameter [33], i.e., as used in Chapter 4.

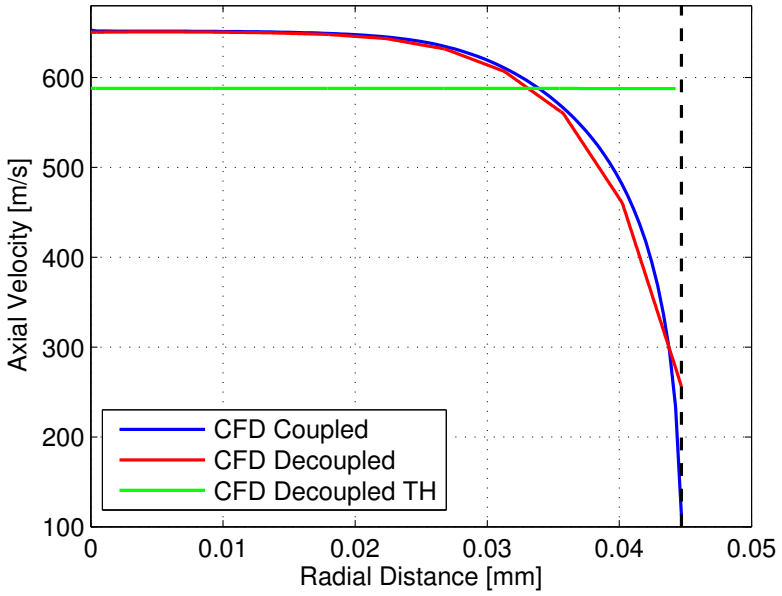

Figure 5.11. *Computed axial velocity profiles at 500 μs after SOI at the orifice for 2D CFD decoupled simulations with different inlet boundary condition. Black dashed line depicts the radius of the nozzle orifice.*

Here, the analysis is started with the projected density along the transverse direction comparing the simulations and x-ray radiography data at 0.1 mm, 2 mm, and 6 mm downstream of the nozzle exit in Figure 5.12. This figure shows the profiles of the 2D coupled simulation, used in the previous sections, as reference against the profiles achieved with the decoupled ones. First, it has to be highlighted that the radial dispersion of all profiles is quite similar, with deviations lower than 5% among the predicted profiles. More differences appear when comparing peak projected density. At the three locations, the profiles predicted with the flat inlet velocity profile achieved a slightly worse value, being at 6 mm downstream the one which diverges more from the experimental measurements, with a maximum error of 17.6%.

In Figure 5.13 the TIM profiles comparison is shown. Once again, the three profiles are quite similar and the trends are well captured. The coupled simulation achieved the best match with the experimental measurements and predicted a less diffusive spray as indicated by slower transverse integrated mass rise. Nonetheless, the decoupled simulations show a promising performance.

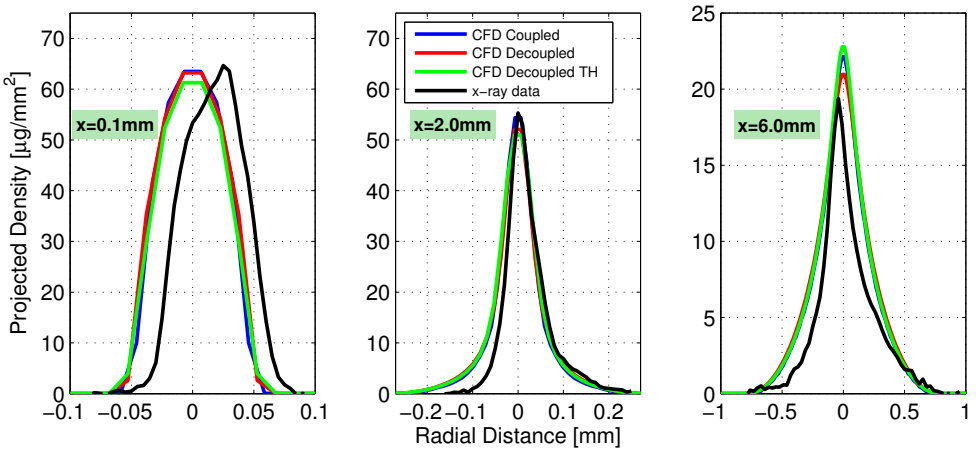

Figure 5.12. *Computed and measured profiles of projected mass density [$\mu g/mm^2$] at 500 μs after SOI at axial locations of 0.1 mm, 2 mm, and 6 mm downstream of the nozzle exit for different types of 2D CFD decoupled simulations.*

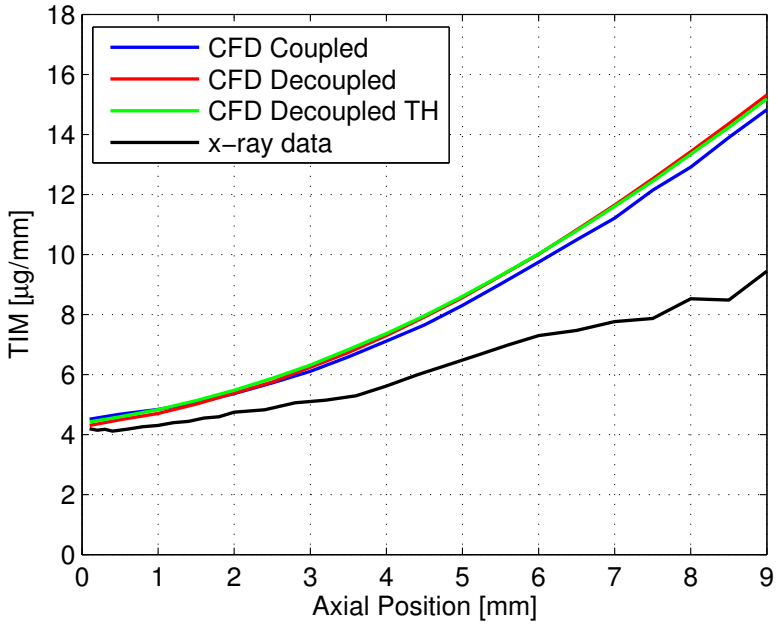

Figure 5.13. *Computed and measured transverse integrated mass along the axis at 500 μs after SOI for different types of 2D CFD decoupled simulations.*

In addition to dense zone investigation of the simulated spray, it is interesting to study the influence of the internal flow simulation on typical global spray parameters such as penetration and also on the liquid volume fraction (Ybar) field, to check effects on the spray tip penetration evolution, spray dispersion and the intact core length. Because of computational costs, only the simulations conducted using the mesh without the internal nozzle geometry have been run to a time of 2.5 ms after start of injection. In Figure 5.14 spray penetration (left) and predicted centerline liquid volume fraction profiles (right) are compared. In terms of spray penetration, some impact in the first 0.5 ms can be observed, being the decoupled simulation, which includes nozzle flow parameters derived from internal nozzle calculations, the only one that is capable of matching the experimental measurements. Then, both simulated curves tend to the same values. In terms of profiles of liquid volume fraction on the axis, it must be noted that experimental measurements are available only within the first 12 mm. This measurements, available at [21], are made by a tomography reconstruction of radiography data for liquid volume fraction [20]. The decoupled simulation, with the nozzle profile derived from the coupled calculations, clearly performs better being able to match exactly the decay of the liquid volume fraction and predicting an intact liquid core ($Ybar > 0.9$) almost in the range estimated by recent analyses in [20]. The differences in near-nozzle liquid volume profiles should be caused by using top-hat nozzle profiles instead of those from coupled nozzle internal and external flow calculations. Largest discrepancies appear between $0.5 - 3$ mm, but downstream of this axial positions the decay of the liquid volume fraction predicted by the top-hat profile case is in good agreement with measurements, which indicates that the effects of the internal nozzle flow are important only in the near nozzle region of the spray.

The tomography reconstruction is also available for radial profiles at different axial positions, so a more detailed comparison between this two simulations is made in Figure 5.15. Three computed and reconstructed liquid volume fraction radial profiles are compared. The axial locations are the same as in the case of projected mass density analyses ($x = 0.1$ mm, 2 mm and 6 mm downstream of the nozzle exit). The radial dispersion at all locations is seen to be quite similar for both simulations. However, remarkable differences for the top-hat profile case can be observed in terms of the peak value, in agreement with Figure 5.14 (right). Thus, for the profile at the axial location of 6 mm a maximum error of around 30% with respect to the experimental data is found.

The previous results have shown that differences in the near-nozzle field tend to disappear further downstream. This can be explained in terms of

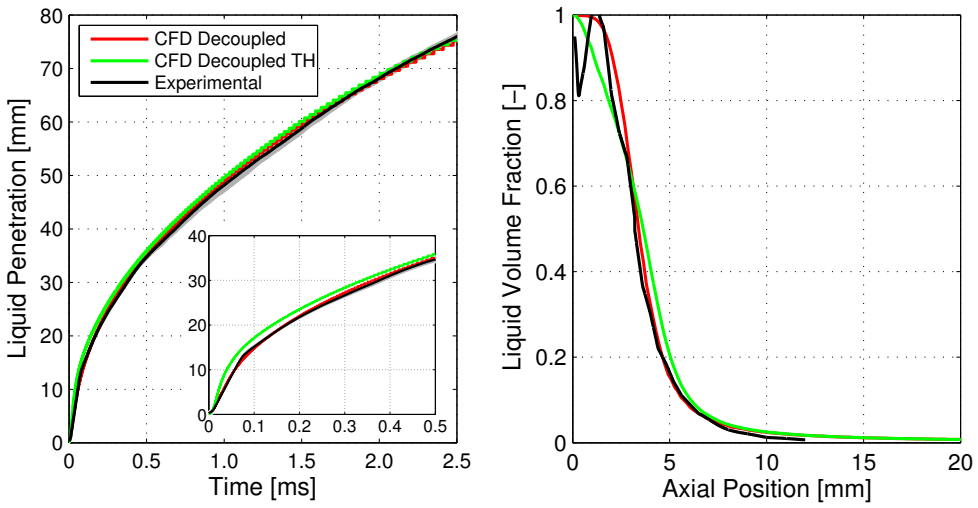

Figure 5.14. *Spray penetration [left] and computed centerline liquid volume fraction at 1 ms after SOI [right] for different types of 2D CFD decoupled simulations.*

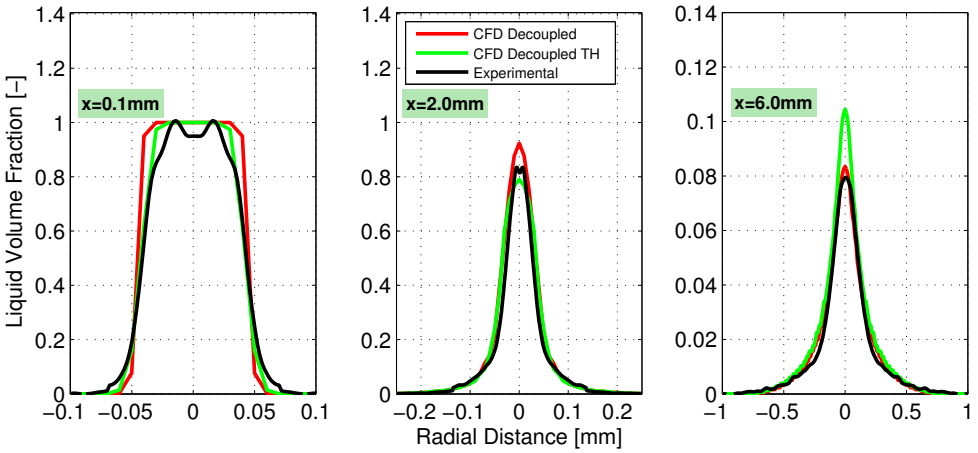

Figure 5.15. *Computed and reconstructed liquid volume fraction radial profiles at 1 ms after SOI at axial locations of 0.1 mm, 2 mm, and 6 mm downstream of the nozzle exit for different types of 2D CFD decoupled simulations.*

turbulent mixing. Figure 5.16 shows the turbulent kinematic viscosity (left) and the turbulent length scale (right) as a function of spray axial location at a time of 2 *ms* after SOI, for the two different decoupled simulations studied.

The turbulent length-scale is given by $l_t = C_\mu^{3/4} k^{3/2}/\varepsilon$. It should be noted that predicted values of l_t have been clipped near the downstream location where the liquid spray ends as the ambient length-scales are not of interest for this discussion. The key issue here is the different level computed, for both variables, in the near nozzle region of the spray for each simulation. Higher values of turbulent viscosity enhance the mixing process which results in shorter intact liquid core, as seen in Figure 5.14. Then, the simulations tend to the same value downstream of 6 mm, as a result of equal injected mass and momentum fluxes, which perfectly explains the impact of nozzle outlet profiles of coupled simulation up to around the already commented axial position of 6 mm. Length scale is also evaluated in order to check the differences between simulations and the suitability of the chosen value for the constant profile (TH). Results show a similar behaviour to turbulent viscosity, depicting a different level in the near nozzle region, though in this case the differences are much lower.

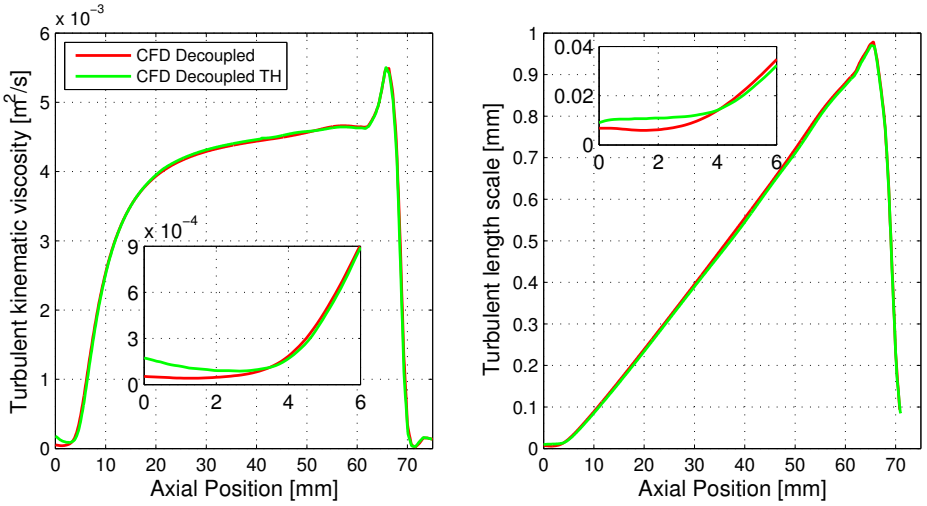

Figure 5.16. *computed centerline turbulent kinematic viscosity [left] and computed centerline integral length scale at 2 ms after SOI [right] for different types of 2D CFD decoupled simulations.*

To sum up this final study, a lower accuracy in the near region (i.e., within 10 mm) is achieved by the simulations without considerations of internal nozzle geometry, although agreement is still quite remarkable with the experimental measurements in the case of the projected density, as shown in Desantes et al. [3]. Nevertheless, the effects of the internal nozzle flow profile in the near region

of the spray are shown in the liquid volume fraction profiles. The different velocity profile and the subsequent induced turbulent viscosity modifies spray dispersion and then liquid volume fraction profiles in the near nozzle region. Further downstream the profile shape effect vanishes, probably due to the fact that mass and momentum fluxes of both simulations are similar. This fact allows the use of the top-hat constant profile boundary condition in further spray applications, where evaporation and combustion are included, due to the accuracy losses are located very near the nozzle exit and the computational cost is almost twice reduced (see Table 5.6).

Table 5.6. *Computational cost comparison between different 2D decoupled simulations.*

Type of simulation	Wall Clock Time (hours)	Number of CPU
2D decoupled	86	8
2D decoupled TH	45	8

5.3 Optimization of primary break-up

The methodology for the optimization of the Σ equation modeling constants is based on Design of Experiments (DOE) techniques, particularly the Response Surface Method (RSM). This method was selected to calibrate the constants that appear at the phenomenological source/sink terms of the surface density model equation. Apart from providing an optimum set of values, it can reveal valuable information about the cause/effect relations between the input and the output parameters.

In these studies, once the liquid fraction field (involved in the Σ equation) is correctly captured as seen previously in Figure 5.14 and Figure 5.15, the three Σ modeling constants (α_1, α_2 and Sc_Σ) are chosen to be optimized and a Central Composite Design (CCD) defined the DOE test plan with 15 simulations, all conducted using the 2D decoupled simulation, i.e. using as inlet boundary condition the nozzle exit profiles obtained with a coupled simulation. The optimization is done based on the SMD droplet size and specifically, the output parameter of RSM is the mean error between the measurements along the axis and the calculated SMD, which is computed at a time late enough to ensure quasi-steady state predictions. Note here that the database of these SMD measurements [23] is different to the one used in Chapter 4. Thus, as explained in [23], the provided experimental SMD is

likewise pathlength-integrated because both the scattering and radiography measurements are pathlength-integrated. As a result, model predictions are processed following the path-averaged ECN method. The SMD of droplets within each CFD cell is integrated through the depth of the spray, collapsing the SMD to a 2-D map (it should be noted that for 2D computations, axisymmetry is assumed). The path-averaged SMD is then obtained by dividing the path-integrated SMD by the path length along which liquid is present. These SMD model predictions are only considered downstream of the intact liquid core ($Ybar > 0.9$), i.e. from $2.5mm$ as seen in Figure 5.14.

Concerning the input factors, the default values of the three modeling constants of the interphase surface density equation are selected at the reference point, while in order to define the parameter ranges of the DOE, maximum and minimum values found in the literature are used; or if they are not present, a 20% variation from the reference point is considered (see Table 5.7). Finally, in Figure 5.17 the three parameters included in the DOE design are compared to those of the reference modeling set-up in a two by two combination plot.

Table 5.7. *Ranges for the input factors for the optimization Stage DOE of 3 parameters.*

	α_1[-]	α_2[-]	Sc_Σ[-]
Reference value	1.0	1.0	0.9
Minimum value	0.2 [*]	0.7 [*]	0.72
Maximum value	1.2	4.0 [**]	1.08
[*] Beheshti et al. [34], [**] Wang et al. [17]			

5.3.1 Optimization stage

Two different optimizations are conducted. In a first step, the optimization is made for the spray A baseline condition, optimization at high pressure injection (HP), but for this operation point experimental results show a particular trend. In contrast to the general thought and the other injection pressures cases measured, the axial evolution of SMD shows a steadily decreasing trend with axial position, with no further increase due to coalescence, which might be expected under this operating conditions (see Figure 5.20). However, CFD model predicts a SMD increase due to coalescence. For this reason, another optimization for the case of the

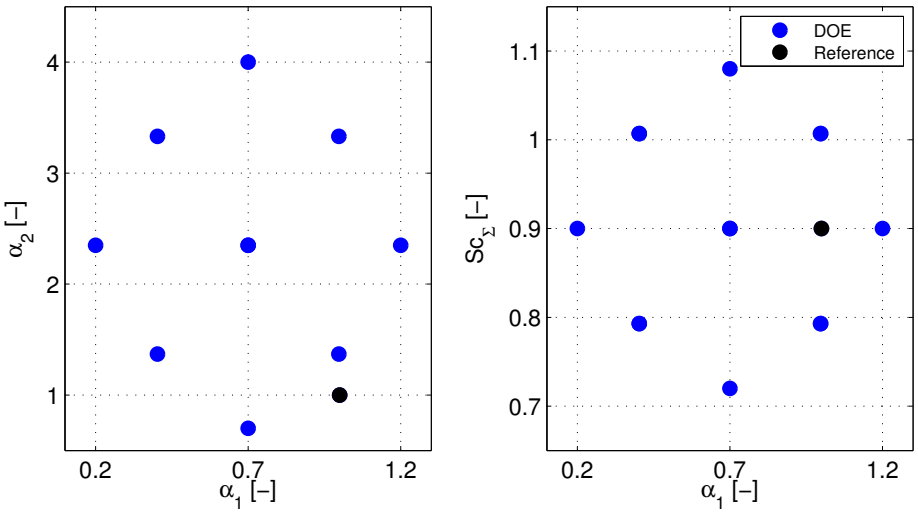

Figure 5.17. *Combinations of input parameters for the optimization DOE.*

intermediate injection pressure is made, optimization at medium pressure injection (MP), at $P_{inj} = 100\ MPa$ compared to $P_{inj} = 150\ MPa$ in the nominal condition. At the end of the process, both optimum sets of model constants values obtained from the response surface are validated for the corresponding operating condition to assure the accuracy of the method and the modeling performance improvement with respect to the original one (Reference in Table 5.7). Then, the different injection pressure conditions and the ambient study (see Table 5.2) are simulated with every set of optimum constants and compared against the experimental measurements in order to finally decide the best choice of modeling parameter values.

Using the results from the 15 simulations of the DOE test plan, a mathematical model is constructed, for each optimization, to correlate the optimized input and the error output, i.e. the mean error between the measurements along the axis and the calculated SMD. This model takes the form shown below:

$$\begin{aligned} Output1 = {} & C_1 + C_2 * \alpha_1 + C_3 * \alpha_2 + C_4 * Sc_\Sigma + C_5 * \alpha_1^2 + C_6 * \alpha_2^2 \\ & + C_7 * Sc_\Sigma^2 + C_8 * \alpha_1 * \alpha_2 + C_9 * \alpha_2 * Sc_\Sigma \\ & + C_{10} * \alpha_1^3 + C_{11} * \alpha_2^3 + C_{12} * Sc_\Sigma^3 \end{aligned} \tag{5.2}$$

where the inputs α_1, α_2 and Sc_Σ are calculated as the following example:

$$\alpha_1 = \big(\alpha_{1value} - (\alpha_{1max} + \alpha_{1min})/2\big)/\big((\alpha_{1max} - \alpha_{1min})/2\big) \tag{5.3}$$

being α_{1value} the value of α_1 parameter of Σ equation that will be calculated [35], α_{1max} and α_{1min} the maximum and minimum values respectively of α_1 in the range used for the optimization (Table 5.7).

The mathematical model have been established with 95% confidence, keeping only the significant terms. The coefficients C_1 to C_{12} are described in Table 5.8 for both optimizations. The fit of this surface compared to the original data is shown by the R^2 value of 0.9924 (HP Optimization) and 0.99 (MP Optimization), which confirm that the mathematical models can predict the response accurately with low prediction error.

Table 5.8. *RSM coefficients for each optimization.*

Coefficient	**HP Optimization**	**MP Optimization**
C_1	69.487	13.961
C_2	-36.721	-12.224
C_3	67.117	-6.276
C_4	-1.662	-0.968
C_5	5.228	49.758
C_6	42.458	45.323
C_7	4.918	1.623
C_8	-5.738	-8.015
C_9	1.877	-1.001
C_{10}	36.631	-24.286
C_{11}	-21.177	2.321
C_{12}	7.382	1.603

Finally, in order to find the optimum parameters, a discretization of 101 points between ranges for each parameter is considered and the 1030301 different combinations are evaluated with the mathematical model. At the end, the minimum error output is found with the constant values, shown in Table 5.9. The optimum combinations of parameters should be tested under different operating conditions, these results appear on Section 5.3.2,

but previously, from the RSM results some trends can be highlighted (apart from the same optimum value for the Sc_Σ parameter).

Table 5.9. *Optimum values of the modeling constants.*

Constant	α_1[-]	α_2[-]	Sc_Σ[-]
HP Optimization	0.96	1.459	0.9468
MP Optimization	0.77	2.482	0.9468

In Figure 5.18 and Figure 5.19, the effects of each modeling constant on the error output are shown respectively for each optimization. Additionally to the complete surface obtained with the RSM results, the error of the reference CFD configuration and the optimum values combination are included as well as the tendency expected by the error while changing only one parameter (red line). This line represents a parametric variation of each constant value while keeping fixed the other two to the mean value of the ranges depicted in Table 5.7, i.e. $\alpha_1 = 0.7$, $\alpha_2 = 2.35$ and $Sc_\Sigma = 0.9$.

Optimization at high pressure injection (HP)

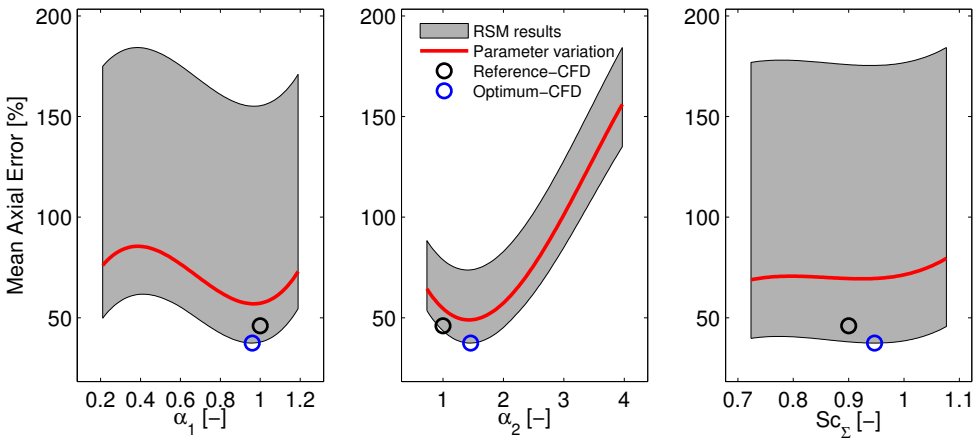

Figure 5.18. *Effect of each input parameter on the mean axial error between SMD model predictions and measurements. HP optimization.*

Results from the first response surface provide really interesting conclusions. The first parameter, α_1, shows a sinusoidal pattern presenting the

minimum value in the vicinity of 1. The impact of the second constant, α_2, is really clear. It can be seen how increasing its value above 2, the error is hugely increased as a consequence of too much coalescence. Finally, the Sc_Σ used in the interphase surface density equation, produces an almost negligible effect on the error as long as its value is below 1, slightly increasing the error on the contrary.

Optimization at medium pressure injection (MP)

Regarding the second response surface, first note that due to the mean value of the modeling parameters ranges is quite close to the optimums, the parametric variation line is located at the bottom of the error surface. A completely negligible impact of the Sc_Σ on the error is found. However, results for the other constants are different in comparison with previous optimization. The first parameter, α_1, presents a well defined minimum in the vicinity of 0.8, hugely increasing the error when it takes values below 0.6. Finally, the effect of the second constant, α_2, follows a quadratic function and as a result, the minimum value occurs at its vertex. Moreover, it should be noted that the predicted mean axial error is more than twice lower to the one achieved with the first optimization (around 16% against 37%).

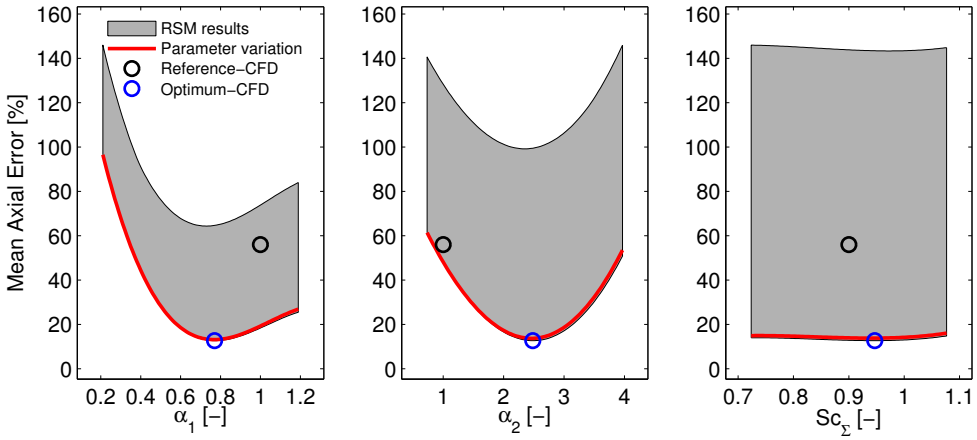

Figure 5.19. *Effect of each input parameter on the mean axial error between SMD model predictions and measurements. MP optimization.*

Validation of optimum parameters

Both optimum sets of model constants values are validated for the corresponding operating condition in Figure 5.20, optimization HP at the left, for the spray A baseline condition, and optimization MP at the right, for the case with injection pressure of 100 MPa. Additionally, modeling predictions for the reference sets of model constants values are depicted in order to check the real improvement.

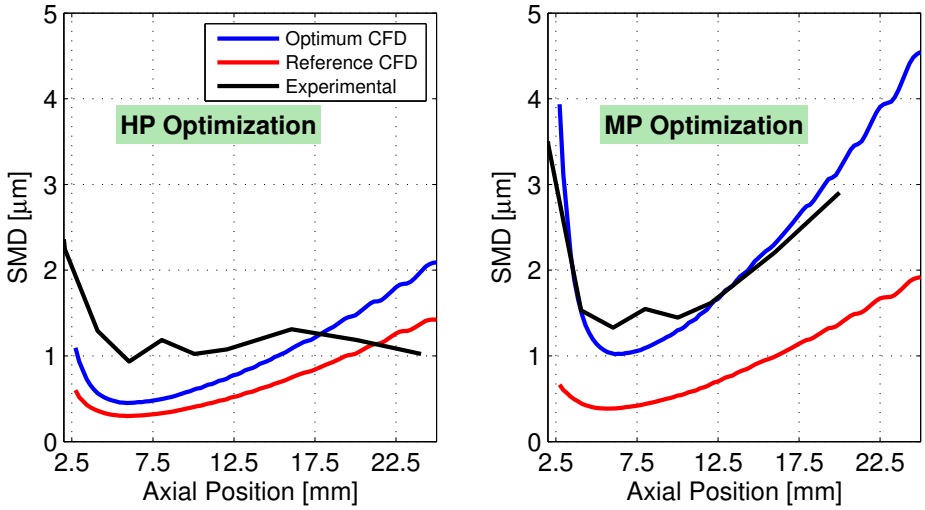

Figure 5.20. *Computed and measured SMD profiles at the reference conditions.*

In view of the results, both optimizations improve the performance achieved by the reference set of values. However, in optimization HP the natural trend of model predictions, i.e. increasing droplet diameter due to coalescence downstream, drives the optimal solution to a compromise. Thus, at the beginning the atomization is more pronounced while from 17.5 mm downstream, the coalescence makes SMD predictions greater than measurements. On the other hand, optimization MP performance is remarkably impressive reproducing the experimental trend overall and providing an important improvement with respect to reference set-up predictions.

5.3.2 Parametric studies

In Figure 5.21 the influence of injection pressure is shown for both sets of constant values. Experimental trends are well reproduced, increased injection pressure decreases the droplet size, for both optimizations as well as the location at which the minimum droplet size occurs, with little changes with injection pressure. Nevertheless, a substantial difference in the quantitative quality of the results is detected. Predictions of the second set of optimum parameters are remarkably close to the experimental data, neglecting the coalescence discrepancy for $P_{inj} = 150\ MPa$, condition for which measurements show an unusual and isolate behaviour with axial distance. Moreover, the decrease of droplet size, especially in the regions nearest the nozzle exit, is more enhanced providing a clear distinction among the three injection pressures, in line with observations.

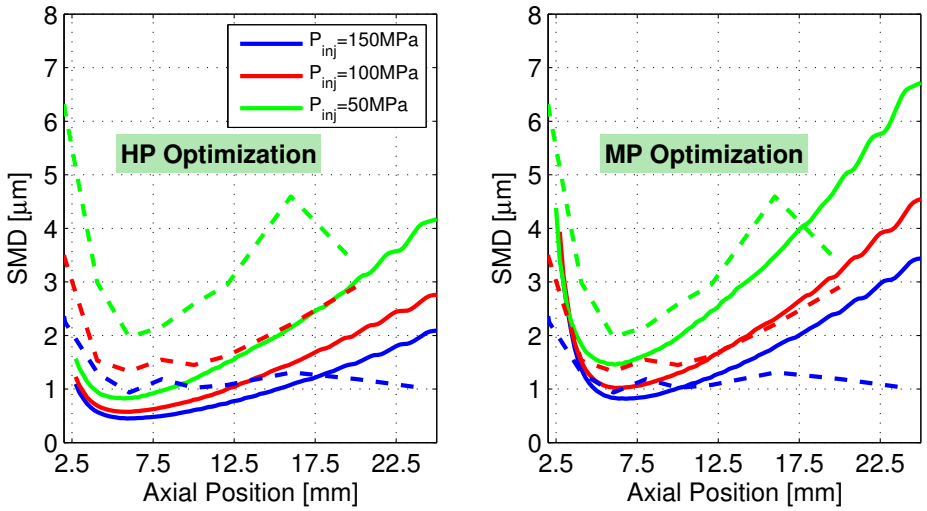

Figure 5.21. *Computed (solid lines) and measured (dashed lines) SMD profiles for different injection pressures.*

Finally, the influence of the back pressure, i.e. ambient density, is shown for both sets of constant values in Figure 5.22. Experimental trends are well reproduced, decreased back pressure shows a lower atomization rate of the droplet size, for both optimizations as well as the position at which the minimum droplet size occurs, located further downstream of the nozzle exit, is well captured. In comparison with the baseline condition, in the case of the lowest back pressure (for both optimizations), the increasing droplet size effect

with the axial distance is minimized and predictions reach an almost constant SMD value. However, once again a remarkable difference between optimization is detected. Predictions of the second set of optimum parameters are in more agreement with the experimental data, concluding that it is the suitable set of optimum values for the interphase surface density equation.

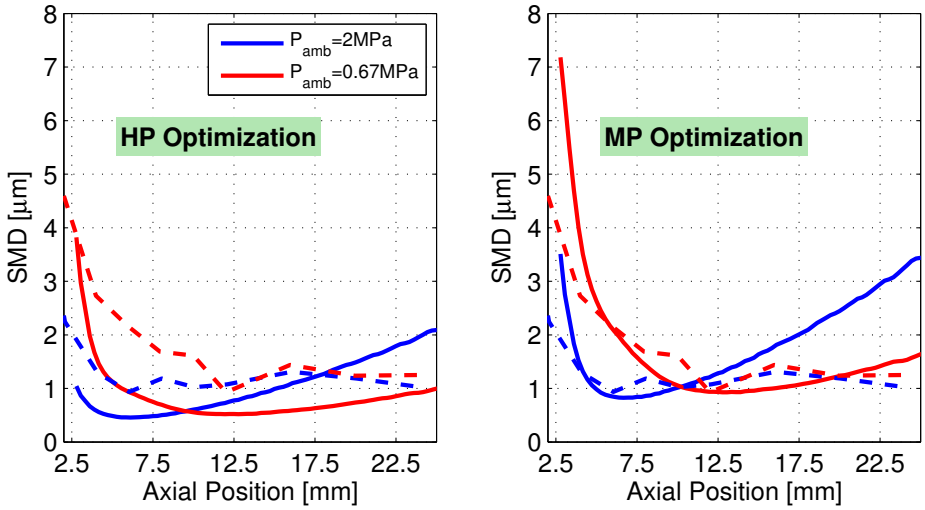

Figure 5.22. *Computed (solid lines) and measured (dashed lines) SMD profiles for different back pressures.*

Additionally, in order to evaluate modeling performance separately of ambient density, i.e. air entrainment is changed because of different densities, the results are normalized in Figure 5.23 with the equivalent diameter, which takes the values of 0.5 for the baseline condition and 0.869 for the reduced back pressure case:

$$d_{eq} = D_o \sqrt{\frac{\rho_f}{\rho_{amb}}}$$

In view of the results, independently of the optimization, almost an equal minimum SMD prediction is reached in both simulated conditions and the same axial increase due to coalescence is depicted. Thus, it is confirmed that modeling atomization is a consequence of air entrainment.

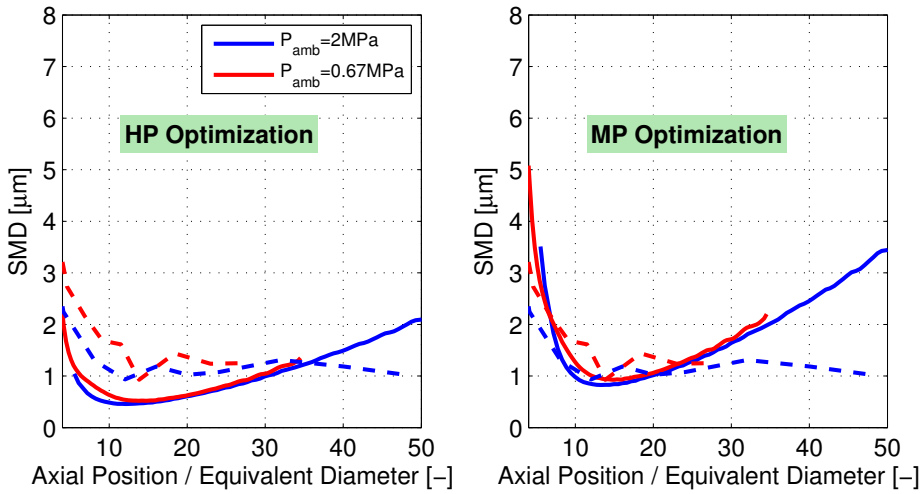

Figure 5.23. *Computed (solid lines) and measured (dashed lines) SMD normalized profiles for different back pressures.*

5.4 Conclusions

The Σ-Y Eulerian atomization model has been applied to the study of direct injection diesel sprays, with a focus on reproducing the internal structure of a diesel spray in the near-field, including the effects of internal nozzle flow. Calculations have been validated against x-ray radiography measurements of non-vaporazing Spray A condition of ECN, conducted at Argonne National Laboratory. The present work is limited to a non-cavitating nozzle, but it has to be noticed that the trend in industry is towards highly tapered nozzles that are less prone to cavitation. So the conclusions may be applied to other nozzles used in Diesel injection systems.

A first study of the effect of including nozzle flow on diesel spray CFD simulations using the Eulerian Σ-Y atomization model has been conducted, by comparing 3D and 2D coupled internal/external flow simulations. Both calculations produced qualitatively and quantitatively good agreement with the experimental data, showing that 3D simulations can capture measured flow asymmetries close to the nozzle outlet, but 2D simulations provides accurate results within the near nozzle region. Neglecting such accuracy losses, a 2D computational domain is suitable for further investigations. In this sense, different turbulence models have been evaluated. Predictions made by the HDR k-ε model with the corrected value of the $C_{1\epsilon}$ constant, the

RNG k-ε model and the SST k-ω model were compared. Only the HDR k-ε turbulence model makes fairly accurate predictions while the other two over-predict the radial dispersion. The HDR k-ε model has been proved to be the best turbulence model for external flow application in the near nozzle region and further downstream (Chapter 4), while showing a great performance in internal nozzle flow development, reproducing the value of the dimensionless coefficients fairly well and with similar accuracy as the other tested models. As a result, this model was selected for all the subsequent calculations.

Additionally, in order to explore the necessity of the coupled simulation, two studies in a domain without the nozzle geometry were run. In one case, the inlet boundary condition is taken from the coupled simulation and in the other, a top-hat velocity profile, obtained from mass flow rate and momentum flux measurements, is applied at the inlet boundary. Apart from the near-field study, the effect on further spray development (i.e. far field) was evaluated. These two simulations have been compared in terms of spray penetration and liquid volume fraction. A noticeable impact on the intact core length prediction and LVF profiles have been reported. However, further downstream the differences vanishes and tip penetration and velocity field are nearly the same, indicating that injected mass and momentum flux plays a major role on spray turbulent mixing. This fact allows the use of the top-hat constant profile boundary condition in further spray applications, where evaporation and combustion are included, in order to reduce the computational cost of conducting nozzle flow simulations to derive the nozzle boundary conditions.

Moreover, a calibration process of the Σ equation constants has been conducted in order to optimize the primary break-up modeling capabilities. This has been made by means of a Design of Experiments (DOE) technique, known as Response Surface Method (RSM) and comparison with SMD measurements. Apart from optimum values, this methodology is able to point out some interesting cause/effect relations between the input and the output parameters, such as the fact that the Schmidt number (Sc_Σ) value used in the diffusion coefficient of the Σ equation presents a negligible effect on the predictions. At the end, a great improvement in modeling performance is achieved in comparison with the reference set-up, and different injection and back pressures conditions are well reproduced proving the great overall effectiveness of the achieved configuration. Nonetheless, the experimental trend shown in the baseline condition could indicate that some development of the density surface model should be made, providing an open topic research area in the field of diesel spray atomization processes.

In view of the results, the Σ-Y Eulerian atomization model has proved its ability to model the internal flow together with the spray, providing fairly good predictions to match the experimental data. A remarkable conclusion of the present chapter is that when a good measurement of rate of injection (ROI) is available, and the study involves a single-hole convergent nozzle, a two-dimensional eulerian study without the internal flow simulation is perhaps sufficient. Obviously, if the aim of the work is evaluating the effects of asymmetries of the nozzle geometry, a full 3D coupled simulation (internal nozzle and spray) will be the proper solution.

Bibliography

[1] *Engine Combustion Network*. http://www.sandia.gov/ecn, accessed in August 2015.

[2] Dukowicz John K. "A particle-fluid numerical model for liquid sprays". *Journal of Computational Physics*, Vol. 35 n^o 2, pp. 229 – 253, 1980.

[3] Desantes J.M., García-Oliver J.M., Pastor J.M. and Pandal A. "A Comparison of Diesel Sprays CFD modelling approaches: DDM vs $\Sigma - Y$ Eulerian Atomization Model". *Atomization and Sprays*, Vol. 26 n^o 7, pp. 713–737, 2016.

[4] Desantes J.M., García-Oliver J.M., Pastor J.M., Pandal A., Baldwin E. and Schmidt D.P. "Coupled/decoupled spray simulation comparison of the ECN spray a condition with the $\Sigma-Y$ Eulerian atomization model". *International Journal of Multiphase Flow*, Vol. 80, pp. 89 – 99, 2016.

[5] Desportes A., Zellat M., Desoutter G., Liang Y. and Ravet F. "Application of the Eulerian-Lagrangian Spray Atomization (ELSA) Model for the Diesel Injection Simulation". In *THIESEL 2010 Conference on Thermo- and Fluid Dynamic Process in Diesel Engines*, 2010.

[6] García-Oliver J.M., Pastor J.M., Pandal A., Trask N., Baldwin E. and Schmidt D.P. "Diesel Spray CFD Simulations based on the $\Sigma - Y$ Eulerian Atomization Model". *Atomization and Sprays*, Vol. 23, pp. 71–95, 2013.

[7] Lebas R., Menard T., Beau P.A., Berlemont A. and Demoulin F.X. "Numerical simulation of primary break-up and atomization: DNS and modelling study". *International Journal of Multiphase Flow*, Vol. 35 n^o 3, pp. 247 – 260, 2009.

[8] Ning W., Reitz R.D., Diwakar R. and Lippert A.M. "An Eulerian-Lagrangian spray and atomization model with improved turbulence modeling". *Atomization and Sprays*, Vol. 19, pp. 727,739, 2009.

[9] Payri R., García-Oliver J.M., Salvador F.J. and Gimeno J. "Using spray momentum flux measurements to understand the influence of diesel nozzle geometry on spray characteristics". *Fuel*, Vol. 84 n^o 5, pp. 551 – 561, 2005.

[10] Payri R., Salvador F.J., Gimeno J. and de la Morena J. "Effects of nozzle geometry on direct injection diesel engine combustion process". *Applied Thermal Engineering*, Vol. 29 n^o 10, pp. 2051 – 2060, 2009.

[11] Belhadef A., Vallet A., Amielh M. and Anselmet F. "Pressure-swirl atomization: Modeling and experimental approaches". *International Journal of Multiphase Flow*, Vol. 39, pp. 13 – 20, 2012.

[12] Som S., Longman D.E., Ramírez A.I. and Aggarwal S.K. "A comparison of injector flow and spray characteristics of biodiesel with petrodiesel". *Fuel*, Vol. 89 n^o 12, pp. 4014 – 4024, 2010.

[13] Som Sibendu, Ramírez Anita I., Longman Douglas E. and Aggarwal Suresh K. "Effect of nozzle orifice geometry on spray, combustion, and emission characteristics under diesel engine conditions". *Fuel*, Vol. 90 n^o 3, pp. 1267 – 1276, 2011.

[14] Salvador F.J., Gimeno J., Pastor J.M. and Martí-Aldaraví P. "Effect of turbulence model and inlet boundary condition on the Diesel spray behavior simulated by an Eulerian Spray Atomization (ESA) model". *International Journal of Multiphase Flow*, Vol. 65, pp. 108–116, 2014.

[15] Xue Q., Battistoni M., Som S., Quan S.P., Senecal P. K., Pomraning E. and Schmidt D. P. "Eulerian CFD Modeling of Coupled Nozzle Flow and Spray with Validation against X-ray Radiography Data". *SAE Int. J. Engines*, Vol. 7(2), pp. 1061–1072, 2014.

[16] Xue Q., Battistoni M., Powell C.F., Longman D.E., Quan S.P., Pomraning E., Senecal P.K., Schmidt D.P. and Som S. "An Eulerian CFD model and X-ray radiography for coupled nozzle flow and spray in internal combustion engines". *International Journal of Multiphase Flow*, Vol. 70 n^o 0, pp. 77 – 88, 2015.

[17] Wang Y., Lee W., Reitz R. and Diwakar R. "Numerical Simulation of Diesel Sprays Using an Eulerian-Lagrangian Spray and Atomization (ELSA) Model Coupled with Nozzle Flow". *SAE Technical Paper*, n^o 2011-01-0386, 2011.

[18] Kastengren Alan L., Powell Christopher F., Wang Yujie, Im Kyoung-Su and Wang Jin. "X-ray radiography measurements of diesel spray structure at engine-like ambient density". *Atomization and Sprays*, Vol. 19 n^o 11, pp. 1031–1044, 2009.

[19] Kastengren A.L., Tilocco F.Z., Duke D., Powell C.F., Moon S. and Zhang X. "Time-Resolved X-Ray Radiography of Diesel Injectors from the Engine Combustion Network". In *12th Triennial International Conference on Liquid Atomization and Spray Systems*, pp. 2–6, 2012.

[20] Pickett L., Manin J., Kastengren A. and Powell C. "Comparison of Near-Field Structure and Growth of a Diesel Spray Using Light-Based Optical Microscopy and X-Ray Radiography". *SAE Int. J. Engines*, Vol. 7 n^o 2, 2014.

[21] *LVF data*. http://www.sandia.gov/ecn/argonne/assets/datafiles/mixture/rad675.php, accessed in August 2015.

[22] Kastengren A., Tilocco F. Z., Powell C. F., Manin J., Pickett L. M., Payri R. and Bazyn T. "Engine Combustion Network (ECN):Measurements of nozzle geometry and hydraulic behavior". *Atomization and Sprays*, Vol. 22, pp. 1011–1052, 2012.

[23] Kastengren A., Ilavsky J., Viera J.P., Payri R., Duke D., Swantek A., Tilocco F.Z., Sovis N. and Powell C.F. "Measurements of Droplet Size in Shear-Driven Atomization Using Ultra-Small Angle X-Ray Scattering". *Fuel*, 2016 (under review).

[24] Naber J. and Siebers D. "Effects of Gas Density and Vaporization on Penetration and Dispersion of Diesel Sprays". *SAE Technical Paper*, n^o 960034, 1996.

[25] Desantes J.M., Salvador F.J., López J.J. and De la Morena J. "Study of mass and momentum transfer in diesel sprays based on X-ray mass distribution measurements and on a theoretical derivation". *Experiments in Fluids*, Vol. 50 n^o 2, pp. 233–246, 2011.

[26] Macian V., Bermudez V., Payri R. and Gimeno J. "New technique for determination of internal geometry of a diesel nozzle with the use of silicone methodology". *Experimental Techniques*, Vol. 27 n^o 2, pp. 39–43, 2003.

[27] Martí-Aldaraví P. *Development of a computational model for a simultaneous simulation of internal flow and spray break-up of the Diesel injection process*. Doctoral Thesis, Departamento de Máquinas y Motores Térmicos, Universidad Politécnica de Valencia, España, 2014.

[28] Pope S. B. *Turbulent Flows*. Cambridge University Press, 2000.

[29] Salvador F.J., Carreres M., Jaramillo D. and Martínez-López J. "Comparison of microsac and VCO diesel injector nozzles in terms of internal nozzle flow characteristics". *Energy Conversion and Management*, Vol. 103, pp. 284 – 299, 2015.

[30] Salvador F.J., Carreres M., Jaramillo D. and Martínez-López J. "Analysis of the combined effect of hydrogrinding process and inclination angle on hydraulic performance of diesel injection nozzles". *Energy Conversion and Management*, Vol. 105, pp. 1352 – 1365, 2015.

[31] Lacaze Guilhem, Misdariis Antony, Ruiz Anthony and Oefelein Joseph C. "Analysis of high-pressure Diesel fuel injection processes using {LES} with real-fluid thermodynamics and transport". *Proceedings of the Combustion Institute*, Vol. 35 n^o 2, pp. 1603 – 1611, 2015.

[32] Ménard T., Tanguy S. and Berlemont A. "Coupling level set/VOF/ghost fluid methods: Validation and application to 3D simulation of the primary break-up of a liquid jet". *International Journal of Multiphase Flow*, Vol. 33 n^o 5, pp. 510 – 524, 2007.

[33] Sallam K. A. and Faeth G. M. "Surface Properties During Primary Breakup of Turbulent Liquid Jets in Still Air". *AIAA Journal*, Vol. 41 n^o 8, pp. 1514–1524, Agosto 2003.

[34] Beheshti Novid, Burluka AlexeyA. and Fairweather Michael. "Assessment of $\Sigma - Y$ liq model predictions for air-assisted atomisation". *Theoretical and Computational Fluid Dynamics*, Vol. 21 n^o 5, pp. 381–397, 2007.

[35] Benajes J., Novella R., Pastor J.M., Hernández-López A., Hasegawa M., Tsuji N., Emi M., Uehara I., Martorell J. and Alonso M. "Optimization of the combustion system of a medium duty direct injection diesel engine by combining CFD modeling with experimental validation". *Energy Conversion and Management*, Vol. 110, pp. 212 – 229, 2016.

Chapter 6

Vaporizing sprays application

Contents

6.1 Introduction

In the present chapter, the implemented Eulerian spray model is applied to external flow simulations with the aim of validate and evaluate the vaporization model performance. Thus, model predictions have been compared to experimental data from free diesel sprays under vaporizing conditions available from the database of the Engine Combustion Network [1]. In this introduction, the reasons why these studies were chosen, the objectives and the followed methodology are outlined.

6.1.1 Motivation

The present investigation is the natural step in the code validation and development procedure. The implemented vaporization model has to be validated against experimental measurements and for this purpose, the experimental database of the ECN [1] results highly attractive.

At first, the vast set of experimental data available for the "Spray A" is an advantage. Such measurements include typical spray characterization parameters such as liquid length and vapor penetration, and also remarkable local air/fuel ratio measurements together with axial velocity profiles within the jet. In addition to the valuable data, an important characteristic of this database is the wide range of ambient and injection conditions in which measurements are available, including parametric variation studies of ambient temperature, ambient density and injection pressure. All these tests should demonstrate the overall utility of the $\Sigma - Y$ modeling approach for diesel spray simulation.

A further advantage is the fact that all the conclusions obtained in Chapter 5 are obviously applicable in this study. As a result, an important computational cost can be saved while high accuracy is kept. Finally, it has to be highlighted that in this database measurements for Spray A reacting conditions are also available, thus the complete evaluation of the model for engine relevant conditions can be performed.

6.1.2 Objectives of the study

The main goal of this research work is to test the application of Σ-Y Eulerian model to vaporizing diesel spray modeling by comparing with experimental data. This overall objective implicitly includes the validation of the implemented vaporization model, based on mixing-controlled

assumptions. Furthermore, the predictive capabilities of the model concerning the performance to capture both global and local parameters, such as tip penetration, liquid length, ambient gas velocity and vapor mixture fraction, on a wide range of ambient and injection conditions. Moreover, the coupled spray/combustion model is finally applied to the reference case of the n-Dodecane ECN Spray A under reacting conditions, which makes it possible to prove the overall utility of the whole model to simulate the diesel spray from the nozzle till the combustion process.

6.1.3 Methodology of the study

In order to evaluate the model under vaporizing conditions the ECN Spray A database [1–5] has been used. Compared to the previous chapter, where Spray A non-vaporizing conditions were used, the present study has been carried out using the full Spray A specifications, i.e. ambient density 22.8 kg/m^3, ambient temperature 900 K and injection pressure 150 MPa. The main conditions of this experiment are presented in Table 6.1.

Table 6.1. *Conditions for vaporazing Spray A baseline condition.*

Fuel	n-Dodecane
Ambient composition	100% N2
Injection pressure [MPa]	150
Ambient temperature [K]	900
Ambient density [kg/m^3]	22.8
Fuel injection temperature [K]	363

In addition to standard spray characterization parameters such as liquid length, measured by using diffused back-illumination (DBI), and vapor tip penetration, performed by means of schlieren imaging [2], the experimental data used for validation include local air/fuel ratio measurements performed using the Rayleigh scattering technique [5]. The latter data enable a complete analysis for validation and evaluation of CFD model, both in global and local terms. Additionally, flow-field measurements by particle image velocimetry (PIV) are available for this baseline condition, from which local velocities can be defined [4]. However, these advanced measurements are made for different Spray A nozzles. While the Rayleigh measurements are made for nozzle serial 210677, PIV images are performed for nozzle serial 210678. Simulations are

conducted for nozzle 210677 and in order to enable a fair comparison with PIV measurements results are presented in terms of normalized magnitudes. These studies correspond to the validation of the model and afterwards, a parametric variation (including injection pressure, ambient density and temperature) is performed based on the reference case. Only spray tip penetration and liquid length measurements are available for these studies, which are conducted for the nozzle serial 210675, as in the previous chapter. In Tables 6.2 and 6.3 the conditions simulated for the model validation and the parametric variation cases are shown. After that, spray computed development under vaporizing and non-vaporizing sprays is investigated.

Table 6.2. *Simulated validation cases conditions.*

Injector Serial#	P_{inj}[MPa]	T_{amb}[K]	ρ_{amb}[kg/m^3]
210677 (Baseline)	150	900	22.8
210677	150	1100	15.2

Table 6.3. *Simulated parametric variations studies conditions.*

Injector Serial#	P_{inj}[MPa]	T_{amb}[K]	ρ_{amb}[kg/m^3]
210675 (Baseline)	150	900	22.8
210675	**100**	900	22.8
210675	**50**	900	22.8
210675	150	900	**15.2**
210675	150	900	**7.6**
210675	150	**1000**	22.8
210675	150	**800**	22.8
210675	150	**700**	22.8

Finally, once the vaporizing model is validated and further assessed, an initial reacting application is performed. The objective in the present work concerning reactive spray is limited to the correct coupling procedure between spray and combustion models. As a result, this study is an evaluation of this achievement, while an extensive investigation, i.e. sprays under different operating conditions, remains future work. First, note that the chemical

mechanism and the ensuing tabulated chemistry is imposed to the model, being the C_χ parameter the unique that must be calibrated in order to simulate a reacting spray. Thus, in a first step, the mixture fraction variance (Equation 3.78) is investigated, under inert conditions (nozzle 210677), by different values of the C_χ parameter of the combustion model and comparison against experimental measurements. Then the nominal Spray A reacting condition (see Table 6.4) is simulated (nozzle 210675) and compared with measurements performed by schlieren imaging [6] that leads to quantitative data for spray tip penetration. PIV images under reacting environment, also available, allow a velocity comparison. Once again this measurements are performed for nozzle serial 210678 [7]. Additionally, global properties of the flame, i.e. the ignition delay and the lift-off length are also evaluated.

Table 6.4. *Conditions for reacting Spray A baseline condition.*

Fuel	*n*-Dodecane
Ambient composition in molar basis	85% N2, 15% O2
Injection pressure [MPa]	150
Ambient temperature [K]	900
Ambient density [kg/m^3]	22.8
Fuel injection temperature [K]	363

Detailed internal nozzle geometric characterization has been performed for the injectors employed in these experiments, where the main characteristics are presented in Table 6.5. D_o, D_{eff} and U_{eff} denote nozzle orifice outlet diameter, effective diameter and effective velocity, respectively. Additionally, stabilized mass and momentum fluxes are also presented.

Table 6.5. *Nozzle geometric and flow characteristics for single-hole Spray A ECN injector.*

Injector Serial#	$D_o[\mu m]$	$D_{eff}[\mu m]$	U_{eff}[m/s]	$\dot{m}$[g/s]	$\dot{M}$[N]
210675	89.4	88.50	585.7	2.558	1.52
210677	83.7	82.86	592.9	2.27	1.46
210678	88.6	87.71	524.5	2.25	1.22

In order to simulate the diesel sprays with the Σ-Y model, a 2D axisymmetric computational domain with 108 x 25 mm extent in the axial

and radial spray directions is used, without considering the nozzle geometry. The mesh is structured with non-uniform grid resolution that consists of cells with an expansion ratio of 1.01 and 1.06 in the axial and radial directions, respectively, i.e., a similar structure to the one used in Chapter 4. There are 10 cells along the orifice diameter, keeping an aspect ratio close to one in the near nozzle region, as depicted in Figure 6.1.

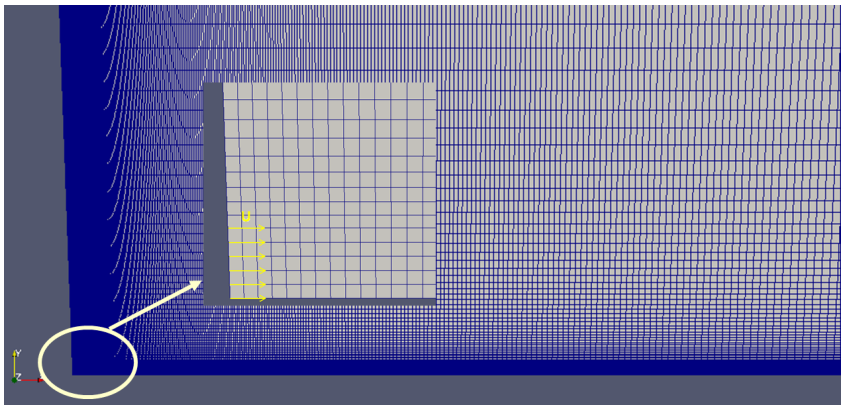

Figure 6.1. *Computational grid. The inset shows the mesh near the nozzle exit.*

In terms of numerical set-up, all the values from previous studies are kept constant (linear solvers, tolerances, Courant number and gradient, laplacian and divergence schemes). The inlet velocity boundary condition is obtained from mass flow rate and momentum flux measurements [8], applying a constant radial profile (top-hat) of axial velocity and density at nozzle outlet. Conclusions from last chapter indicate that this configuration is suitable for such studies. Moreover, regarding the turbulence model, the HDR k-ε model is used with the corrected value (1.60) for $C_{1\epsilon}$ [9], and turbulent intensity is set to 5% [10–13] while the turbulent integral length scale to 10% of nozzle diameter [14], i.e., as used in previous chapters as well as Prandtl and Schmidt numbers set to $S_c = P_r = 0.9$.

6.2 Inert vaporizing sprays – Spray A

In this section, the vaporization model is initially validated against measurements of liquid length, vapor penetration, local air/fuel ratio measurements and velocities. In these first studies, the nozzle serial 210677 is simulated under two operating conditions (baseline and ambient variation

study). In the second part of this section, the accuracy of model predictions for the different parametric studies is investigated by simulations using the corresponding characteristics for nozzle 210675. Due to different injector nozzles are used throughout this chapter, all the figures are presented in normalized coordinates by means of the equivalent diameter, defined in previous chapter, which takes the following values: 0.5 (nozzle 210675), 0.4681 (nozzle 210677) and 0.4955 (nozzle 210678).

6.2.1 Validation cases

In order to compare modeling predictions with measurements, note here that the computational spray vapor penetration and liquid length are calculated as defined by the Engine Combustion Network (ECN). The maximum distance from the nozzle outlet to where the fuel vapor mass fraction is 0.1% and the further distance along the injector axis having a liquid volume fraction higher than 0.1% [2], respectively.

Baseline Case

The validation of the vaporization model starts with the simulation of the baseline Spray A condition. However, before starting the quantitative analysis of inert vaporizing sprays, in Figure 6.2, the contours of liquid and vapor mass fractions, together with a contour of the evaporation source term are depicted. Paying some attention to the source term, on the right, it can be seen that the evaporation occurs within the liquid volume fraction isoline of 0.1% (criterion of liquid length). It should be noted that evaporation occurs when the source term takes positive values, while the negative ones correspond to regions where too much vapor has been generated in a previous time step and the model tends to correct them towards the equilibrium composition. The effect of the evaporation source term can be seen in the mass fraction contours. First on the liquid, which takes values quite close to zero in the region where the source term is positive. Then, this liquid mass is transferred to the vapor field, which reaches its maximum in the vicinity of the liquid limit region (black isoline).

Quantitatively, in Figure 6.3 at the top, spray vapor penetration and liquid length evolution are shown while at the bottom, an analysis of the spray vapor contours compared with the ones obtained from Rayleigh measurements is made. Overall, good agreement is depicted. In terms of spray penetration, model predictions seem to fall within the experimental uncertainty of measured values but in the case of liquid length, modeling values are slightly underpredicted.

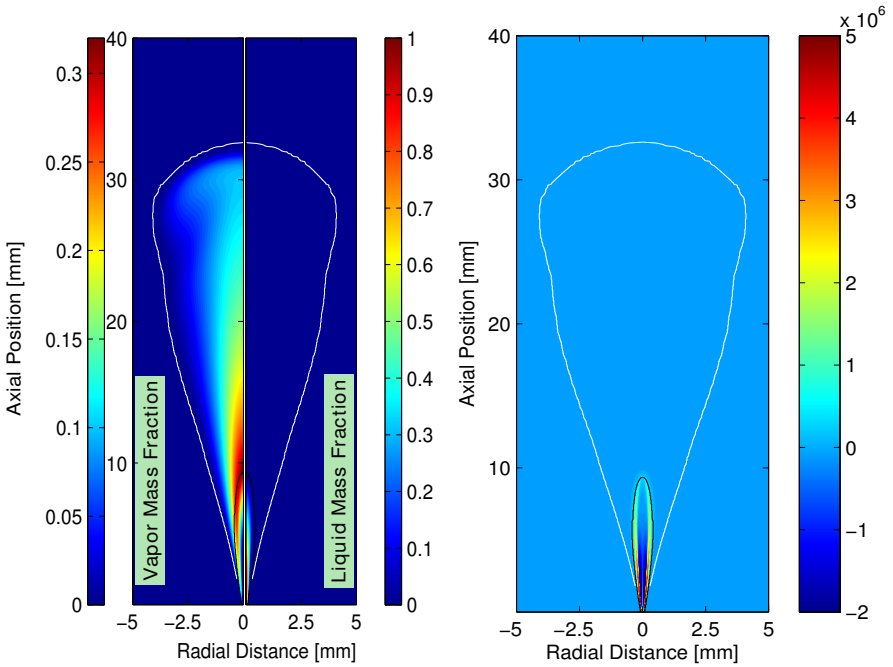

(a) Computed contours of liquid and vapor mass fractions

(b) Computed contour of evaporation source term

Figure 6.2. *Contours of liquid and vapor mass fractions and evaporation source term at 0.5 ms after SOI. Black line: liquid volume fraction isoline of* 0.1%. *White line: vapor mass fraction isoline of* 0.1%. *Injector 210677,* $P_{inj} = 150$ *MPa,* $T_{amb} = 900$ *K and* $\rho_{amb} = 22.8 kg/m^3$.

Regarding spray vapor contours, solid lines correspond to contours of 1% the on-axis mixture fraction value, while dashed lines show the stoichiometric iso-surface (considering an ambient with 21% of O2 in molar basis). It must be noted that, Rayleigh data are only available in an interval between 20 *mm* (42 d_{eq}) and 50 *mm* (106 d_{eq}). Initially, model predictions are in good agreement with the measurements, but from 75 d_{eq} downstream they progressively become slightly narrower. In spite of these slight differences, the spray radius predicted by the model is remarkably close to the experimental data. On the other hand, in terms of stoichiometric iso-surface a similar trend is depicted, they are slightly narrower compared to the experimental measurements with increasing axial distance.

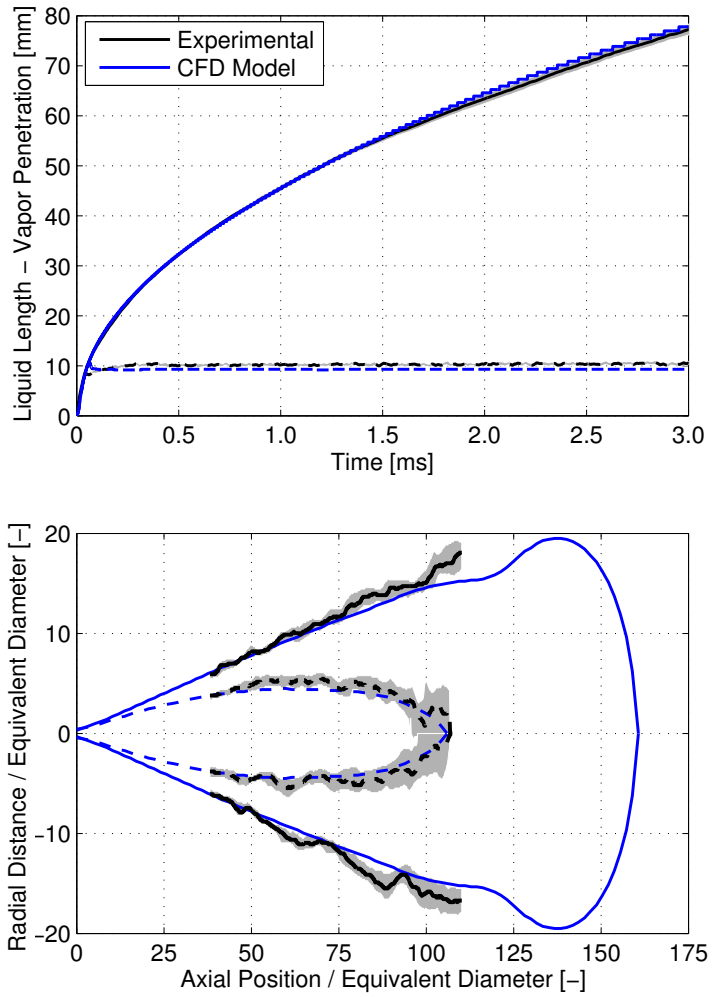

Figure 6.3. *Computed and measured liquid and vapor penetration [top] and contours of vapor region at 2.8 ms after SOI [bottom]. Injector 210677,* $P_{inj} = 150$ *MPa,* $T_{amb} = 900$ *K and* $\rho_{amb} = 22.8 kg/m^3$.

Although good agreement is achieved by the model, a more detailed investigation is made by quantification of the air/fuel ratio predictions. Rayleigh data are also used to compare predicted vs measured values of mixture fraction, as shown in Figure 6.4. Predicted values on the axis, Figure 6.4 (left), always fall within the confidence interval. Regarding radial dispersion of mixture fraction, results have been plotted in normalized coordinates (i.e. X-axis is the radial divided by the axial coordinates, while

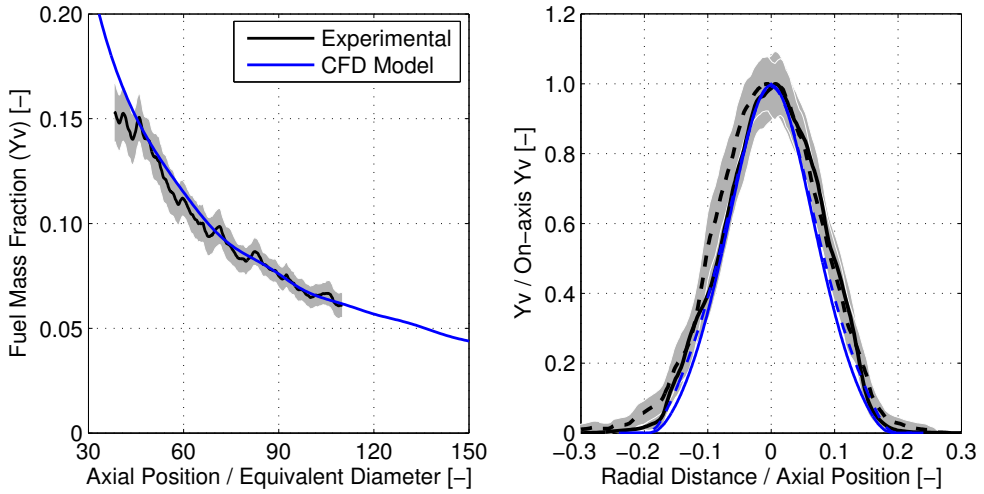

Figure 6.4. *Computed and measured centerline mixture fraction [left] and mixture fraction radial profiles normalized at* 50 d_{eq} *(solid line) and* 90 d_{eq} *(dashed line) [right] at 2.8 ms after SOI: Injector 210677,* P_{inj} = 150 *MPa,* T_{amb} = 900 *K and* $\rho_{amb} = 22.8kg/m^3$.

the Y-axis is the local mixture fraction divided by the on-axis one). The shape of the profiles is adequately predicted, as shown in Figure 6.4 (right). There is a slight bias towards narrower radial profiles in the calculation compared to the experimental ones at both axial locations, which is essentially coherent with the lowest radial dispersion observed in the spray vapor contours.

It is interesting to consider that the axial value is well reproduced while the radial profiles are slightly narrower compared to measurements, even using a turbulent Schmidt number of $S_c = 0.9$. This means that the mass fraction profiles are wider in comparison with velocity ones. Considering flow conservation, although CFD model can have been calibrated in order to computed wider mass fraction profiles, it would provide a lower on-axis value. As a result, it seems that with the present model predictions cannot be highly improved.

Finally, for the baseline case, an analysis of local axial component of the velocity vector is shown in Figure. 6.5. As in the case of mixture fraction profiles, a comparison on the axis, Figure 6.5 (left), and for radial profiles at 50 d_{eq} and 90 d_{eq}, Figure 6.5 (right), is made. In this case, as previously introduced, a normalization should be conducted in order to make a fair comparison between measurements (nozzle 210678) and CFD modeling (nozzle

210677). This is made by means of the axial velocities reached at the nozzle exit (see Table 6.5), which leads to the normalized axial velocity (Unorm = U/Uo), and the equivalent diameter for the axial position (xnorm = x/deq).

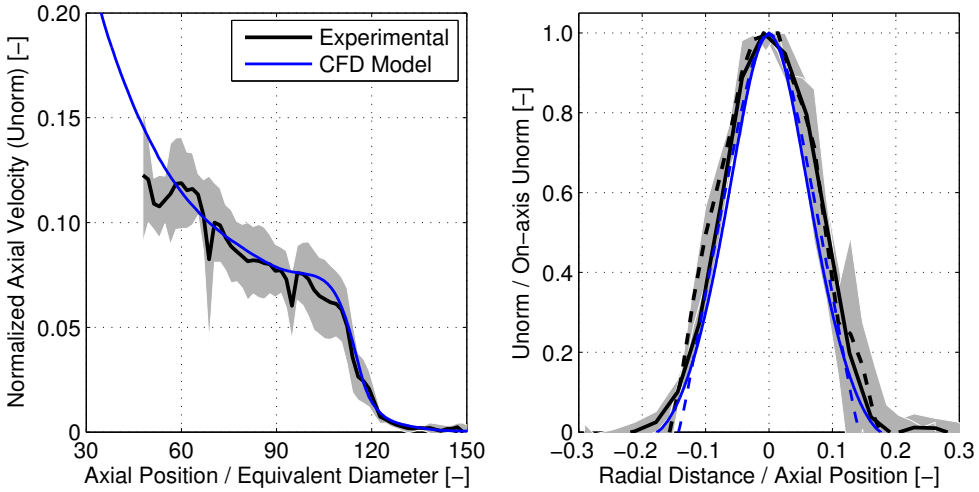

Figure 6.5. *Computed and measured centerline axial velocity normalized [left] and axial velocity radial profiles normalized at* 50 d_{eq} *(solid line) and* 90 d_{eq} *(dashed line) [right] at 1.5 ms after SOI:* P_{inj} = 150 *MPa,* T_{amb} = 900 *K and* ρ_{amb} = 22.8kg/m^3.

Thus, predicted velocity values on the axis show great agreement with measurements, being nearly all the time within the experimental data. In terms of radial profiles, the shape of them is adequately captured. As in the case of mixture fraction, computed profiles are slightly narrower. But in this case, at 90 d_{eq} this behaviour is more noticeable, probably as a result of being too close to the transient tip of the spray. Conversely, in terms of peak value, while at 50 d_{eq} model overpredict the measurement, it produces at 90 d_{eq} an almost identical result to experimental data. Nonetheless, Σ-Y predictions are in good agreement with experimental measurements, showing a maximum error of around 20% located where the axial experimental velocity presents noise values. Thus, considering all these results, the overall performance of the model is quite remarkable.

Ambient Conditions Variation

Apart from the baseline Spray A condition, an additional operating condition (P_{inj}=150MPa, T_{amb}=1100K and ρ_{amb}=15.2kg/m^3) in which

ambient conditions are modified is selected to evaluate the performance of the model. This study is selected to evaluate the modeling performance under low density conditions, but increasing ambient temperature to keep constant the liquid length. As in the nominal condition, a complete range of experimental data is also available with the exception of velocity profiles.

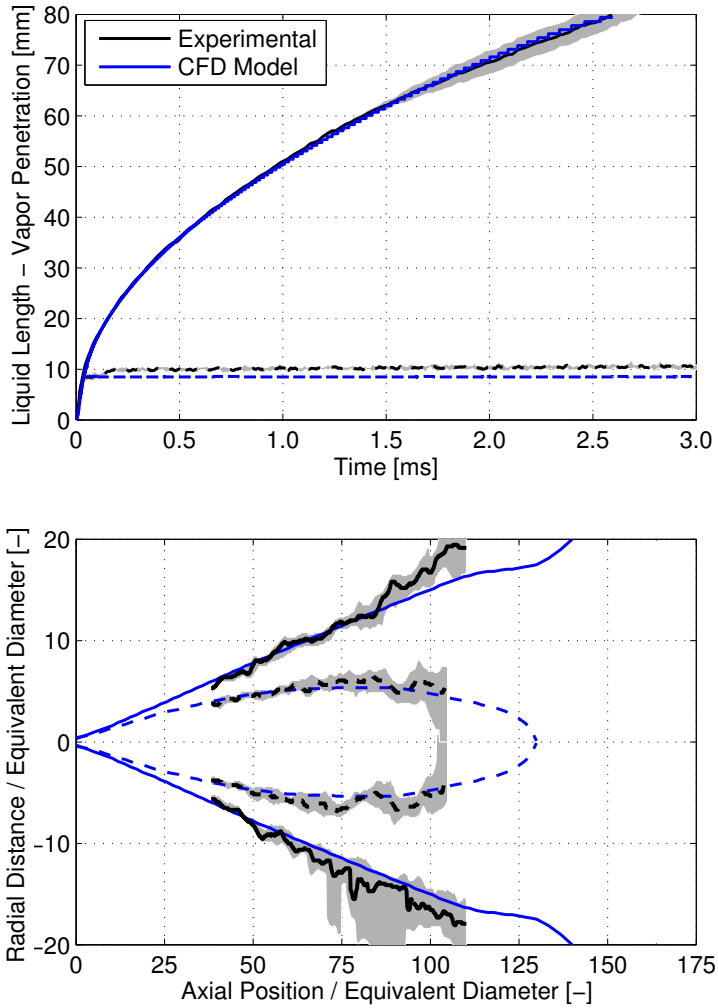

Figure 6.6. *Computed and measured liquid and vapor penetration [top] and contours of vapor region at 2.8 ms after SOI [bottom]. Injector 210677,* $P_{inj} = 150$ *MPa,* $T_{amb} = 1100$ *K and* $\rho_{amb} = 15.2 kg/m^3$.

Results shown in Figure 6.6 (top) depict good agreement in terms of vapor penetration. Model predictions are within the experimental uncertainty of measured values in an overall view. However, the predicted liquid penetration is clearly underestimated in this operating point. In the same way as in the reference case, the measured spray vapor contours are studied, as shown in Figure 6.6 (bottom). From the spray origin up to 75 d_{eq}, the computed radial contour is in good agreement and even slightly wider, in certain regions, in comparison with the measurements. But then, from 75 d_{eq} to 110 d_{eq}, Σ-Y model predictions become narrower. This behaviour, also noted in the nominal condition, could be explained because of a slightly less intense mixing rate than experiments due to less air entrainment [10]. Even though there are some differences, the predicted radial contour has a remarkable accuracy in similarity with experimental data. Moreover, taking into account the experimental iso-surface of stoichiometric equivalence ratio (considering an ambient with 21% of O2 in molar basis), i.e. dashed lines, the behaviour of CFD model is the same as in the baseline condition showing a similar performance to predicting spray contour. The radial width of the stoichiometric surface is reproduced adequately over most of the length however, the furthest axial location cannot be validated due to the absence of experimental data for $x \geqslant 50\ mm$.

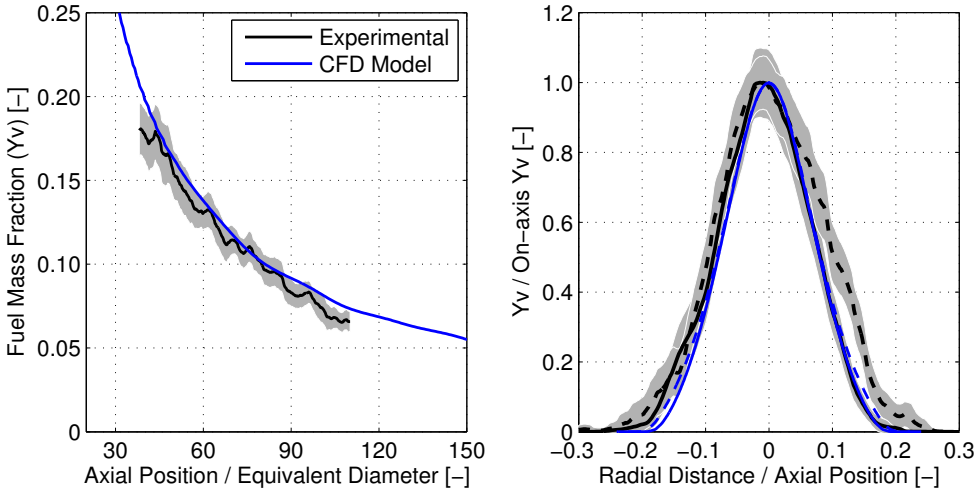

Figure 6.7. *Computed and measured centerline mixture fraction [left] and mixture fraction radial profiles normalized at* 50 d_{eq} *(solid line) and* 90 d_{eq} *(dashed line) [right] at 2.8 ms after SOI: Injector 210677,* $P_{inj} = 150\ MPa$, $T_{amb} = 1100\ K$ *and* $\rho_{amb} = 15.2 kg/m^3$.

Further experimental data are the mixture fraction profiles on the axis and the radial distribution. Predicted vs measured values of mixture fraction are shown in Figure 6.7. Predicted values on the axis, Figure 6.7 (left), fall within the confidence interval up to around 90 d_{eq}. However, from this axial position downstream, the predicted values are higher than measurements. Regarding radial distribution of mixture fraction, again plotted in normalized coordinates, the shape of the profiles is adequately predicted, as shown in Figure 6.7 (right). The results in this particular operation condition are very similar to the baseline case of the Spray A previously considered. Predicted profiles at both axial locations are really close to the experimental data in terms of peak value, while show a less radial dispersion.

6.2.2 Parametric studies

To conclude the evaluation of the Σ-Y Eulerian vaporizing model, a series of parametric studies with nozzle 210675 are conducted, Figure 6.8 to Figure 6.13. In these studies only spray vapor penetration and stabilized value of liquid length are compared against experimental measurements, as no more detailed measurements are available.

Spray vapor penetration and liquid length predictions for the parametric studies with different injection conditions have been summarized in Figure 6.8. Trends of decreasing vapor penetration with decreasing injection pressure are well captured by the model. In general, good agreement between calculations and experiments is obtained, with predicted results within experimental uncertainties. In terms of quasi-steady values of liquid length, model depicts good agreement with experimental measurements keeping almost invariable predictions regarding the injection pressure and depicting a maximum deviation of 5% with respect to the experiments for the lowest injection pressure.

A change in the injection pressure produces a variation in the momentum flux at the orifice and thus, it changes the velocity field (higher injection pressure leads to higher momentum and velocity), see Figure 6.9 where the axial profiles of velocity and mixture fraction together with vapor mass fraction are shown. Because of that, the spray penetrates faster for higher injection pressures, but the air entrainment also changes in such degree that the mixture fraction does not change, i.e. it causes exactly the same change in the overall fuel evaporation [15], see Figure 6.9 right. Thus, the liquid length prediction that is mixing controlled remains constant.

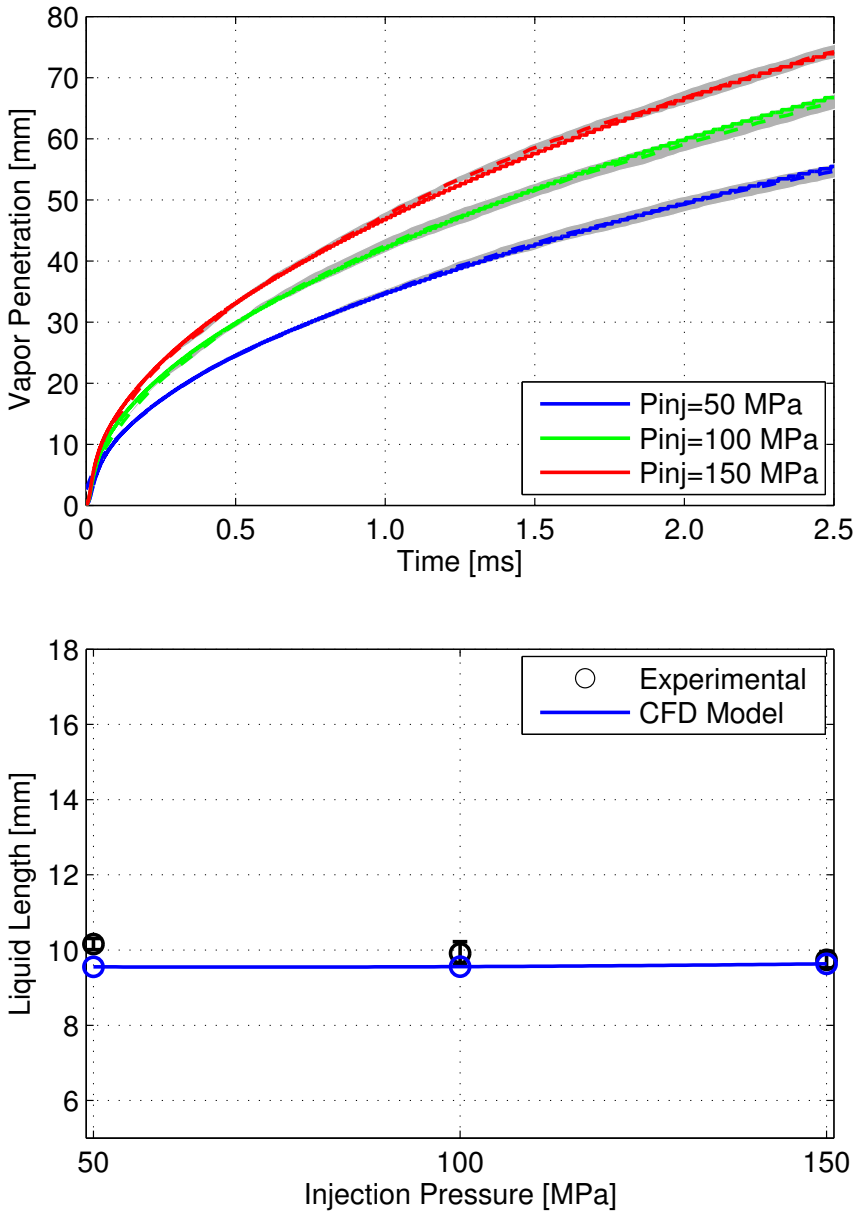

Figure 6.8. *Computed and measured spray tip penetration [top] and liquid length values [bottom] for different injection pressures. Injector 210675,* $\rho_{amb} = 22.8kg/m^3$ *and* $T_{amb} = 900\ K$.

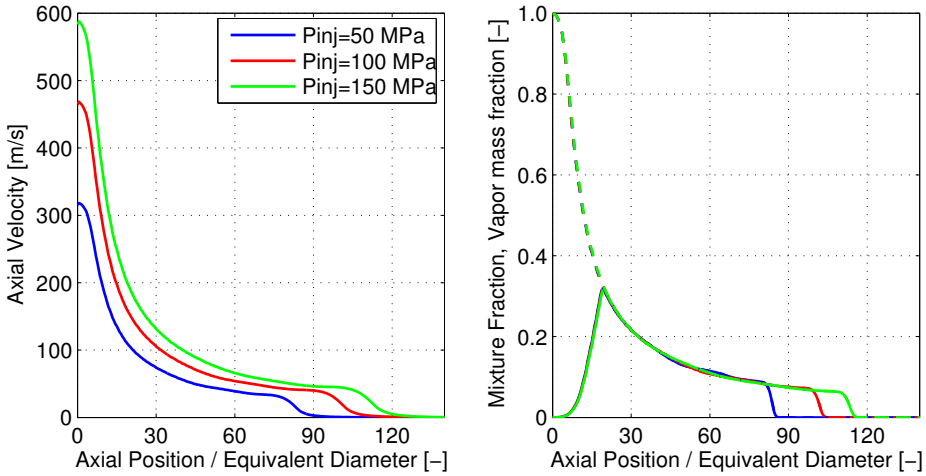

Figure 6.9. *Computed profiles of axial velocity [left] and vapor mass fraction (solid line) and mixture fraction (dashed line) [right] for different injection pressures at 1.5 ms after SOI. Injector 210675,* $\rho_{amb} = 22.8kg/m^3$ *and* $T_{amb} = 900\ K$.

Results for different ambient density conditions are depicted in Figure 6.10. Regarding spray vapor penetration, the model is capable of capturing the trends of increasing penetration when decreasing ambient density. Overall, predictions always fall within the confidence interval. On the other hand, the effects of ambient density on quasi-steady values of liquid length are also well predicted. However, a slight departure (the model underpredicts the measurement in around a 10% for lowest ambient density) appears as ambient gas density is decreased, which could be expected from the ambient conditions variation study of the validation cases. This confirms that the model is slightly less sensitive to density variations and presents more limitations at low density conditions, as it was previously seen in Chapter 4.

Modeling behaviour under different ambient density conditions can be also understand in terms of mixing. Density value affects mainly the amount of air entrained into the spray. When density is decreased, the entrainment also does and because of that the velocity rises, which makes that sprays injected under lower ambient density conditions penetrate faster. On the other hand, when the rate of entrainment is decreased, the amount of air needed for evaporating the fuel is reach further downstream, which leads to longer liquid lengths, i.e. mixture fraction decreases slowly causing delayed evaporation. On Figure 6.11, please note that results are presented in normalized axial coordinate, which normalizes the different entrainments, with the following

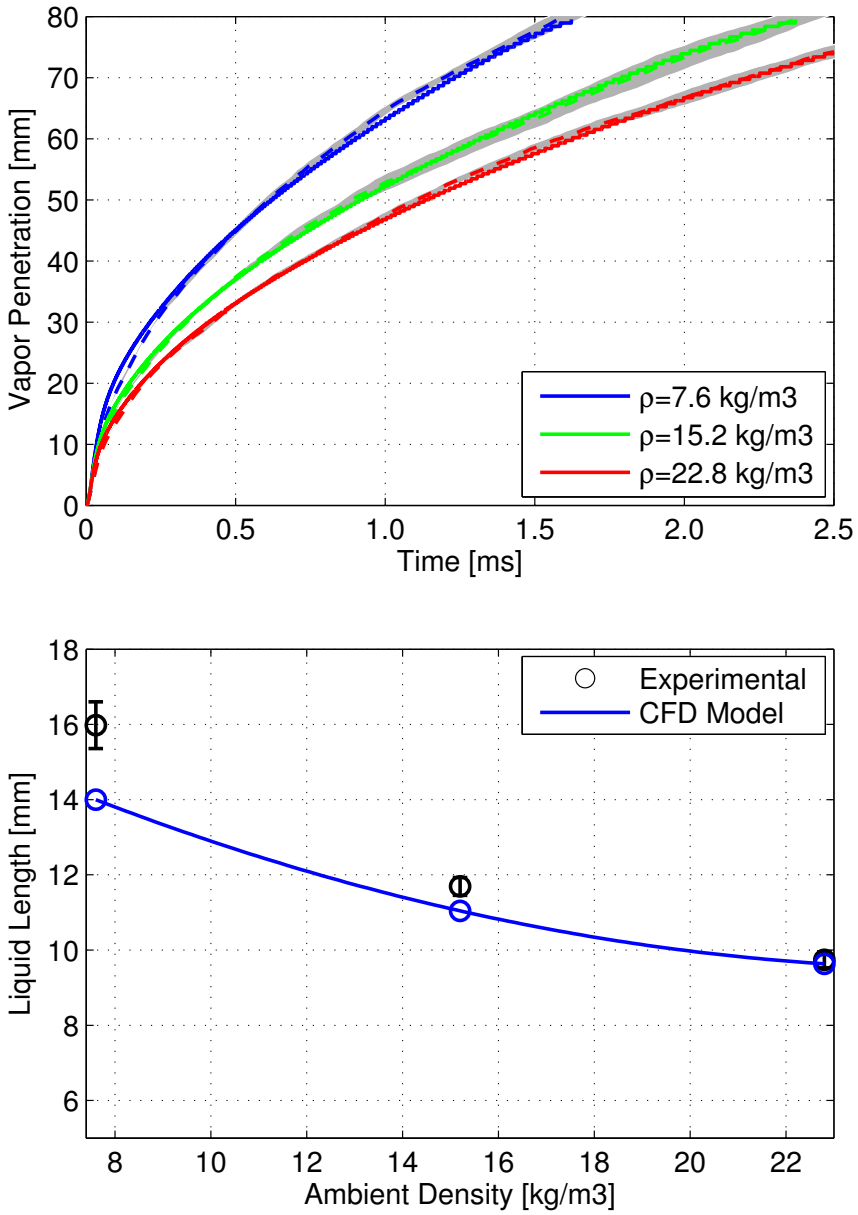

Figure 6.10. *Computed and measured spray tip penetration [top] and liquid length values [bottom] for different conditions of ambient density. Injector 210675,* P_{inj} = 150 *MPa and* T_{amb} = 900 *K.*

values for the equivalent diameter: 0.5 ($\rho_{amb} = 22.8kg/m^3$), 0.612 ($\rho_{amb} = 15.2kg/m^3$) and 0.866 ($\rho_{amb} = 7.6kg/m^3$).

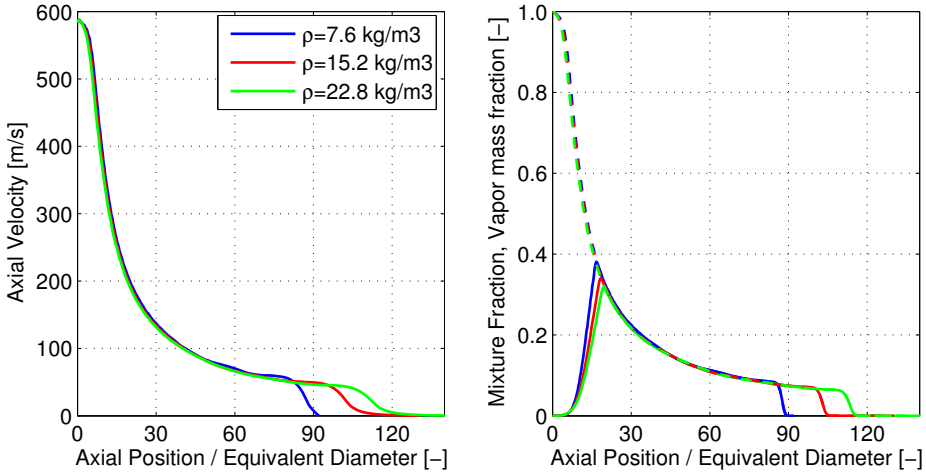

Figure 6.11. *Computed profiles of axial velocity [left] and vapor mass fraction (solid line) and mixture fraction (dashed line) [right] for different conditions of ambient density at 1.5 ms after SOI. Injector 210675,* $P_{inj} = 150$ *MPa and* $T_{amb} = 900$ *K.*

Finally, Figure 6.12 shows the ambient temperature studies. In this case, vapor penetration predictions, shown at the top, present no departure in results among the different operating conditions evaluated, as expected and depicted in Figure 6.12 (top) as it is controlled by the in nozzle momentum flux. On the other hand, effects of ambient temperature on quasi-steady values of liquid length are also well predicted, showing a maximum deviation with respect to the experimental measurements below 5%.

In this case, a change in ambient temperature does not modify the rate of entrainment. This explains the almost equal spray tip penetration and axial velocity among different temperatures (Figure 6.13). However, the entrained higher temperature ambient gas contains more energy and heats the liquid fuel to a higher temperature. The result is an overall increase in the vaporization rate and a shortening of the length of spray required to entrain enough hot gas to vaporize the fuel. [15], i.e. shortening liquid length. The overall agreement confirms that evaporation model hypothesis (vaporization controlled by air entrainment into the spray) are valid over a wide range of operating conditions of current diesel engines.

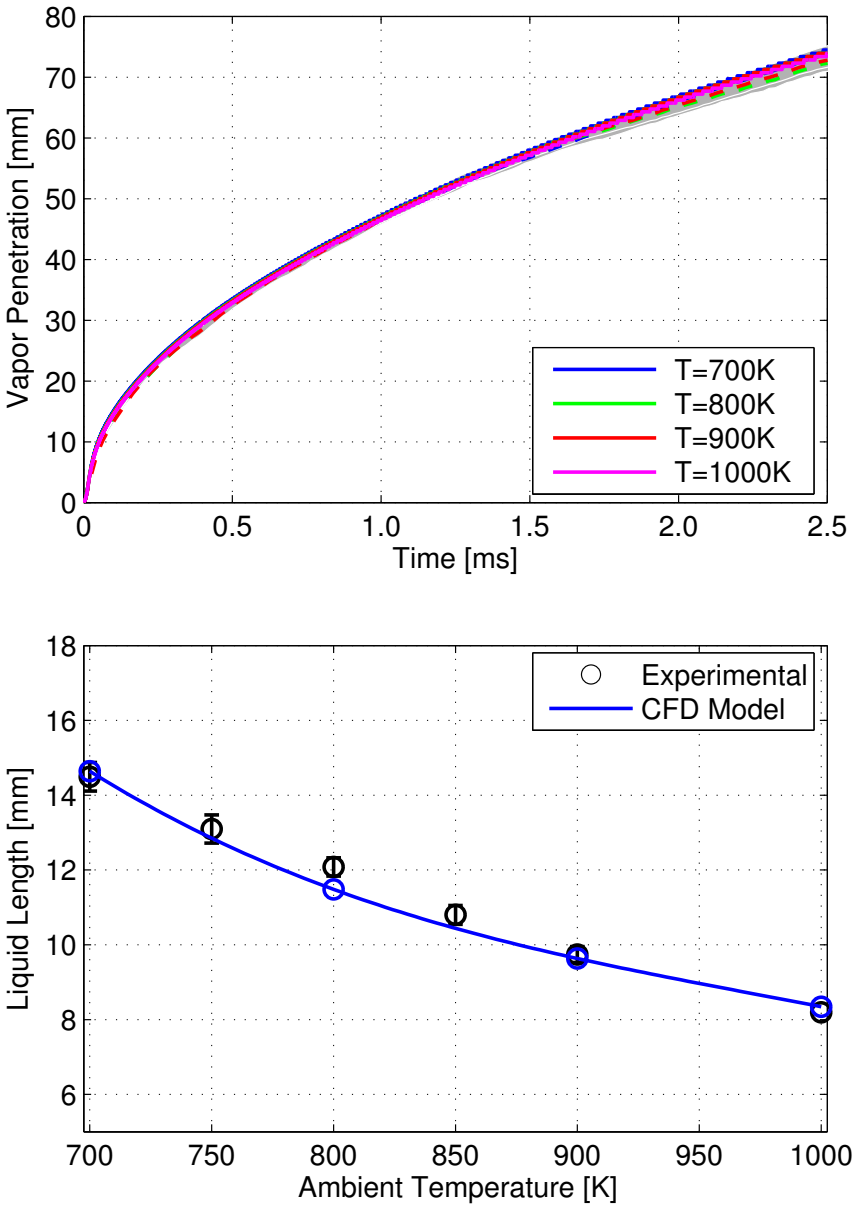

Figure 6.12. *Computed and measured spray tip penetration [top] and liquid length values [bottom] for different conditions of ambient temperature. Injector 210675,* $P_{inj} = 150$ *MPa and* $\rho_{amb} = 22.8 kg/m^3$.

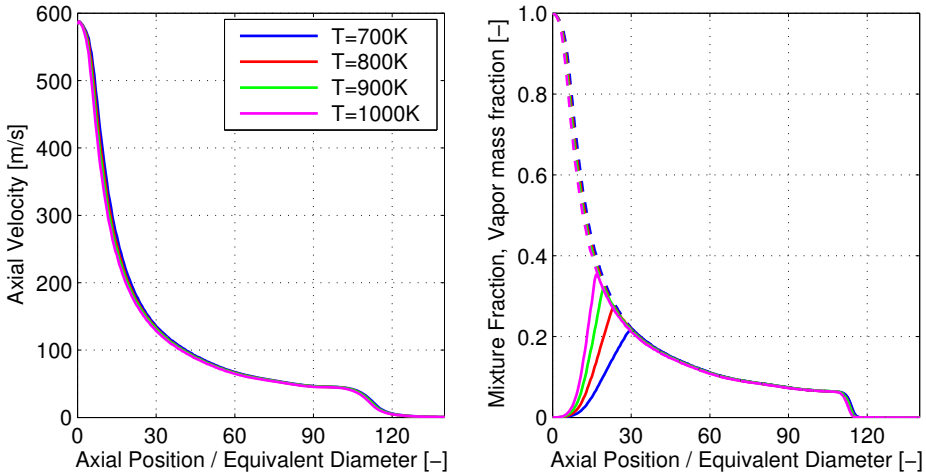

Figure 6.13. *Computed profiles of axial velocity [left] and vapor mass fraction (solid line) and mixture fraction (dashed line) [right] for different conditions of ambient temperature at 1.5 ms after SOI. Injector 210675,* $P_{inj} = 150$ *MPa and* $\rho_{amb} = 22.8kg/m^3$.

6.3 Vaporizing/non-vaporizing sprays comparison

Once the evaporation model is validated, computations have been performed to compare the behaviour of vaporizing and non-vaporizing sprays using the injector nozzle 210675. Thus, the spray A nominal conditions for vaporizing and non-vaporizing sprays are simulated, i.e. injection pressure $P_{inj} = 150$ MPa, ambient density $\rho_{amb} = 22.8kg/m^3$ and ambient temperatures of $T_{amb} = 900$ K and $T_{amb} = 303$ K, respectively.

In Figure 6.14 (left), a comparison of the spray tip penetration as a function of time for the vaporizing and non-vaporizing sprays is made. In the case of the evaporative ambient conditions, the liquid length evolution is also shown. In view of the results, it is depicted that two identical sprays penetrate differently depending on the temperature of the ambient gas in the discharge chamber. Non-vaporizing spray penetrates faster, with a maximum deviation of 5% with respect to a vaporizing spray. It is important to note the independence of these results to the flux at the nozzle orifice exit, due to it is exactly the same as well as the ambient density, imposed by the operating condition. As a result, it can be concluded that the physic state of the fluid (liquid or gas) influences spray development, as observed in experiments [16, 17]. Local density in the case of non-vaporizing spray is lower and because of that, it penetrates

faster. At vaporizing conditions, a cooling process of entrained hot gases by fuel evaporation occurs [16], which leads to higher local density with respect to the isothermal spray. Another important observation is the fact that both curves start to diverge at the axial position of 10 mm, i.e. when liquid length is reached. This evidences the different development of an isothermal spray, in which a two-phase flow is always present, against the vaporizing one, in which after the liquid is evaporated only gas flow exits.

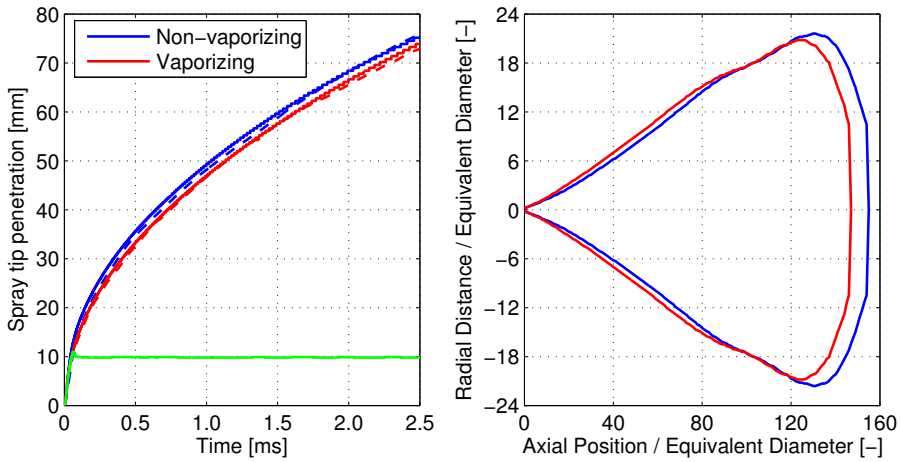

Figure 6.14. *Computed (solid line) and measured (dashed line) spray tip penetration and liquid length [left] and spray contour [right] at 2.5 ms after SOI for vaporizing and non-vaporizing sprays: Injector 210675,* $P_{inj} = 150$ *MPa and* $\rho_{amb} = 22.8 kg/m^3$.

Additionally, in Figure 6.14 (right), the spray contour comparison is made according to a spray radial limit defined as the 1% of the on-axis mixture fraction value. The figure depicts a wider vaporizing spray in comparison with the non-vaporizing one, in accordance with the spray tip penetration. Both penetration and spreading angle are closely related to air entrainment and mixing and thus, in Figure 6.15 (left), an analysis of the air entrainment process is made in terms of the total to initial mass flux ratio ($\dot{m}/\dot{m}_0$), in a similar way as used in Chapter 4. Entrainment plot shows that the isothermal spray depicts a significantly lower entrainment, which explains the higher penetration reached and the narrower spray contour. It seems that vaporizing sprays exchange momentum with the surrounding air in a noticeable faster way which results in higher entrainment, as a result of quite similar densities between vapor fuel and ambient gas. On the contrary, the high density liquid spray (isothermal), due to the the high density ratio, mixes slowly.

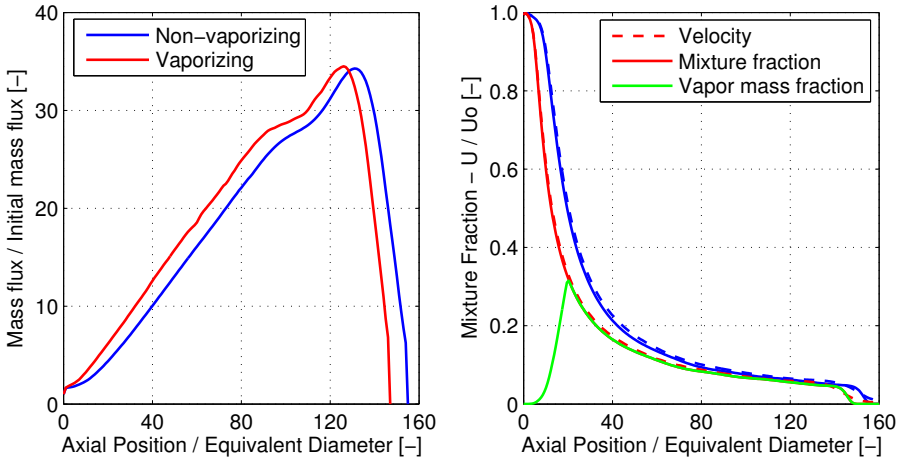

Figure 6.15. *Computed air entrainment normalized [left] and axial mixture fraction (solid line) and velocity (dashed line) profiles [right] at 2.5 ms after SOI for vaporizing and non-vaporizing sprays: Injector 210675,* $P_{inj} = 150$ *MPa and* $\rho_{amb} = 22.8 kg/m^3$.

Finally, the discussion can be also considered in terms of mixture fraction profiles as well as velocity normalized with the orifice exit velocity (U/U_0). In Figure 6.15 (right), the axial profiles of both fields are considered together with the axial vapor mass fraction profile of the vaporizing spray. All previous observations are confirmed with mixture fraction results. Non-evaporative sprays are more fuel rich, mix slowly, due to not as fast momentum transfer inducing lower entrainment rate of the ambient gas. Considering flow conservation, it is clear that this result leads to wider radial mixture fraction profiles in the case of vaporizing spray in accordance with the spray contours already shown. Finally, it can be noted the slightly higher value of the velocity profile with respect to the mixture fraction one due to the turbulent Schmidt number $S_c = 0.9$ used, which provides, as previously commented, more radial dispersion in terms of mixture fraction in comparison with velocity.

6.4 Reactive spray – Spray A

A first application of the coupled Eulerian spray model and the combustion model is presented in this section. The previous results of the inert spray behaviour show a high quality spray modeling performance, which is the basis for reliable modeling of the combustion process. However, as seen in Chapter 3, the mixture fraction variance is a key parameter for the combustion model and

as a result, its correct prediction should be investigated. Then, the results of the inert spray mixture fraction variance are presented for different values of the modeling parameter C_χ and the baseline Spray A condition (nozzle 210677).

6.4.1 Set-Up – Inert spray variance distribution

The variance of the mixture fraction is depicted along the symmetry axis (left) and at two axial positions, 50 d_{eq} and 90 d_{eq}, showing the radial distribution (right) for different values of C_χ constant in Figure 6.16. Overall a similar trend can be observed as for the "Spray H" spray condition, which uses n-heptane as fuel, shown in Winklinger PhD Thesis [18]. An increase of C_χ parameter leads to a decrease of the variance. Concentrating at first on the axial profiles, a special attention is paid to the region closer to the injector, since expected lift-off lengths lay around this distance ($\simeq 20\ mm$).

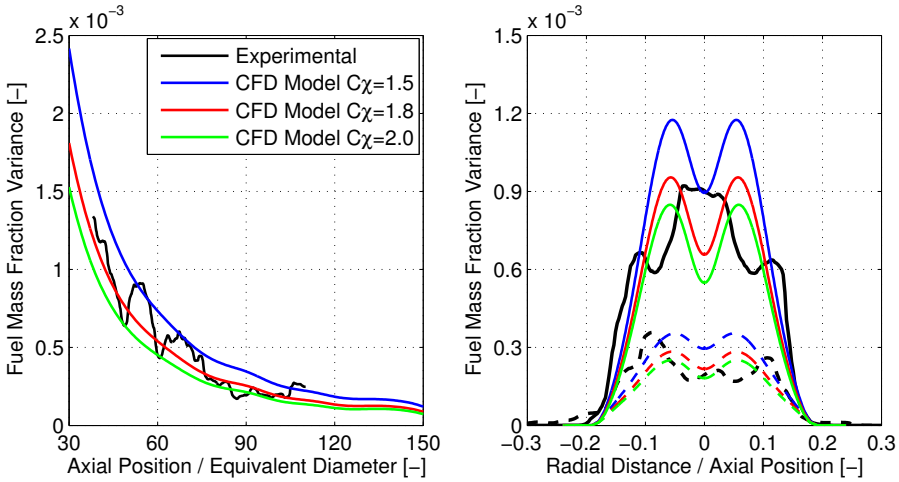

Figure 6.16. *Computed and measured centerline mixture fraction variance [left] and mixture fraction variance radial profiles at* 50 d_{eq} *(solid line) and* 90 d_{eq} *(dashed line) [right] at 2.8 ms after SOI: Injector 210677,* $P_{inj} = 150\ MPa$, $T_{amb} = 900\ K$ *and* $\rho_{amb} = 22.8 kg/m^3$.

In view of the results, a value of $C_\chi = 1.8$ seems to be a reasonable value to accurately model the region closer to the injector but additionally, good compromise is achieved overall. In terms of radial profiles, first a different profile shape is provided by simulations compared to measurements. Then, measured profiles show a slight asymmetry, whereas the calculated profiles

are perfectly symmetric due to the applied assumption of axial symmetry. Considering its limitations of shape, lower value of the parameter leads to higher levels of variance, specially at the first axial location, while the higher value slightly underpredicts the results for both width and peak value. In the end, it is a matter of reaching a good compromise and one can observe generally reasonable agreement of the calculated distribution with experimental data for the value of $C_\chi = 1.8$. Concluding, the mean mixture fraction (previously investigated) and its variance are predicted with reasonable accuracy. The setup of the spray modeling can therefore be considered well adjusted and suitable for its subsequent use in the modeling of the reactive sprays.

6.4.2 Reactive spray evaluation

Although the analysis of the reacting simulation is focused on flow characteristics (highly influenced by the spray model), global properties of the flame, i.e. the ignition delay and the lift-off length are also evaluated. Thus, the mean temperature distribution of the igniting flame is plotted during the autoignition sequence in Figure 6.17. It can be seen the autoignition process located at the tip of the spray, really close to the stoichiometric isoline towards regions slightly richer. As a result, the spatial behaviour of the ignition process is well reproduced but also the time evolution. No unique criteria for the evaluation of the ID exists, quite the contrary, many different definitions can be found in the literature (e.g. in [19]). However, in this work the proposed criteria of the ECN is employed for the evaluation of the ID, which corresponds to the time of maximum gradient in maximum temperature. The ID is predicted in the simulation in about 0.521 ms against the experimental measurement of 0.435 ms, denoting a quite remarkable performance.

Lastly, the flame structure at quasi-steady state is investigated in the following. The quasi-steady state is here defined by means of a temporally constant lift-off length. As for the ID, different criteria for the evaluation of the lift-off length (LOL) exits and, in this case, are employed. The lift-off is then the shortest axial distance between the injector tip and a certain threshold value in the flame domain defined as (1) 2% of the maximum of the mean mass fraction of OH in the flame, (2) an OH mean mass fraction of $1 \cdot 10^{-4}$, and (3) a mean temperature of $T_{amb} + 400K$, in a similar way as in [18].

The mean temperature distribution at quasi-steady state is shown in Figure 6.18, together with the experimental LOL (white line) and the predicted values by the three different criteria (symbols). Predictions by criteria (2)

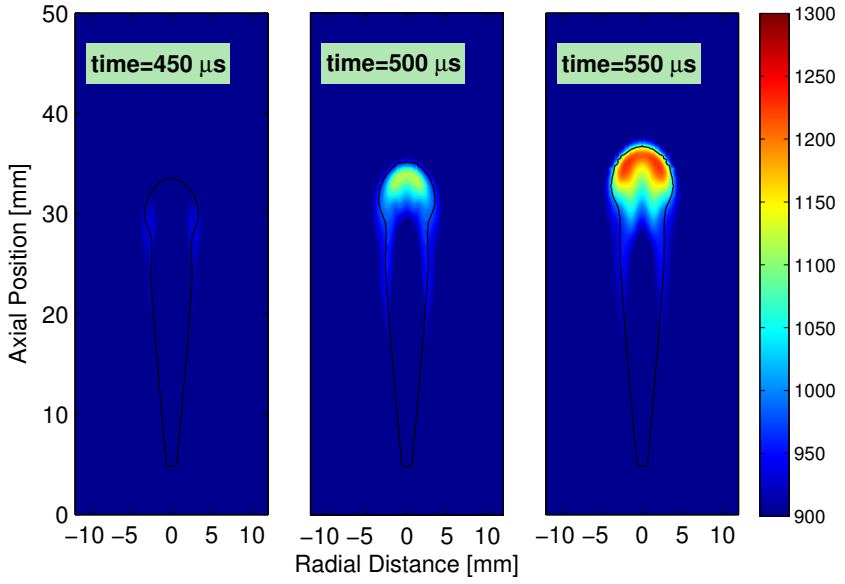

Figure 6.17. *Mean temperature contours during the autoignition sequence. Black line: stoichiometric isoline. Injector 210675,* $P_{inj} = 150$ *MPa,* $\rho_{amb} = 22.8 kg/m^3$ *and* $T_{amb} = 900$ *K.*

and (3) are in quite agreement with the measurement while a noticeable discrepancy is found for the first criterion. Here, it should be highlighted that at the spatial position predicted as the base of the stabilized flame, the temperature is only around $100K$ over the ambient temperature, which is a controversial value for comparison with combustion measurements of high-temperature chemiluminescence. Furthermore, the very strict and rigid criterion of a fixed value of OH mean mass fraction can be also a subject for discussion, especially when different ranges of oxygen ambient composition will be considered. As a result, the criterion involving the temperature seems to be very promising, though only after a complete parametric study of reacting conditions under different ambient temperature, density, oxygen composition and pressure injection could be confirmed.

After considering the global properties of the flame, the analysis of the reactive spray is focused on flow characteristics highly influenced by the inert spray evolution. Because of that, a comparison is made against the inert Spray A baseline condition results [6, 20]. Thus, in Figure 6.19 the first evaluation is made in terms of spray tip penetration defined, as already mentioned, as the maximum distance from the nozzle outlet to where the fuel mixture fraction

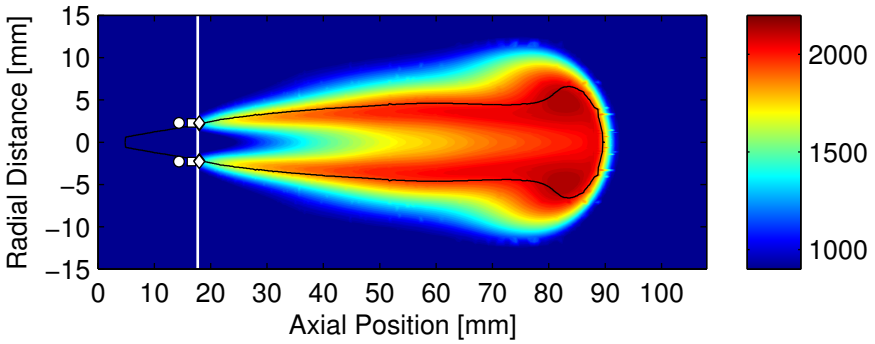

Figure 6.18. *Mean temperature contours at quasi-steady state. White line: experimental lift-off length. Circle: 2% of max. of* $\tilde{Y}_{OH}$ */ Square:* $\tilde{Y}_{OH} = 1 \cdot 10^{-4}$ */ Diamond:* $T_{amb} + 400K$*. Black line: stoichiometric isoline. Injector 210675,* $P_{inj} = 150$ *MPa,* $\rho_{amb} = 22.8kg/m^3$ *and* $T_{amb} = 900$ *K.*

is 0.1%. Both inert (blue) and reactive (red) spray penetration are depicted at the top of the figure, while at the bottom, the ratio between penetrations (i.e. reacting divided by inert penetration at each time step) is shown.

Inert spray vapor penetration is perfectly matched by the simulation, model predictions fall exactly on top of experimental measurements. However, in the case of reacting conditions, the trend is well captured and after the auto-ignition process the reacting spray penetration is enhanced, though in this case modeling values are slightly overpredicted. Then, to further analyze this behaviour, at the bottom plot the penetration ratio is depicted. It should be noted that for the experimental measurements at the non-reacting phase, there is a little deviation between inert and reacting penetration values and while the ratio should be essentially one, lower values are shown. This is due to the small penetration values reached in this initial part of the tip evolution, so that scattering between inert and reacting tests may result in a relatively important deviations of the ratio from one. The final decay is due to the spray penetration reaches the optical window access limit and no further distance could be measured.

Overall, CFD model predictions depict good agreement in spray penetration ratio and reproduce the general features of combustion on the flow [20]. First, the auto-ignition process, the stabilization phase (longer for CFD modeling results in comparison with the almost non-existent in measurements), the acceleration period where the penetration ratio starts increasing with time and finally, the quasi-steady phase in which the reacting

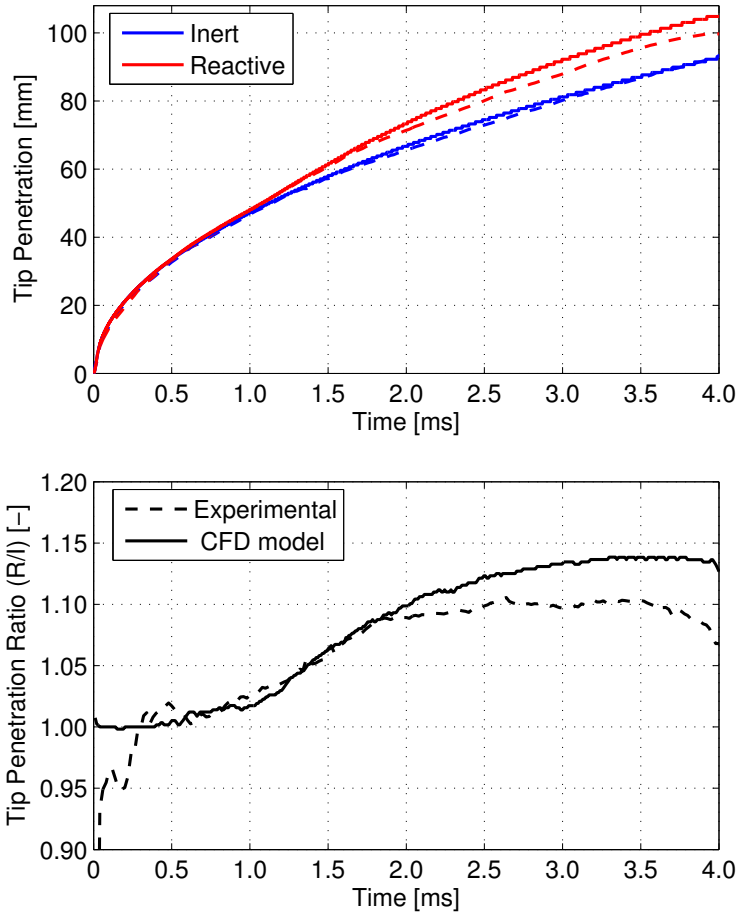

Figure 6.19. *Computed (solid line) and measured (dashed line) spray penetration for inert (blue) and reactive (red) conditions [top] and penetration ratio (reactive over inert) [bottom]. Injector 210675,* $P_{inj} = 150\ MPa$, $\rho_{amb} = 22.8 kg/m^3$ *and* $T_{amb} = 900\ K$.

spray penetration evolves with a similar slope as the inert one. However, the longer stabilization phase produces a slightly shifted evolution of combustion processes in terms of penetration.

Figure 6.20 shows the centerline axial velocity profiles at the top and the spray contours, which correspond to contours of 5% the on-axis velocity value, at the bottom. As in the case of the vaporizing validation studies, Section 6.2.1, a normalization should be conducted again in order to make a fair comparison between measurements (injector 210678) and CFD modeling

(injector 210675). To do that, velocity values are normalized by the axial velocities reached at the nozzle exit and the axial position with the equivalent diameter in each case, already used.

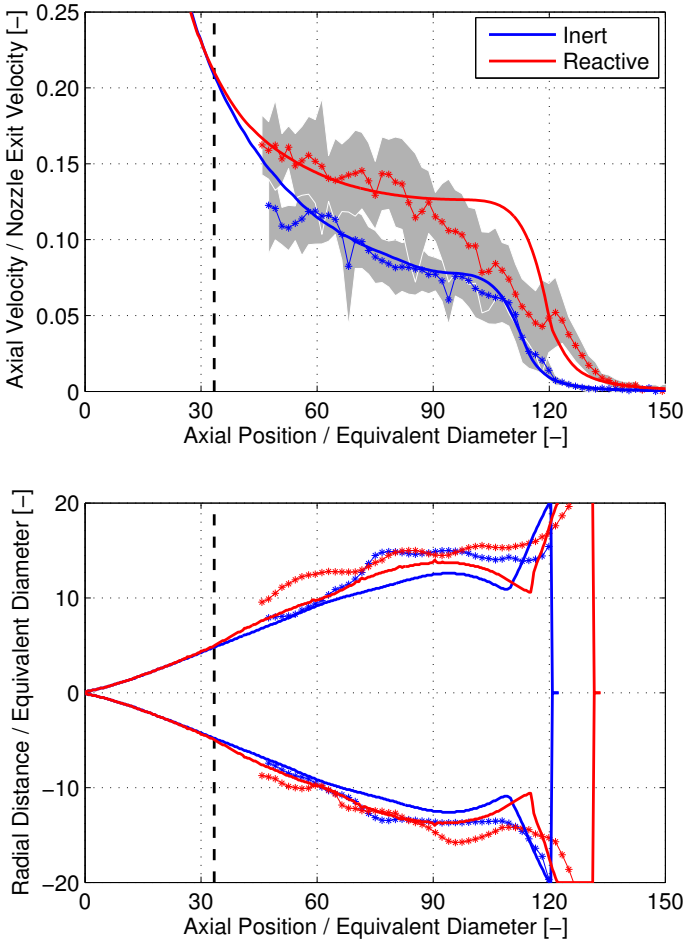

Figure 6.20. *Computed and measured centerline axial velocity normalized [top] and contours of spray from velocity [bottom] at 1.5 ms after SOI for inert (blue elements) and reactive (red elements) conditions, together with lift-off length position (dashed black line). Injector 210675,* $P_{inj} = 150$ *MPa,* $\rho_{amb} = 22.8 kg/m^3$ *and* $T_{amb} = 900$ *K.*

Predicted velocity values on the axis show good agreement with measurements, for both the inert and the reactive ambient conditions, being nearly all the time on top of the experimental measurements. CFD model reproduces perfectly the acceleration process in velocity, considering

momentum conservation, as ambient density drops the velocity value has to be increased. Moreover, it can be seen that this acceleration is experimented from the lift-off length (LoL) axial position downstream. The reacting acceleration of the flow is also related with the radial expansion of the spray, which can be seen in Figure 6.20 at the bottom. This radial dilation is more clearly depicted in the modeling behaviour due to the well defined profiles without vortex. But probably more important, the starting point at which this dilation begins is well predicted, just around the zone at which the flame LoL is located. In general, the limits of the spray are reasonably predicted by the eulerian model for both situations, denoting a quite remarkable performance.

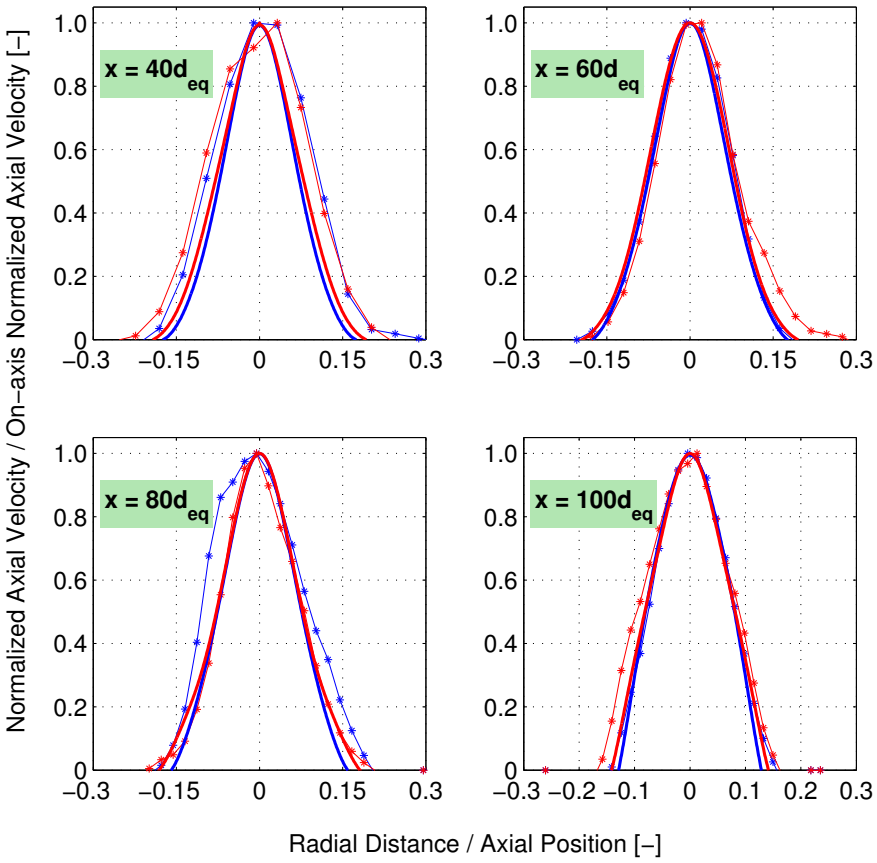

Figure 6.21. *Computed and measured velocity radial profiles normalized at $40d_{eq}$, $60d_{eq}$, $80d_{eq}$ and $100d_{eq}$ at 1.5 ms after SOI for inert (blue elements) and reactive (red elements) conditions. Injector 210675, $P_{inj} = 150$ MPa, $\rho_{amb} = 22.8kg/m^3$ and $T_{amb} = 900$ K.*

In order to complete the analysis, four velocity radial profiles at the axial positions of $40d_{eq}$, $60d_{eq}$, $80d_{eq}$ and $100d_{eq}$ are depicted in Figure 6.21. In general, the shape of them is adequately captured by model predictions, although computing slightly narrower profiles. Greatest discrepancies are shown at $40d_{eq}$ for both, inert and reacting conditions, depicting width errors of around 16% and 25% respectively.

Independently, results provided by the Eulerian coupled combustion model are quite good, which encourages its further application.

6.5 Conclusions

The Σ-Y Eulerian atomization model has been applied to the study of direct injection diesel sprays under vaporizing conditions. Calculations have been validated against spray test rig experiments for vaporizing sprays under different operating conditions. Spray tip penetration and liquid-phase lengths, as well as spatial distribution of axial velocity and fuel mass fraction have been used for validation. Additionally, a first evaluation of the coupled spray/combustion Eulerian model has been conducted and validated against measurements of penetration and spatial distribution of axial velocity.

This studies consider only the external flow and simulations have been conducted in a 2D axisymmetric computational domain with a similar structure to the one used in Chapter 4. Modeling numerical set-up have been kept constant, i.e. equal to the one established in previous chapters, and the conclusions reached for boundary inlet conditions in Chapter 5 have been used for the proper configuration of the present studies.

In first term, vaporization model has been validated under two different conditions of the so-called Spray A. The reference one and an ambient conditions variation, in which ambient density and temperature are changed. For these studies, predicted spray tip penetration and fuel mass fraction field are in good agreement with experimental data. Nevertheless, some small discrepancies (around 9%) are found for computed liquid-phase length, being more pronounced for the ambient variation case. Moreover, spatial distribution of axial velocity measurements are available for the baseline condition. Model predictions are quite close to the data for both, centerline and radial distribution, showing a remarkable overall performance. After the validation process, parametric studies have been performed including injection pressure, ambient density and ambient temperature variations. Spray vapor penetration and quasi-steady liquid length values are compared against

experimental data being in almost all conditions always within the uncertainty region of measurements. Only in the case of the lowest density, liquid length value is slightly underpredicted (around 10%), as can be expected from the validation case results.

Additionally, the comparison of sprays under non-vaporizing and vaporizing ambient conditions is conducted. The general behaviour is that isothermal sprays penetrate faster than vaporizing ones. This result is related with a wider vaporizing spray due to higher entrainment rate of ambient gas, as a result of quite similar densities between vapor fuel and surrounding air. The momentum exchange in the case of the isothermal spray is clearly slower and therefore, the spray is more fuel rich. Thus, it can be concluded that the physic state of the fluid (liquid or gas) influences spray modeling development, capturing the trends observed in experiments.

Finally, some preliminary investigations are conducted for reacting ambient conditions. The analysis is focused on flow variables and spray penetration as well as the comparison between inert and reacting conditions. Results depicted good agreement in terms of velocity profiles and an accurate spatial prediction of the dilatation spray process suffered under reacting conditions. In addition, the trends in reacting spray penetration are well predicted (though a small overprediction is reported) as well as reasonable predictions of global properties of the flame, i.e. the ignition delay and the lift-off length. In summary, spray reacting behaviour is well reproduced and promising results have been provided.

The overall consistency of the $\Sigma - Y$ modeling approach is confirmed by the validation studies. The model is applicable to ambient gas density conditions which are normally present in diesel engines, providing fairly good predictions to match with experimental data. At the sight of the initial evaluation, the coupled Σ-Y Eulerian atomization model with the UFPV combustion approach produces encouraging results which should be further investigated and lead to the development of the advanced turbulent spray combustion model.

Bibliography

[1] *Engine Combustion Network*. http://www.sandia.gov/ecn, accessed in August 2015.

[2] Bardi M., Payri R., Malbec L.M., Bruneaux G., Pickett L.M., Manin J., Bazyn T. and Genzale C. "ENGINE COMBUSTION NETWORK: Comparison of spray development, vaporization, and combustion in different combustion vessels". *Atomization and Sprays*, Vol. 22 n^o 10, pp. 807–842, 2012.

[3] Kastengren Alan L., Tilocco F. Zak, Powell Christopher F., Manin Julien, Pickett Lyle M., Payri Raul and Bazyn Tim. "Engine Combustion Network (ECN): measurements of nozzle geometry and hydraulic behavior". *Atomization and Sprays*, Vol. 22 n^o 12, pp. 1011–1052, 2012.

[4] Meijer M., Malbec L.M., Bruneaux G. and Somers L.M.T. "Engine Combustion Network: "Spray A" basic measurements and advanced diagnostics". *ICLASS Paper*, 2012.

[5] Pickett L.M., Manin J., Genzale C.L., Siebers D.L., Musculus M.P.B. and Idicheria C.A. "Relationship between diesel fues spray vapor penetration/dispersion and local fuel mixture fraction". *SAE Int. J. Engines*, Vol. 4, pp. 764–799, 2011.

[6] Payri Raul, García-Oliver Jose M., Xuan Tiemin and Bardi Michele. "A study on diesel spray tip penetration and radial expansion under reacting conditions". *Applied Thermal Engineering*, Vol. 90, pp. 619 – 629, 2015.

[7] Eagle W.E., Musculus M.P.B., Malbec L.M. and Bruneaux G. "Measuring transient entrainment rates of a condfined vaporizing diesel jet". *ILASS Paper*, 2014.

[8] Payri R., García-Oliver J.M., Salvador F.J. and Gimeno J. "Using spray momentum flux measurements to understand the influence of diesel nozzle geometry on spray characteristics". *Fuel*, Vol. 84 n^o 5, pp. 551 – 561, 2005.

[9] Pope S. B. *Turbulent Flows*. Cambridge University Press, 2000.

[10] Desantes J.M., García-Oliver J.M., Pastor J.M. and Pandal A. "A Comparison of Diesel Sprays CFD modelling approaches: DDM vs $\Sigma - Y$ Eulerian Atomization Model". *Atomization and Sprays*, Vol. 26 n^o 7, pp. 713–737, 2016.

[11] García-Oliver J.M., Pastor J.M., Pandal A., Trask N., Baldwin E. and Schmidt D.P. "Diesel Spray CFD Simulations based on the $\Sigma - Y$ Eulerian Atomization Model". *Atomization and Sprays*, Vol. 23, pp. 71–95, 2013.

[12] Lacaze Guilhem, Misdariis Antony, Ruiz Anthony and Oefelein Joseph C. "Analysis of high-pressure Diesel fuel injection processes using {LES} with real-fluid thermodynamics and transport". *Proceedings of the Combustion Institute*, Vol. 35 n^o 2, pp. 1603 – 1611, 2015.

[13] Ménard T., Tanguy S. and Berlemont A. "Coupling level set/VOF/ghost fluid methods: Validation and application to 3D simulation of the primary break-up of a liquid jet". *International Journal of Multiphase Flow*, Vol. 33 n^o 5, pp. 510 – 524, 2007.

[14] Sallam K. A. and Faeth G. M. "Surface Properties During Primary Breakup of Turbulent Liquid Jets in Still Air". *AIAA Journal*, Vol. 41 n^o 8, pp. 1514–1524, Agosto 2003.

[15] Siebers D. "Liquid-Phase Fuel Penetration in Diesel Sprays". *SAE Technical Paper*, n^o 980809, 1998.

[16] Naber J. and Siebers D. "Effects of Gas Density and Vaporization on Penetration and Dispersion of Diesel Sprays". *SAE Technical Paper*, n^o 960034, 1996.

[17] Manin J. *Analysis of mixing processes in liquid and vaporized sprays through LIF and Rayleigh Scattering measurements.* Doctoral Thesis, Departamento de Máquinas y Motores Térmicos, Universidad Politécnica de Valencia, España, 2011.

[18] Winklinger J.F. *Implementation of a Combustion Model based on the Flamelet Concept and its Application to turbulent reactive Sprays.* Doctoral Thesis, Departamento de Máquinas y Motores Térmicos, Universidad Politécnica de Valencia, España, 2014.

[19] Bajaj Chetan, Ameen Muhsin and Abraham John. "Evaluation of an Unsteady Flamelet Progress Variable Model for Autoignition and Flame Lift-Off in Diesel Jets". *Combustion Science and Technology*, Vol. 185 n^o 3, pp. 454–472, 2013.

[20] Desantes José M., Pastor José V., García-Oliver José M. and Briceño Francisco J. "An experimental analysis on the evolution of the transient tip penetration in reacting Diesel sprays". *Combustion and Flame*, Vol. 161 n^o 8, pp. 2137 – 2150, 2014.

Chapter 7

Conclusions and future work

Contents

7.1 Summary and conclusions

A fully compressible Eulerian single phase atomization and spray dispersion model was implemented in the CFD platform OpenFOAM in this work. The current implemented spray CFD model, constructed under the PISO algorithm, presents an appropriate physics description of the dense region of the diesel spray, where the hypothesis behind the traditional models used for spray modeling struggles due to the fact that it does not hold in this spray region. Additionally, this model offers other interesting features as the possibility of including nozzle effects by coupling internal and external flow simulations together in one continuous domain. This procedure avoids the issues derived from the methodology required to transfer all the spatial and temporal fields from an internal flow simulation to a primary break-up (blob) model. Thus, not only the Eulerian model developed in this PhD Thesis enables a better representation of reality, it also offers benefits for simulations accuracy.

An evaporation model has been implemented based on the Locally Homogeneous Flow (LHF) concept, i.e. local equilibrium exists both in thermal and dynamic conditions. This vaporization mechanism is developed

around the particular characteristics of the current engine technologies, which result in the physical processes of evaporation limited by fuel-air mixing rate in DI diesel sprays. Under the assumption of an adiabatic mixing, in the liquid/vapor region, the spray is supposed to have a trend towards adiabatic saturation conditions and the equilibrium between phases is determined by Raoult's ideal law. Together with evaporation, a thermodynamic model for the mixture enthalpy has been implemented, which accounts for liquid and vapour contributions using the respective specific heat capacities at constant pressure ($c_{p,i}$), evaluated as a function of temperature T. In case of the fuel, the polynomials could not be directly applied. The issue is solved, upon the principle of corresponding states, by the Rowlinson-Bondi equation that makes use of the departure heat capacity function to evaluate the liquid fuel specific heat capacity. Then, the vapor fuel phase is calculated by means of the enthalpy of vaporization ΔHv, which is sometimes referred to as the latent heat of vaporization.

Using this complete thermodynamics and a relatively advanced equation of state (HBT correlation), which accounts for the influence of both temperature and pressure, leads to a more precise description of vaporizing sprays being able to reproduce phenomena like quasi-steady liquid length. Such advanced features have enabled the coupling of the spray model with an advanced combustion model, which supposes a natural step in the simulation process of diesel sprays and provides a complete CFD tool able to simulate a diesel spray from inside the injector nozzle until combustion.

The behaviour of the spray model was first investigated in a basic external flow simulation of a free diesel spray under non-vaporizing conditions. This configuration is generated by means of a single-hole conical nozzle with the orifice oriented along the injector axis, which leads to an important simplification of the modeling effort and avoids cavitation (not considered in the present work). Moreover, a vast amount of data including typical spray macroscopic characteristics, namely penetration and cone angle, as well as spatial distribution of droplet size and velocity, enable a complete analysis of the capability of the model to simulate diesel sprays, both in global and local terms. After a definition of a proper modeling set-up (grid resolution, turbulence model and divergence numerical interpolation scheme), very good agreement with experimental data was obtained under medium and high ambient gas density conditions (ambient density higher than $25 kg/m^3$). However, for very low ambient gas density condition ($10 kg/m^3$, the agreement was not as good, suggesting some limitations due to more significant interfacial

dynamics and not fulfilled model assumptions (atomization regime). Finally, SMD model predictions showed correct trends and really promising results, but also indicated that a more detailed calibration process of the Σ equation constants should be conducted.

After the successful evaluation of Σ-Y Eulerian model for non-vaporizing sprays, the spray model is applied to more complex configurations, i.e. coupled internal/external flow and external vaporazing flow simulations, under inert and reacting conditions. In order to validate all these investigations, the best available database is used, which corresponds to the Engine Combustion Network (ECN). Thus, the "Spray A" configuration of ECN is selected. In first term, a study has been carried out to obtain the internal structure of a diesel spray in the near-field, including the effects of internal nozzle flow. In order to achieve this purpose, the non-vaporizing condition of the Spray A was used. Initially, a comparison between 3D and 2D coupled internal/external flow simulations was made, showing that 3D simulations captured measured flow asymmetries, although 2D simulations also provided accurate results with a huge reduction of the computational cost. As a result, a 2D computational domain was used for further investigations. After that, different turbulence model were evaluated regarding the accuracy of the flow simulation inside the nozzle. The three RANS turbulence models tested showed reasonably and similar performance in internal nozzle flow development, reproducing the value of the dimensionless nozzle flow coefficients fairly well, but only the HDR k-ε turbulence model makes fairly accurate predictions for external flow applications (including near nozzle region), as seen in Chapter 4 and it was definitively selected for all the subsequent calculations.

Additionally, the necessity of the nozzle-spray coupled simulations was explored, and therefore two studies in a domain without the nozzle geometry were run. In the first one, the nozzle boundary conditions were fed with the fields taken from the nozzle-spray coupled simulation and in the other one, a top-hat velocity profile, obtained from mass flow rate and momentum flux measurements was applied. This investigations reported a noticeable impact on the intact core length prediction and LVF profiles which vanished further downstream ($\geqslant$ 6 mm). This fact allows the use of the top-hat constant profile boundary condition in further spray applications, where evaporation and combustion are included, in order to reduce the computational cost. Finally, having the large scale of the flow correctly captured, an optimization of primary break-up modeling was conducted. By means of a DOE technique, known as Response Surface Method, values of modeling constants were

calibrated. A great improvement in modeling performance was achieved under different injection and back pressures conditions, proving the great overall effectiveness of the achieved configuration.

A final application of the CFD model to study direct injection diesel sprays under vaporizing conditions was conducted. First, the vaporization model was validated against spray test rig experiments, including spray tip penetration and liquid lengths, spatial distribution of axial velocity and fuel mass fraction, for vaporizing sprays under different operating conditions. After the validation process, parametric studies have been performed including injection pressure, ambient density and ambient temperature variations. In almost all conditions good agreement could be observed, though a small deviation in liquid length prediction was showed for low ambient density conditions. Then, a comparison of sprays injected in ambient and hot temperature conditions is conducted, showing significant difference on their development. Isothermal sprays penetrate faster than vaporizing ones due to lower air entrainment. Finally, taking advantage of the Spray A database, a simulation for reacting ambient nominal conditions was made. Model predictions were compared against spatial distribution of axial velocity and spray tip penetration pointing out the differences between an inert simulation and a reacting one. Accurate velocity profiles and spatial prediction of spray dilation process were reported together with correct trends in penetration, although quantitatively slightly overpredicted. Nonetheless, CFD model predictions depict good agreement and reproduce the general features of combustion on the flow.

Concluding, the overall performance of the model is quite remarkable. It is applicable to ambient gas density conditions that are normally present in diesel engines, providing a better description of the physic problem with a great deal of accuracy an overcoming typical spray modeling issues. Additionally, the successful coupled implementation together with a flamelet combustion model leads to a complete CFD Eulerian model, in-house developed, able to reproduce spray formation from inside the injector nozzle until combustion process takes place. However, the small limitations found for low ambient density conditions cannot be neglected. These make the model less prone to be used in highly premixed combustion strategies. Nevertheless, the obtained results surely encourage the further development of the Eulerian model both, independently from combustion and in the reacting version one. Some potential improvements are proposed in the following section.

7.2 Future work

Some suggestion for future work may be given according to the logical structure of the present research, from model implementation improvements and development point of view to application and assessment of diverse technical problems. In this sense, the first task that should be performed is the extension of reactive studies for the whole range of operating conditions available at the "Spray A" database, which include ambient temperature, density and composition (oxygen percentage) variations as well as injection pressure. These simulations complement the reactive CFD Eulerian model evaluation and validation presented here, providing an overall conclusion of its capabilities and limitations. Additionally, it should be noted that any further improvements in the computational performance of the combustion model itself can be directly imported to the Eulerian coupled solver.

Concerning the inert spray model, the necessity of development of the interphase surface density (Σ) to make it more predictable has been pointed out in the present work. This complex task should be made in a closed investigation in combination with measurements available by means of modern experimental techniques and with an increasingly use of DNS results, which for such a basic research are very valuable inputs. Another recent research line is the use of gasoline-diesel blends in diesel engines. Possibly, the most important advantage of these blends is the reduction of emissions and improvement of engine efficiency. As a result, adding the proper capabilities to the spray model to deal with multi-fuel blends could be an interesting feature to the present CFD model for further investigations on spray modeling of diesel engines. Moreover, the model could be also extended in terms of internal nozzle flow simulations. The inclusion of a cavitation model would be a logical topic for future work as well as needle movement simulation in order to properly simulate transients of the injection process.

On the other hand, an improvement in model thermodynamic seems to be possible. Replacing the actual approach for equation of state (ideal gas for gas and HBT correlation for liquid) with a cubic equation of state (e.g. Peng-Robinson) that can describe both the gaseous and liquid states with a simple equation capable of fast calculations is an interesting option to be explored. It can be used to predict phase-equilibrium properties, such as vapor pressure, heat of vaporization, etc. and achieves a great performance for mixtures containing hydrocarbons. As for the evaporation model, instead of using the ideal Raoult Law, a more complex, advanced and representative

of reality liquid-vapor equilibrium by means of fugacities of real substances could be used.

Additionally, the possible transfer of the model to a LES environment should be seriously considered in the mid-term. Improvements may be expected not only in issues with the relatively simple turbulence modeling of a RANS approach but also in the quality of predictions, especially unsteady combustion phenomena such as extinction and re-ignition. Fortunately, the actual mesh size used in RANS eulerian simulations is almost in the order needed for LES simulations and therefore no large increase in computational effort should be expected.

Finally, from the numerical point of view, the typical segregated implementation of model equations has revealed some numerical difficulties when the liquid mass transport equation is solved in a compressible context due to the fact that the solution of velocity and pressure (after solving density and liquid mass fraction) results in a combination of density, liquid mass fraction, and pressure that are often inconsistent with the equation of state. Because of that, it could be interesting to move away from the typical elliptic pressure equation that is at the core of many PISO-like implicit algorithms by introducing a density-based approach, which is well-suited to the highly compressible flow that accompanies diesel sprays and must accomplish exactly the equation of state. Moreover, following a standard Runge-Kutta explicit procedure would offer a formal sequence determining exactly when fields should be updated, which avoids the conundrums that are a consequence of segregated methods. The order of field updates within a substep is immaterial. An additional benefit of relying on a more explicit formulation is that parallel scalability should be excellent. The inter-processor communication required for solution of linear systems is greatly reduced. The time step will be smaller with an explicit scheme, but the cost per time step should be greatly reduced. As a result, it seems really attractive to explore the capabilities that should offer this new numerical implementation that resolves difficulties while maintaining consistency between hydrodynamic and thermodynamic variables, providing some improvements in accuracy and also offering benefits in stability and parallel scalability. With the inexorable march towards large, parallel computations and LES environments, the scalability is a key indicator of the future utility of these models.

Bibliography

-.
Regulation (EC) No 715/2007 of the European Parliament and of the Council of 20 June 2007 on type approval of motor vehicles with respect to emissions from light passenger and commercial vehicles (Euro 5 and Euro 6) and on access to vehicle repair and maintenance information and amending Regulations (EC) No 692/2008, (EC) No 595/2009, (EC) No 566/2011 and (EC) No 459/2012.
Official Journal of the European Union, 2007. (cited on p. 3)

-.
Regulation (EC) No 595/2009 of the European Parliament and of the Council of 18 June 2009 on type-approval of motor vehicles and engines with respect to emissions from heavy duty vehicles (Euro VI) and on access to vehicle repair and maintenance information and amending Regulation (EC) No 715/2007 and Directive 2007/46/EC and repealing Directives 80/1269/EC, 2005/55/EC and 2005/78/EC.
Official Journal of the European Union, 2009. (cited on p. 3)

Engine Combustion Network.
http://www.sandia.gov/ecn, accessed in August 2015. (cited on pp. 116, 117, 152, 153)

LVF data.
http://www.sandia.gov/ecn/argonne/assets/datafiles/mixture/rad675.php, accessed in August 2015. (cited on pp. 117, 132)

Abramovich G.N.
The theory of turbulent jets.
MIT Press. ISBN 0-262-01008-9, 1963. (cited on p. 33)

Adler D. and Lyn W-T.
The Evaporation and Mixing of a Liquid Fuel Spray in a Diesel Air Swirl.
Proceedings of the Institution of Mechanical Engineers, Conference Proceedings, Vol. 184 n^o 10, pp. 171–180, 1969. (cited on p. 33)

Araneo L. and Tropea C.
Improving Phase Doppler Measurements in a Diesel Spray.
SAE Technical Paper, n^o 970799, 2000. (cited on p. 102)

Arcoumanis C., Gavaises M. and French B.
Effect of Fuel Injection Processes on the Structure of Diesel Sprays.
SAE Technical Paper, n^o 970799, 1997. (cited on p. 23)

Arcoumanis C. and Kamimoto T.
Flow and Combustion in Reciprocating Engines.
Springer-Verlag, 2009. (cited on p. 25)

Arcoumanis C., Whitelaw J. and Wong K.
Gaseous Simulation of Diesel-Type Sprays in a Motored Engine.
SAE Technical Paper, n^o 890793, 1989. (cited on p. 27)

Arrègle J.
Análisis de la estructura y dinámica interna de chorros Diesel.
Doctoral Thesis, Departamento de Máquinas y Motores Térmicos, Universidad Politécnica de Valencia, España, 1998. (cited on pp. 21, 32)

Bajaj Chetan, Ameen Muhsin and Abraham John.
Evaluation of an Unsteady Flamelet Progress Variable Model for Autoignition and Flame Lift-Off in Diesel Jets.
Combustion Science and Technology, Vol. 185 n^o 3, pp. 454–472, 2013. (cited on p. 174)

Bardi M., Payri R., Malbec L.M., Bruneaux G., Pickett L.M., Manin J., Bazyn T. and Genzale C.
ENGINE COMBUSTION NETWORK: Comparison of spray development, vaporization, and combustion in different combustion vessels.
Atomization and Sprays, Vol. 22 n^o 10, pp. 807–842, 2012. (cited on pp. 31, 93, 153, 157)

Barroso G., Schneider B. and Boulouchos K.
An Extensive Parametric Study on Diesel Spray Simulation and Verification with Experimental Data.
SAE Technical Paper, 10 2003. (cited on p. 41)

Baumgarten C.
Mixture formation in internal combustion engines.
Springer, 2006. (cited on pp. 20, 24, 25)

Beau P.A., Funk M., Lebas R. and Demoulin F.X.
Applying Quasi-Multiphase Model to Simulate Atomization Processes in Diesel Engines: Modeling of the Slip Velocity.
SAE Technical Paper 2005-01-0220, 2005. (cited on pp. 53, 56, 100, 106, 110)

Beér J.M. and Chigier N.A.
Combustion Aerodynamics.
Robert E. Krieger Publishing Company, Inc. ISBN 0-89874-545-4, 1983. (cited on p. 33)

Beheshti Novid, Burluka AlexeyA. and Fairweather Michael.
Assessment of $\Sigma - Y$ liq model predictions for air-assisted atomisation.
Theoretical and Computational Fluid Dynamics, Vol. 21 n^o 5, pp. 381–397, 2007.
(cited on pp. 53, 60, 61, 136)

Belhadef A., Vallet A., Amielh M. and Anselmet F.
Pressure-swirl atomization: Modeling and experimental approaches.
International Journal of Multiphase Flow, Vol. 39, pp. 13 – 20, 2012.
(cited on pp. 61, 116, 117)

Benajes J., Novella R., Pastor J.M., Hernández-López A., Hasegawa M., Tsuji N., Emi M., Uehara I., Martorell J. and Alonso M.
Optimization of the combustion system of a medium duty direct injection diesel engine by combining CFD modeling with experimental validation.
Energy Conversion and Management, Vol. 110, pp. 212 – 229, 2016. (cited on p. 138)

Blokkeel G., Barbeau B. and Borghi R.
A 3D Eulerian Model to Improve the Primary Breakup of Atomizing Jet.
SAE Technical Paper 2003-01-005, 2003. (cited on pp. 38, 53)

Bondi A.
Estimation of Heat Capacity of Liquids.
Industrial & Engineering Chemistry Fundamentals, Vol. 5 n^o 4, pp. 442–449, 1966. (cited on p. 76)

Bracho G.C.
Experimental and theoretical study of direct diesel injection process at low temperatures.
Doctoral Thesis, Departamento de Máquinas y Motores Térmicos, Universidad Politécnica de Valencia, España, 2011. (cited on p. 90)

Brennen C.
An oscillating-boundary-layer theory for ciliary propulsion.
Journal of Fluid Mechanics, Vol. 65, pp. 799–824, 10 1974. (cited on p. 16)

Browne K., Partridge I. and Greeves G.
Fuel Property Effects on Fuel/Air Mixing in an Experimental Diesel Engine.
SAE Technical Paper, n^o 860223, 1986. (cited on p. 26)

Bruneaux Gilles.
Liquid and vapor spray structure in high-pressure common rail diesel injection.
Atomization and Sprays, Vol. 11 n^o 5, 2001. (cited on p. 71)

Candel S.M. and Poinsot T.J.
Flame Stretch and the Balance Equation for the Flame Area.
Combustion Science and Technology, Vol. 70 n^o 1-3, pp. 1–15, 1990. (cited on p. 59)

Chavez M.
Modelado CFD Euleriano-Lagrangiano del Chorro Diesel y evaluación de su combinación con modelos fenomenológicos y unidimensionales.
Doctoral Thesis, Departamento de Máquinas y Motores Térmicos, Universidad Politécnica de Valencia, España, 2013. (cited on p. 97)

Chiu W., Shahed S. and Lyn W.
A Transient Spray Mixing Model for Diesel Combustion.
SAE Technical Paper, n^o 760128, 1976. (cited on p. 34)

Corradini M. L., Blanchard J. P. and Baik S.
Development of micro-diesel injector nozzles via MEMS Technology and effects on spray characteristics.
Atomization and Sprays, Vol. 13 n^o 5&6, pp. 443–474, 2003. (cited on p. 102)

Correas D.
Estudio teórico–experimental del chorro libre Diesel isotermo.
Doctoral Thesis, Departamento de Máquinas y Motores Térmicos, Universidad Politécnica de Valencia, España, 1998. (cited on p. 33)

Dahms Rainer N., Manin Julien, Pickett Lyle M. and Oefelein Joseph C.
Understanding high-pressure gas-liquid interface phenomena in Diesel engines.
Proceedings of the Combustion Institute, Vol. 34 n^o 1, pp. 1667 – 1675, 2013. (cited on p. 53)

Dan T., Yamamoto, T. amd Senda J. and Fujimoto H.
Effect of nozzle configurations for characteristics of non-reacting diesel fuel sprays.
SAE technical paper, n^o 970355, 1997. (cited on p. 21)

Delacourt E., Desmet B. and Besson B.
Characterisation of very high pressure diesel sprays using digital imaging techniques.
Fuel, Vol. 84, pp. 859 – 867, 2005. (cited on p. 31)

Delhaye J.M., Giot M. and Riethmuller M.L.
Thermohydraulics of two-phase systems for industrial design and nuclear engineering.
Series in thermal and fluids engineering. Hemisphere Pub. Corp., 1981. (cited on p. 59)

Demoulin Francois-Xavier, Reveillon Julien, Duret B., Bouali Zakaria, Desjonqueres P. and Menard Thibaut.
Toward using direct numerical simulation to improve primary break-up modeling.
Atomization and Sprays, Vol. 23 n^o 11, pp. 957–980, 2013. (cited on pp. 53, 56)

Demoulin F.X., Beau P.A., Blokkeel G., Mura A. and Borghi R.
A New Model for Turbulent Flows with Large Density Fluctuations: application to Liquid Atomization.
Atomization and Sprays, Vol. 17, pp. 315–345, 2007. (cited on pp. 53, 56, 70)

Dent J.
A Basis for the Comparison of Various Experimental Methods for Studying Spray Penetration.
SAE Technical Paper, n^o 710571, 1971. (cited on p. 29)

Desantes J.M., García-Oliver J.M., Pastor J.M. and Pandal A.
A Comparison of Diesel Sprays CFD modelling approaches: DDM vs $\Sigma - Y$ Eulerian Atomization Model.
Atomization and Sprays, Vol. 26 n^o 7, pp. 713–737, 2016.
(cited on pp. 53, 90, 116, 129, 134, 156, 163)

Desantes J.M., García-Oliver J.M., Pastor J.M., Pandal A., Baldwin E. and Schmidt D.P.
Coupled/decoupled spray simulation comparison of the ECN spray a condition with the $\Sigma - Y$ Eulerian atomization model.
International Journal of Multiphase Flow, Vol. 80, pp. 89 – 99, 2016.
(cited on pp. 116, 117, 124)

Desantes J.M., Payri R., Salvador F.J. and Gil A.
Development and validation of a theoretical model for diesel spray penetration.
Fuel, Vol. 85 n^o 7-8, pp. 910 – 917, 2006. (cited on pp. 29, 33)

Desantes J.M., Payri R., Salvador F.J. and Soare V.
Study of the Influence of Geometrical and Injection Parameters on Diesel Sprays Characteristics in Isothermal Conditions.
SAE Technical Paper, n^o 2005-01-0913, 2005. (cited on pp. 30, 31)

Desantes J.M., Salvador F.J., López J.J. and De la Morena J.
Study of mass and momentum transfer in diesel sprays based on X-ray mass distribution measurements and on a theoretical derivation.
Experiments in Fluids, Vol. 50 n^o 2, pp. 233–246, 2011. (cited on pp. 33, 119)

Desantes José M., Pastor José V., García-Oliver José M. and Briceño Francisco J.
An experimental analysis on the evolution of the transient tip penetration in reacting Diesel sprays.
Combustion and Flame, Vol. 161 n^o 8, pp. 2137 – 2150, 2014. (cited on pp. 175, 176)

Desportes A., Zellat M., Desoutter G., Liang Y. and Ravet F.
Application of the Eulerian-Lagrangian Spray Atomization (ELSA) Model for the Diesel Injection Simulation.
In *THIESEL 2010 Conference on Thermo- and Fluid Dynamic Process in Diesel Engines*, 2010. (cited on p. 116)

Dukowicz John K.
A particle-fluid numerical model for liquid sprays.
Journal of Computational Physics, Vol. 35 n^o 2, pp. 229 – 253, 1980.
(cited on pp. 40, 116)

Dumouchel C.
On the experimental investigation on primary atomization of liquid streams.
Experiments in Fluids, Vol. 45 n^o 3, pp. 371–422, 2008. (cited on p. 19)

Eagle W.E., Musculus M.P.B., Malbec L.M. and Bruneaux G.
Measuring transient entrainment rates of a condfined vaporizing diesel jet.
ILASS Paper, 2014. (cited on p. 155)

Espey C. and Dec J.
The Effect of TDC Temperature and Density on the Liquid-Phase Fuel Penetration in a D. I. Diesel Engine.
SAE Technical Paper, n^o 952456, 1995. (cited on p. 26)

Faeth G.M.
Evaporation and combustion of sprays.
Progress in Energy and Combustion Science, Vol. 9 n^o 1-2, pp. 1–76, 1983.
(cited on p. 72)

Faeth G.M.
Mixing, transport and combustion in sprays.
Progress in Energy and Combustion Science, Vol. 13 n^o 4, pp. 293 – 345, 1987.
(cited on p. 4)

Faeth G.M.
Spray combustion phenomena.
Symposium (International) on Combustion, Vol. 26 n^o 1, pp. 1593 – 1612, 1996.
(cited on p. 22)

Faeth G.M, Hsiang L.-P and Wu P.-K.
Structure and breakup properties of sprays.
International Journal of Multiphase Flow, Vol. 21, Supplement, pp. 99 – 127, 1995.
Annual Reviews in Multiphase Flow 1995. (cited on p. 4)

Favre Alexandre J.A.
Équations des gaz turbulents compressibles.
Journal of Méchanique, Vol. 4 n^o 3, pp. 361–390, 1965. (cited on p. 55)

Favre Alexandre J.A.
Statistical equations of turbulent gases.
In *Problems of Hydrodynamics and Continuum Mechanics*, pp. 231–266. Soc. for Ind. and Appl. Mathematics, Philadelphia, 1969. (cited on p. 55)

Fedkiw Ronald P, Aslam Tariq, Merriman Barry and Osher Stanley.
A Non-oscillatory Eulerian Approach to Interfaces in Multimaterial Flows (the Ghost Fluid Method).
Journal of Computational Physics, Vol. 152 n^o 2, pp. 457 – 492, 1999. (cited on p. 40)

Ferziger J.H. and Peric M.
Computational Methods for Fluid Dynamics.
Springer, Berlin, 2002.
pp. 176–178. (cited on pp. 37, 39, 68, 91)

García-Oliver J.M.
Aportaciones al Estudio del Proceso de Combustión Turbulenta de Chorros en Motores Diesel de Inyección Directa.
Doctoral Thesis, Departamento de Máquinas y Motores Térmicos, Universidad Politécnica de Valencia, España, 2003. (cited on p. 27)

García-Oliver J.M., Pastor J.M., Pandal A., Trask N., Baldwin E. and Schmidt D.P.
Diesel Spray CFD Simulations based on the $\Sigma - Y$ Eulerian Atomization Model.
Atomization and Sprays, Vol. 23, pp. 71–95, 2013.
(cited on pp. 53, 67, 90, 100, 116, 129, 156)

Gimeno J.
Desarrollo y aplicación de la medida del flujo de cantidad de movimiento de un chorro Diesel.
Doctoral Thesis, Departamento de Máquinas y Motores Térmicos, Universidad Politécnica de Valencia, España, 2008. (cited on p. 14)

Gorokhovski Mikhael and Herrmann Marcus.
Modeling Primary Atomization.
Annual Review of Fluid Mechanics, Vol. 40, pp. 343–366, 2008. (cited on p. 4)

Guildenbecher D.R., López-Rivera C. and Sojka P.E.
Secondary atomization.
Experiments in Fluids, Vol. 46 n^o 3, pp. 371–402, 2009. (cited on p. 22)

Haenlein A.
Über den Zerfall eines Flüssigkeitsstrahles.
Forschung auf dem Gebiet des Ingenieurwesens A, Vol. 2 n^o 4, pp. 139–149, 1931.
(cited on p. 17)

Hankinson R. W. and Thomson G. H.
A New Correlation for Saturated Densities of Liquids and Their Mixtures.
AIChE Journal, Vol. 25 n^o 4, pp. 653–663, 1979. (cited on p. 74)

Hay N. and Jones P.
Comparison of the Various Correlations for Spray Penetration.
SAE Technical Paper, n^o 720776, 1972. (cited on p. 28)

Hayashi Kosuke, Hosoda Shogo, Tryggvason Gretar and Tomiyama Akio.
Effects of shape oscillation on mass transfer from a Taylor bubble.
International Journal of Multiphase Flow, Vol. 58, pp. 236 – 245, 2014. (cited on p. 37)

Hayashi Kosuke and Tomiyama Akio.
Interface Tracking Simulation of Mass Transfer from a Dissolving Bubble.
The Journal of Computational Multiphase Flows, Vol. 3 n^o 4, pp. 247–262, 2011.
(cited on p. 37)

Heywood J.
Internal Combustion Engine Fundamentals.
McGraw-Hill Education, 1988. (cited on pp. 26, 27)

Hinze J. O.
Turbulence.
New York, N.Y. : McGraw-Hill, 2nd edition edition, 1975. (cited on p. 33)

Hiroyasu H.
Experimental and Theoretical studies on the structure of fuel sprays in Diesel engines.
In *The Fifth International Conference on Liquid Atomization and Spray Systems, ICLASS-91, paper B*, 1991. (cited on p. 27)

Hiroyasu H. and Arai M.
Structures of Fuel Sprays in Diesel Engines.
SAE Technical Paper, n^o 900475, 1990. (cited on pp. 29, 30)

Hiroyasu H. and Kadota T.
Fuel droplet size distribution in Diesel combustion chamber.
SAE Technical Paper, n^o 740715, 1974. (cited on p. 32)

Hiroyasu H., Kadota T. and Arai M.
Development and Use of a Spray Combustion Modeling to Predict Diesel Engine Efficiency and Pollutant Emissions : Part 1 Combustion Modeling.
Bulletin of JSME, Vol. 26 n^o 214, pp. 569–575, 1983. (cited on p. 34)

Hirt C.W and Nichols B.D.
Volume of fluid (VOF) method for the dynamics of free boundaries.
Journal of Computational Physics, Vol. 39 n^o 1, pp. 201 – 225, 1981. (cited on p. 37)

Ishii M.
Thermofluid Dynamics of Two-phase Flows.
Eyrolles, Paris, France, 1975. (cited on pp. 58, 59)

Jasak H.
Error Analysis and Estimation for the Finite Volume Method with Applications to Fluid Flows.
Doctoral Thesis, Imperial College, 1996. (cited on p. 63)

Jasak H., Weller H.G. and Gosman A.D.
High resolution NVD differencing scheme for arbitrarily unstructured meshes.
International Journal for Numerical Methods in Fluids, Vol. 31 n^o 2, pp. 431–449, 1999.
(cited on p. 97)

Jones W.P and Launder B.E.
The prediction of laminarization with a two-equation model of turbulence.
International Journal of Heat and Mass Transfer, Vol. 15 n^o 2, pp. 301 – 314, 1972.
(cited on p. 70)

Kamimoto T., Yokota H. and Kobayashi H.
Effect of High Pressure Injection on Soot Formation Processes in a Rapid Compression Machine to Simulate Diesel Flames.
SAE Technical Paper, n^o 871610, 1987. (cited on p. 27)

Kastengren A., Ilavsky J., Viera J.P., Payri R., Duke D., Swantek A., Tilocco F.Z., Sovis N. and Powell C.F.
Measurements of Droplet Size in Shear-Driven Atomization Using Ultra-Small Angle X-Ray Scattering.
Fuel, 2016 (under review). (cited on pp. 117, 118, 135)

Kastengren A. and Powell C.F.
Spray density measurements using X-ray radiography.
Proceedings of the Institution of Mechanical Engineers, Part D: Journal of Automobile Engineering, Vol. 221 n^o 6, pp. 653–662, 2007. (cited on p. 22)

Kastengren A., Tilocco F. Z., Powell C. F., Manin J., Pickett L. M., Payri R. and Bazyn T.
Engine Combustion Network (ECN):Measurements of nozzle geometry and hydraulic behavior.
Atomization and Sprays, Vol. 22, pp. 1011–1052, 2012. (cited on pp. 117, 121)

Kastengren A.L., Tilocco F.Z., Duke D., Powell C.F., Moon S. and Zhang X.
Time-Resolved X-Ray Radiography of Diesel Injectors from the Engine Combustion Network.
In *12th Triennial International Conference on Liquid Atomization and Spray Systems*, pp. 2–6, 2012. (cited on pp. 22, 52, 117, 118, 122)

Kastengren Alan L., Powell Christopher F., Wang Yujie, Im Kyoung-Su and Wang Jin.
X-ray radiography measurements of diesel spray structure at engine-like ambient density.
Atomization and Sprays, Vol. 19 n^o 11, pp. 1031–1044, 2009.
(cited on pp. 22, 52, 117, 118, 123)

Kastengren Alan L., Tilocco F. Zak, Powell Christopher F., Manin Julien, Pickett Lyle M., Payri Raul and Bazyn Tim.
Engine Combustion Network (ECN): measurements of nozzle geometry and hydraulic behavior.
Atomization and Sprays, Vol. 22 n^o 12, pp. 1011–1052, 2012. (cited on p. 153)

Krzeczkowski S.A.
Measurement of liquid droplet disintegration mechanisms.
International Journal of Multiphase Flow, Vol. 6 n^o 3, pp. 227 – 239, 1980.
(cited on p. 22)

Lacaze Guilhem, Misdariis Antony, Ruiz Anthony and Oefelein Joseph C.
Analysis of high-pressure Diesel fuel injection processes using {LES} with real-fluid thermodynamics and transport.
Proceedings of the Combustion Institute, Vol. 35 n^o 2, pp. 1603 – 1611, 2015.
(cited on pp. 90, 129, 156)

Launder B. E., Reece G. J. and Rodi W.
Progress in the development of a Reynolds-stress turbulence closure.
Journal of Fluid Mechanics, Vol. 68, pp. 537–566, 4 1975. (cited on p. 35)

Lebas R.
Modélisation Eulérienne de l'Atomisation Haute Pression Influences sur la Vaporisation et la Combustion Induite.
Doctoral Thesis, Université de Rouen, 2007. (cited on p. 53)

Lebas R., Blokkeel G., Beau P.A. and Demoulin F.X.
Coupling Vaporization Model With the Eulerian-Lagrangian Spray Atomization (ELSA) Model in Diesel Engine Conditions.
SAE Technical Paper 2005-01-0213, 2005. (cited on p. 53)

Lebas R., Blokkeel G., Beau P.A. and Demoulin F.X.
ELSA model for atomization: to benefit of the Eulerian and Lagrangian descriptions of the liquid phase.
ICLASS Paper, 2006. (cited on p. 53)

Lebas R., Menard T., Beau P.A., Berlemont A. and Demoulin F.X.
Numerical simulation of primary break-up and atomization: DNS and modelling study.
International Journal of Multiphase Flow, Vol. 35 n^o 3, pp. 247 – 260, 2009.
(cited on pp. 38, 53, 73, 90, 116)

Lee Byung Ik and Kesler Michael G.
A generalized thermodynamic correlation based on three-parameter corresponding states.
AIChE Journal, Vol. 21 n^o 3, pp. 510–527, 1975. (cited on p. 73)

Lefebvre A.H.
Atomization and sprays.
Hemisphere Publishing Corporation, New York, 1989. (cited on pp. 16, 19, 20, 25)

Lin S. P. and Reitz R. D.
Drop and spray formation from a liquid jet.
Annual Review of Fluid Mechanics, Vol. 30 n^o 1, pp. 85–105, 1998. (cited on p. 19)

Linne M., Paciaroni M., Hall T. and Parker T.
Ballistic imaging of the near field in a diesel spray.
Experiments in Fluids, Vol. 40 n^o 6, pp. 836–846, 2006. (cited on p. 22)

Liu A. B., Mather D. and Reitz R. D.
Modeling the Effects of Drop Drag and Breakup on Fuel Sprays.
SAE Technical Paper, n^o 930072, 1993. (cited on p. 22)

Macian V., Bermudez V., Payri R. and Gimeno J.
New technique for determination of internal geometry of a diesel nozzle with the use of silicone methodology.
Experimental Techniques, Vol. 27 n^o 2, pp. 39–43, 2003. (cited on pp. 12, 89, 119)

Malmström Tor G., Kirkpatrick Allan T., Christensen Brian and Knapp-miller Kevin D.
Centreline velocity decay measurements in low-velocity axisymmetric jets.
Journal of Fluid Mechanics, Vol. 346, pp. 363–377, 9 1997. (cited on p. 33)

Manin J.
Analysis of mixing processes in liquid and vaporized sprays through LIF and Rayleigh Scattering measurements.
Doctoral Thesis, Departamento de Máquinas y Motores Térmicos, Universidad Politécnica de Valencia, España, 2011. (cited on p. 170)

Marble F.E. and Broadwell J.E.
The Coherent Flame Model for Turbulence Chemical Reactions.
Technical report, Project Squid Headquarters. Chaffee Hall, Purdue University, West Lafayette, Indiana, 1977. (cited on p. 59)

Martí-Aldaraví P.
Development of a computational model for a simultaneous simulation of internal flow and spray break-up of the Diesel injection process.
Doctoral Thesis, Departamento de Máquinas y Motores Térmicos, Universidad Politécnica de Valencia, España, 2014. (cited on pp. 58, 92, 106, 120)

McCarthy M.J. and Molloy N.A.
Review of stability of liquid jets and the influence of nozzle design.
The Chemical Engineering Journal, Vol. 7 n^o 1, pp. 1 – 20, 1974.
An International Journal of Research and Development. (cited on p. 19)

Meijer M., Malbec L.M., Bruneaux G. and Somers L.M.T.
Engine Combustion Network: "Spray A" basic measurements and advanced diagnostics.
ICLASS Paper, 2012. (cited on p. 153)

Ménard T., Tanguy S. and Berlemont A.
Coupling level set/VOF/ghost fluid methods: Validation and application to 3D simulation of the primary break-up of a liquid jet.
International Journal of Multiphase Flow, Vol. 33 n^o 5, pp. 510 – 524, 2007.
(cited on pp. 90, 129, 156)

Miesse C.C.
Correlation of Experimental Data on the Disintegration of Liquid Jets.
Industrial & Engineering Chemistry, Vol. 47 n^o 9, pp. 1690–1701, 1955.
(cited on pp. 19, 21, 106)

Morena J.
Estudio de la influencia de las características del flujo interno en toberas sobre el proceso de inyección Diésel en campo próximo.
Doctoral Thesis, Departamento de Máquinas y Motores Térmicos, Universidad Politécnica de Valencia, España, 2011. (cited on p. 16)

Mugele R. A. and Evans H. D.
Droplet Size Distribution in Sprays.
Industrial & Engineering Chemistry, Vol. 43 n^o 6, pp. 1317–1324, 1951.
(cited on p. 32)

Naber J. and Siebers D.
Effects of Gas Density and Vaporization on Penetration and Dispersion of Diesel Sprays.
SAE Technical Paper, n^o 960034, 1996. (cited on pp. 30, 31, 33, 118, 170, 171)

Narayanaswamy Krithika, Pepiot Perrine and Pitsch Heinz.
A chemical mechanism for low to high temperature oxidation of n-dodecane as a component of transportation fuel surrogates.
Combustion and Flame, Vol. 161 n^o 4, pp. 866 – 884, 2014. (cited on p. 80)

Navarro-Martinez S.
Large eddy simulation of spray atomization with a probability density function method.
International Journal of Multiphase Flow, Vol. 63, pp. 11 – 22, 2014. (cited on p. 53)

Ning W., Reitz R.D., Diwakar R. and Lippert A.M.
An Eulerian-Lagrangian spray and atomization model with improved turbulence modeling.
Atomization and Sprays, Vol. 19, pp. 727,739, 2009. (cited on p. 116)

Oefelein J., Dahms R. and Lacaze G.
Detailed Modeling and Simulation of High-Pressure Fuel Injection Processes in Diesel Engines.
SAE Int. J. Engines, Vol. 5 n^o 3, pp. 10, 2012. (cited on p. 53)

Oefelein J. C., Dahms R. N., Lacaze G., Manin J. L. and Pickett L. M.
Effects of Pressure on the Fundamental Physics of Fuel Injection in Diesel Engines.
ICLASS Paper, 2012. (cited on p. 53)

Ohnesorge Wolfgang V.
Die Bildung von Tropfen an Düsen und die Auflösung flüssiger Strahlen.
ZAMM - Journal of Applied Mathematics and Mechanics / Zeitschrift für Angewandte Mathematik und Mechanik, Vol. 16 n^o 6, pp. 355–358, 1936. (cited on pp. 17, 19)

Osher Stanley and Sethian James A.
Fronts propagating with curvature-dependent speed: Algorithms based on Hamilton-Jacobi formulations.
Journal of Computational Physics, Vol. 79 n^o 1, pp. 12 – 49, 1988. (cited on p. 37)

Park S. H., Suh H. K. and Lee C. S.
Effect of Cavitating Flow on the Flow and Fuel Atomization Characteristics of Biodiesel and Diesel Fuels.
Energy & Fuels, Vol. 22 n^o 1, pp. 605–613, 2008. (cited on p. 32)

Pastor J. V., López J. J., García-Oliver J. M. and Pastor J. M.
A 1D model for the description of mixing-controlled inert diesel sprays.
Fuel, Vol. 87 n^o 13–14, pp. 2871–2885, Octubre 2008. (cited on pp. 31, 34)

Pastor José V., Arrègle Jean, García José M. and Zapata L. Daniel.
Segmentation of diesel spray images with log-likelihood ratio test algorithm for non-Gaussian distributions.
Appl. Opt., Vol. 46 n^o 6, pp. 888–899, Feb 2007. (cited on p. 88)

Payri R., García-Oliver J. M., Bardi M. and Manin J.
Fuel temperature influence on diesel sprays in inert and reacting conditions.
Applied Thermal Engineering, Vol. 35 n^o 0, pp. 185–195, Marzo 2012. (cited on p. 31)

Payri R., García-Oliver J.M., Salvador F.J. and Gimeno J.
Using spray momentum flux measurements to understand the influence of diesel nozzle geometry on spray characteristics.
Fuel, Vol. 84 n^o 5, pp. 551 – 561, 2005. (cited on pp. 14, 116, 129, 156)

Payri R, Salvador F J, Gimeno J and Garcia A.
Flow regime effects over non-cavitating diesel injection nozzles.
Proceedings of the Institution of Mechanical Engineers, Part D: Journal of Automobile Engineering, Vol. 226, pp. 133–144, 2012. (cited on p. 88)

Payri R., Salvador F.J., Gimeno J. and de la Morena J.
Effects of nozzle geometry on direct injection diesel engine combustion process.
Applied Thermal Engineering, Vol. 29 n^o 10, pp. 2051 – 2060, 2009. (cited on p. 116)

Payri R., Salvador F.J., Gimeno J. and Novella R.
Flow regime effects on non-cavitating injection nozzles over spray behavior.
International Journal of Heat and Fluid Flow, Vol. 32 n^o 1, pp. 273 – 284, 2011.
(cited on p. 88)

Payri R., Salvador F.J., Gimeno J. and Zapata L.D.
Diesel nozzle geometry influence on spray liquid-phase fuel penetration in evaporative conditions.
Fuel, Vol. 87 n^o 7, pp. 1165 – 1176, 2008. (cited on p. 31)

Payri R., Tormos B., Salvador F.J. and Araneo L.
Spray droplet velocity characterization for convergent nozzles with three different diameters.
Fuel, Vol. 87 n^o 15–16, pp. 3176–3182, 2008. (cited on p. 88)

Payri Raul, Araneo Lucio, Shakal Joseph and Soare Vlad.
Phase doppler measurements: system set-up optimization for characterization of a diesel nozzle.
Journal of Mechanical Science and Technology, Vol. 22 n^o 8, pp. 1620–1632, 2008.
(cited on pp. 88, 102)

Payri Raul, García-Oliver Jose M., Xuan Tiemin and Bardi Michele.
A study on diesel spray tip penetration and radial expansion under reacting conditions.
Applied Thermal Engineering, Vol. 90, pp. 619 – 629, 2015. (cited on pp. 155, 175)

Pickett L., Manin J., Kastengren A. and Powell C.
Comparison of Near-Field Structure and Growth of a Diesel Spray Using Light-Based Optical Microscopy and X-Ray Radiography.
SAE Int. J. Engines, Vol. 7 n^o 2, 2014. (cited on pp. 22, 52, 117, 118, 122, 132)

Pickett L.M., Kook S. and Williams T.C.
Visualization of Diesel Spray Penetration, Cool-Flame, Ignition, High-Temperature Combustion, and Soot Formation Using High-Speed Imaging.
SAE Int. J. Engines, Vol. 2 n^o 1, pp. 439–459, 2009. (cited on p. 31)

Pickett L.M., Manin J., Genzale C.L., Siebers D.L., Musculus M.P.B. and Idicheria C.A.
Relationship between diesel fues spray vapor penetration/dispersion and local fuel mixture fraction.
SAE Int. J. Engines, Vol. 4, pp. 764–799, 2011. (cited on p. 153)

Pilch M. and Erdman C.A.
Use of breakup time data and velocity history data to predict the maximum size of stable fragments for acceleration-induced breakup of a liquid drop.
International Journal of Multiphase Flow, Vol. 13 n^o 6, pp. 741 – 757, 1987.
(cited on p. 22)

Pitzer Kenneth S., Lippmann David Z., Jr. R. F. Curl, Huggins Charles M. and Petersen Donald E.
The Volumetric and Thermodynamic Properties of Fluids. II. Compressibility Factor, Vapor Pressure and Entropy of Vaporization1.
Journal of the American Chemical Society, Vol. 77 n^o 13, pp. 3433–3440, 1955.
(cited on p. 77)

Pope S. B.
Turbulent Flows.
Cambridge University Press, 2000. (cited on pp. 35, 70, 97, 122, 156)

Post S.L. and Abraham J.
Modeling the outcome of drop – drop collisions in Diesel sprays.
International Journal of Multiphase Flow, Vol. 28 n^o 6, pp. 997 – 1019, 2002.
(cited on p. 24)

Prasad C. M. and Subir K.
An Investigation of the Influence of Back Pressure on the Diffusion of Mass and Momentum of Fuel in Diesel Spray.
ASME J. Eng. Power, pp. 1–11, 1976. (cited on pp. 33, 34)

Qian J. and Law C. K.
Regimes of coalescence and separation in droplet collision.
Journal of Fluid Mechanics, Vol. null, pp. 59–80, 1 1997. (cited on p. 24)

Ranz W.E.
Some experiments on orifice sprays.
The Canadian Journal of Chemical Engineering, Vol. 36 n^o 4, pp. 175–181, 1958.
(cited on pp. 21, 30)

Rayleigh L.
On The Instability Of Jets.
Proceedings of the London Mathematical Society, Vol. s1-10 n^o 1, pp. 4–13, 1878.
(cited on p. 16)

Rayleigh L.
On the Capillary Phenomena of Jets.
Proceedings of the Royal Society of London, Vol. 29 n^o 196-199, pp. 71–97, 1879.
(cited on p. 16)

Reid R.D., Prausnitz J.M. and Poling B.E.
The Properties of Gases and Liquids.
McGraw-Hill, 1987. (cited on pp. 63, 74)

Reitz R. and Bracco F.
On the Dependence of Spray Angle and Other Spray Parameters on Nozzle Design and Operating Conditions.
SAE Technical Paper, n^o 790494, 1979. (cited on p. 30)

Reitz R. D.
Atomization and other breakup regimes of a liquid jet.
Doctoral Thesis, 08544, Princeton, New Jersey, United States of America: Princeton University, 1978. (cited on pp. 17, 19, 21)

Reitz R. D.
Modeling Atomization Processes in High-Pressure Vaporizing Sprays.
Atomization and Spray Technology, Vol. 3, pp. 309–337, 1987. (cited on p. 110)

Reitz R. D. and Bracco F. V.
Mechanism of atomization of a liquid jet.
Physics of Fluids, Vol. 25 n^o 10, pp. 1730–1742, 1982. (cited on pp. 17, 21)

Reitz R. D. and Diwakar R.
Effect of Drop Breakup on Fuel Sprays.
SAE Technical Paper, n^o 860469, 1986. (cited on p. 16)

Reitz R. D. and Diwakar R.
Structure of High-Pressure Fuel Sprays.
SAE Technical Paper, n^o 870598, 1987. (cited on p. 16)

Reitz R. D., Liu Z. and Hwang S. S.
Breakup mechanisms and drag coefficients of High-Speed vaporizing liquid drops.
Atomization and Sprays, Vol. 6 n^o 3, pp. 353–376, 1996. (cited on p. 22)

Rife J. and Heywood J.
Photographic and Performance Studies of Diesel Combustion With a Rapid Compression Machine.
SAE Technical Paper, n^o 740948, 1974. (cited on p. 34)

Rowlinson John Shipley.
Liquids and liquid mixtures.
Butterworths, London, 1969. (cited on p. 76)

Sallam K. A. and Faeth G. M.
Surface Properties During Primary Breakup of Turbulent Liquid Jets in Still Air.
AIAA Journal, Vol. 41 n^o 8, pp. 1514–1524, Agosto 2003. (cited on pp. 90, 129, 156)

Salvador F.J., Carreres M., Jaramillo D. and Martínez-López J.
Analysis of the combined effect of hydrogrinding process and inclination angle on hydraulic performance of diesel injection nozzles.
Energy Conversion and Management, Vol. 105, pp. 1352 – 1365, 2015.
(cited on pp. 122, 125)

Salvador F.J., Carreres M., Jaramillo D. and Martínez-López J.
Comparison of microsac and VCO diesel injector nozzles in terms of internal nozzle flow characteristics.
Energy Conversion and Management, Vol. 103, pp. 284 – 299, 2015.
(cited on pp. 122, 125)

Salvador F.J., Gimeno J., Pastor J.M. and Martí-Aldaraví P.
Effect of turbulence model and inlet boundary condition on the Diesel spray behavior simulated by an Eulerian Spray Atomization (ESA) model.
International Journal of Multiphase Flow, Vol. 65, pp. 108–116, 2014.
(cited on pp. 116, 120, 122, 125)

Sangiah D.K. and Ganippa L.C.
Application of spray impingement technique for characterisation of high pressure sprays from multi-hole diesel nozzles.
International Journal of Thermal Sciences, Vol. 49 n^o 2, pp. 409 – 417, 2010.
(cited on p. 14)

Schmidt D. P. and Corradini M. L.
The internal flow of diesel fuel injector nozzles: a review.
Journal of Engine Research, Vol. 2 n^o 1, pp. 1–22, 2001. (cited on p. 4)

Siebers D.
Liquid-Phase Fuel Penetration in Diesel Sprays.
SAE Technical Paper, n^o 980809, 1998. (cited on pp. 26, 27, 31, 53, 71, 164, 168)

Siebers D.
Scaling Liquid-Phase Fuel Penetration in Diesel Sprays Based on Mixing-Limited Vaporization.
SAE Technical Paper, n^o 1999-01-0528, 1999. (cited on p. 27)

Sirignano W.A.
Fluid Dynamics and Transport of Droplets and Sprays.
Cambridge University Press, 1999. (cited on p. 26)

Soare V.
Phase doppler measurement in diesel dense sprays: optimisation of measurements and study of the orifice geometry influence over the spray at microscopic level.
Doctoral Thesis, Departamento de Máquinas y Motores Térmicos, Universidad Politécnica de Valencia, España, 2007. (cited on p. 32)

Som S., Longman D.E., Ramírez A.I. and Aggarwal S.K.
A comparison of injector flow and spray characteristics of biodiesel with petrodiesel.
Fuel, Vol. 89 n^o 12, pp. 4014 – 4024, 2010. (cited on pp. 116, 122, 125)

Som Sibendu, Ramírez Anita I., Longman Douglas E. and Aggarwal Suresh K.
Effect of nozzle orifice geometry on spray, combustion, and emission characteristics under diesel engine conditions.
Fuel, Vol. 90 n^o 3, pp. 1267 – 1276, 2011. (cited on p. 116)

Soteriou C., Andrews R. and Smith M.
Direct Injection Diesel Sprays and the Effect of Cavitation and Hydraulic Flip on Atomization.
SAE Technical Paper, n^o 950080, 1995. (cited on p. 16)

Spalding D. B.
Combustion and Mass Transfer.
Pergamon Press, ISBN 0-08-022105-8, 1979. (cited on p. 33)

Sterling A. M. and Sleicher C. A.
The instability of capillary jets.
Journal of Fluid Mechanics, Vol. 68, pp. 477–495, 4 1975. (cited on p. 21)

Suh H. K. and Lee C. S.
Effect of cavitation in nozzle orifice on the diesel fuel atomization characteristics.
International Journal of Heat and Fluid Flow, Vol. 29 n^o 4, pp. 1001 – 1009, 2008. (cited on p. 32)

Sussman Mark, Smereka Peter and Osher Stanley.
A Level Set Approach for Computing Solutions to Incompressible Two-Phase Flow.
Journal of Computational Physics, Vol. 114 n^o 1, pp. 146 – 159, 1994. (cited on p. 39)

Tait P. G.
Physics and Chemistry of the Voyage of H.M.S, volume 2.
Challenger. HMSO, London, 1888. (cited on p. 75)

Tanguy Sébastien and Berlemont Alain.
Application of a level set method for simulation of droplet collisions.
International Journal of Multiphase Flow, Vol. 31 n^o 9, pp. 1015 – 1035, 2005. (cited on p. 40)

Thomson G. H., Brobst K. R. and Hankinson R. W.
An Improved Correlation Compressed Liquids and Liquid Mixtures.
AIChE Journal, Vol. 28 n^o 4, pp. 671–676, 1982. (cited on p. 75)

Tindal M.J., Williams T.J. and Harcombe A.T.
Fuel spray modelling in swirling flows.
ASME ICE, Vol. 6, pp. 51–60, 1989. (cited on p. 33)

Torda T. P.
Evaporation of drops and breakup of sprays.
Astronautica Acta, Vol. 18, pp. 383–393, 1973. (cited on p. 19)

Trask N.
Implementation of an Eulerian atomization model to characterize primary spray formation.
Master's thesis, University of Massachusetts Amherst, 2010. (cited on p. 52)

Trask N., Schmidt D.P., Lightfoot M.D.A. and Danczyk S.A.
Compressible Modeling of the Internal Flow in a Gas-Centered Swirl-Coaxial Fuel Injector.
Journal of Propulsion and Power, Vol. 28(4), pp. 685–693, 2012.
(cited on pp. 63, 67, 68)

Unverdi Salih Ozen and Tryggvason Grétar.
A front-tracking method for viscous, incompressible, multi-fluid flows.
Journal of Computational Physics, Vol. 100 n^o 1, pp. 25 – 37, 1992. (cited on p. 37)

Vallet A. and Borghi R.
Modélisation Eulerienne de l'atomisation d'un jet liquide.
C.R. Acad. Sci, Paris, Vol. 327, pp. 1015–1020, 1999. (cited on pp. 4, 38, 52, 53, 59)

Vallet A., Burluka A.A. and Borghi R.
Development of a Eulerian Model for the Atomization of a Liquid Jet.
Atomization and Sprays, Vol. 11, pp. 619–642, 2001. (cited on pp. 53, 56, 60, 61, 71)

Versteeg H. K. and Malalasekera W.
An Introduction to Computational Fluid Dynamics.
Pearson, 2007. (cited on p. 36)

Wakuri Y., Fujii M., Amitani T. and Tsuneya R.
Studies on the Penetration of Fuel Spray in a Diesel Engine.
Bulletin of the Japan Society of Mechanical Engineers, Vol. 3 n^o 9, 1960. (cited on p. 29)

Wang, Y. andGrover R.O., Schmidt D.P., Diwakar R. and Kuo T.-W.
Application of Interface Area Density Modeling to Define Spray Plume Boundary.
ILASS Paper, 2015. (cited on p. 62)

Wang Y., Lee W., Reitz R. and Diwakar R.
Numerical Simulation of Diesel Sprays Using an Eulerian-Lagrangian Spray and Atomization (ELSA) Model Coupled with Nozzle Flow.
SAE Technical Paper, n^o 2011-01-0386, 2011. (cited on pp. 61, 117, 136)

Weber C.
Disintegration of Liquid Jets.
Z. Angew., Math. Mech., Vol. 11 n^o 2, pp. 136–154, 1931. (cited on p. 17)

Weller H.G., Tabor G., Jasak H. and Fureby C.
A Tensorial Approach to Computational Continuum Mechanics Using Object-Oriented Techniques.
Computers in Physics, Vol. 12, pp. 620–631, 1998. (cited on p. 52)

Wierzba A.
Deformation and breakup of liquid drops in a gas stream at nearly critical Weber numbers.
Experiments in Fluids, Vol. 9, pp. 59–64, Abril 1990. (cited on pp. 22, 23)

Winklinger J.F.
Implementation of a Combustion Model based on the Flamelet Concept and its Application to turbulent reactive Sprays.
Doctoral Thesis, Departamento de Máquinas y Motores Térmicos, Universidad Politécnica de Valencia, España, 2014. (cited on pp. 5, 36, 78, 79, 80, 173, 174)

Xue Q., Battistoni M., Powell C.F., Longman D.E., Quan S.P., Pomraning E., Senecal P.K., Schmidt D.P. and Som S.
An Eulerian CFD model and X-ray radiography for coupled nozzle flow and spray in internal combustion engines.
International Journal of Multiphase Flow, Vol. 70 n^o 0, pp. 77 – 88, 2015.
(cited on pp. 116, 117, 124)

Xue Q., Battistoni M., Som S., Quan S.P., Senecal P. K., Pomraning E. and Schmidt D. P.
Eulerian CFD Modeling of Coupled Nozzle Flow and Spray with Validation against X-ray Radiography Data.
SAE Int. J. Engines, Vol. 7(2), pp. 1061–1072, 2014. (cited on pp. 116, 117)

Yeh C., Kamimoto T., Kobori S. and Kosaka H.
2-D Imaging of Fuel Vapor Concentration in a Diesel Spray via Exciplex-Based Fluorescence Technique.
SAE Technical Paper, n^o 932652, 1993. (cited on p. 26)

Yue Y., Powell C. F., Poola R., Wang J. and Schaller J. K.
Quantitative measurements of Diesel fuel spray characteristics in the near-nozzle region using X-Ray absorption.
Atomization and Sprays, Vol. 11 n^o 4, pp. 471–490, 2001. (cited on p. 22)